ISSN 0915-6348

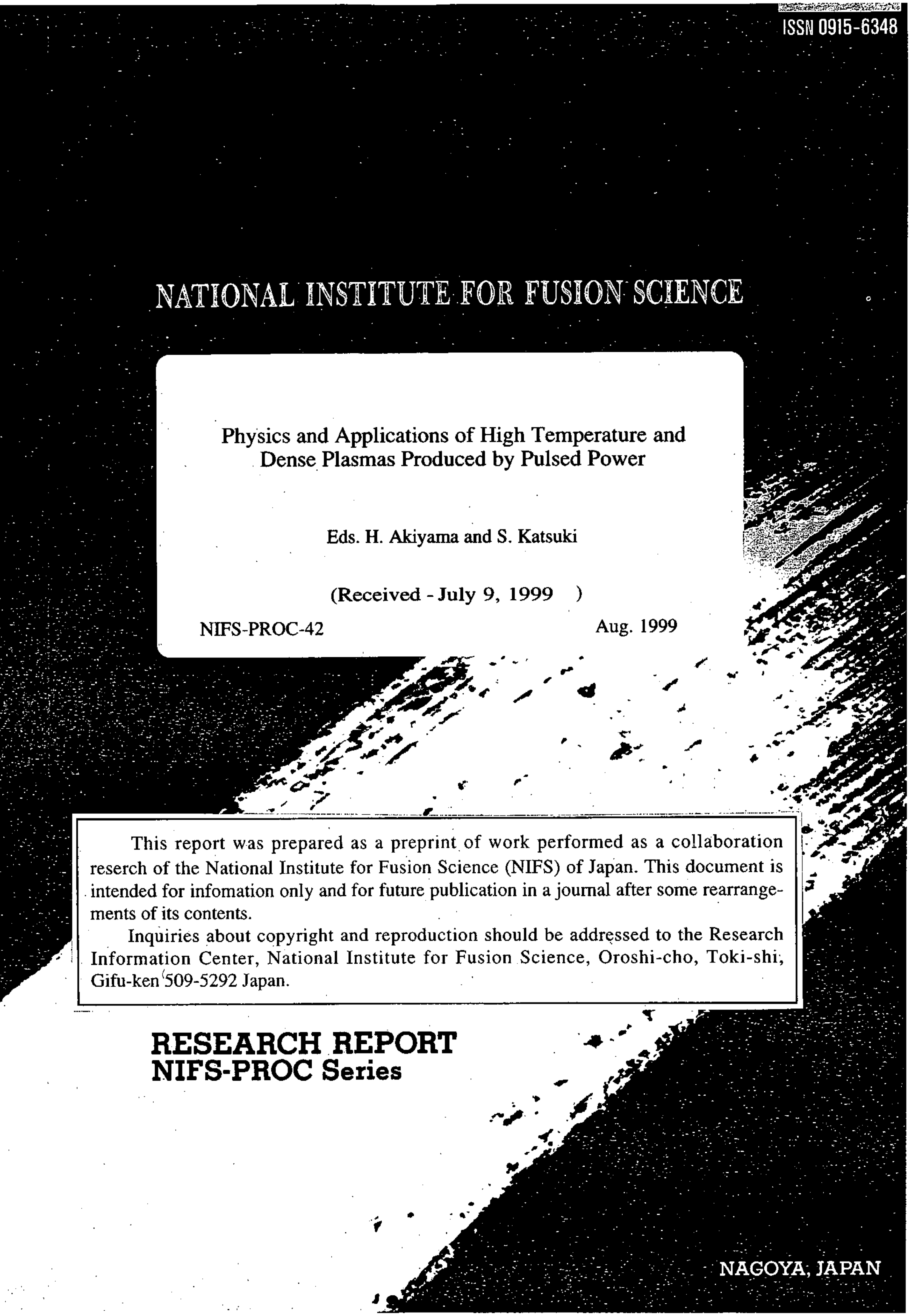

NATIONAL INSTITUTE FOR FUSION SCIENCE

Physics and Applications of High Temperature and Dense Plasmas Produced by Pulsed Power

Eds. H. Akiyama and S. Katsuki

(Received - July 9, 1999)

NIFS-PROC-42 Aug. 1999

RESEARCH REPORT
NIFS-PROC Series

NAGOYA, JAPAN

Physics and Applications of High Temperature and Dense Plasmas Produced by Pulsed Power

Edited by H. Akiyama and S. Katsuki

December 17-18, 1998
National Institute for Fusion Science
Toki, Japan

Abstract

This is the proceedings of the symposium on "Physics and Applications of High Temperature and Dense Plasmas Produced by Pulsed Power" held at National Institute for Fusion Science. Recent progress of experimental and theoretical works on high temperature and density plasmas produced by pulsed power is presented.

Keywords: high energy density plasma, z-pinch, pulsed power, ion beam, electron beam, soft x-ray, plasma focus, high power microwave

PREFACE

This publication is a collection of papers presented at the research meeting on "Physics and Applications of High Temperature and Dense Plasmas Produced by Pulsed Power" held at National Institute for Fusion Science in December 17-18, 1998, in which fifty two persons attended from the eighteen organizations, and twenty five papers were given orally.

High temperature and dense plasmas are able to be produced by pulsed power, which is an extremely large power with a short pulse width. Physics and applications of these plasmas were presented.

The researchers from different kinds of fields attended to discuss the physics and applications of high temperature and dense plasmas, which are common targets to all attendants.

Hidenori Akiyama
Sunao Katsuki
Kumamoto University

Contents

List of Participants

H. Akiyama	Kumamoto University	akiyama@eecs.kumamoto-u.ac.jp
R. Ando	Kanazawa University	ando@plasma.s.kanazawa-u.ac.jp
T. Atsumura	Toyama University	
M. Aulerian	Nagaoka Institute of Technology	marcu@stan.nagaokaut.ac.jp
B. Han	Gunma University	m8e672@edu.cc.gunma-u.ac.jp
H. Hanashima	Tokyo Institute of Technology	
D. Hasegawa	Kanazawa University	daisuke@plasma.s.kanazawa-u.ac.jp
N. Hashimoto	Nagaoka Institute of Technology	nozomu@stn.nagaokaut.ac.jp
Y. Hashimoto	Kobe National College of Technology	dhashimo@kobe-kosen.ac.jp
T. Hayashida	Himeji Institute of Technology	shayasid@elct.eng.himeji-tech.ac.jp
K. Hirano	Gunma University	hirano@cc.gunma-u.ac.jp
K. Hiraoka	Tokyo Institute of Technology	
K. Horioka	Tokyo Institute of Technology	khorioka@es.titech.ac.jp
S. Ifuka	Tokyo Institute of Technology	ifuka@ee.titech.ac.jp
H. Ishihara	Tokyo Institute of Technology	ishihara@iyl.ee.titech.ac.jp
S. Ishii	Tokyo Institute of Technology	ishii@ee.titech.ac.jp
K. Kamada	Kanazawa University	kkamada@plasma.s.kanazawa-u.ac.jp
M. Kashani	Nihon University	kashani@shotgun.phys.cst.nihon-u.ac.jp
S. Katsuki	Kumamoto University	katsuki@eecs.kumamoto-u.ac.jp
Y. Kawasaki	Tokyo Institute of Technology	kawasaki@iyl.ee.titech.ac.jp
K. Kinbara	Toyama University	
S. Kurashima	Nagaoka Institute of Technology	noel@stn.nagaokaut.ac.jp
I.V. Lisitsyn	Kumamoto University	lisitsyn@eecs.kumamoto-u.ac.jp
H. Maeda	Gunma University	m8e622@edu.cc.gunma-u.ac.jp
T. Majima	Ishikawajima-Harima Heavy Industries, Co. Ltd.	Takashi_Majima@ihi.co.jp
H Maruyama	Gunma University	m8e625@edu.cc.gunma-u.ac.jp
K. Masugata	Toyama University	masugata@eng.toyama-u.ac.jp
K. Masuzaki	Kanazawa University	masuzaki@plasma.s.kanazawa-u.ac.jp
H. Matsuzawa	Yamanashi University	matuzawa@es.yamanashi.ac.jp
Y. Mitamura	Nihon University	mitamura@shotgun.phys.cst.nihon-u.ac.jp
T. Miyamoto	Nihon University	miyamoto@phys.cst.nihon-u.ac.jp
R. Morita	Himeji Institute of Technology	srmorita@elct.eng.himeji-tech.ac.jp
A. Muravich	Nihon University	muravich@shotgun.phys.cst.nihon-u.ac.jp
T. Nakamura	Tokyo Institute of Technology	takehiko@iyl.ee.titech.ac.jp

T. Nakasendo	Gunma University	m7e626@edu.cc.gunma-u.ac.jp
M. Ogawa	Tokyo Institute of Technology	mogawa@nr.titech.ac.jp
K. Ogura	Niigata University	teogura@eng.niigata-u.ac.jp
Y. Ono	Gunma University	m8e608@edu.cc.gunma-u.ac.jp
M. Sato	Gunma University	satom@el.gunma-u.ac.jp
N. Sato	Nihon University	naoto@shotgun.phys.cst.nihon-u.ac.jp
N. Shimomura	The University of Tokushima	simomura@ee.tokushima-u.ac.jp
M. Sonoda	Tokyo Institute of Technology	sonoda@iyl.ee.titech.ac.jp
S. Suzuki	Tokyo Institute of Technology	ssuzuki@iyl.ee.titech.ac.jp
K. Takasugi	Nihon University	takasugi@phys.cst.nihon-u.ac.jp
T. Tazima	National Institute for Fusion Science	tazima@nifs.ac.jp
A. Tokuchi	Nichicon Corporation	tokuchi@nichicon.co.jp
T. Yamamoto	Fukushima National College of Technology	yamamoto@fukushima-nct.ac.jp
D. Yamamura	Toyama University	
T. Yanagidaira	Gunma University	d5e032@cc.gunma-u.ac.jp
K. Yatsui	Nagaoka Institute of Technology	yatsui@nagaokaut.ac.jp
M. Yatsuzuka	Himeji Institute of Technology	yatuzuka@elct.eng.himeji-tech.ac.jp
H. Yoshida	Kanazawa University	yoshida@plasma.s.kanazawa-u.ac.jp

Observation of an Intense Pulsed Ion Beam Irradiated Ti Surface

Yoshiyuki Hashimoto and Mitsuyasu Yatsuzuka*

Department of Electronic Engineering, Kobe City College of Technology,
8-3 Gakuen-Higashimachi Nishiku, Kobe, Hyogo 651-2194

*Department of Electrical Engineering, Himeji Institute of Technology,
2167 Shosha, Himeji, Hyogo 671-2201

Abstract

The pure Ti was irradiated with intense pulsed ion beams (76MW/cm^2, 65 nsec) of 1 shot. An AFM observation show that the average values of the surface roughness of the IPIB irradiated Ti reduces to 1/6 of that of the IPIB non-irradiated Ti. It is found that the high frequency component (>5Hz) of surface envelope is decreased in IPIB irradiated Ti from measurement of surface roughness tester. These results indicate that the target Ti surface is smooth by the IPIB irradiation in this experimental condition.

§1. Introduction

Intense pulsed ion beams (IPIBs) with the medium energy density up to 10 J/cm^2 have been used as a tool for material surface processing[1-6]. The IPIB irradiation of target results in rapid heating of the target surface above its melting point. After the beam is turned off, the heated region is immediately cooled down by thermal conduction at a fast cooling rate typical of 10^6 - 10^9 °C/sec. Such a rapid cooling and resolidification of the heated region produces nonequilibrium micro structures such as amorphous and nanostructured phases. We have already succeeded in production of nanostructured crystallites on a pure Ti surface and an amorphous layer on a nickel alloy by an IPIB irradiation[3-6]. In this paper, we report the results of observation of IPIB irradiated Ti surface.

§2. Production of Intense Pulsed Ion Beams

Figure 1 shows a schematic drawing of experimental setup. A pulsed power generator "HARIMA-II" (400kV, 3Ω and 50ns) at Himeji institute of technology was used as a power supply. An IPIB was produced by an inverse pinch ion diode (IPD)[7,8] consisted with a ring anode (diameter: 50 mm) and an annular cathode (diameter: 16 mm). An acrylic plate (thickness: 2 mm) was attached to the anode surface as an ion source. Then, the dominant ion species was hydrogen. The anode-cathode (A-K) gap length was 3 mm. The typical pressure for diode operation was in the range of 10^{-3} Pa. A resistive voltage divider and a single-pinhole biased ion collector were used to measure the diode voltage and the ion beam current density, respectively. A target was pure Ti, which was polished with emery paper (#1000) and annealed in a vacuum. The target Ti was located at the focal point 120 mm from anode for IPIB irradiation. The surface of Ti targets were examined using scanning electron microscope (SEM) and atomic force microscope (AFM). A surface roughness of the target was estimated with a surface roughness tester.

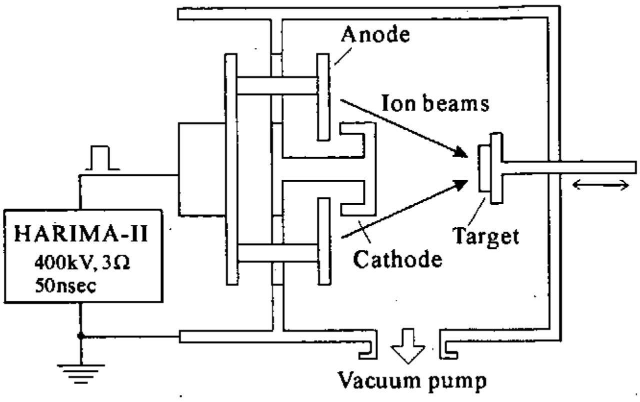

Fig.1. Experimental setup for IPIB irradiation.

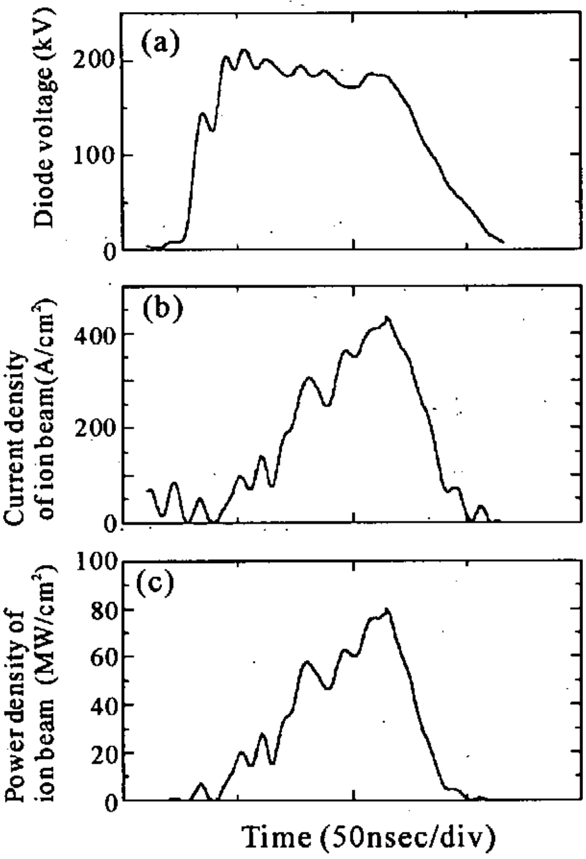

Fig.2 Typical time evolution of diode voltage, ion beam current density and ion beam power density.

Figure 2 shows the typical time history of (a) a diode voltage, (b) an ion beam current density at 120 mm behind the anode, and (c) an ion beam power density calculated with the diode voltage and the ion beam current density, respectively. As seen in Fig.2, the maximum accelerating voltage, current density and pulse duration of ion beams were 180 kV, 450 A/cm^2 and 65 nsec, respectively. The ion beam power density is not constant in time and has the largest value of 80 MW/cm^2. The total beam energy is estimated to be 4.02 J/cm^2 by integrating the power density with respect to time. We assume the ideal rectangular beam with the same total beam energy as 4.02 J/cm^2 estimated above. Supposing that the pulse duration equals to the FWHM value of 65 nsec in Fig. 2, we obtain the uniform power density of 76 MW/cm^2. The dominant ion species was H$^+$[8].

§3. Results and Discussion

To investigate the effect of IPIB irradiation on the surface roughness, target Ti was irradiated with the IPIB (76MW/cm^2, 65 nsec) of 1 shot. Figure 3 shows the SEM micrograph of (a) the IPIB non-irradiated and (b) the IPIB irradiated Ti surface. Transverse Scratches produced by polishing as pretreatment were found on the IPIB non-irradiated Ti surface in Fig.3 (a). After IPIB radiation, these scratches almost disappear on the target surface in Fig.3 (b). Simultaneously, there are some new damages as a crater on the IPIB irradiated Ti surface.

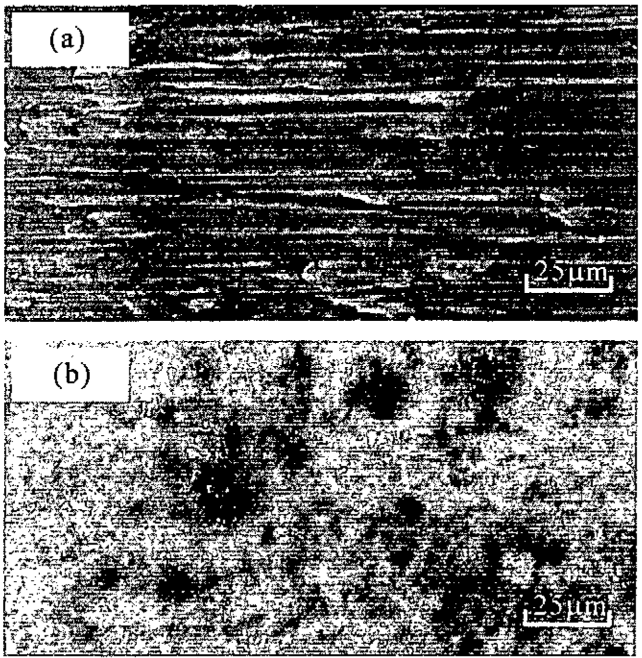

Fig.3 The SEM micrograph of (a) the IPIB non-irradiated Ti surface and (b) the IPIB irradiated Ti surface.

Figure 4 shows the topography of the target surface observed by AFM, where (a) the IPIB non-irradiated Ti surface and (b) the IPIB irradiated Ti surface, respectively. As seen in Fig.4, the existence of deep scratches on the IPIB non-irradiated Ti surface was confirmed. Besides, it is found that the target Ti surface in Fig.4 (b) is almost smooth by the IPIB irradiation. This result is in good agreement with the result of the SEM observation. Table 1 gives numerical results of the surface roughness estimated by the AFM, where R_a is the average values of the surface roughness and P_V is the difference between the bottom and the top of the envelope in the target Ti surface. It is found that R_a of the IPIB irradiated Ti reduces to 1/6 of that of the IPIB non-irradiated Ti. Furthermore, P_V was decreased from 730 nm to 160 nm by the IPIB irradiation.

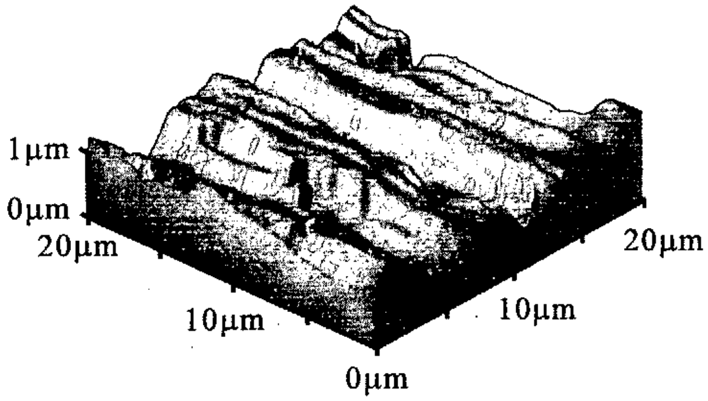

(a) IPIB non-irradiated Ti

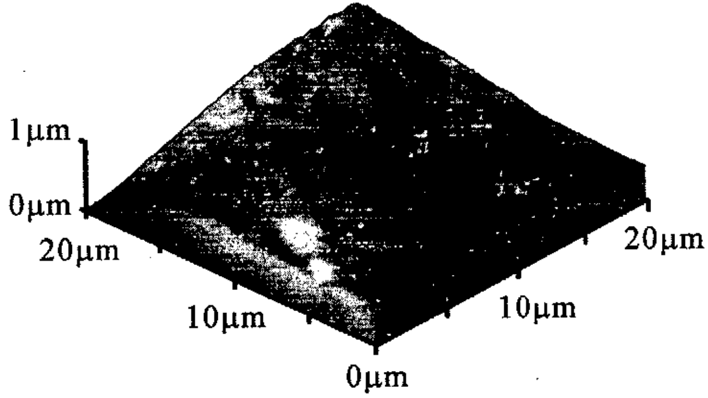

(b) IPIB irradiated Ti

Fig.4 The topography of the Ti target observed by AFM.

Table.1 Comparison of surface roughness, where R_a is the average values of the surface roughness and P_v is the difference between the bottom and the top of the envelope in the target Ti surface.

	R_a (nm)	P_v (nm)
IPIB non-irradiated Ti	161	730
IPIB irradiated Ti	27	160

Next, a surface roughness in range of 1 mm in the target Ti was measured by a surface roughness tester. Figure 5 shows envelopes of (a) IPIB non-irradiated Ti surface and (b) IPIB irradiated Ti surface, respectively. From Fig.5, it is seen that the amplitude of the envelope in the target surface is reduced by the IPIB irradiation. Here, the envelope of the target surface can be assumed a periodic function. Therefore, the envelopes of the target surface shown in Fig.5 were performed Fourier analysis. These results are shown in Fig.6 (a) IPIB non-irradiated Ti and (b) IPIB irradiated Ti, where frequency f_s is defined by the wave number in 1 mm length. In Fig.6, a high frequency (>5Hz) component of target Ti surface is decreased and a low frequency component is increased after IPIB irradiation. This result indicates that the IPB irradiated Ti surface has gentle slope.

From the experimental results described above, it is clear that the target Ti surface is smooth by the IPIB irradiation in this experimental condition.

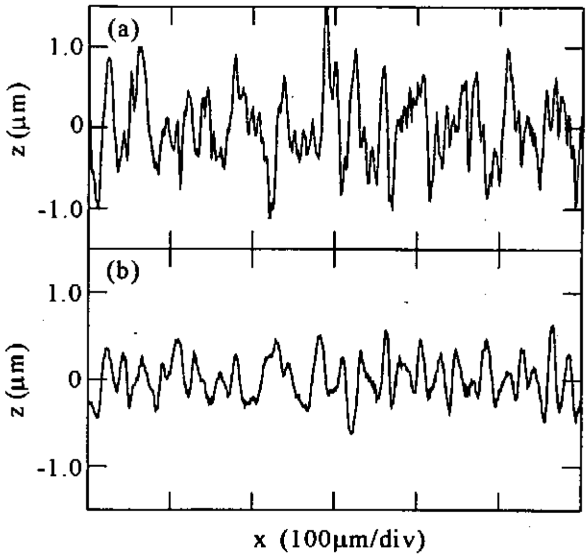

Fig.5 Surface observation of the target Ti by a surface roughness tester, where (a) the IPIB non-irradiated Ti and (b) the IPIB irradiated Ti.

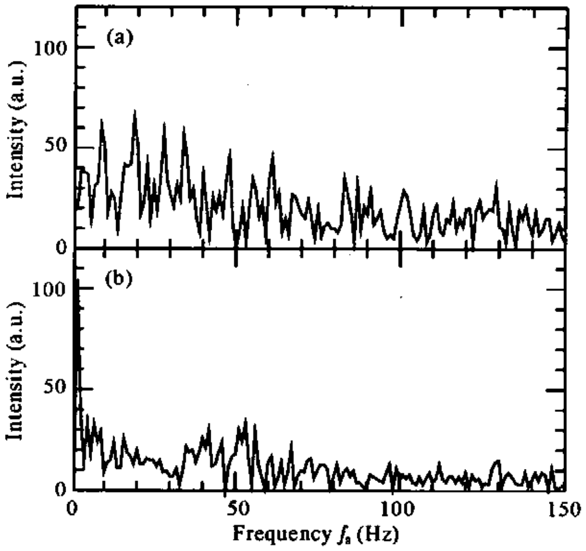

Fig.6 Comparison of the frequency component of (a) the IPIB non-irradiated Ti surface and (b) the IPIB irradiated surface.

§4. Conclusion

The target Ti was irradiated with the IPIB (76MW/cm^2, 65 nsec) of 1 shot. As a result, the average values of the surface roughness of the IPIB irradiated Ti reduces to 1/6 of that of the IPIB non-irradiated Ti. It is found that the high frequency component (>5Hz) of target Ti surface is decreased and a low frequency component is increased after IPIB irradiation. These results indicate that the target Ti surface is smooth by the IPIB irradiation in this experimental condition.

References

[1] G. E. Remnev and V. A. Shulov: Laser and Particle Beams **11** (1993) 707.

[2] E. L. Neau: IEEE Trans. on Plasma Science **22** (1994) 2.

[3] M. Yatsuzuka, T. Yamasaki, H. Uchida and Y. Hashimoto: Appl. Phys. Lett. **67** (1995) 206.

[4] M. Yatsuzuka, Y. Hashimoto, T. Yamasaki and H. Uchida: Jpn. J. Appl. Phys. **35** (1996) 1857.

[5] Y. Hashimoto, M. Yatsuzuka, H. Uchida, and T. Yamasaki: *Proc. of 11th Int Conf. on High Power Particle Beams* (Praque, 1996) Vol.2, p.848.

[6] Y. Hashimoto, M. Yatsuzuka, H. Uchida, and T. Yamasaki: *Proc. 1996 Int. conf. on Plasma Physics* (Nagoya, 1996) Vol.2, p.1406.

[7] Y. Hashimoto, M. Sato, M. Yatsuzuka and S. Nobuhara: Jpn. J. Appl. Phys. **31** (1992) 1922.

[8] Y. Hashimoto, M. Yatsuzuka, and S. Nobuhara: Jpn. J. Appl. Phys. **32** (1993) 4838.

Focusing Characteristics of a Melt-Processed YBCO Superconducting Tube (Supertron) for Intense Electron Beams

Hidenori MATSUZAWA, Yoshinori WATANABE, Koji MIKAMI, and Kenjirou FUKASAWA
Faculty of Engineering, Yamanashi University, Kofu 400-8511

Abstract: Previously we proposed a double-layered superconducting tube consisting of an inner powder-pressed high-T_c Bi(2223) tube and an outer melt-processed high-T_c Y(123) tube. The tube thus assembled will focus electron beams ranging from single short-pulsed to continuous electron beams. This is because the inner powder-pressed tube focuses single short-pulsed electron beams effectively as our many experimental results had demonstrated and the outer melt-processed tube will focus continuous electron beams because of its high flux-pinning force and few grain boundaries through which magnetic fields of electron beams diffuse. In this paper, as the first step toward realizing such a double-layered tube (Supertron), a melt-processed (MPMG) YBCO tube (an outer and inner diameters of 22 and 20 mm, respectively) was examined for single short-pulsed electron beams (~340 keV, ~1 kA, and ~10 ns) for the range from 70 K to room temperature.

INTRODUCTION

Since the discovery of the high-T_C superconductor [1], we have demonstrated a novel lens named *Supertron* [2] made from high-T_C superconducting tubes to focus and guide electron beams. We think that Supertrons will be applicable to ion beams, too. The principle of Supertrons is as follows: When electron beams are injected into superconducting tubes along their axes, the self-magnetic fields of the beams are confined within the bores of the tubes owing to the Meissner effect and shielding effect. The fields thus confined are enhanced through their compression. Then, these fields focus the beams themselves to thinner ones. When the tube axis is zigzaged, the electron beams propagate along the the axis as in wigglers of free electron lasers [2, 3].

Our previous experimental results [2] showed that powder-pressed Bi(2223) Supertrons are most suitable for focusing single short-pulsed electron beams (~340 keV, ~1 kA, ~10 ns), while melt-processed Y(123) Supertrons are least effective for the electron beams among the lenses examined: a melt-processed and powder-pressed Y(123) lenses, a melt-processed Bi(2212) lens, a powder-pressed Bi(2223) lens, a powder-pressed Tl-compound lens, and a copper-block made lens. To explain these results we proposed a "ferrite-core model" [2, 4]. This is because Supertrons are likely to operate in a way similar to that of ferrite cores.

To focus and guide both single pulsed and continuous electron beams with a single Supertron, we proposed [5] a double-layered Supertron which consists of an inner powder-pressed tube and an outer melt-processed tube (Fig. 1). When a pulsed electron beam

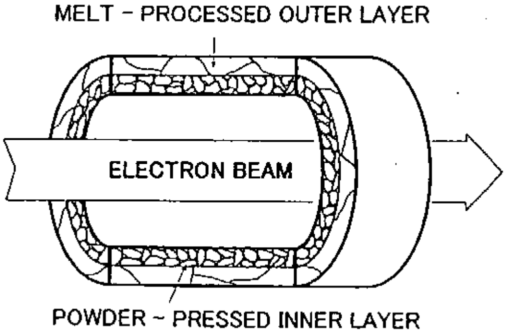

Fig. 1. Schematic structure of double-layered Supertrons.

enters the double-layered tube, the inner powder-pressed tube focuses the beam effectively as the ferrite-core model explains. When a continuous electron beam is injected, then the outer melt-processed tube will focus the beam because of its few grain boudaries through which self-magnetic fields of continuous electron beams diffuse. This paper describes the focusing characteristics of a melt-processed YBCO Supertron for single short-pulsed electron beams as the basic data for a double-layered Supertron. We had already reported focusing characteristics of powder-pressed Bi(2223) Supertrons in previous papers [6, 7].

Roth treated Supertrons theoretically [8, 9] and found good agreements between his simulated results and our experimental ones. Furthermore, after introducing a parameter named Supertron number Su, he gave [10] a figure from which one can deduce axial focal lengths of Supertrons for electron currents of 10^3 to 10^9 eV.

EXPERIMENTAL DEVICES

Figure 2 shows schematic experimental devices used. A melt-processed YBCO Supertron, which had an inner and outer diameters of 20 and 22 mm, respectively, was glued onto the inner surface of a copper-made heat sink with electrically conducting silver paste. The sink thus prepared was mounted on the cold head of a compact helium-gas refrigerator. A 12-μm-thick dielectric film was inserted between the sink and cold head to electrically insulate them. The sink was grounded with a radially extended stainless-steel plate at the exit of the sink. Operation temperatures were monitored with thermocouples at the upper edge of the sink exit. The heat sink played a role of an anode of the diode generating primary intense electron currents. High-voltage pulses were applied between the anode and cold carbon-made cathode to field-emit primary electron currents (~340 keV, ~1 kA, ~10 ns). To neutralize space charges of the primary electron currents, neon gas was intro-duced into the diode space at pressures of 0.1-Torr order. The primary electron currents ejected from the Supertron were detected with a Faraday cup isolated from the diode space with a 20-μm-thick titanium foil. Therefore, the Faraday cup detected electron currents of energies higher than 60 keV. The Faraday cup was kept in a high vacuum to detect correct primary electron currents. A Rogowski coil outside the Supertron detected the magnetic fields penetrating through the 1-mm-thick wall of the Supertron and through the annular gap of the heat sink. The Supertron was composed of three short straight tubes and a funnel-type tube. In assembling these tubes, we payed much attention for the junction of the short tubes not to coincide in location with the annular gap of the heat sink. Thus, the magnetic fields detected are those penetrating through the melt-processed tube and partially diffusing through boundaries of the grains composing the melt-processed YBCO Supertron.

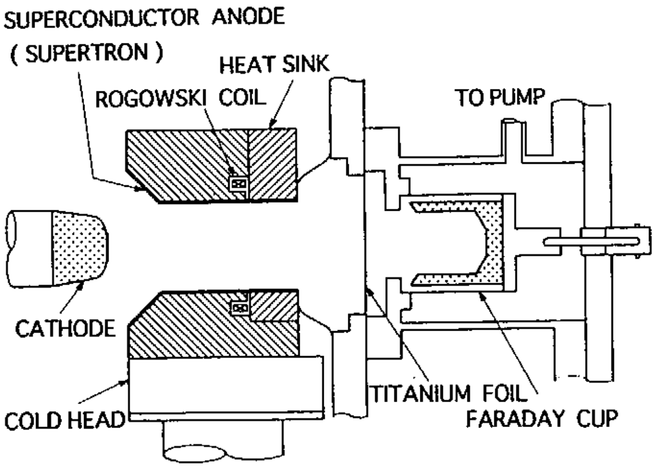

Fig. 2. Experimental setup.

EXPERIMENTAL RESULTS

First we observed focusing characteristics of only the copper-made heat sink for the temperature range from 70 K to room temperature. Next, after the melt-processed YBCO tubes were glued onto the inner surface of the heat sink, the Supertron was operated for the same temperature range.

Figures 3a and 3b show temporal behaviors of the electron currents detected with the Faraday cup (first peaks) and of the magnetic fields detected with the Rogowski coil (second peaks) for identical shots. The second waveforms were delayed 26 ns from the first waveforms with an additional coaxial cable inserted at the input terminal of a high-speed oscilloscope. Notice in Fig. 3 the difference in the horizontal time scale. In Fig. 3a for the heat sink, the duration times of magnetic fields of electron currents are comparable to those of the electron currents detected with the Faraday cup. On the other hand, the magnetic fields in Fig. 3b for the YBCO Supertron have much wider pulse widths. These facts mean that the self-magnetic fields of electron currents diffused the 1-mm-thick YBCO wall slowly.

Figures 4a and 4b indicate the tempearture dependences of peak values of the electron currents and magnetic fields for the heat sink and YBCO Supertron, respectively. For both

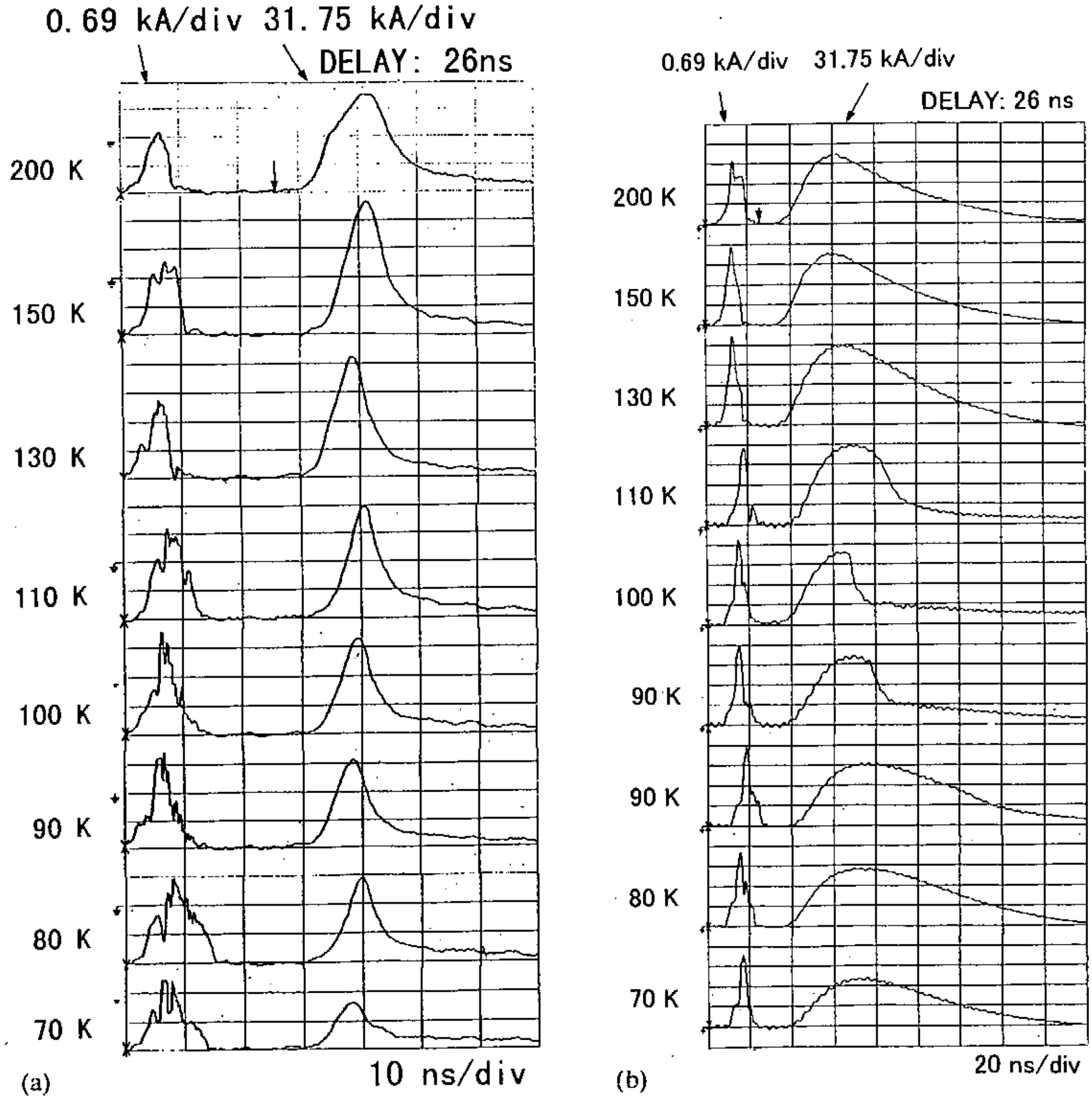

Fig. 3. Temporal behaviors of electron currents detected with Faraday cup (first peaks) and magnetic fields produced by electron currents and detected with Rogowski coil (second peaks) for copper-made heat sink (a) and melt-processed YBCO Supertron (b). The second peaks were delayed 26 ns from the first peaks.

the heat sink and YBCO Supertron, the electron currents and magnetic fields showed their maxima at ~100 K or higher temperatures as the operation temperature was lowered. These results arose probably from the trade-off between the increasing in focusing ability of the heat sink or the Supertron with decreasing electrical resistivity and the increasing in responce time (increasing Q values) of electrical loop paths along which induced intracurrents flow inside the copper block and melt-processed superconductor grains [2, 4].

Figure 5 shows radial profiles of electron beams emerging from the YBCO Supertron. Even when its temperature was lowered beyond its T_C, the profiles were little narrowed, in contrast to those for powder-pressed Bi(2223) Supertrons [2, 4, 7]. These results assist the ferrite-core model. For a powder-pressed Bi(2223) Supertron, as we had reported in Ref. 4 and partially in Ref. 2, the electron currents and magnetic fields increased in peak values as the temperature decreased down to the critical temperature T_C of the materials. For further

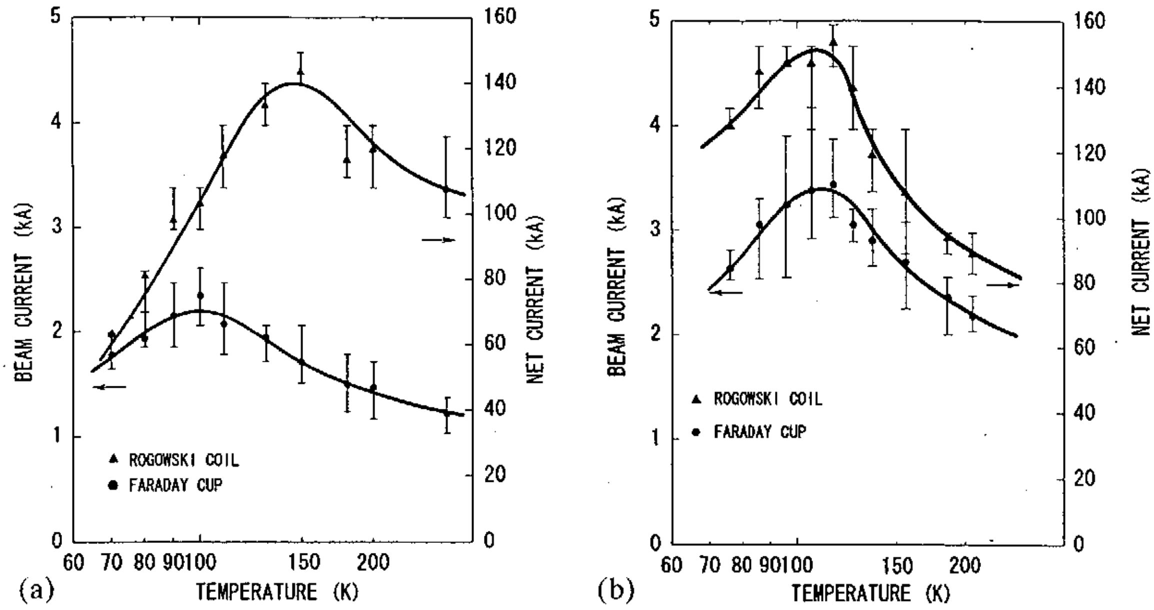

Fig. 4. Temperature dependences of electron currents detected with Faraday cup (●) and electron currents evaluated from magnetic fields detected with Rogowski coil (▲) for copper-made heat sink (a) and melt-processed YBCO Supertron (b).

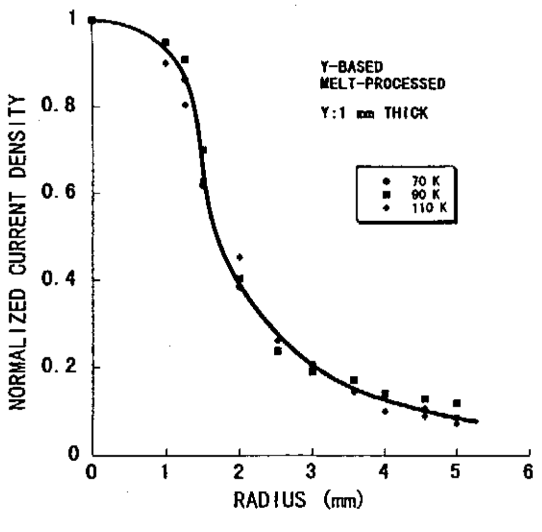

Fig. 5. Radial profiles of electron beams focused with melt-processed YBCO Supertron.

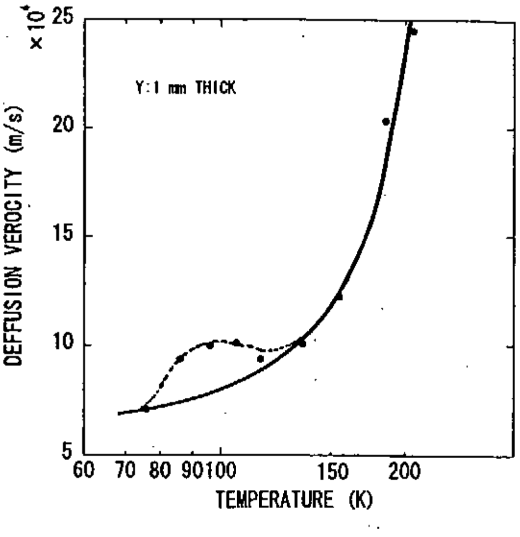

Fig. 6. Diffusion velocities of magnetic fields through melt-processed YBCO wall.

cooling, their values were almost unchanged. However, radial profiles of electron beams narrowed with decrasing temperatures: the focusing ability of powder-pressed Supertrons increased with lowering temperatures, compared with the temperature-independent radial profiles in Fig. 5.

After deducing the difference in time at which the peaks of the waveforms of magnetic fields of the heat sink and of the YBCO Supertron for respective operation temperatures, we evaluated diffusion velocities of magnetic fields through the melt-processed YBCO wall. The velocities thus obtained are summarized in Fig. 6 as a function of operation temperatures. The diffusion velocities decrease to the order of $\sim 10^{-4}$ m/s with lowering temperatures. At ~100 K in Fig. 6, a small hump exits. For powder-pressed Bi(2223) Supertrons, no hump was observed [6]. At present, we cannot understand the hump.

CONCLUSIONS

In the previous experiments [2], a melt-processed YBCO Supertron cooled with liquid nitrogen focused electron beams least effectively among the lenses examined. Present paper described that even when the melt-processed Supertron was cooled more than in the previous paper radial profiles of the electron beams focused were little improved. These results are explainable by a ferrite-core model. We are now preparing a double-layered Supertron. From the experimental results thus far obtained, we expect that the double-layered Supertron will show the same focusing characteristics as those of a single powder-pressed Bi(2223) Supertron. Then, we could say that the functioning of the double-layered Supertron is confirmed for single short-pulsed electron beams. For continuous electron currents, another experimental scheme is required, because a source of continuous electron currents of the same order of the present experiments would hardly be available.

REFERENCES

1. M. K. Wu, J. R. Ashburn, C. J. Torng, P. H. Hor, R. L. Meng, L. Gao, Z. J. Huang, Y. Q. Wang, and C. W. Chu, Phys. Rev. Lett. **58** (1987) 908.
2. For a review, see H. Matsuzawa, J. Appl. Phys. **74** (1993) 111 [Erratum: H. Matsuzawa, J. Appl. Phys. **76** (1994) 624.
3. H. Matsuzawa, Y. Ishibashi, M. Ariizumi, and H. Saegusa, Appl. Phys. Lett. **59** (1991) 141.
4. H. Matsuzawa, H. Kobayashi, H. Mochizuki, N. Yoneyama, A. Ohshima, S. Hirano, E. Mori, G. Horigome, Y. Ishida, and Y. Chino, Jpn. J. Appl. Phys. **33** (1994) 2526 [Eraatum: H. Matsuzawa, et al., Jpn. J. Appl. Phys. **33** (1994) 4799].
5. H. Matsuzawa, H. Watanabe, Y. Fukasawa, and K. Mikami, *11th International Symposium on Superconductivity* (November 16-19, 1998, Fukuoka) DAP-18.
6. H. Matsuzawa, A. Matsushita, Y. Ueda, H. Matsubara, Y. Chino, and S. Suganomata, Jpn. J. Appl. Phys. **35** (1996) 5315.
7. H. Matsuzawa, A. Matsushita, P. Roth, H. Matsubara, Y. Ueda, and S. Suganomata, Jpn. J. Appl. Phys. **36** (1997) 98.
8. P. Roth, J. Appl. Phys. **77** (1995) 4914.
9. P. Roth, J. Appl. Phys. **78** (1995) 2874.
10. P. Roth, Jpn. J. Appl. Phys. **36** (1997) 4537.

Plume Behavior and Thin Film Deposition by Pulsed Laser Deposition using Helicoidal Shadow Mask

Aurelian MARCU, Constantin GRIGORIU, Weihua JIANG,
and
Kiyoshi YATSUI

Laboratory of Beam Technology, Nagaoka University of Technology,
Nagaoka, Niigata, 940-2188, Japan

Abstract

The behavior of the plume produced by pulsed laser ablation and related thin film deposition were studied. A planar reflector was used to change the direction of the plume movement. The behavior of the plume reflection was monitored by high-speed photography. Meanwhile, thin film deposition was carried out by the reflected plume. The deposition rate and surface roughness of the films prepared were studied by scanning electron microscopy and atomic force microscopy, respectively. The results have shown that both the deposition rate and the surface roughness of the film strongly depend on the reflection angle of the plume. These results are believed to be useful to the quality control of the thin films in the pulsed laser deposition.

1. Introduction

Pulsed laser deposition (PLD) is a useful technology to prepare various kinds of films. Basically, it uses the high power laser beam to deposit energy into the target surface in a time interval much shorter than the time scale of thermal conduction. Due to the high energy density, the irradiated area will be evaporated to produce an ablation plasma, which expands in the direction perpendicular to the target surface. The ablation plasma (the plume) can be used to prepare thin films, or ultrafine nanosize powders as well.

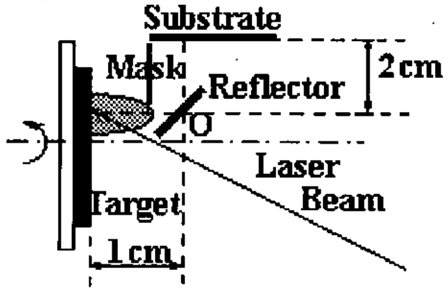

Fig. 1 **Experimental setup.**

For the thin-film deposition, a substrate is located on the way of plume expansion so that the plume material is condensed on the substrate surface. However, many earlier experimental results have shown that the quality of the film surface is strongly degraded by *droplets* that are relatively large particles of the target material in solid or liquid state carried by the plume. Several techniques, such as an eclipse deposition[1)] and an off-axis deposition[2)], have been proposed to avoid droplets in PLD. Furthermore, a new method called backside deposition[3-6)] has been successfully developed in an intense pulsed ion-beam evaporation. However, the results obtained by these techniques have shown that the film deposition rate is significantly reduced as a trade-off for the improvement of the surface roughness.

Table I. Experimental conditions and parameters.

LASER	Wavelength	1.064 μm
	Energy	200 mJ
	Density	2.5 J/cm^2
	Frequency	10 Hz
	Duration	7 ns
TARGET	Material	YBCO
AMBIENT GAS	Composition	O_2
	Pressure	25 Pa
SUBSTRATE	Material	MgO
	Temperature	25° C

To study a configuration of PLD which gives both high deposition rate and good film quality, we have investigated the process of plume reflection on a planar surface. Using the reflected plume, we have carried out thin film deposition on various reflection angles. The deposition rate and film surface roughness were studied by scanning electron microscopy (SEM) and atomic force microscopy (AFM), respectively.

2. Experimental Setup

Figure 1 shows the experimental setup. A Q-switched YAG laser beam is irradiated on the target, producing the ablation plume that expands perpendicularly to the target surface into ambient gas. A planar reflector is located 1 cm away from the target with an angle of 45^0 to the target. The substrate is located at 2 cm from the reflector, oriented perpendicularly to the target. A mask is inserted to avoid droplets between the target and the substrate. The experimental conditions and parameters are presented in Table I. The plume behavior was monitored by a high speed camera (Ultranac FS501).

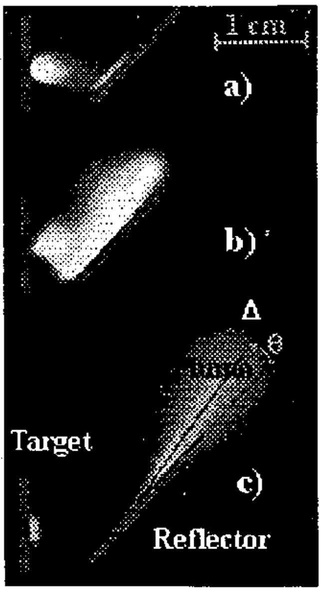

Fig. 2 Plume reflection in the absence of substrate : a) t = 0.3 μs, b) t =1.5 μs, c) t =7.5 μs.

3. Experimental Results

Figure 2 shows a typical photograph. In order to observe the natural behavior of the reflected plume, the photograph was obtained in the absence of the substrate. A photograph taken in the presence of the substrate is shown in Fig. 3. From Fig. 2, we see that the process may be divided into three phases: emission, reflection and deposition. Clearly, we see the emission (Fig. 2a) for 1.5 μs - 2 μs. The duration of the emission in the presence of a plane reflector has been found to be a few times longer than that in the absence of reflector (normal deposition). A part of the reflected particles will be reflected back to the target, which will keep the irradiated area to be high

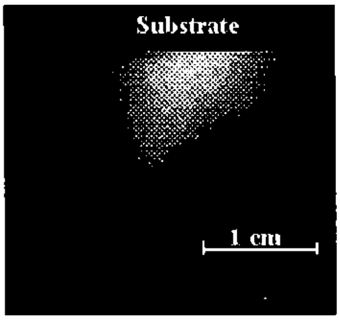

Fig. 3 Plume reflection on substrate at t = 8 μs.

temperature for a longer time. Actually, the reflection process (Fig 2b) can be clearly observed. In the incipient stage, the reflected plume has an eliptical shape. The plume starts to move along the reflector surface, and finally forms a clear conical shape (Fig. 2c). It is noted that the central axis of the cone makes an angle of 10^0 with respect to the reflector surface (Fig. 2c). It is also noticed that the solid angle described by the reflected plume seems to be considerably smaller than the incident angle. The plume reaches the substrate after about 8 μs, which can be seen in Fig. 3 from the interaction between the plume and the substrate. Finally, the plume becomes a semi-spherical shape.

From the measurement of the film thickness by SEM, we have found that after the reflection the plume still has a radial symmetry, and that it is strongly dependent on the direction. At 2 cm from the reflector, therefore, the film thickness is decreased to the half. Using a simple polynomial approximation for the thickness dependence on the reflection angle, we have estimated the solid angle to be 0.5 rad, in which the plume deposits about 65% (volume) of the total amount of the deposited particles. In order to make a comparison with the incident plume directivity, films were deposited on the reflector at 1 cm from the target. Using a similar polynomial approximation for the thickness variation, it has been found that the strong directivity of the reflected plume yields bigger fluence than the incident plume.

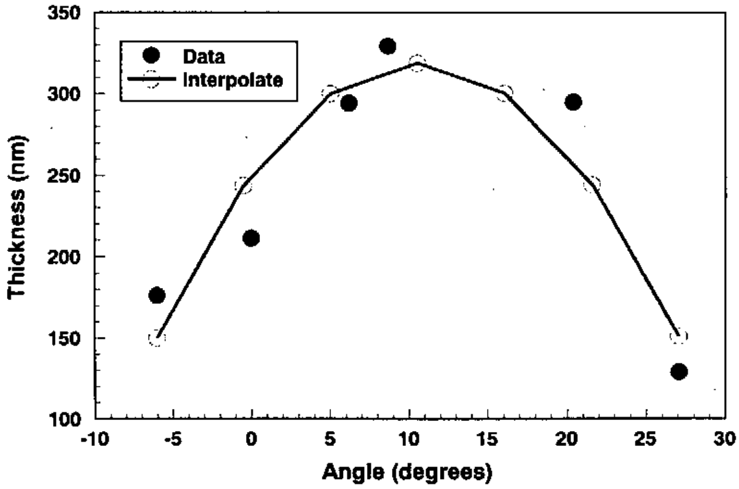

Fig. 4 Film thickness on reflection angle.

Figure 4 shows the film thickness dependence on the reflection angle at a pressure of 25 Pa (O_2). The maximum deposition rate has been achieved at the reflection angle of 10^0. Correspondingly, it has been found that the area covered by droplets is about 6% - 7%, and that the maximum droplets size is about 0.6 μm. Furthermore, the characteristic roughness (RMS) was observed to be approximately 25 nm.

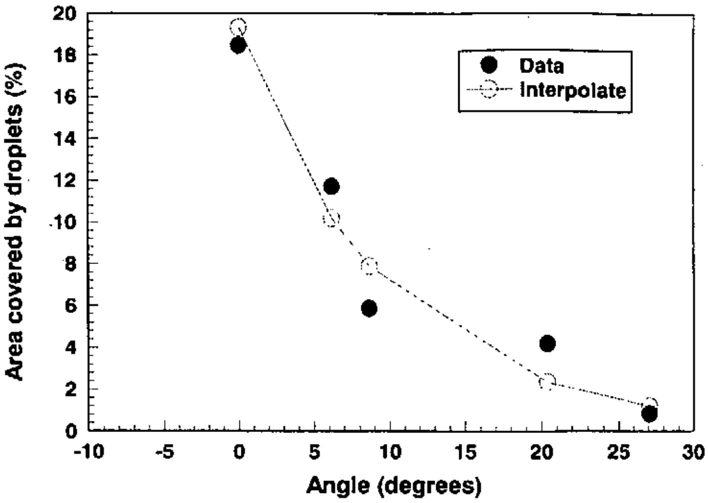

Fig. 5 Aerial percentage covered by droplets on reflection angle.

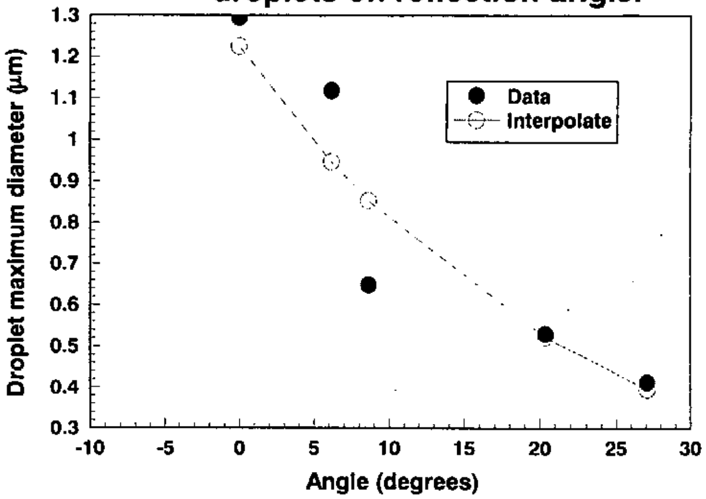

Fig. 6 Maximum diameter of droplets on reflection angle.

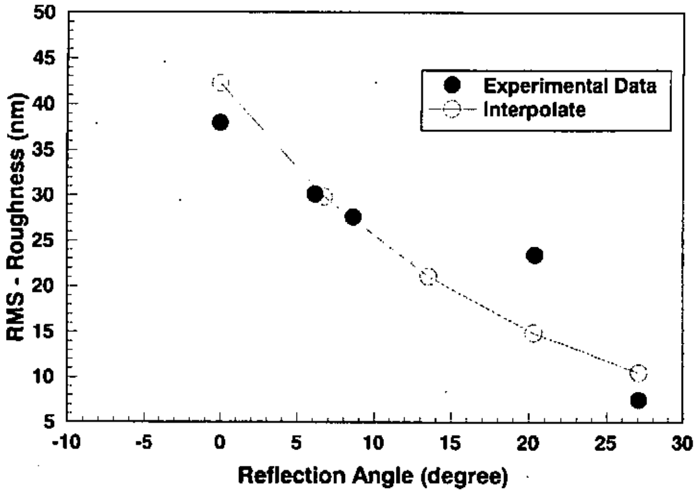

Fig. 7 Roughness (RMS) on reflection angle.

Important fact for the reflection process here is that big particles (droplets) ejected from the target have a different distribution on the film surface than the small particles. Droplets are not concentrated along the Δ direction but along the 0^0 direction. The size and the percentage of the area covered by the droplets decrease exponentially with increasing reflection angle. At an angle of 0^0, which corresponds to the reflector surface direction, the area covered by droplets is about 20 % from the SEM data. The maximum size of the droplets is 1.3 μm. In addition, the AFM has shown the characteristic roughness (RMS) to be about 40 nm. Comparing the film parameters at 27^0 angle, the area covered by the droplets decreases about 10 times (Fig. 5), while the droplets size about 4 times (Fig. 6), and the roughness (RMS) about 4 times (Fig. 7). Thus, it is found that smaller particles will be reflected much strongly. Figure 8 shows the AFM result of the thin film deposited on the reflection angle of 27^0.

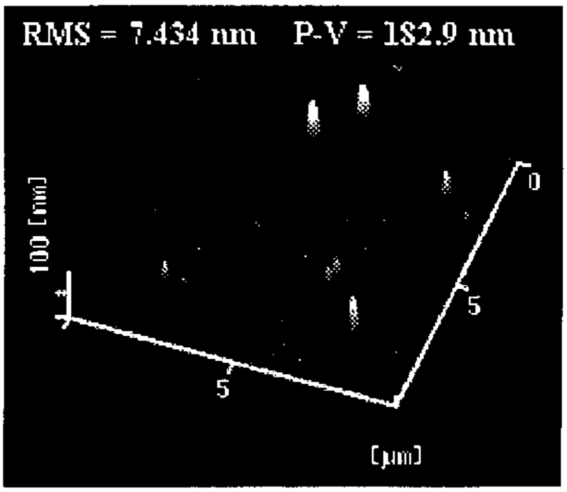

Fig. 8 AFM data of YBCO thin film deposited on 27^0 reflection angle.

The quality of the film surface was strongly improved in the reflected configuration compared with the straight flight from the target (D zone in Fig. 9). In this area, it is difficult to evaluate the aerial percentage covered by the droplets or droplets size. On the other hand, the estimate can be possible for big reflection angles.

We have made a theoretical interpretation of the film quality on the mass difference between the fine particles and the big particles (droplets) of the plume. If the fine particles have a fluid-like behavior (shown in Fig. 2 and Fig. 3), we may assume a linear trajectory for the droplets (Fig. 9). Thus, the droplets will mainly be deposited on the reflector or plane mask, or on the substrate. Small droplets will be more (trajectory a in Fig. 9) or less (trajectory c in Fig. 9) deflected by the interaction with the reflected particles depending on their masses. If small droplet less than 100-200 nm in diam. might be

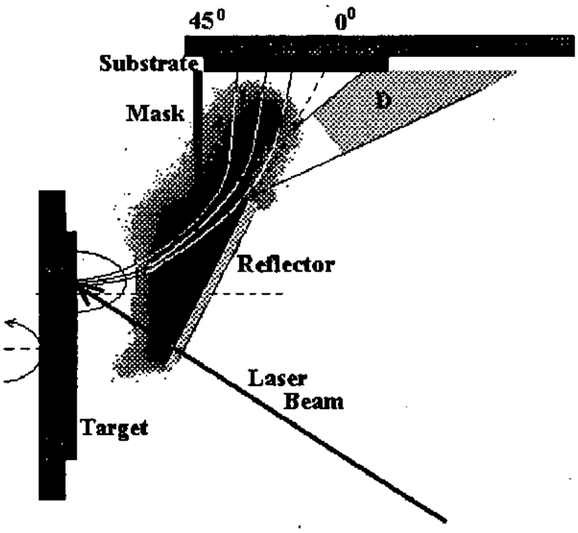

Fig. 9 Theoretical movement of droplets of reflected plume at t = 2.5 μs.

deviated at 25^0 or bigger, big droplet of 1 μm could not be deviated more than 5^0, because of its big mass and its initial speed orientation in the interaction with the fine particles of the reflected plume. Such a big particle will simply follow the movement to the D zone or outside the substrate area. Hence, we may understand the concentration of the particles in the small reflection angle and the absence of such big droplets from the film surface at big reflection angle.

4. Concluding Remarks

After the reflection by 45^0 plane reflector of the PLD plume obtained by the experimental conditions ($YBa_2Cu_3O_{7-x}$, 25 Pa (O_2), 1.064 μm, 7 ns, 2.5J/cm^2, 10 Hz), we have observed the increase in the plume directivity and the maximum deposition rate on 10^0 plume reflection angle. The droplets reflection has been found to be strongly different, where the maximum appears at a reflection angle of $\theta = 0^0$, and the distribution decreases exponentially with the angle. Thus, quality control of the surface morphology will be possible. For 27^0 plume reflection, the thin film has been deposited by the deposition rate of 0.08 A/pulse. We have found that the maximum aerial percentage covered by the droplets was < 2%, and that the surface characteristic roughness (RMS) < 10 nm.

References

1) K. Kinoshita, et al.: Jpn. J. Appl. Phys., **33**, L417 (1994).
2) B. Holzaphel, et al.: Appl. Phys. Lett., **61**, 3178 (1992).
3) T. Sonegawa, et al.: Appl. Phys. Lett., **69**, 2193 (1996).
4) T. Sonegawa, et al.: Laser and Particle Beams **14**, 537 (1996).
5) K. Yatsui, et al.: Jpn. J. Appl. Phys., **36**, 4928 (1997).
6) T. Sonegawa and K. Yatsui: J. Mater. Sci. Lett., **17**, 1685 (1998).

Preparation of Fullerenes by Intense, Pulsed Ion-Beam Evaporation

S. Kurashima, W. Jiang, and K. Yatsui
Laboratory of Beam Technology, Nagaoka University of Technology,
Nagaoka, Niigata 940-2188
T. Hirata, R. Hatakeyama and N. Sato
Graduate School of Engineering, Tohoku
University, Sendai, Miyagi 980-8579

Abstract

As a new method for the production of fullerenes, intense, pulsed ion-beam evaporation (IBE) is proposed for the first time. It has been shown that, by using the IBE technique, fullerenes have been produced even in vacuum (10^{-4} Torr). On the contrary of the conventional common sense, the production rate in vacuum is much better than that in the presence of helium gas.

1. Introduction

Fullerenes are expected as a new electronic material. In the past, there are several methods to produce fullerenes, such as arc discharge with graphite electrodes, resistive heating of graphite, laser ablation of a graphite target, and so on.[1)]

If we irradiate an intense, pulsed, light ion beam (LIB) on a solid target, very high energy density can be achieved near the surface of the target due to the short range of the LIB. Some part of the target material which absorbs the LIB energy tends to be melted and evaporated, resulting in the production of high-density, high-temperature ablation plasma. The target material in the ablation plasma can be deposited on the substrate that is placed nearby the target. This process is called ion beam evaporation (IBE). We have succeeded in preparing various thin films.[2-15)] Recently, Ultrafine nanosize powders have been synthesized as well by using the IBE.

In this paper, we would like to report the preparation of fullerenes by use of the IBE. The soot prepared and collected were analyzed by LD-TOF (laser desorption time-of-flight) method to obtain the mass spectrum.

2. Experimental Setup

Figure 1 shows the experimental setup of the IBE. The LIB is extracted from a magnetically insulated ion diode (MID) with a geometrically focused configuration. The MID is driven by the pulsed power generator "ETIGO-II".[16] Typical beam parameters are ion energy ~ 1 MeV, ion current density ~ kA/cm^2, and pulse width ~ 50 ns.

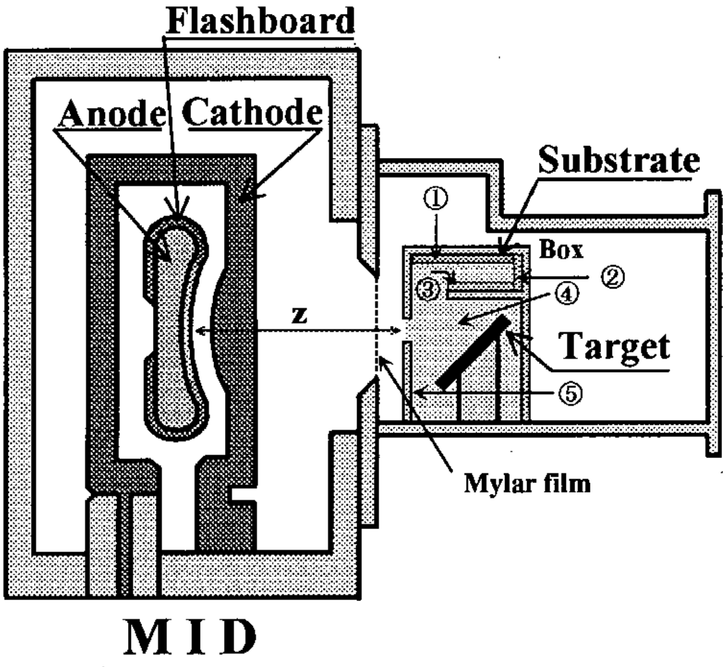

Fig. 1 Experimental setup of IBE.

The LIB has been irradiated on a carbon target (99.99% in purity) with an angle of 45 degree to its normal. The distance from the anode to the target was varied from 130 to 180 mm, so as to change the energy density deposited on the target. We set up a box in front of the target to confine the ablation plasma so that most of the ablation plasma can be deposited on it. In Fig. 1, z is the distance from the anode to the aperture on the box surface.

Figure 2 shows the LIB energy density as a function of the distance from the anode surface. The experiments were carried out in vacuum (10^{-4} Torr), or in the ambient gas of 1, 5, 10 Torr of helium. Since the MID should be operated in vacuum, a plastic thin film of Mylar (2 μm thick) was used to separate the target chamber and the MID chamber in the case of He ambient gas. Either glass or silicon was used as the substrate.

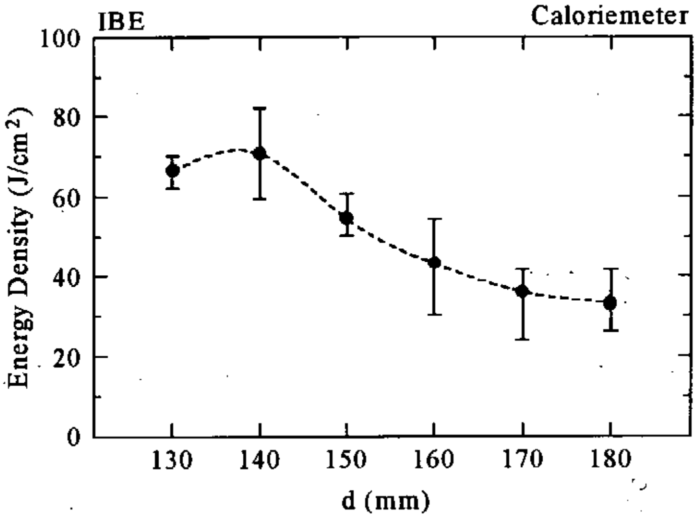

Fig. 2 Energy density distribution of LIB as a function of the distance from the anode measured by caloriemeter.

3. Experimental results

3-1 SEM observation

Figure 3 typically shows a SEM (scanning electron microscope) photograph of the soot deposited and collected on Si substrate, which was obtained by 10 shots of the irradiation. The background base is the carbon film, prepared on a Si substrate. We see a bunch of carbon soot on the surface. Furthermore, we see clearly the presence of thin and long tube, the diameter of which is approximately 300 nm. Since it is considerably thicker than normal nanotube found elsewhere, the following studies have been carried out on the relation each other.

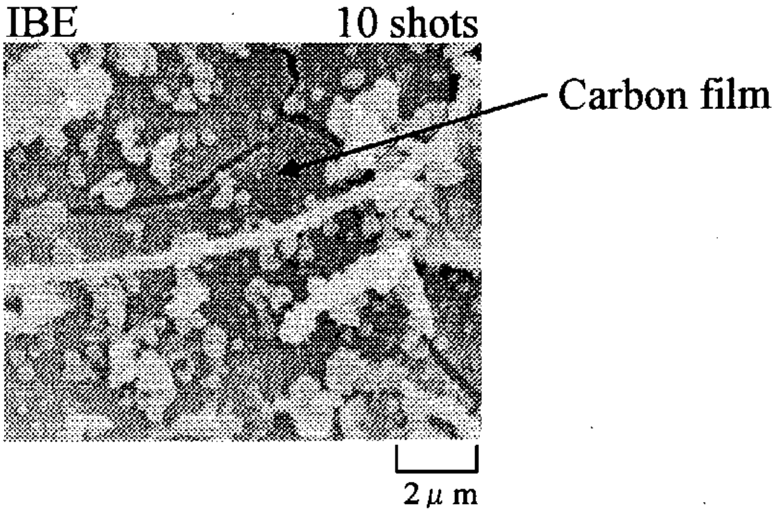

Fig. 3 Typical SEM photograph of carbon soot at z = 180 mm, Sub.②.

3-2 LD-TOF measurement

Figure 4 shows the LD-TOF mass spectrum of the soot prepared in vacuum, where the carbon target was placed at z = 130 mm.

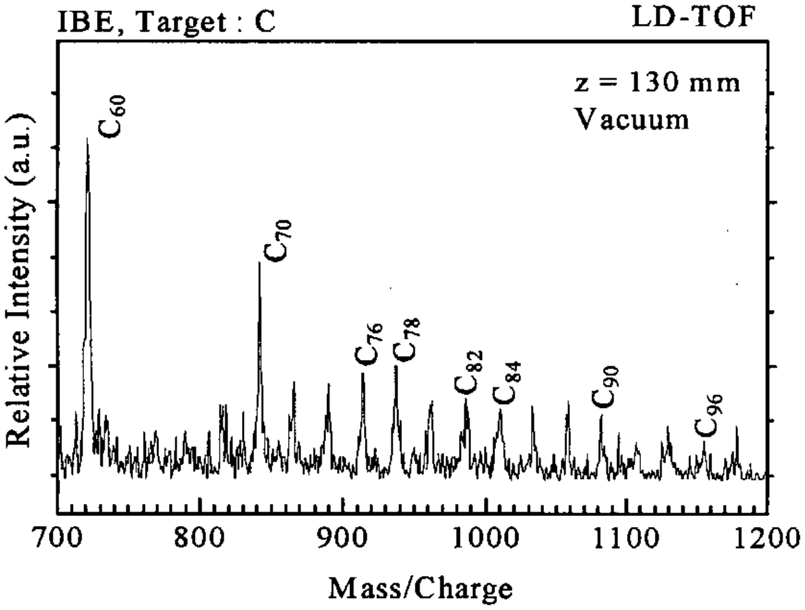

Fig. 4 Mass spectrum by LD-TOF, obtained at z = 130 mm, vacuum.

It is clearly found from Fig. 4 that fullerenes, not only C_{60}, but also C_{70} and even higher fullerenes, are prepared by the IBE technique even in vacuum. Furthermore, the samples obtained at z = 140, 155 and 170 mm have shown similar results.

Figure 5 shows the LD-TOF mass spectrum of the sample prepared in vacuum at z = 130 mm, which were collected at the position ① indicated in Fig. 1. As is similar as in Fig. 4, we can see the presence of fullerenes of C_{60} and its higher order even in vacuum.

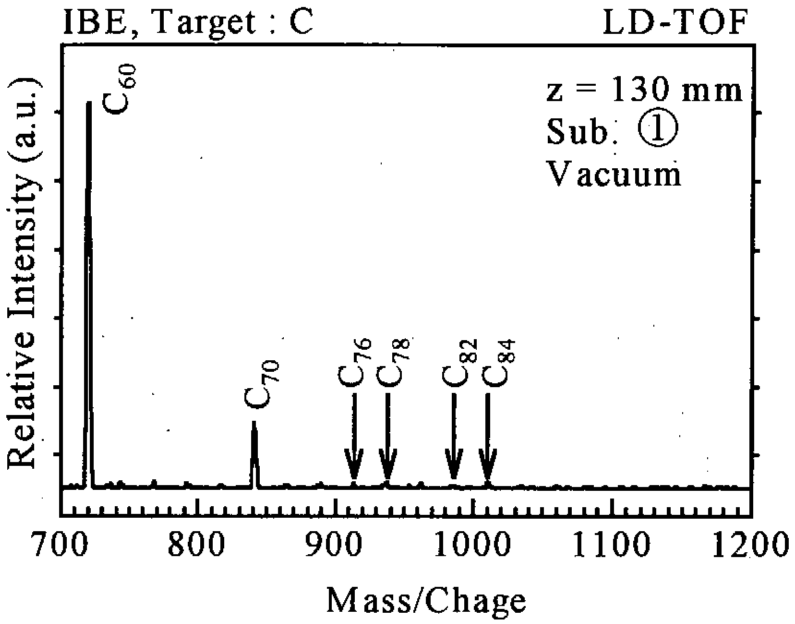

Fig. 5 Mass spectrum at substrate ①, obtained at z = 130 mm, vacuum.

Figure 6 shows the peak intensity of C_{60} normalized by that at the position ①. The peak intensities can be seen to be strongly dependent on the positions where the soot are collected. In addition, they are much stronger at higher plasma density nearby the target.

Figure 7 shows the LD-TOF mass spectrum of the soot prepared in the ambient gas of helium (5 Torr) at z = 130 mm. It is observed that fullerenes are also prepared in ambient gas of helium by using the IBE.

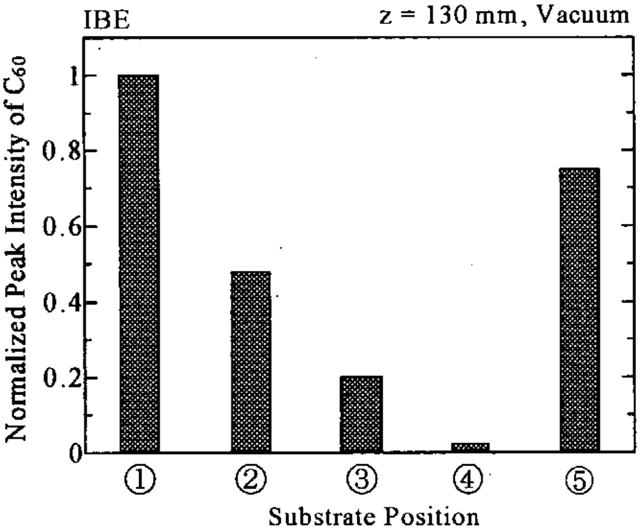

Fig. 6 Normalized peak intensity of C_{60}, obtained at z = 130 mm, vacuum.

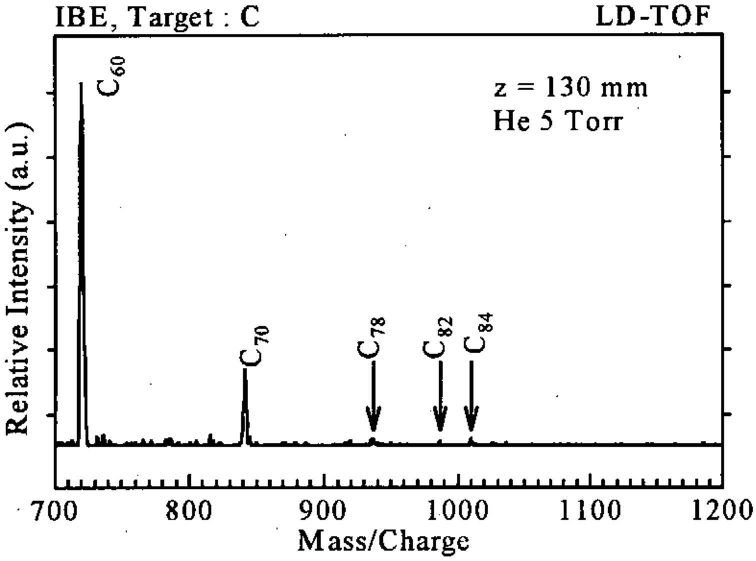

Fig. 7 Mass spectrum obtained at z = 130 mm, He 5 Torr.

Figure 8 shows the peak intensity of C_{60} normalized by that at 10 Torr of helium. As seen from Fig. 8, the peak intensities increase with increasing helium pressure. Interesting characteristics to be noted here are that the maximum peak intensity of C_{60} in vacuum is about four times stronger than that in helium. Such a fact is completely opposite from the fact reported elsewhere that the intensities of fullerenes in the presence of helium gas are much stronger than in vacuum, although we have not yet understood the reasons.

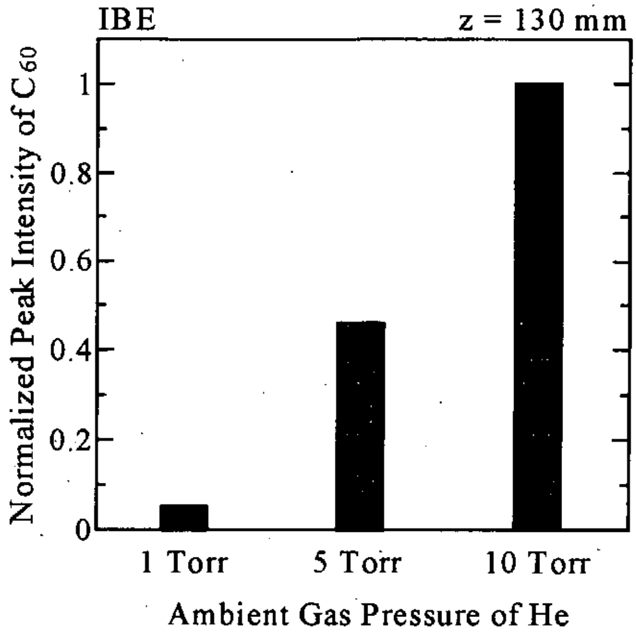

Fig. 8 Normalized peak intensity of C_{60} in the presence of helium gas, obtained at z = 130 mm.

4. Conclusions

From these experimental results of the SEM together with the LD-TOF analysis, we have obtained the following conclusions.

1) Fullerenes can be produced in both vacuum (10^{-4} Torr) and ambient gas of helium.
2) The content of C_{60} of the soot strongly depends on the position of the soot collected.
3) A thin tube has been observed in the soot.
4) The total amount of fullerenes in vacuum is much larger than that in helium gas.

References

1) L. D. Lamb and D. R. Huffman: J. Phys. Chem. Solids. **54**, 1635 (1993).
2) Y. Shimotori, et al.: J. Appl. Phys. **63**, 968 (1989).
3) Y. Shimotori, et al.: Jpn. J. Appl. Phys. **28**, 468 (1989).
4) K. Yatsui: Laser and Particle Beams **7**, 733 (1989).
5) X. D. Kang, et al.: Jpn. J. Appl. Phys. **33**, 1155 (1994).
6) X. D. Kang, et al.: Jpn. J. Appl. Phys. **33**, L1041 (1994).
7) K. Yatsui, et al.: Phys. Plasma **1**, 1730 (1994).
8) G. P. Johnston, et al.: J. Appl. Phys. **76**, 5949 (1994).
9) K. Yatsui, et al.: Appl. Phys. Lett. **67**, 1214 (1995).
10) T. Sonegawa, et al.: Appl. Phys. Lett. **69**, 2193 (1996).
11) T. Sonegawa, et al.: Laser & Particle Beams **14**, 537 (1996).
12) K. Yatsui, et al.: Jpn. J. Appl. Phys. **36**, 4928 (1997).
13) K. Yatsui, et al.: Mater. Chem. and Phys. **54**, 219 (1998).
14) W. Jiang, et al.: Nucl. Instr, and Methods **A415**, 533 (1998).
15) T. Sonegawa, et al.: J. Mater. Sci. Lett. **17**, 1685 (1998).
16) A. Tokuchi, et al.: Proc. 2nd Int'l Topical Symp. on Inertial Confinement Fusion Res. by High-Power Particle Beams, ed. by K. Yatsui (Lab. of Beam Tech., Nagaoka Univ. of Tech.) 430 (1986).

Diagnostics of Behavior of Pulsed, Ion-Beam Ablation Plasma

N. Hashimoto, W. Jiang and K. Yatsui

Laboratory of Beam Technology, Nagaoka University of Technology,
Nagaoka, Niigata 940-2188

Abstract

Intense, pulsed, ion-beam evaporation (IBE) is a new technology for the effective preparation of various kinds of thin films by using the ion-beam ablation plasma. We have investigated the behavior of the ablation plasma around the target and the substrate by using high-speed photography. In addition, we have measured the energy deposition on the substrate surface by the ablation plasma, by using calorimetric technique. From the energy deposition and the time evolution of the ablation plasma obtained above, we were able to calculate the maximum temperature on the substrate surface. The results have provided the physical explanation for the crystallized thin films obtained by the IBE, even with the substrate kept at the room temperature.

1. Introduction

When an intense, pulsed, light ion beam (LIB) is irradiated on solid targets, high-density ablation plasma has been found to be produced. By using such a plasma, we have successfully demonstrated the preparation of various kinds of thin films[1~14].

The properties of the thin films prepared by the IBE strongly depend on the behavior of the ablation plasma. Understanding the behavior of the ablation plasma, we will be able to improve the properties of the thin films prepared by the IBE. In this paper, we would like to report on the experimental results of 1) time- and spatially-resolved measurements of the behaviors of the ablation plasma by using high-speed photograph, and

2) measurement of energy deposition on the substrate surface by using calorimeter. From these studies, we have calculated the instantaneous temperature distribution on the substrate by using one-dimensional thermal conduction equation.

2. Experimental Setup

Figure 1 shows the experimental setup. The experiment has been carried out using the intense, pulsed power generator "ETIGO-Ⅱ"[15] at the Nagaoka University of Technology. The ion diode utilized in the experiment was a magnetically insulated diode (MID). As a flashboard anode of the MID, polyethylene was used, where protons have been dominant species of the ions extracted. Typically, the MID was operated by the following conditions: beam energy ~ 1 MV and ion current ~ 70 kA. The pulse width was ~ 70ns (FWHM), and the beam energy density on the target ~30 J/cm^2. The ion beam was focused at 140mm downstream from the anode of the MID, and the SiC target was installed with an angle of 30 degrees relative to the beam axis. The vacuum chamber was evacuated to approximately 10^{-4} Torr.

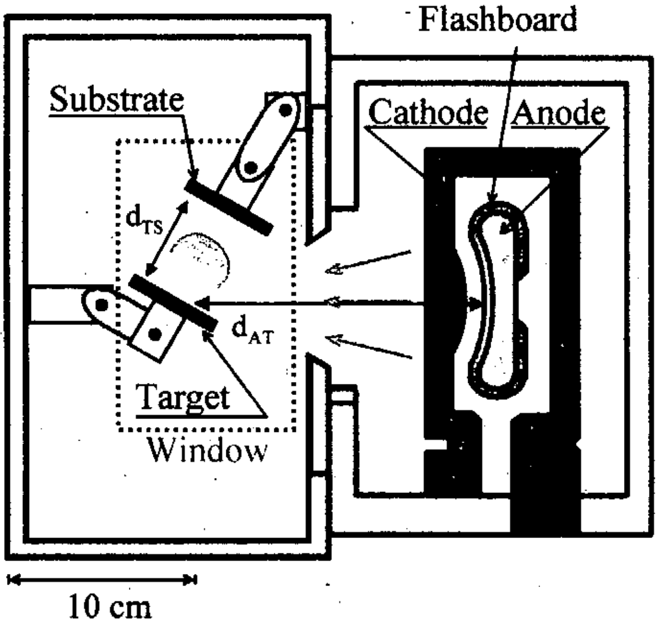

Fig.1 Cross-sectional view of experimental setup of IBE.

3. Experimental Results

3.1. Time-resolved measurement of ablation plasma

Figure 2 typically shows high-speed photographs of the ablation plasma, where the exposure time for each frame was 100 ns. These photographs were obtained at d_{AT} (anode-target distance) = 170 mm, and d_{TS} (target-substrate distance) = 50 mm. The time on the figure indicates that after the rise of the ion beam pulse. The wavelength of the photographs, determined by the sensitivity of the high-speed camera, ranged from 400 to 900 nm.

In Fig. 2, the ablation plasma produced on the target surface is seen to expand in the vertical direction of the target. It is seen that the light intensity of the ablation plasma becomes much stronger near the substrate surface. Hence, the plasma density is enhanced near the substrate. The light emission from the plasma lasted for ~ 40 μs.

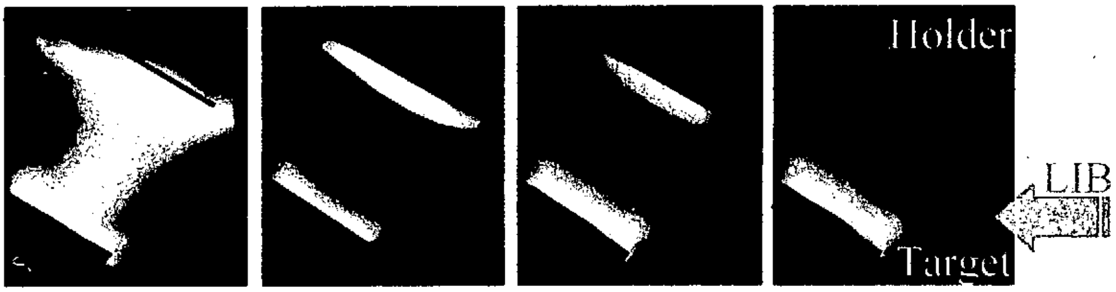

(a) t = 10 ms (b) t = 20 ms (c) t = 30 ms (d) t = 40 ms

Fig.2 High-speed photographs of light emission form ablation plasma, where the exposure time of each photographs is 100ns, and t means the time after the LIB irradiation. d_{AT} = 170mm, d_{TS} = 50mm.

3.2. Energy deposition of ablation plasma on substrate

A calorimeter has been utilized to measure the energy deposition by the ablation plasma on the substrate (see Fig. 3). A mask with the size of 2×2 cm^2 was placed in front of the substrate. The energy density deposited on the substrate by the ablation plasma is given by

$$Q' = mc\Delta T/S, \tag{1}$$

where m is the mass of the substrate, c is the specific heat of the substrate material, Δ T is the temperature rise of the substrate, and S is the area.

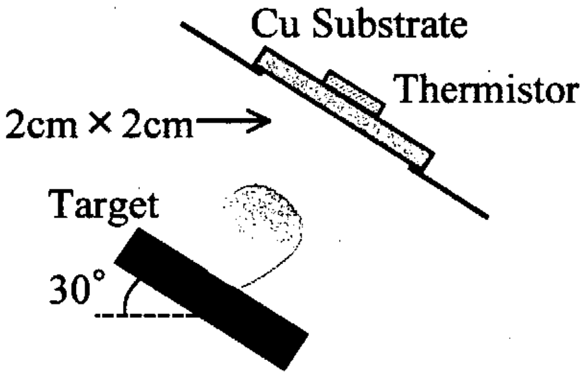

Fig.3 Experimental setup to measure temperature rise of substrate using thermistor.

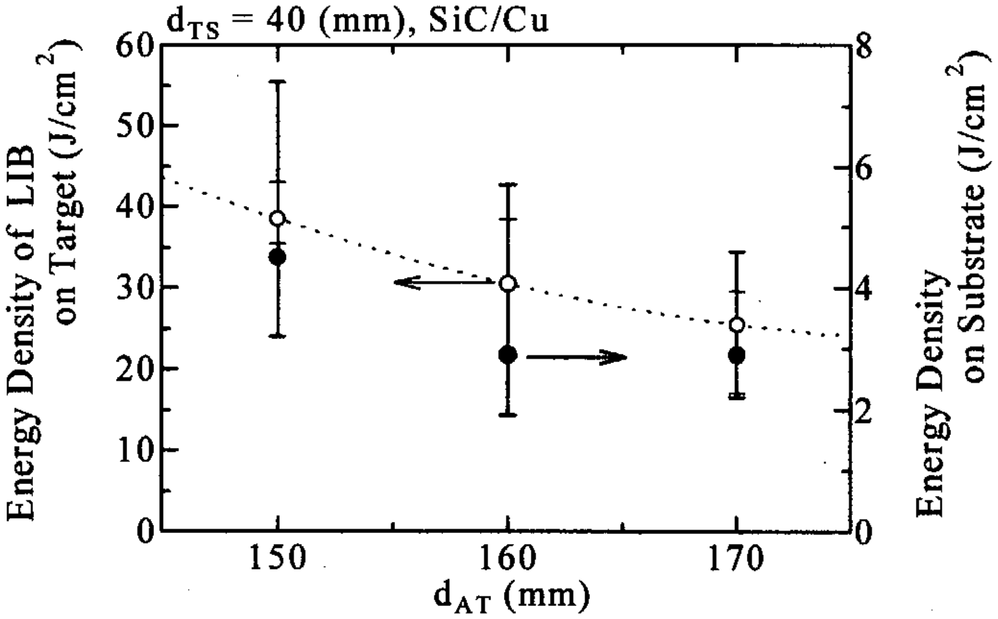

Fig.4 Energy density of LIB on target and of ablation plasma on substrate as a function of d_{AT}. Each dot represents the averaged value being fired by five shots.

Figure 4 shows the energy density of the pulsed light ion beam on the target and the energy density on the substrate as a function of d_{AT}. With increasing d_{AT}, being far away from the geometrically focus point (d_{AT} = 140mm), the energy density of the ion beam on the target is seen to decrease. Furthermore, the energy density of the plasma is also decreased. In addition, it is observed that approximately 10 % of the ion beam energy is transferred to the substrate by the ablation plasma.

3.3. Estimate of instantaneous substrate temperature

It has been found that the ablation plasma deposits its thermal energy to the substrate. Although such an energy is not so large, the substrate temperature will be eventually increased after being fired even in a short time of ~40μs (see Fig.2). Since this time is shorter than the time scale of the thermal conduction on the substrate, the substrate surface is expected to be instantaneously heated up to considerably high temperature. Let us now evaluate the temperature rise by use of a thermal conduction model. Furthermore, we have assumed one - dimensional model, where the temperature rise only takes place in the depth direction of the substrate because we have used a substrate little bit larger than the musk window.

The thermal conduction in solid materials will be governed by the thermal conduction equation,

$$\frac{\partial T}{\partial t} = k\frac{\partial^2 T}{\partial z^2}, \qquad (2)$$

where T, k, z and t is the temperature, the thermal conductivity, the depth, and the time, respectively. With a constant thermal flow (F_0) on the material surface, the surface temperature can be given by

$$T(z=0,t) = \frac{2F_0}{K}\left(\frac{kt}{\pi}\right)^{1/2}, \qquad (3)$$

where K is the thermal diffusion coefficient[16].

Figure 5 shows the temperature rise of several kinds of substrates, which was calculated by eq. (3). Here, we have used $F_0 = 7.3\times10^4$ J/cm$^2\cdot$s, which was obtained by the energy density of 2.9 J/cm^2 measured by calorimetric method, and the deposition time of 40 μs determined by high-speed photograph. It is found that the surface temperature of the substrate increases as the time goes by. For example, the surface temperature of Si will be heated up to 330°C, while that of SUS substrate to 980°C. It is found that the substrate temperature strongly depends on the kind of the substrate materials. The temperature is almost the same order or exceeds the substrate temperature of the other deposition methods where the substrate is heated continuously to prepare crystallized thin films. Considering the above experimental and theoretical results, in the preparation of various thin films by use of the IBE, it is very important for us to select substrates from the consideration of the temperature rise.

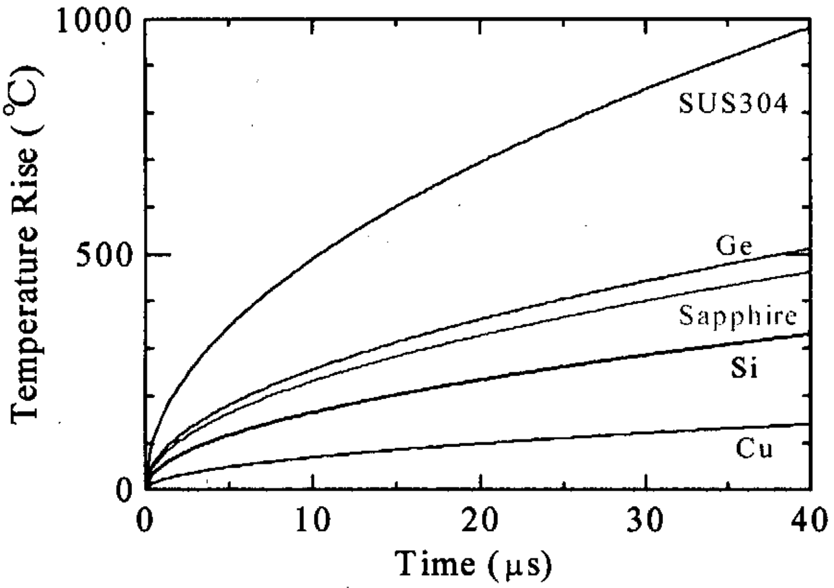

Fig. 5 Calculated result of temperature rise of the surface for several kinds of substrates.

4. Conclusions

The following conclusions have been obtained from the above studies.

1) The ablation plasma exists for ~ 40 μs on the substrate surface.
2) The ablation plasma deposits the thermal energy of ~ 2.9 J/cm^2 to substrate at the ion-beam energy density on the target of 25J/cm^2.
3) The substrate surface may be instantaneously heated up to the temperature of 100 ~1000°C, which strongly depends on the material of the substrate.

References

1) Y. Shimotori, et al.: J. Appl. Phys. **63**, 968 (1989).
2) Y. Shimotori, et al.: Jpn. J. Appl. Phys. **28**, 468 (1989).
3) K. Yatsui: Laser and Particle Beams **7**, 733 (1989)
4) X. D. Kang, et al.: Jpn. J. Appl. Phys. **33**, 1155 (1994).
5) X. D. Kang, et al.: Jpn. J. Appl. Phys. **33**, L1041 (1994).
6) K. Yatsui, et al.: Phys. Plasma **1**, 1730 (1994).
7) G. P. Johnston, et al.: J. Appl. Phys. **76**, 5949 (1994).
8) K.Yatsui, et al.: Appl. Phys. Lett. **67**, 1214 (1995).
9) T. Sonegawa, et al.: Appl. Phys. Lett. **69**, 2193 (1996).
10) T. Sonegawa, et al.: Laser & Particle Beams **14**, 537 (1996).
11) K. Yatsui, et al.: Jpn. J. Appl. Phys. **36**, 4928 (1997).
12) K. Yatsui, et al.: Mater. Chem. And Phys. **54**, 219 (1998).
13) W. Jiang, et al.: Nucl. Instr, and Methods **A415**, 533 (1998).
14) T. Sonegawa, et al.: J. Mater. Sci. Lett. **17**, 1685 (1998).
15) A. Tokuchi, et al. : Proc. 2nd Int'l Topical Symp. on Inertial Confinement Fusion Res. by High-Power Particle Beams, ed. by K. Yatsui (Lab. of Beam Tech., Nagaoka Univ. of Tech.) 430 (1986).
16) H. S. Carslaw and J. C. Jaeger: in *Conduction of Heat in Solids*, 2nd ed. (Oxford Univ. Press, 1959).

Influence of Cross-sectional Discontinuity on Power Flow of Magnetically Insulated Transmission Line

Kazuki HIRAOKA, Mitsuo NAKAJIMA, Kazuhiko HORIOKA and Makoto SHIHO*

Department of Energy Sciences. Tokyo Institute of Technology
Nagatsutacho 4259, Midori-ku Yokohama, Japan 226-8502

**Japan Atomic Energy Research Institute*
Tokai-mura, Ibaraki, Japan 319-11

Abstract

In the Magnetically Insulated Transmission Lines (MITLs), space-charge electrons flowing in the gap carry considerable fraction of electric power. The power flow behave in different way from normal vacuum transmission line because of electron momentum and interaction between electrons and fields. Especially in case that the transmission line has abrupt geometrical change, the electron flow can not follow changes of fields, and causes power losses and deformation of the pulse forms. We studied these effects of space-charge electron flow numerically using 2.5D PIC code in cylindrical negative-polarity MITL. We have obtained following results: in case that cathode radius shrinks toward downstream, power transport efficiency increased more than 15% compared with step discontinuity when cathode had the groove whose width is longer than radius of gyro-motion of electrons, space-charge electron made vortexes, which cause large delay and modulation on the power pulse.

1. Introduction

The Magnetically Insulated Transmission Line (MITL) insulates the field emitted electrons by bending their trajectories with self magnetic field. The power density of electro-magnetic (EM) wave is described by the magnitude of Poynting vector $|\boldsymbol{S}|=|\boldsymbol{E}|^2/377(\Omega)$, which means achievement of high power density goes with high electric fields. Generally, fields in the range of over $0.2\mathrm{MV/cm}^2$ cause field emission of electrons from the negative conductor. If these electrons go across the vacuum gap, large losses of current take place. Because of this reason, magnetically insulated mode is necessarily needed for efficient EM power transportation at high power level. In order to achieve inertial confinement fusion, ion beam[1], soft X-ray source utilizing fast Z-pinch[2], and so on are being developed as driver. These appication needs MITL to transport Terra Watt electric power.

MITLs under high power operation are dominated with space charge current flowing in the gap. This flow considerably reduce the effective inductance and increase the effective capacitance from the vacuum values and carries large fraction of total current[3,4]. The fraction of space charge current varies as a function of local voltage and current level and vice versa. So these non-linear effects are essential for analyses of the high power transportaion.

The characteristics of space-charge electron flow has been investigated well for parallel coaxiall lines or gentle taper[5-14]. However, loads of MITLs such as diodes, Z-pinch, and so on, have various shapes and abrupt cross-sectional change is unavoidable. When an MITL has such a geometrical discontinuity, the electron flow is disturbed and cause significant power loss.

Consequently, to evaluate influence of geometrical discontinuity, numerical approach is required. We have made a parametric survey about the power flow efficiency through the MITLs using 2.5D PIC code MAGIC.

2. Simulations

2.1 Case of shrinking cathode toward downstream

At first, we simulated the case that cathode radius shrinks toward downstream and anode radius is constant as Fig.1. Here, cell size is 0.5~1.0mm in r direction and 2.5~5.0mm in z direction. The time step is 2~3ps and the number of macro particles is 0.5~2million. At the input boudary(z=0), voltage pulse of 2MV is applied and at the output boundary(z=1m), electrons and EM wave go out without any reflections. Simulations are done with case of r_a=5cm and r_{c1}=2.5cm, and case of r_a=6cm and r_{c1}=5cm.

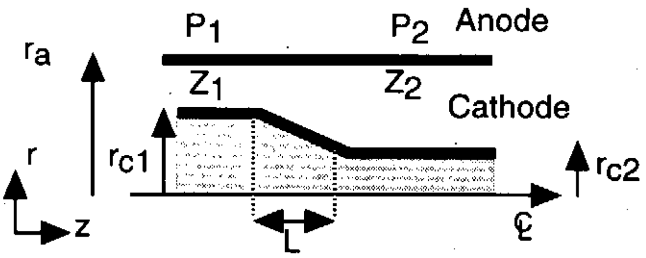

Fig.1 Vacuum cylindrical transmission line which has cross-sectional change.

In normal (without emission) line, power transport efficiency can be analytically expressed as follows:

$$P_2/P_0 = 4Z_1Z_2 / (Z_1+Z_2)^2 = 4 \ln (r_a/r_{c1}) \ln (r_a/r_{c2}) / \{\ln (r_a/r_{c1})+\ln (r_a/r_{c2})\}^2, \qquad (1)$$

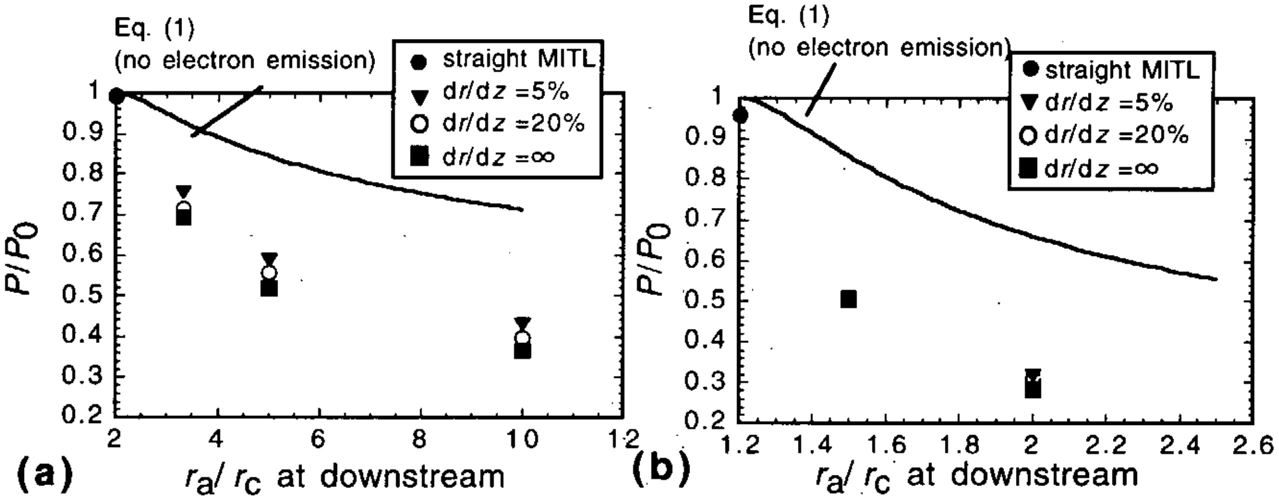

Fig.2 Power losses of ordinary vacuum transmissions and MITLs which has cross-sectional change. The solid line shows the curve of formula (1).
(a)For upstream radius r_a=5cm and r_c=2.5cm. (b)For upstream radius r_a=6cm and r_c=5cm.

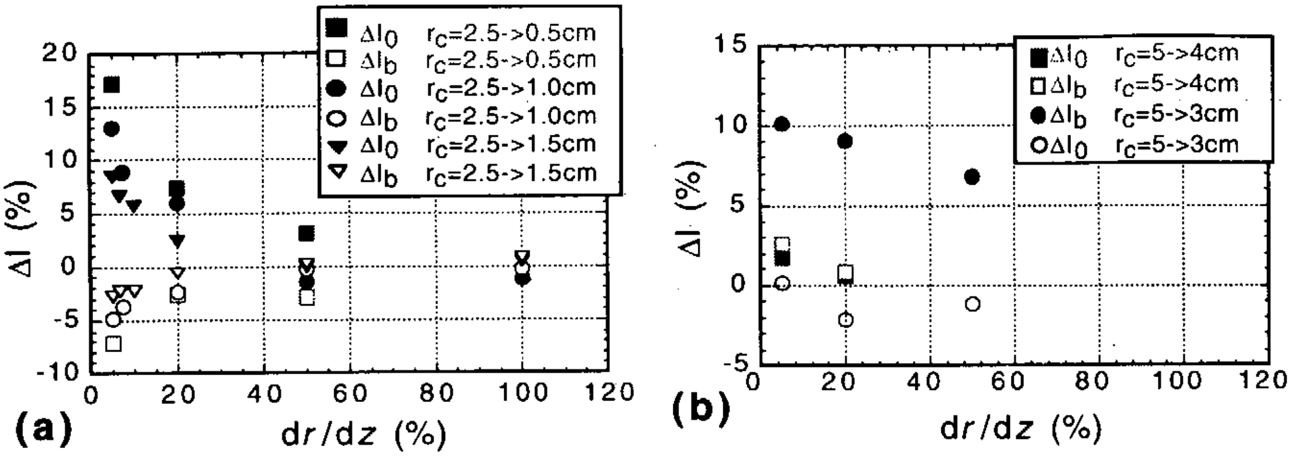

Fig.3 Relations between gradient(d*r*/d*z*) of cathodes and current losses. This plot shows differences of total currents I_0 and boundary currents I_b from those of the case d*r*/d*z*=∞.
(a)For upstream radius r_a=5cm and r_c=2.5cm. (b)For upstream radius r_a=6cm and r_c=5cm.

thus it depends on only radial ratio not on the gradient(d*r*/d*z*) and voltage between electrodes(*V*). However, as shown in Fig.2, simulation results show that in MITLs, losses due to radial geometrical change are larger than those of norml vacuum line, and larger the gradient became, larger the loss become. The relationship between current vs. d*r*/d*z* is also shown in Fig.3. Here ordinate(ΔI) shows the difference of current of certain gradient from that of right angle (d*r*/d*z*=∞), I_0 is the total current and I_b is the boudary current.

Behavior of space-charge electron flows through step (d*r*/d*z*=∞) and tapered cathode are shown in Fig.4 and Fig.5. When the cathode radius changes with right angle(Fig.4), a significant fraction of space-charge electrons in the vicinity of the anode is lost into the anode. However when the

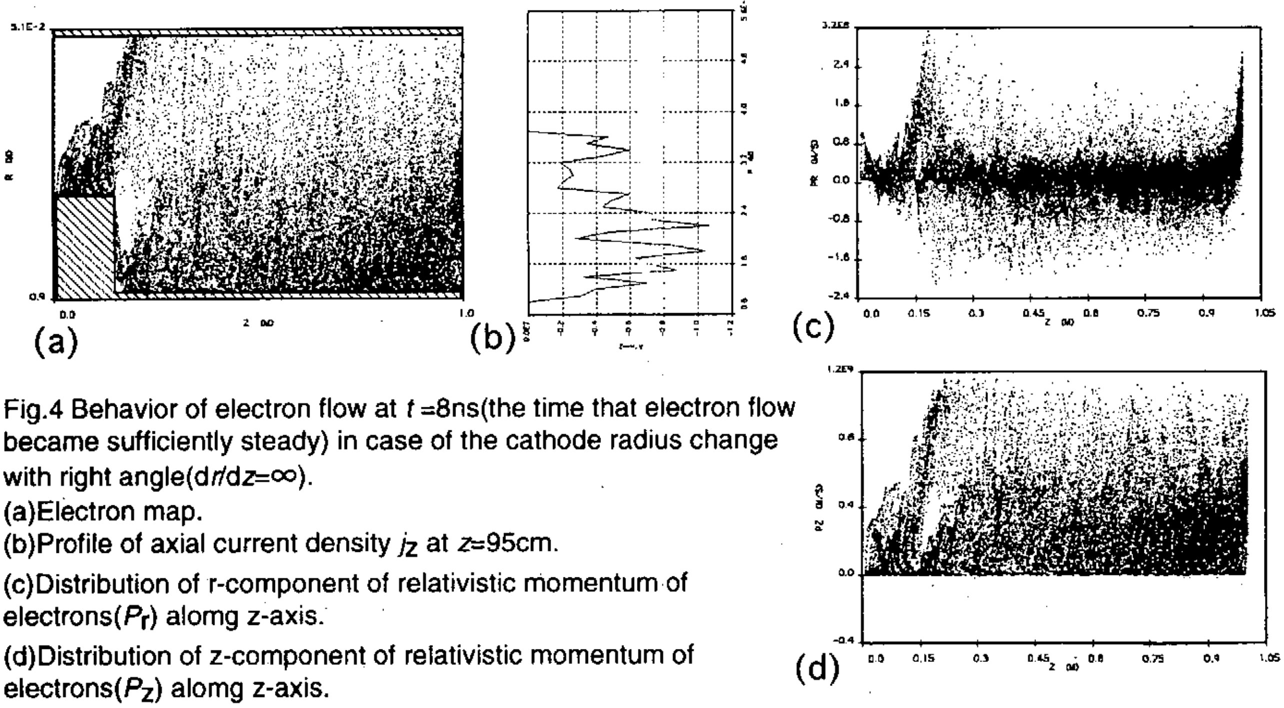

Fig.4 Behavior of electron flow at *t* =8ns(the time that electron flow became sufficiently steady) in case of the cathode radius change with right angle(d*r*/d*z*=∞).
(a)Electron map.
(b)Profile of axial current density j_z at *z*=95cm.
(c)Distribution of r-component of relativistic momentum of electrons(P_r) alomg z-axis.
(d)Distribution of z-component of relativistic momentum of electrons(P_z) alomg z-axis.

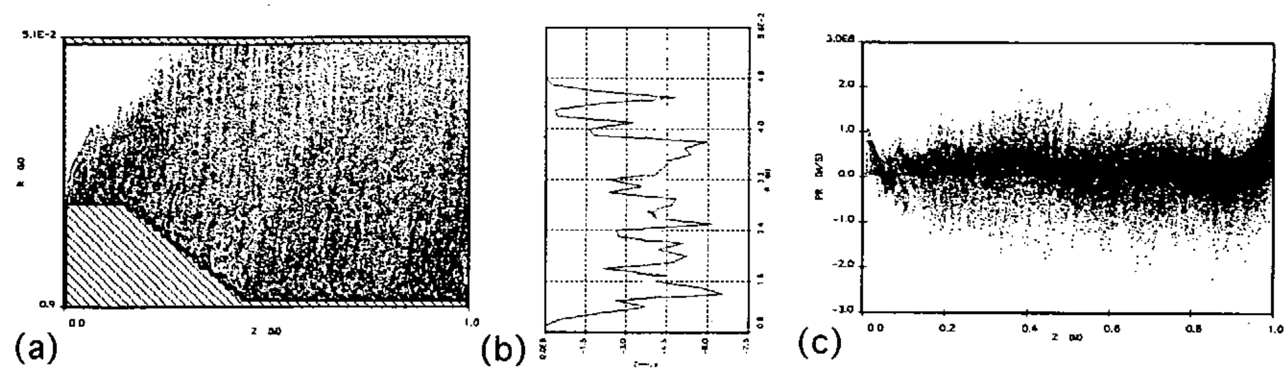

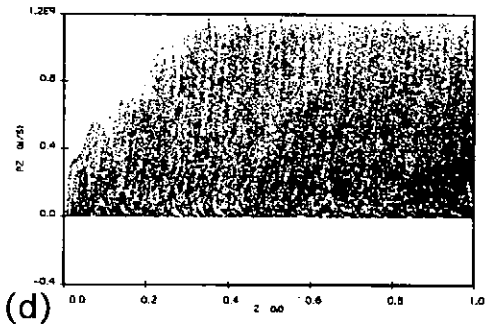

Fig.5 Behavior of electron flow at t=8ns(the time that electron flow became sufficiently steady) in case of the cathode radius change with dr/dz=5%.
(a)Electron map 8ns after the pulse application.
(b)Profile of axial current density j_z at z=95cm.
(c)Distribution of r-component of relativistic momentum of electrons(P_r) along z-axis.
(d)Distribution of z-component of relativistic momentum of electrons(P_z) along z-axis.

gradient is gentle(Fig.5), space-charge electrons spread widely between the gap. In case of dr/dz=∞, power of electrons lost into the electrode(mostly of anode) at t=8~10ns was nearly the same value of power $P(= I_0 \times V)$ loss between upstream(z=5cm) and downstream(z=95cm). These results show that loss of current occurred at the geometrical discontinuity is mainly due to shunt current to the anode.

Fig.6 shows voltage dependence of the power losses. As shown, higher voltage makes the loss smaller and large geometrical gradient makes this tendency larger. This shows that higher voltage increase the effective mass of electrons and decrease the influence of field disturbance.

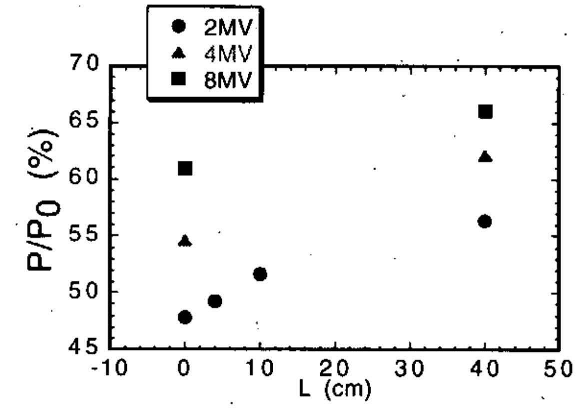

Fig.6 Applied voltage dependance of power loss.

2.2 Power flow along cathode with groove

MITLs which have grooves are also simulated. In this case, we evaluated the influence of groove width W and depth D on electron flow. Here, applied voltage is fixed at 2MV. Figure 7(a)~(c) shows charge distribution of electron flow at t=8ns with groove of W=5cm, 10cm, and 20cm. Obviously, wider groove causes larger disturbance on the space charge flow. Phase space plots in case of Fig.7(c) are shown in Fig.8. These plots show that the electron makes vortex flow at the groove. Trajectory plots(Fig.9) indicates that when width of groove is much longer than the

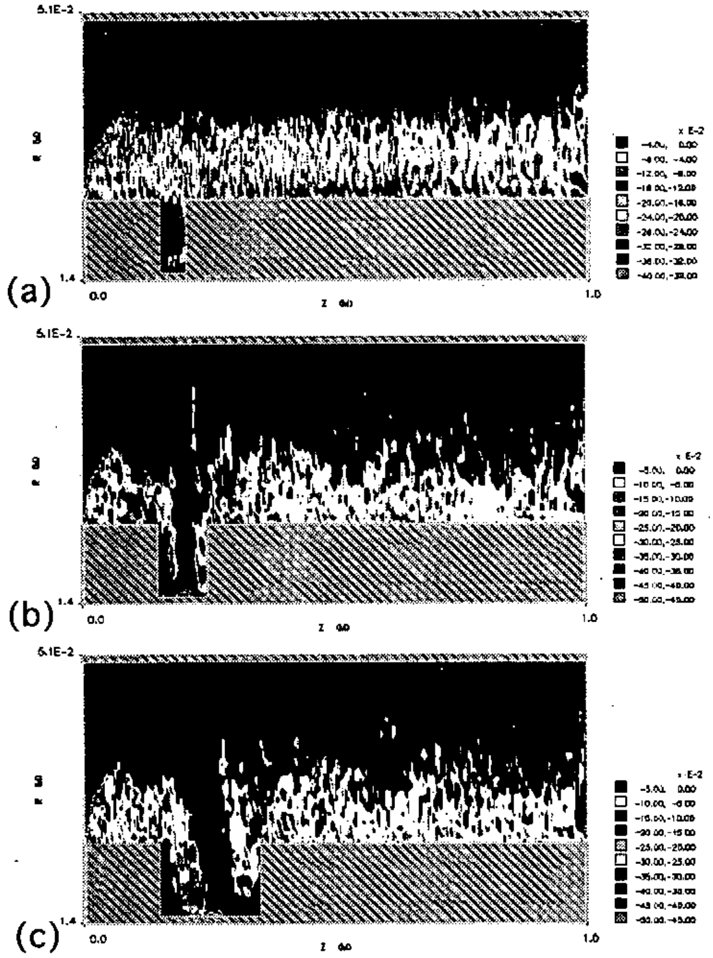

Fig.7 Contour plot of electron charge density at t= 8ns.
(a) W=5cm D=2cm
(b) W=10cm D=2cm
(c) W=20cm D=2cm

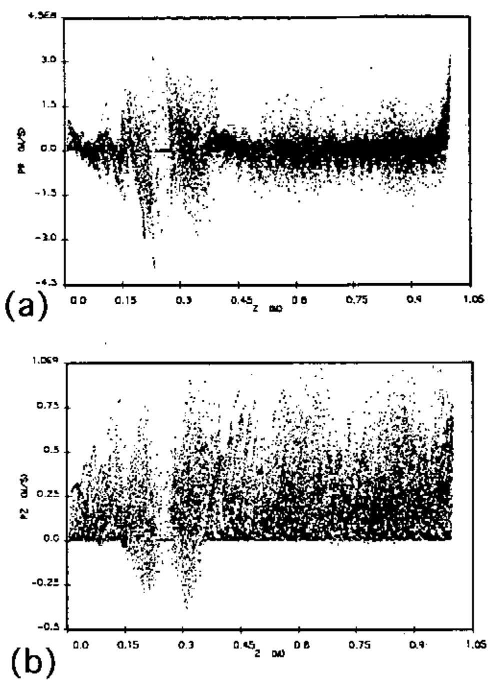

▲ Fig.8 Distributions of relativistic momentum of electron flow.
(a)Distribution of r-component of relativistic momentum of electrons.
(b)Distribution of z-component of relativistic momentum of electrons

▼ Fig.9 Typical electron trajectories for$t$=20ns$\sim$20.5ns.
(a)For case of W=30cm and D=2cm.
(b)For case of W=5cm and D=2cm.

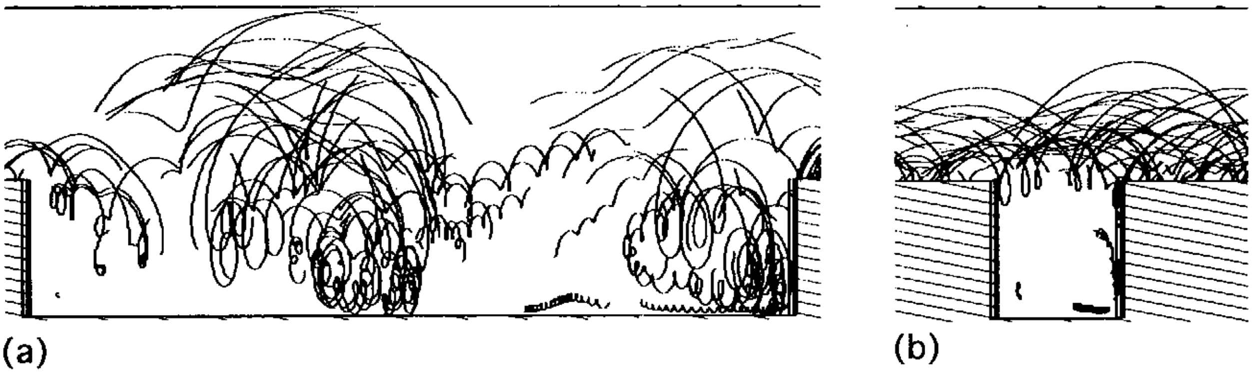

diameter of typical gyromotion, the vortex will appear. The dependence of groove width on the power loss is shown in Fig.10. Here, power loss is defined as the power at upstream of MITL with no groove ($P_U{}^N$) minus power at downstream of MITL with groove(P_d). Fig.11 shows time evolution of the power $P(=I_0 \times V)$ at upstream(z=5cm), middle of the groove(z=30cm), and downstream(z=95cm) in case of r_a=5cm, r_c=2.5cm, W=30cm and D=2cm. In addition to power decrease, fluctuation due to the vortex is observed at downstream.

To examine details of the power loss, we compared the power of electrons flowing into electrodes with decrease of the transported power $P(=I_0 \times V)$ in case of Fig.11. The values are averages for t=10~20ns. From numerical calculation, power of electrons flowing into electrodes is estimated to be 7.0x10^{9}W (cathode 3.4x10^{9}W; anode 3.6x10^{9}W) and the loss of P between upstream and downstream is 1.4x10^{9}W. It follows that power loss due to shunt current to the electrodes is only 50%. The rest power is accumulated as magnetic field energy. Fig.12 shows field energies of upstream region(1), groove region(2), and downstream region(3). As shown with this figure, only magnetic field enegy of groove region $B_{\theta 2}$ is increasing. The increasing rate of the magnetic field energy is 7.0x10^{9}W, and this corresponds to the rest power of 50%.

This magnetic energy almost saturates at t=20ns then power loss gets smaller but power fuctuation still remains due to the vortex formation of electron flow. Consequently, we can conclude that the large groove of cathode causes not only the delay of power rise(order of 10ns) but also power fluctuation on the load.

3.Discussions

In case of section 2.1, the output boundary is impedance matching condition and MITL operates with the self-impedance limited mode. There is

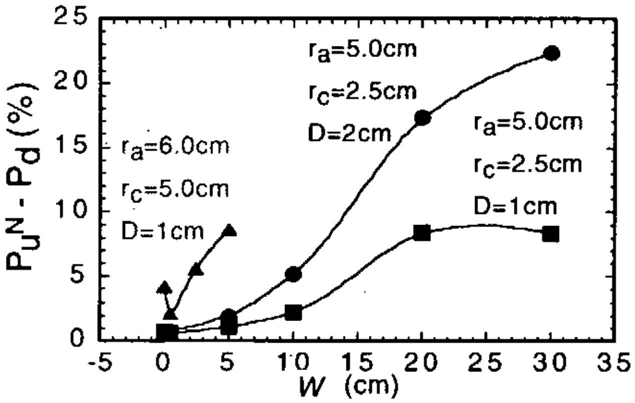

Fig. 10 Dependance oт power losses on width of the groove.

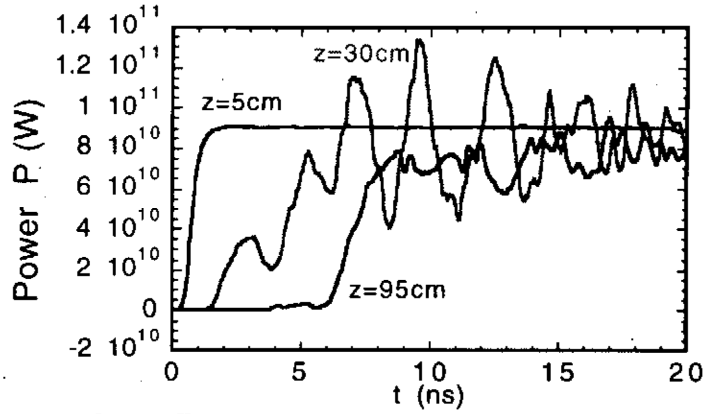

Fig.11 Transported electric power P (=I$_0$×V) at upstream, downstream and middle of the groove vs.time.

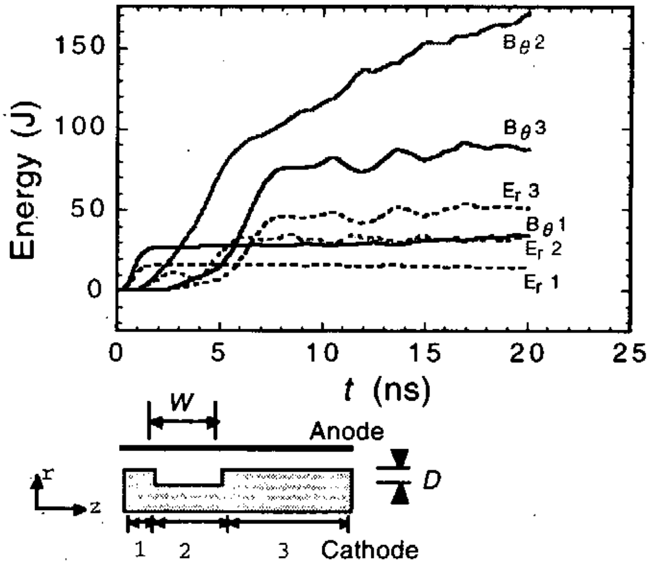

Fig.12 Temporal evolution of electric and magnetic field energy in MITL gap.

no reflection at downstream end, and because of electron current shunt into anode, no reflection at geometrical(impedance) discontinuity. The current in the downstream of the discontinuity is smaller than that of upstream, so abrupt decrease of magnetic field makes the electron flow to anode and maintains it. This is the main cause of current loss. The shunt current can be reduced by making the gradient gentler.

In case of section 2.2, the MITL oprates with load limited mode. In this case, power loss of electron flow into anode is relatively small. This is because current at the groove region is nearly same as current at the upstream. However strong magnetic field within the groove forms the vortex of electron flow. The vortex motion of space charge electron causes not only delay of power rise at the load but the fluctuation of load power. These effects can be avoided by making width of the groove smaller than characteristic length of electron gyration.

4.Concludion

In MITLs, considerable fraction of current is curried by space-charge electron flows. Thus, there are power loss mechanisms induced by the interaction of this current and electromagnetic field in the gap. They are;

(1)Power loss caused by shunt current into anode due to geometrical discontinuity of cathode,

(2)Power loss caused by electrons flowing into cathode surface induced by abrupt field change,

(3)Power loss at pulse rising because of accumulation of magnetic field enegy in discontinuity region.

The dominant loss mechanism is determined by the downstream condition. In addition to the power loss, geometrical discontinuity of the electrode sometimes causes power fluctuation on the load.

4. Refferences

[1] S. Humphries, Jr, Nuclear Fusion, **20** No.12, p1549 (1980)

[2] M. K. Matzen, Physics of Plasmas, **4** No.5 part2, p1519 (1997)

[3] J. P. VanDevender, Journal of Applied Physics, **50** No.6 p3928 (1979)

[4] M. S. Di Capua and D. G. Pellinen, Journal of Applied Physics, **50** No.5 p3713 (1979)

[5] D. D. Ryutov and R. N. Sudan, Proc. Beam's 94, p.144 (1994)

[6] J. M. Creedon, Journal of Applied Physics, **48** No.3 p1070 (1977)

[7] C. W. Mendel, Jr., S. E. Rosenthal, and D. B. Seidel, Physical Review A, **45** No.8, p5854 (1992)

[8] C. W. Mendel Jr. , Journal of Applied Physics, **50** No.6 ,p3830 (1979)

[9] C. W. Mendel, Jr., J. A. Swegle, and D. B. Seidel, Physical Review A, **32** No.2, p1091 (1985)

[10] S. A. Slutz, Journal of Applied Physics, **61** No.5, p2087 (1979)

[11] M. S. Di Capua, *IEEE TRANSACTIONS ON PLASMA SCIENCE, PS-11* No.3, p.205 (1983)

[12] C. W. Mendel Jr. and S. E. Rosenthal, Physics of Plasmas, **2** No.4, p.1332 (1995)

[13] R. I. Lawconnell and Jesse Neri, Physics of Fluids B **2** No.3 (1990)

[14] K. Hiraoka, M. Nakajima, K. Horioka and M. Shiho, Proc. 10th Intl. Conf. of High Power Particle Beams (to be published) (1998)

Simplified model for inhomogeneous and heavily saturated laser amplifier

Hikaru HANAJIMA, Mitsuo NAKAJIMA and Kazuhiko HORIOKA

Department of Energy Sciences, Tokyo Institute of Technology
Nagatsuta 4259, Midoriku Yokohama, Japan 226-8502

Abstract. Although gain saturation had been achieved using a fast discharge scheme [1], a detailed description of the amplification process up to saturation level is far from completion. For the evaluation of effective gain volume and laser energy extraction, refraction effects must be included because the fast discharge makes a complex internal structure in the high energy density plasma [2]. In connection with Z-pinch X-ray laser, a ray-tracing and independently saturating cell model was developed. With this model, the complex problem of refraction and gain depletion process was treated self-consistently. Typical values of plasma parameter at each cell were calculated by 1-D MHD simulation code. For heavier Ne-like schemes, the output beam patterns and the extraction efficiency are discussed based on this scheme.

1.Introduction

The wavelength shortening is one of the most important subject on laser research. While the exicimer laser with wavelength down to 180 nm is made practicable, the laser in soft X-ray region is still under studying. The refraction problem necessarily exists with wavelength shortening because the lasing plasma has high electron density and large density gradient [3]. The refraction causes the shortening of effective gain length. This effect is larger, when wavelength is shorter. In addition, in order to get larger output energy, the plasma must become longer and the laser should operate at gain saturation region. So, we need a self-consistent model for inhomogeneous and heavily saturating laser medium to examine the feasibility of wavelength shortened schemes. For the laser amplification process, however, only a few models exist at present. In this paper, we propose a simplified ray-trace model including the refraction and the saturation effect self-consistently.

2.Modeling

A schematic diagram of our model is shown in Fig.1. The gain region of plasma is divided to some cells, and a light source is set in the center of each cell. Initial electron density, ion density, and gain coefficients at each cell are calculated by the Z-scaling [3] and MHD simulations [2]. A number of rays start as spontaneous emission in the center of cell. Using the following ray equation [4]

$$\frac{d^2r}{dz^2} = \frac{1}{\eta}\frac{d\eta}{dr}\left\{\left(\frac{dr}{dz}\right)^2 + 1\right\} \quad , \qquad (1)$$

we ray-trace in the inhomogeneous plasma for the emitted rays. Here, η, the index of refraction is the function of the electron density. The electron density profile is assumed to be constant while the ray-tracing. The ray intensities are calculated along the ray trajectories at constant interval. Two kinds of amplification formula are used. For small signal region, a general amplification formula [3] is used and for gain saturating region, the following proportional distribution equation

$$I_{i+1}S = I_iS + \frac{I_i}{SI_k}\Delta N h\nu V \quad , \qquad (2)$$

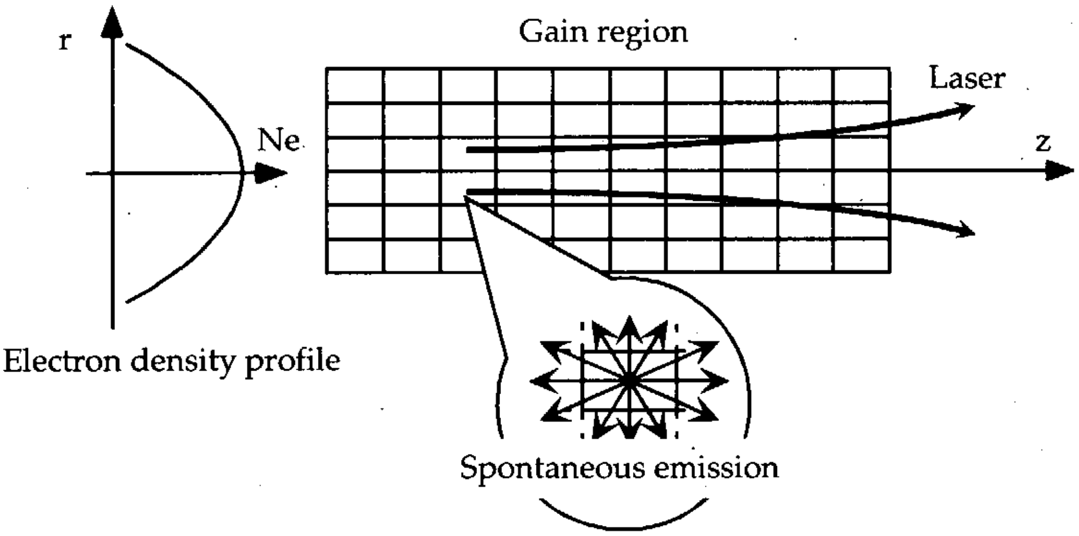

Fig.1. Schematic configuration of ray-trace model

is used. Here, I_i is the ray intensity entering cell, S is the cross section of ray, V is the volume of cell, and ΔN is the total population inversion in the cell.

At first, we calculate amplification of rays using the general amplification formula at each time. If the population inversion is large enough to amplify the rays, we put the next time step forward, and if population inversion is too small to amplify(it means saturation), we recalculate the ray intensity using Eq.(2). This means we distribute the excited energy to each ray proportional to the ray intensity. A self-consistent population of the exited levels at each cell is determined by the depletion process of exited ions, and rate equations. Therefore the depletion of gain is independently determined at each cell. Finally, by integrating the ray intensity at the end of plasma column, the output energy and beam patterns are calculated.

3.Intensity-energy problem

While the amplification formula is based on the ray intensity, the rate equation describes the time evolution of energy density. So that, we must determine the cross section of each ray to connect the amplification formula with the rate equations. We name it the intensity-energy problem [5]. But we confirmed that the calculated output beam pattern didn't vibrate(or diverge) but converge by increasing the number of rays as shown in Fig.2. This means that the ray number could make up this intensity-energy problem.

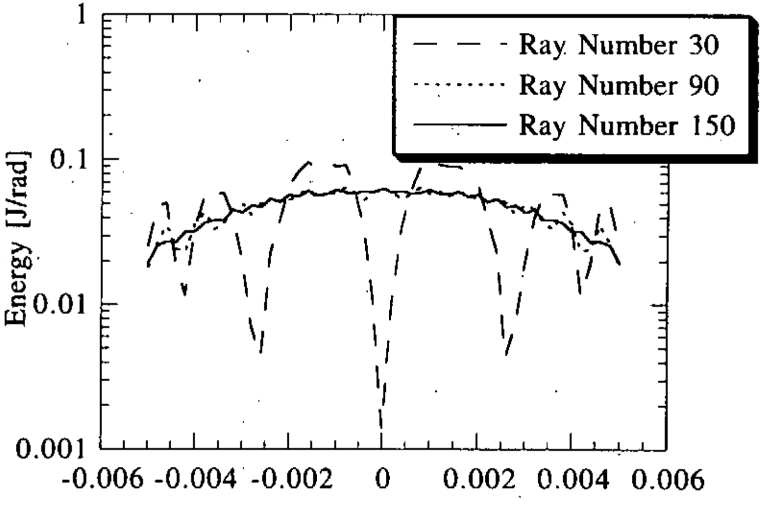

Fig.2. Typical output beam pattern versus ray number for cylindrical plasma with r = 519μm, L = 10cm, ne ≈10^{18}cm^{-3}(Ar).

4.Result and discussions

Fig.3. shows time evolutions of the output power for Ne-like[3p-3s] Ar , Kr and, Xe schemes. Cylindrical plasma is assumed here. The solid line and the dashed line represents the case of refraction and no refraction, respectively. The electron density profile is assumed to be parabolic whose maximum density equals the optimum electron density. The gain profile is also assumed to be parabolic. The ray number of each cell is 310-610. In case of this study, the plasma is split to 25(z)x20(r). The number of cell is important to discuss the calculated result. We often need to increase the number of cell to examine the beam pattern strictly. The spontaneous emission is proportional to the excited ion density of cell. These figures indicate that the saturation effect is well illustrated with this model, and that refraction effect of Ne-like Kr and Xe are larger than that of Ne-like Ar. As also shown, Ne-like Kr and Xe scheme reach saturating region earlier than Ne-like Ar scheme because the gain coefficient is larger.

Fig.4. shows the angle profile of output laser energy from Ne-like Ar and Ne-like Kr laser. This angle profile directly corresponds to the far field beam pattern from the gain region regarded. The output energy is calculated by integrating powers in Figs.3.(a), (b) and (c). So, each parameter is same as that in Fig.3. As shown in these figures, the ray refraction strongly affects the beam pattern. Since refraction effect is small for Ne-like Ar , the form of output energy has Gaussian-like profile. On the other hand, the angle profile of Ne-like Kr and Xe scheme form beam patterns with 2-peaks. This comes from the fact that the rays which have large intensity are refracted out of the center axis. For axial symmetrical gain region, this means that the far field beam pattern makes an annular profile. Compared the angle profile of Ne-like Kr scheme with that of Xe scheme, the ring size of Ne-like Xe is larger because of the refraction effect.

Table.1 shows the connection between initial energy for spontaneous emission, amplification ability of cell, and output energy calculated from Fig.3. The amplification ability of cell includes the initial population inversion of cell and the pumping effect. As shown in this table, the output energy is calculated consistently. Conventional amplification models describe small signal gain region such as t=0-0.1 ns in Figs.3.(a). On the contrary, by using our saturation cell model, the output energy and beam pattern can be calculated self-consistently including the refraction effect and the saturation effect.

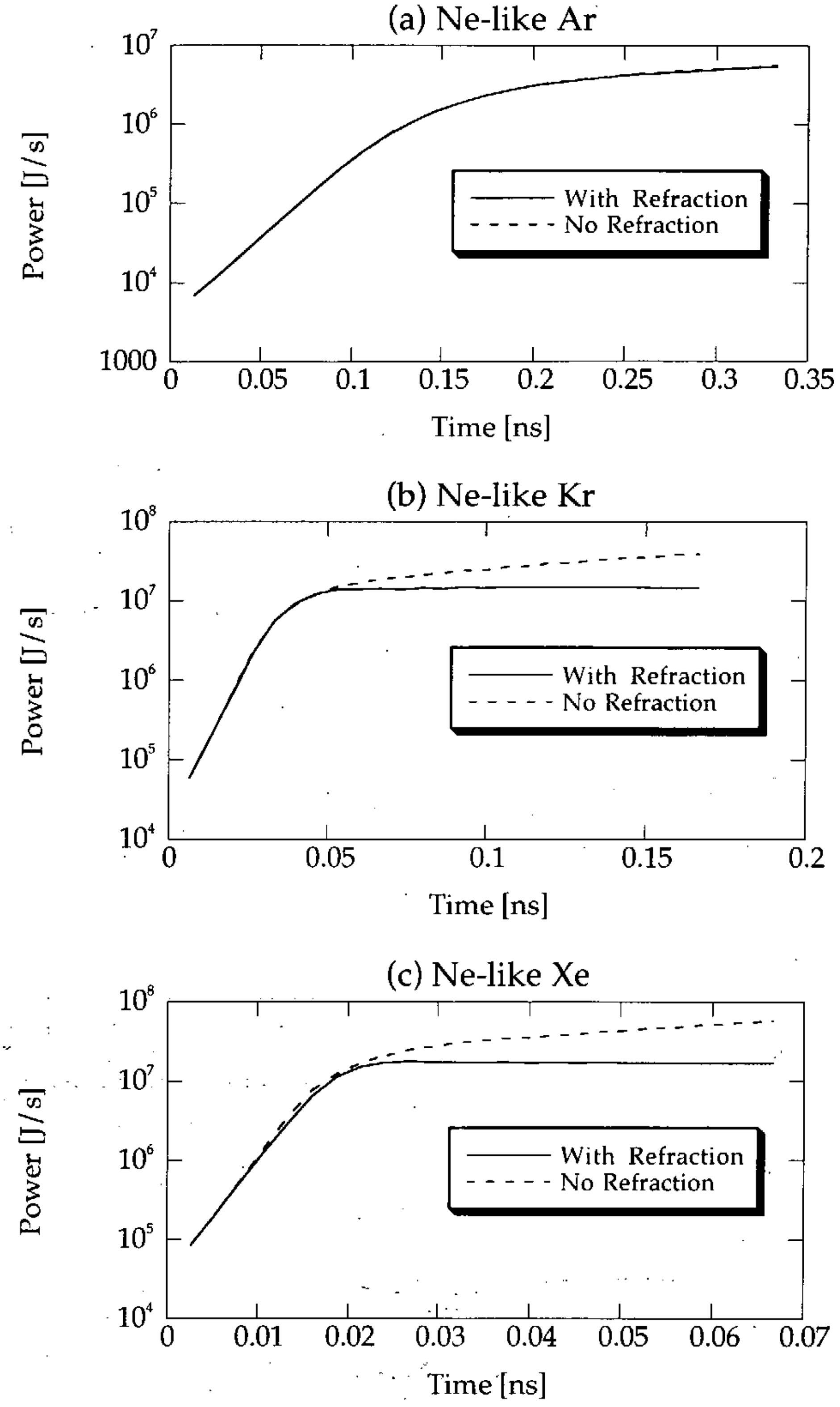

Fig.3. Time evolution of output power (a) Ne-like Ar ; λ = 51.1nm, r = 519μm, L = 10cm, ne $\approx 10^{18}$cm^{-3} (b) Ne-like Kr ; λ = 17.0nm, r = 119μm, L = 5cm, ne $\approx 10^{20}$cm^{-3} (b) Ne-like Xe ; λ = 10.2nm, r = 59.6μm, L = 2cm, ne $\approx 10^{21}$cm^{-3}

(a) Ne-like Ar

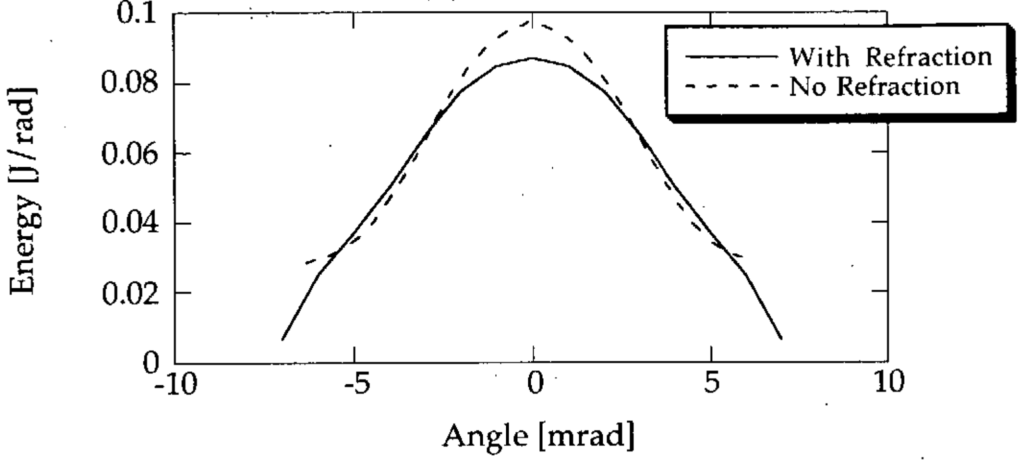

(b) Ne-like Kr

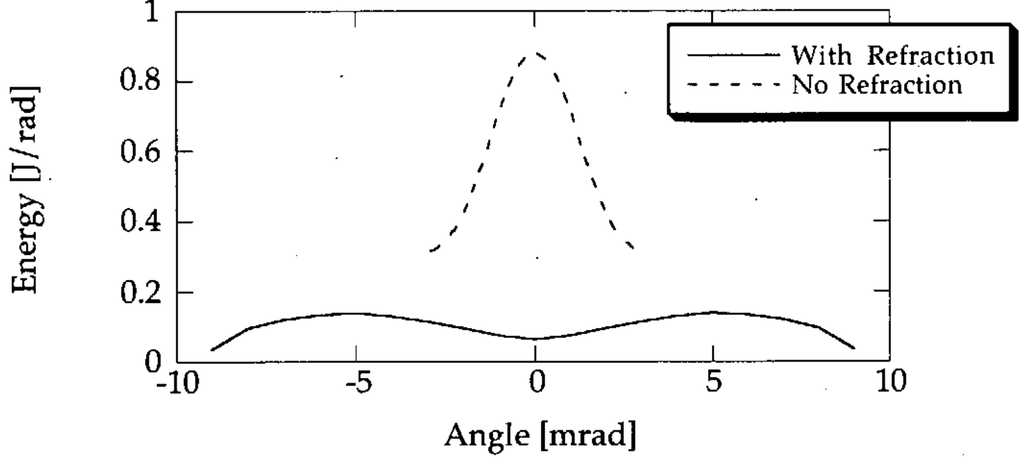

(c) Ne-like Xe

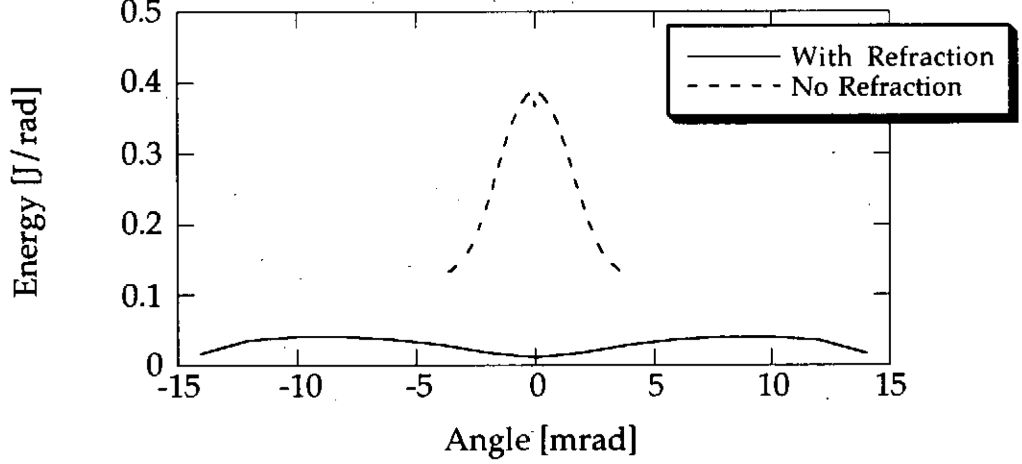

Fig.4. Angle profile of output energy from (a) Ne-like Ar laser, (b) Ne-like Kr laser and (c) Ne-like Xe laser produced by capillary discharge plasma columns with parabolic electron density.

	Initial Energy [J]	Amplification Ability of Cell [J]	Output Energy [J]
Ne-like Ar	9.1×10^{-6}	3.1×10^{-3}	7.8×10^{-4}
Ne-like Kr	3.9×10^{-5}	1.5×10^{-2}	1.9×10^{-3}
Ne-like Xe	2.2×10^{-5}	8.1×10^{-3}	8.6×10^{-4}

Table.1. Typical values of initial energy, amplification ability of cell, and output energy.

5.Conclusions

For parametric calculation of the energy out-put, the extraction efficiency and the beam patterns, a ray tracing and independently saturating cell model was developed. The intensity-energy problem could be made up by increasing the ray number. Using this model, output beam patterns and energy extraction for various Ne-like ions were discussed. The results indicate that the refraction made an annular output profile especially in case of shorter wavelength laser scheme.

6.References

[1] J. J. Rocca, D. P. Clark, and J. L. A. Chilla *Phys. Rev. Lett.* **77** 1476-1479 (1996)

[2] T. Hosokai, M. Nakajima and K. Horioka *J. J. Appl. Phys.* **36** 2327-2335 (1997)

[3] R. C. Elton 1990 *X-ray Lasers* (Academic Press, New York)

[4] Richard A. London *Phys. Fluids.* **31** 184-191 (1988)

[5] H. Hanajima, M. Nakajima and K. Horioka, Proc. 6th X-ray Laser Conf. (Kyoto, 1998)

Pulsed Power Systems for High Efficiency, Highly Repetitive Pulse Generation

D. Yamamura, K. Kinbara, I. Kitamura,
T. Takahashi, and K. Masugata

Faculty of Eng., Toyama Univ.,
3190, Gofuku, Toyama, 930-8555 Japan
Department of Electrical Engineering,

Abstract

A highly repetitive pulsed power system and a pulse compression circuit are proposed. In the highly repetitive system current breaker is used which is assisted by a magnetic switch (MS). The system is very simple and high efficiency is expected. In the preliminary experiment the characteristics of MS is evaluated.

On the other hand in the pulse compression circuit proposed, high efficiency, low load of switching device and reduction of reflected pulse are expected and it is suitable to produce low impedance pulses. Performance of the system is evaluated experimentally and by the computer simulation. Energy transfer efficiency of 94 % is obtained on a computer simulation, which is 15 % higher than the conventional one.

1. Introduction

Pulsed power technology$^{1)}$ has been extensively studied since it has a wide area of applications such as generation of high power particle beams, intense radiation sources of microwave, X-ray or neutrons, or excitation of gas lasers. In those applications the pulsed power system should be operated with high repetition rate. The efficiency of the system is also important for those applications. Conventionally, Marx generators have been utilized in the pulsed power systems to charge pulse-forming lines (PFL). However, since many discharge gap switches are utilized in the Marx generator, energy transfer efficiency is usually not high and it is difficult to operate with high repetition rate. To realize highly repetitive operation with high efficiency, a new type of the system is proposed where magnetic current breaker assisted by a magnetic switch (MS) is utilized. The system is very simple and uses no special switching device. In the paper, the concept of the proposed system is described with the result of the preliminary experiment.

For the generation of low impedance pulse desirable for example for z-pinch experiments, combination of Marx generator with PFL is not sufficient since the rise time of the pulse is limited by the inductance of output switch. To reduce the rise time, multi-stage pulse compression systems[2)] are used where intermediate storage capacitors (ISC) are inserted between PFL and Marx generator. However, in the system, pulse reflection occurs due to the mismatching between PFL and ISC, which reduces efficiency and reliability of the system. In the paper, a new type of pulse compression circuit is proposed, which produces no reflection and can efficiently produce a low impedance pulses[3)].

2. Highly repetitive pulsed power system using magnetic assisted current breaker

Figure 1 shows the conceptual drawing of the highly repetitive pulsed power generator using current breaker assisted by MS. As seen in Fig.1 (a) the circuit consists of a first stage capacitor (C_1), a discharge gap switch (SW_1), a magnetic switch (MS) and a second stage capacitor (C_2). The waveforms of V_{C1} (charging voltage of C_1), V_{C2} (charging voltage of C_2) and I_1 (charging current) are shown in Fig. 1(b). The operation of the circuit is as follows. C_1 is connected to a high voltage power supply and it is initially charged to V_0 and the MS is initially rested to the direction of I_1. When SW_1 is triggered, C_2 is resonantly charged since MS is in saturation (ON). In the case V_{C2} is described by

$$V_{C2} = V_{C1} \cdot \frac{C_1}{C_1 + C_2}\left(1 - \cos\omega \cdot t\right), \quad [t = 0 \text{ to } t = t_1 = \pi/\omega] \tag{1}$$

where ω is the resonance frequency of the circuit. Here, on the condition of $C_1 >> C_2$, maximum charging voltage of C_2 reaches twice of V_0 due to the ringing gain. At $t = t_1$ I_1 is reversed and MS becomes OFF (unsaturation). Hence I_1 is blocked and V_{C2} is kept at the peak value until MS becomes in saturation. If the duration of the OFF phase is sufficient to cool down the arc column of the gap switch the insulation of the switch is recovered and the system becomes ready for next shot. After the recovery of the SW_1, SW_2 is triggered and the charge of C_2 is transferred to the PFL. The feature of the system is as follows:

1. The circuit is very simple and highly repetitive operation is expected.
2. Charging efficiency of C_1 is expected to be high since change of V_{C1} is very small and voltage deference between C_1 and H.V. power supply is always small.
3. Charging voltage of C_2 is enhanced by the ringing gain.

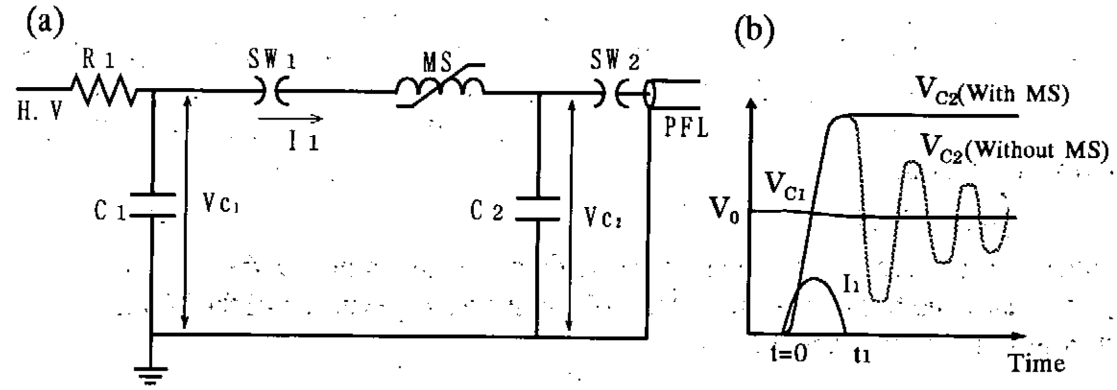

Fig.1 Conceptual drawing of the highly repetitive pulsed power generator proposed.

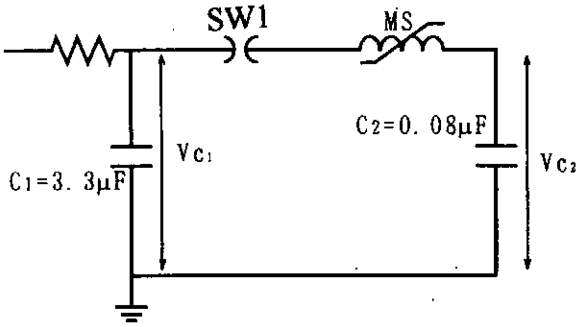

Fig. 2 The experimental circuit.

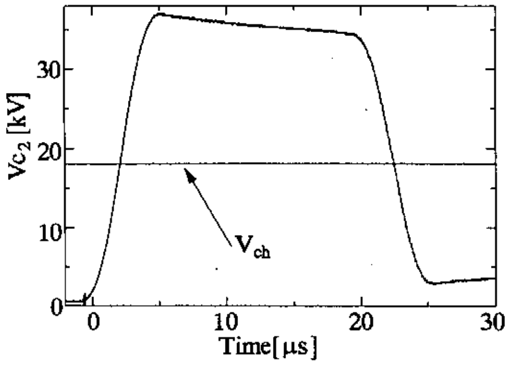

Fig. 3 Waveform of V_{C2} when V_{C2} is 18 kV.

Figure 2 shows the experimental circuit to confirm the operation of the proposed circuit. The circuit consists of C_1, SW1, MS, and C_2. To obtain a high value of ringing gain C_1 and C_2 are designed to be 3.3 μF and 0.08 μF, respectively. As the MS Co based amorphous metallic core (TDK AC30T265x24x96B) of saturation flux density (Bs) 0.78 T, magnetic flux swing ($\Delta B = B_s + B_r$) 1.55 T. The dimension of the core is, outer diam. 265 mm, inner diam. 48 mm, length 24 mm x 7. To get a sufficient duration of the OFF phase, the MS should have high value of the product of the applied voltage (V) and the duration (τ). Since $V \cdot \tau$ is equal to nΔBs (n is the turn number), n is designed to be 10, which gives design value of nΔBs = 0.22 V sec. In the experiment SW_1 was operated on a self-breakdown mode.

Figure 3 shows the waveforms of V_{C2} when V_{C2} was 18 kV. As seen in the figure, C_2 is charged in 6 μs and peak voltage of 36 kV is obtained, which corresponds to the twice of V_{C1}. After the peak V_{C2} is sustained for 15 μs. The Vt value of the MS is evaluated from Fig. 3 by the following equation

$$V \cdot t = \int (V_{C2} - V_{C1}) dt, \qquad (2)$$

and is evaluated to be 0.25 V sec. which agrees with the design value. After t_1, V_{C2} gradually decreases due to the leakage of the MS and the leakage current of the MS is evaluated from Fig. 2 to be around 14 A.

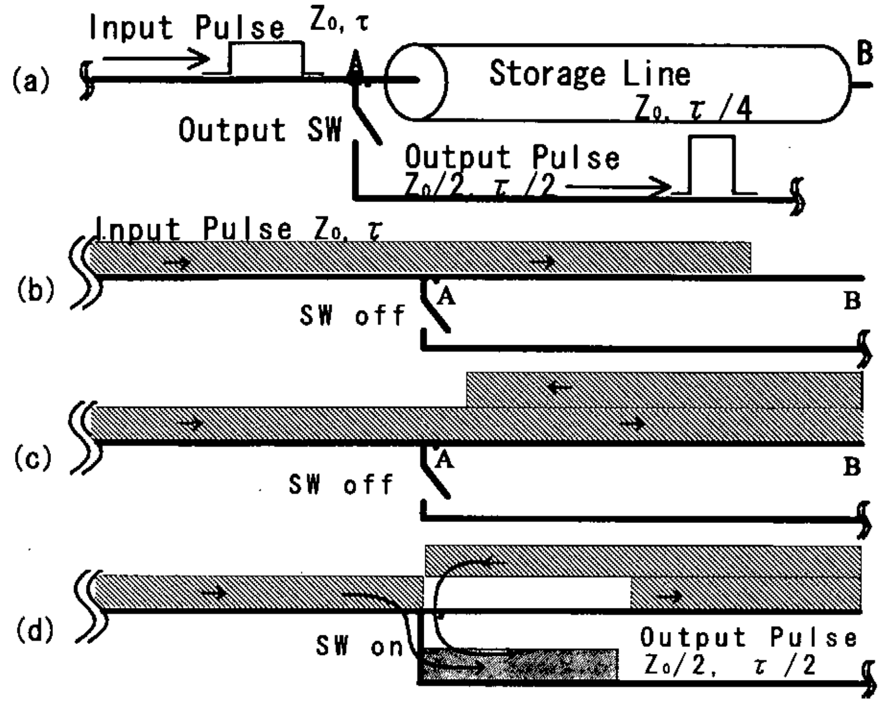

Fig. 4 Schematic of the proposed pulse compression circuit (a), and the principle of the circuit (b)-(d).

3. Development of new pulse compression circuit

Figure 4 shows the concept of the proposed pulse compression circuit. The basic idea of the circuit is, by adding the current of first half of the pulse with the latter half to get a current doubled, duration halved pulse. The circuit is constructed of a storage line of characteristic impedance $(Z) = Z_0$ and output switch as shown in Fig. 4 (a). At first, shaped pulse (duration $= \tau$) is injected. Since Z of input pulse is Z_0 and that the output switch is initially open, the input pulse passes point A without causing reflection (Fig.4 (b)). At point B, the input pulse is reflection and voltage doubled wave transports to the up stream since point B is open end (Fig.4 (c)). When voltage doubled pulse reaches point A, an output switch is closed and pulses from input line and storage line are started to be injected into the output line (Fig.4 (d)). Since the characteristic impedance of the output line is $Z_0/2$, pulses from both lines are added without causing reflection. Consequently, current doubled, duration halved pulse is produced without reflection.

The features of the circuit are, in principle causing no reflection, and $V\tau$ value sustained by the output switch is only half of the input pulse. Since the inductance and energy loss in the switch has a strong dependence on that value, efficient generation of low impedance, short pulse becomes possible by using the circuit.

3.1 Numerical evaluation of the circuit

Characteristics of the circuit are evaluated by using a circuit simulator "p-spice"[4)] and are compared with conventional PFL. Figure 5 shows circuit models used in the simulation. In both models, same device parameters are used for pulsed voltage source (1 MV, 100 ns, rise/fall time =10 ns/10 ns), input line (TL1), switch (SW, off/on resistance = 1 MΩ /0.1 Ω, L

= 50 nH, τ_{on} = 10 ns) output line (TL2) and load. The parameters of the devices are common except for the storage line/PFL.

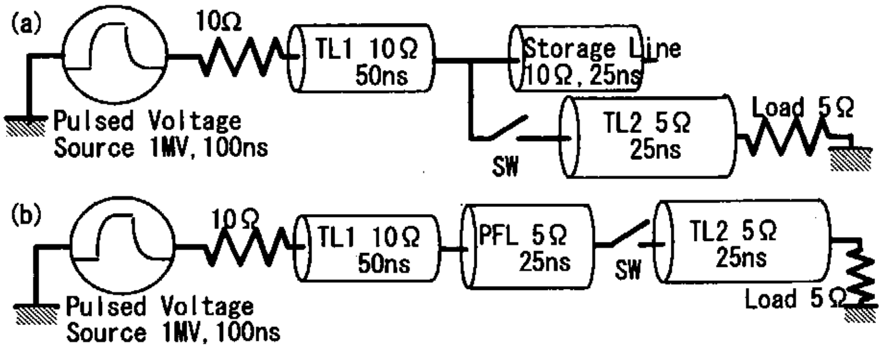

Fig. 5 Circuit models for a proposed circuit (a) and for a conventional circuit (b), used in the simulation.

Since performance of PFL strongly depend on the closing time of output switch (t_{sw}, time after the rise of input pulse) simulation has been done prior to the main simulation under the assumption of switch inductance (L) = 0 to get the optimum timing. At t_{sw} = 120 ns, maximum efficiency has been obtained as far as the duration of output pulse (FWHM) is less than 50 ns. For the proposed circuit, on the other hand, duration of the output pulse is insensitive to t_{sw} in the range of t_{sw} = 90-125 ns, t_{sw} = 90 and 100 ns is used for the main simulation.

Figure 6 shows waveforms obtained by the simulation. As seen in the figure, shaped pulse of duration around 55 ns are observed in V_{out} in both case. In Fig. 6 (a), the duration and height of reflected pulse in V_{in} is very small as compared with Fig. 6 (b). Table I summarize the results of the simulation. For proposed circuit, output voltage and output energy are extremely enhanced without reducing the rise time. The energy transfer efficiency of 94 % is obtained which is 15 % higher than that of conventional circuit. The reduction of energy loss is caused by the reduction of reflected pulse transported to the upstream. For the case of t_{sw} = 90 ns in the proposed circuit, $V\tau$ value of the switch (time integration of V_{SW} before t_{on}) is evaluated to be 15 mVs, which is 56 % of that for conventional system. Since

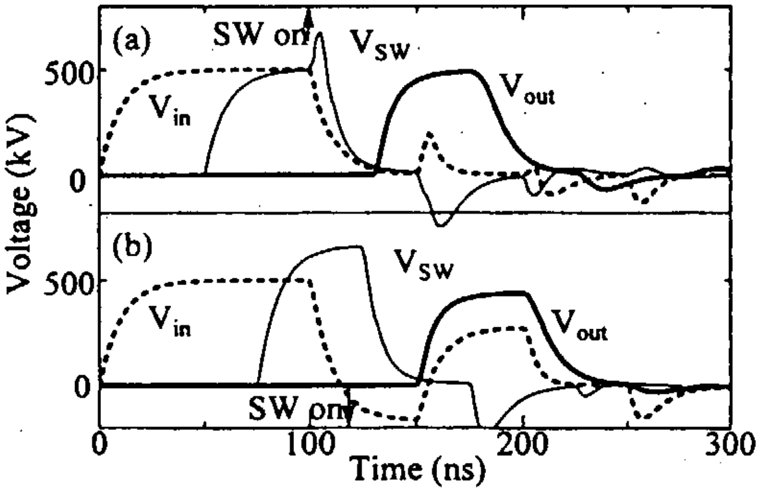

Fig. 6 Wave forms obtained by the simulation for a proposed circuit (a) and for a conventional circuit (b).

Table I Results of the simulation.

Circuit model	Proposed		Conventional
t_{sw}	90 ns	100 ns	120 ns
V_{out}(peak)	489 kV	492 kV	438 kV
Pulse width	56 ns	54 ns	56 ns
10-90% Rise	25 ns	17.5 ns	17.2 ns
$V\tau$ value	15 mVs	20 mVs	26.7 mVs
Efficiency	94 %	93 %	79 %

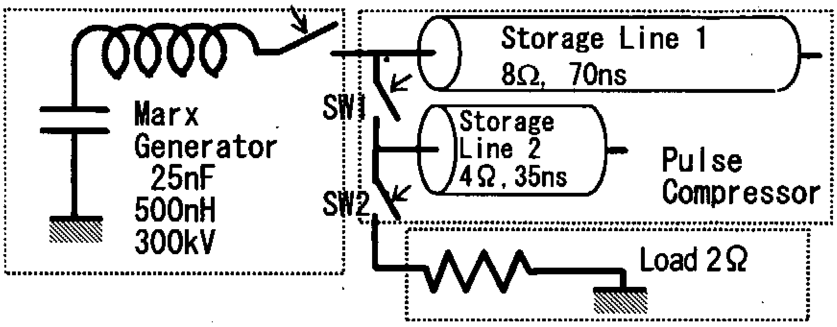

Fig. 7 Example of the application of the proposed circuit.

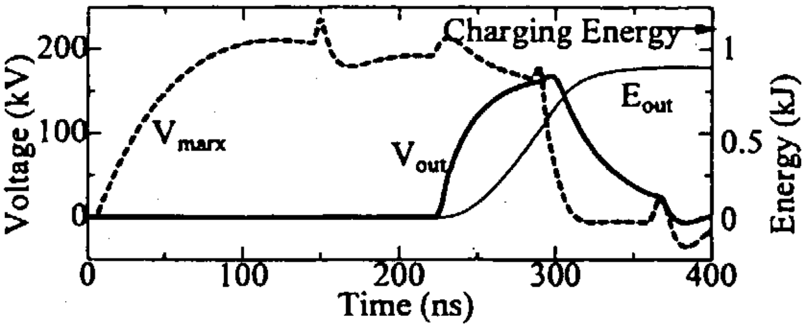

Fig.8 Waveforms obtained by the simulation.

inductance and energy loss in the switch has a strong dependence on $V\tau$, additional enhancement of the performance is expected in the proposed circuit.

Figure 7 shows the example of the application of proposed circuit. In the system, 2-stage compression circuit is utilized, which is directory connected to a Marx generator. The capacitance, inductance, and charging voltage of the Marx generator are 25 nF, 500 nH, and 300 kV, respectively, which are the actual parameters of the device[5)]. For SW1 and SW2, switching inductance of 100 nH and 50 nH, respectively, are assumed with off/on resistance = 1 MΩ /0.1 Ω.

Figure 8 shows wave- forms of the circuit obtained by the simulation. The output pulse of 169 kV, 84 kA, 84 ns, has been obtained with energy transfer efficiency of 80 %. In contrast to the conventional Marx-PFL system where energy of Marx generator is resonantly transferred to PFL, Marx generator acts as if it has a load of resistance equal to the value of critical damping. As a result, the output current of Marx generator is extremely reduced. Energy loss in the Marx switch has a strong dependence on the output current, reduction of output current enable the reduction of energy loss. Further more, two stage compression unable further reduction of $V\tau$ value of final switch and hence reduce the inductance, which make possible the reduction of rise time of output pulse.

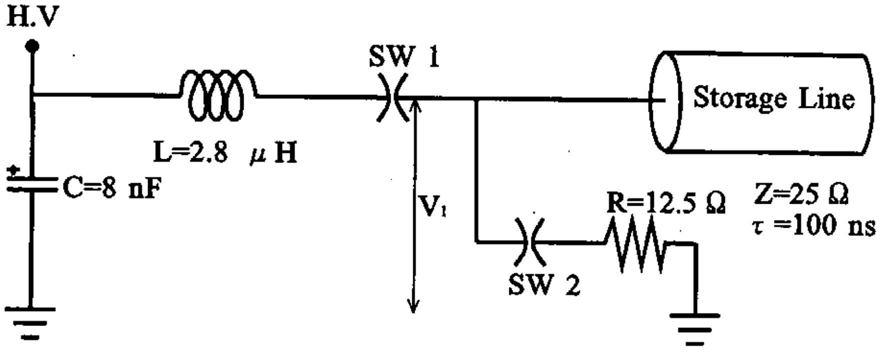

Fig. 9 Experimental circuit.

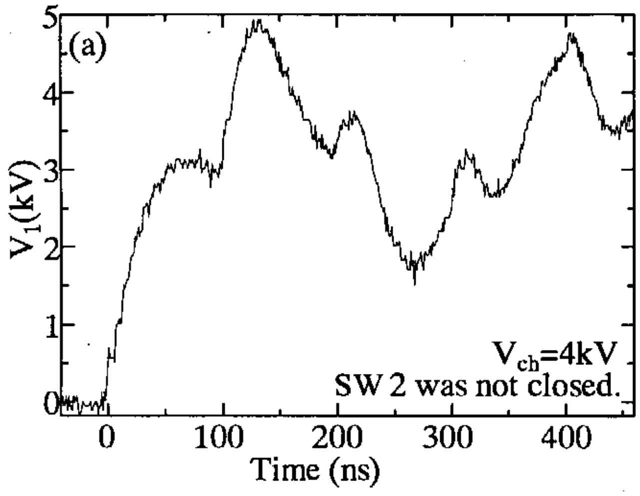

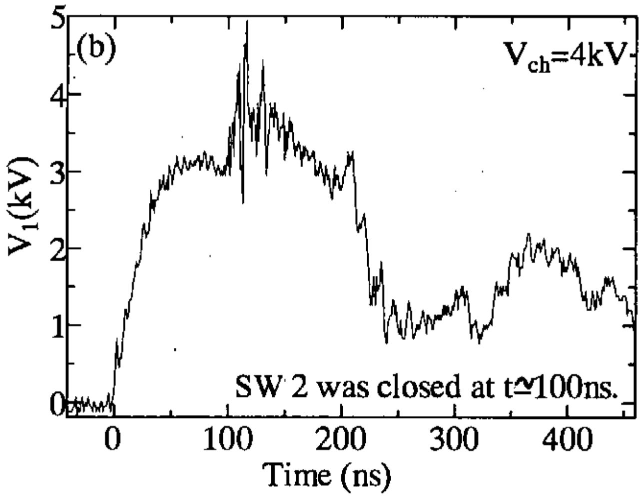

Fig. 10 Voltage waveforms at the entrance of the storage line. (a) SW2 was not closed. (b) SW2 was closed.

3.2 Experiment

Figure 9 shows the experimental circuit to confirm the operation of the proposed circuit. The circuit consists of a ceramic capacitor (C = 8 nF), inductor (L = 2.8 μH), gap switches (SW1, SW2), storage line and a resistive load (R = 12.5 Ω). As the storage line two coaxial cables of impedance 50 Ω, length 10 m (single way transit time 50 ns) each are connected in parallel. In the experiment the capacitor was charged to 4 kV and SW1 and SW2 are operated on a self-breakdown mode.

Figure 10 shows the voltage waveforms observed at the entrance of the storage line. As seen in Fig. 10 (a) refracted pulse rises at t = 100 ns (after the turn on time of SW1) and peak voltage of 5 kV is observed at t = 130 ns. Figure 10 (b) shows the waveforms observed when SW2 is closed. In the case SW2 was operated on a self breakdown mode however, the switch was closed on a proper timing due to the rise of applied voltage at t = 90 ns. Comparing with Fig 10 (a) the refracted pulse was reduced and hence we see the energy transfer to R. However, the reflected pulse was not perfectly removed and we see the insufficient energy transfer to R. This seems to be due to the resistance or inductance of SW2.

4. Summary

A highly repetitive pulsed power system and a pulse compression circuit are proposed. In the highly repetitive system current breaker is used which is assisted by a magnetic switch (MS). The system is very simple and high efficiency is expected. In the preliminary experiment the characteristics of MS is evaluated.

In the pulse compression circuit newly proposed, high efficiency, low load of switching device and reduction of reflected pulse are expected and it is suitable to produce low impedance pulses. The principle of the circuit is confirmed experimentally. Energy transfer efficiency of 94 % is obtained on a computer simulation, which is 15 % higher than the conventional one.

References

1)J. C. Martin; Proceedings of IEEE 80, 934-945 (1992).
2)N. Canarcat, et al; Laser and Particle Beams, 3 415-455 (1985).
3)K. Masugata, Rev. Sci. Instrum. 66, 5640-5641 (1995)
4)Micro Sim Corporatio1n, 20 Fairbanks Irvine, CA 92718 USA.
5)K. Masugata et al., Proc. BEAMS92, p.485 (1992).

Electrostatic Multi-Stage Accelerators for High Current Pulsed Ion Beam

K. Masugata, T. Atsumura, T. Takahashi, I. Kitamura
Faculty of Eng., Toyama Univ., Gofuku, Toyama, 930-8555 Japan

Abstract

Two types of electrostatic linear accelerators (time of flight isolation type (type A) and bi-directional pulse type (type B)) are proposed as a substitute for an induction linac to accelerators a high current pulsed ion beam. In type A, acceleration tube sufficiently long compared to the length of ion beam is used, inside of which multi-stage acceleration gaps are placed. Square pulses are sequentially applied to the acceleration gaps where the beam is passing and compensating voltages are applied to the gaps where the beam is absent to realize multistage acceleration without increasing the beam potential. On the other hand, in type B, bi-directional pulses are utilized which are sequentially applied to the acceleration gaps to realize the multistage acceleration. Compare to the ion beam induction linacs, proposed accelerators are simple, low cost and a higher acceleration gradient is expected since magnetic cores or induction cells are not utilized. Electrical behaviors of both systems are numerically simulated and demonstrated the performances. In addition, two types of pulse forming lines are proposed to produce bi-directional pulses for the type B accelerator. The performance of the lines was demonstrated numerically and experimentally.

1. Introduction

In recent years, an intense pulsed ion beam (PIB) has been actively studied as an energy driver of inertial confinement fusion. Linear induction linacs have been considered to be a hopeful source of PIB since multi-stage acceleration of high current PIB is possible [1-4]. In the induction linacs, however, induction cores of ferromagnetic materials are utilized to sustain the acceleration voltages, which makes the accelerator expensive and the structure complicated [2]. In addition, the average gradient of the acceleration in the induction linacs is limited by the size of the ferromagnetic cores. Even for a short pulse of 50 ns duration, the obtainable gradient is only 1 MV/m, whereas the maximum stress at the vacuum interface in the acceleration tube is more than 10 MV/m [5]. In this article, two types of high current, electrostatic, multi-stage accelerators are proposed. The accelerators are simple and are expected to have a higher acceleration gradient [6,7] .

2. Electrostatic Linac using time of flight isolation

Figure 1 (a) shows the concept of the proposed accelerator (as an example, a ten-stage system is shown). In the accelerator, the ion beam is injected from the left side. Here we assume that the length of the beam (l_b) is much shorter than the accelerator length (l_a). By using the velocity (v_b) and the duration (τ) of the beam, l_b is described as

$$l_b = v_b \times \tau. \qquad (1)$$

For example, l_b for a C^+ beam of 50 MeV with duration of 50 ns is only 142 cm and the condition $l_a >> l_b$ is realized in a 10-m accelerator. In the figure, l_b is supposed to be two times of the interval of the acceleration gap (l_i).

In the accelerator, points A and B in Fig.1(a) are kept at ground potential. Consequently, the sum the voltages applied to the gaps ($V_{g1}, V_{g2} \cdots V_{g10}$) is always kept to be zero and the following relation is satisfied.

$$V_{g1} + V_{g2} + V_{g3} + \cdots + V_{g10} = 0, \qquad (2)$$

An acceleration voltage (V_0) is applied to the gaps where the beam is just passing (in the figure, the beam is passing g_2 and g_3 at time t_1) and

$$V_{g2} = V_{g3} = V_0. \quad (\text{at } t_1) \qquad (3)$$

To satisfy eq. (2), a voltage of -(1/4)V_0 (the negative voltage is called as "compensating voltage") is applied to the gaps where beam is absent.

The waveforms of the gap voltages are shown in Fig. 1 (b). As seen in the figure, the acceleration voltage is compensated by the "compensating voltage" and the multi-

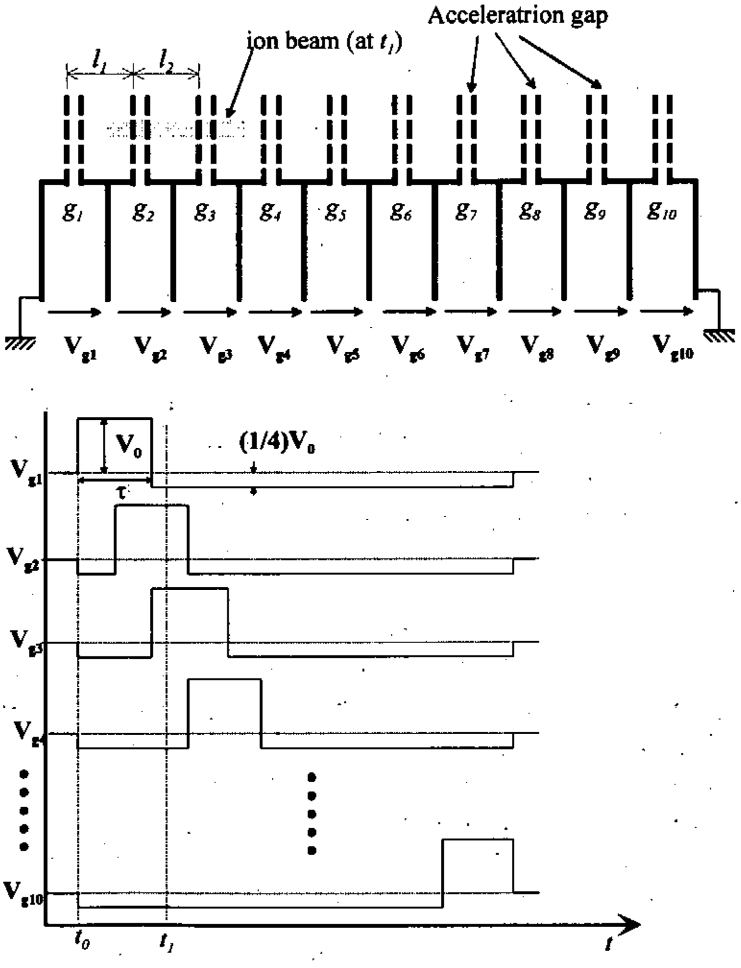

Fig. 1
(a) The concept of the accelerator proposed (a ten stage system is shown as an example). (b) Example of the gap voltage waveforms.

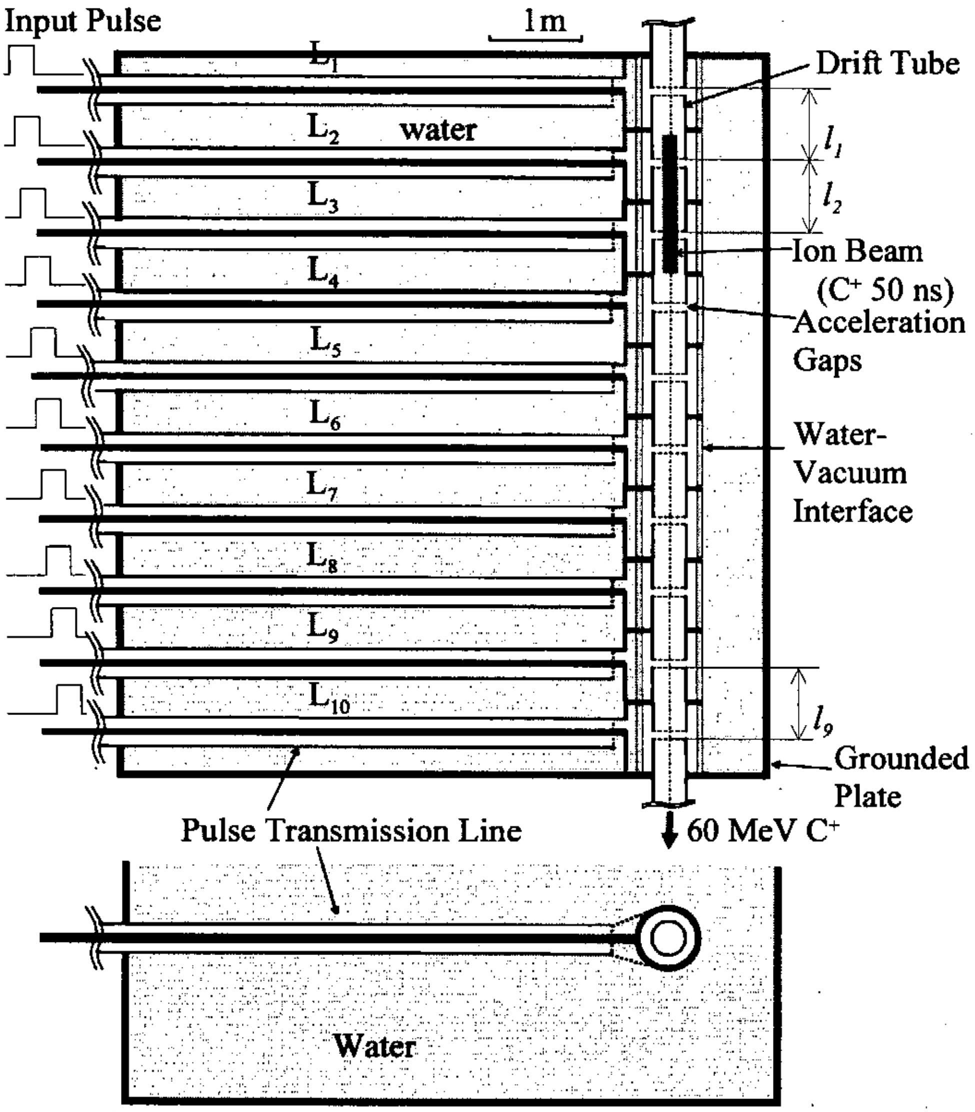

Fig. 1. The example of the accelerator design to demonstrate the operation.

stage acceleration is realized. This is in complete contrast to the induction linacs where acceleration voltage is compensated by an inductively produced field. In other words, in the proposed accelerator, the application of the acceleration voltages becomes possible due to a time-of-flight effect of the ion beam.

Figure 2 shows an example of the accelerator design to demonstrate the operation. The accelerator is designed to accelerate a 50 MeV 100 kA, 50 ns beam of C^+ ions to 60 MeV in ten acceleration gaps. The accelerator consists of an acceleration tube and pulse transmission lines which are put in a de-ionized water pool. The acceleration tube consists of acceleration gaps, drift tubes and water-vacuum interfaces. The gap intervals (l_1, l_2, $\cdots$, l_9) are adjusted to be 25 ns, being equal to the time-of-flight delay of the beam (a half of the beam duration). Since the velocity of the beam and hence the length of the beam increases as the beam is accelerated, the intervals are elongated downstream (for example, l_1 and l_9 are designed to be 71cm and 77cm, respectively).

The structure of the acceleration gaps is not designed in detail. However, the gap structure is flexible and many types of the structure including a magnetically insulated gap [4,5] or the multi-beam accelerator concept [1,2] will be acceptable. One of the subject of developing the high current pulsed ion beam linac is to obtain a stable propagation of the beam, which is not considered.

For the acceleration gaps, pulse transmission lines are used to apply the acceleration voltages. The lines have characteristic impedance of 10 ohms and an electrical length of 150 ns (which corresponds to a physical length of 5 m for a water filled line). For each line, the acceleration pulse is applied with an interval of 25 ns. The electrical length of 150 ns is important to isolate the gap voltage.

In conclusion, a new type of multi-stage accelerator is proposed to produce high current pulsed ion beam. Compared with the conventional induction linacs, the proposed accelerator is of great advantage since it is simpler and has a higher acceleration gradient. As an example, a ten stage accelerator is shown, which is designed to accelerate a 50 MeV, 100 kA, 50 ns beam of C^+ ions to 60 MeV, to demonstrate its performance. The results of the numerical simulation of the accelerator circuit is shown in the literature [6] and shown that the acceleration pulses are successfully applied to each gap.

3. Electrostatic linac using bi-directional pulses

Figure 3 (a) shows the principle of the proposed accelerator (as an example, a three-stage system is described). The accelerator consists of three drift tubes (D_1, D_2, D_3), four acceleration gaps (G_1, G_2, G_3, G_4) and grounded electrodes (A, B). The length of the drift tubes (l_1, l_2, l_3) are designed to be little longer than the beam length (l_b). When the ion beam of duration τ_b is injected to G_1, bi-directional pulse is applied to D_1 and accelerates the beam in G_1. The bi-directional pulse consists of negative and positive pulses of voltage $\pm V_0$ and duration τ_p each, which is adjusted to τ_b. When whole length of the beam passes G_1 and the beam is in the drift tube, the polarity of the pulse is reversed and when the beam is passing G_2, positive voltage is applied to D_1. On the timing, V_2 is applied to D_2, giving the total potential difference of $2V_0$ in G_2 and the beam is accelerated in G_2. In the same manner, ion beam is accelerated in G_3 and

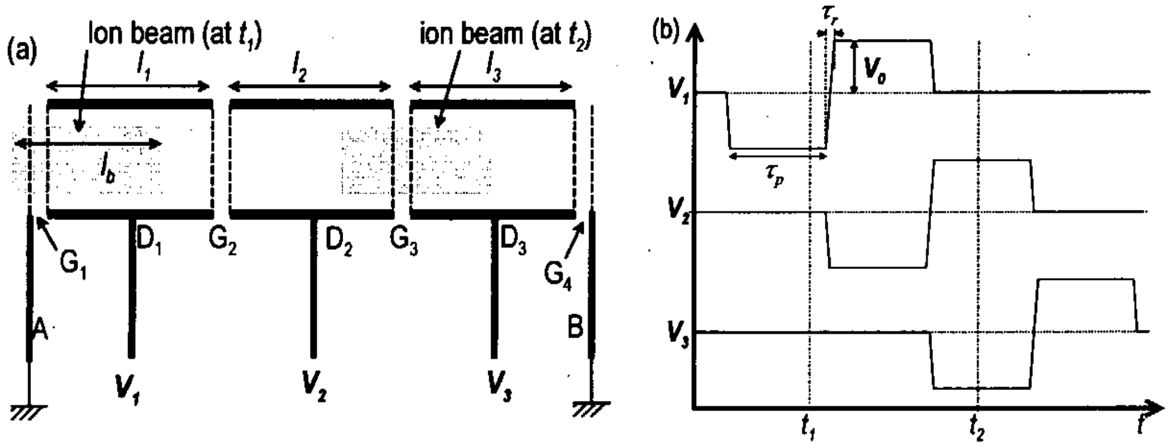

Figure 3 (a) The principle of the proposed accelerator (as an example, a three-stage system is described) (b)The time diagram of the applied pulses.

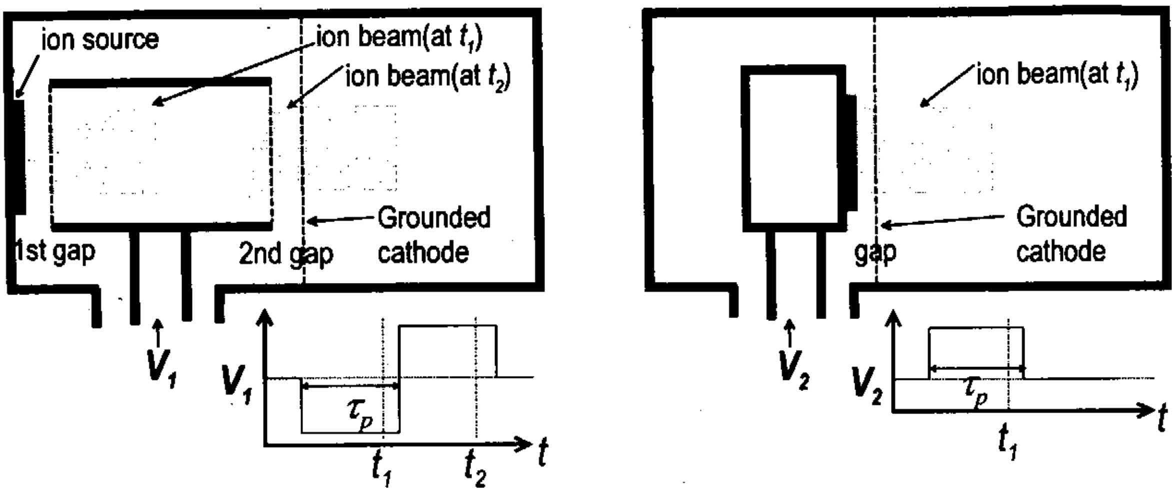

Fig. 4 (a) Conceptual drawing of the proposed pulsed ion source (ion diode).
(b) Conventional pulsed ion diode.

in G_4, and the beam experiences total acceleration potential of $6V_0$ in the accelerator.

The polarity of the bi-directional pules should be reversed when whole length of the beam is in the drift tube, hence the length of the drift tube (l_n) is described as follows.

$$l_n = l_b + v_b \times \tau_r = v_b \times (\tau_b + \tau_r) \qquad (4)$$

Here v_b is the beam velocity, l_b is the length of the beam and τ_r is the time to reverse the pulse (see Fig.3 (b)). Since v_b increases in the accelerator, the length gradually increases in the down stream. For example, l_b for a C^+ beam of 10 MeV with $\tau_b = 50$ ns is 0.63 m and if τ_r is assumed to be 10 ns, l_n is calculated to be 0.76 m.

The time diagram of the applied pulses is shown in Fig. 3 (b). As seen in the figure, bi-directional pulses are sequentially applied to each drift tube with adjusted delay time.

The accelerator is in principle similar to the RF linac proposed by D. H. Sloan and E. O. Lawrence [8]. However, since high power pulses are applied to each drift tube, high current acceleration of more than kA is realized.

Figure 4 shows the conceptual drawing of the proposed PIB source (ion diode). A conventional pulsed ion diode is also shown for comparison. The proposed ion diode shown in Fig. 4 (a) consists of a grounded ion source, a drift tube and a grounded cathode. In the diode, bi-directional pulse (V_1) is applied to the drift tube and by the negative voltage of V_1, ion beam is accelerated towered the drift tube. When the top of the ion beam approaches the 2nd gap, the pulse is reversed to the positive voltage and the ion beam is again accelerated in the 2nd gap.

As seen in Fig. 4 (b), in the conventional ion diode, ion source is placed on the anode where a high voltage positive pulse is applied. In contrast, in the proposed ion diode, ion source is placed on the grounded anode, which extremely enhance the accessibility to the anode. This is favorable especially for the active ion sources [9,10] where discharge power supplies or gas-puff valves are placed on the anode. In addition, ion beam is accelerated in two gaps and the beam energy is enhanced.

Here, estimating the length of the drift tube. Assuming the bi-directional pulse of V_0 = 1MV, $\tau_p = 50$ ns, $\tau_r = 10$ ns, the length of the drift tube is calculated to be 0.83 m for proton beam and 0.24 m for C^+. Hence the length of the drift tube is not too long.

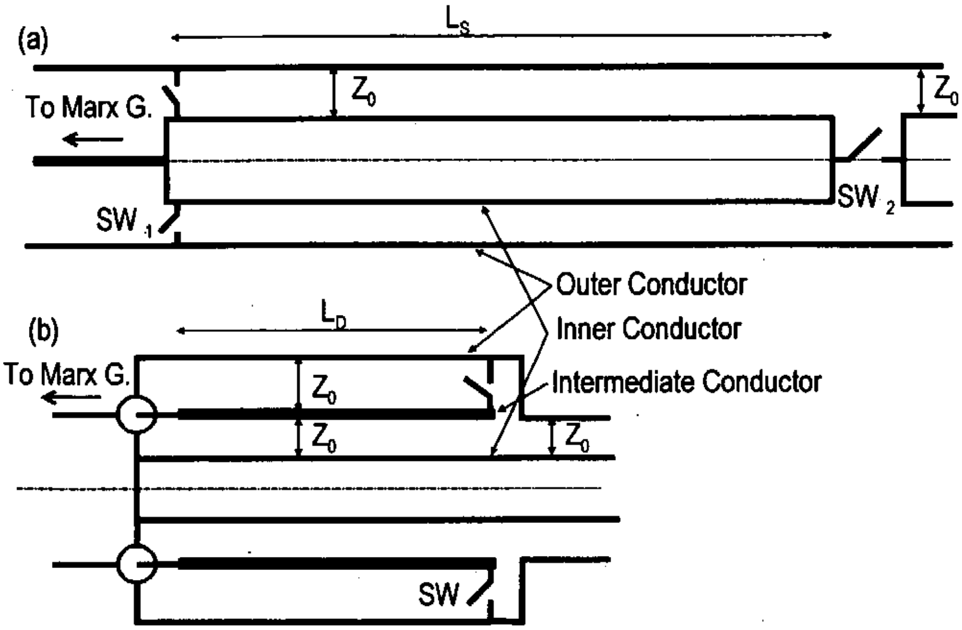

Fig. 5. The pulse forming lines proposed to generate bi-directional pulse. (a) Single coaxial type. (b) Double coaxial type.

3.1 Pulse forming lines for bi-directional pulse generation

Figure 5 shows the pulse forming lines (PFL's) proposed to generate bi-directional pulses. Two types of PFL's are proposed, i.e., single coaxial type and double coaxial type. For single coaxial type (Fig. 5 (a)) a reversing switch (SW_1) and an output switch (SW_2) are used with single coaxial transmission line of length L_S. The electrical length of the line (single way transit time, L_S/v, v is the transmission velocity of the electrical signal on the line) is designed to be same as τ_p. In the operation the center conductor of the line is charged negatively by a high voltage power source such as the Marx generator. When charging is finished, two switches are triggered simultaneously and produce a bi-directional pulse. The feature of the line is as follows; it is simple and by changing the trigger timing of two switches the ratio of the duration of negative and positive pulses can be adjusted.

Figure 5 (b) shows the double coaxial type PFL. The PFL is the application of the pulse line cavity used in the air core type liner induction accelerator [11-13]. The line consists of a double coaxial line and a switch. The switch is placed between the outer conductor and the intermediate conductor. The electrical length of the line is designed to be $\tau_p/2$, hence the length of the line is half of the single coaxial type. In the operation, intermediate conductor is charged positively by a high voltage source and after the charging the switch is triggered. The feature of the line is as follows; the length of the line is short and since single switch is used, power loss in the switch is reduced.

Figure 6 shows the experimental circuit to simulate the double coaxial type PFL. The circuit consists of two coaxial cables (which act as transmission lines between

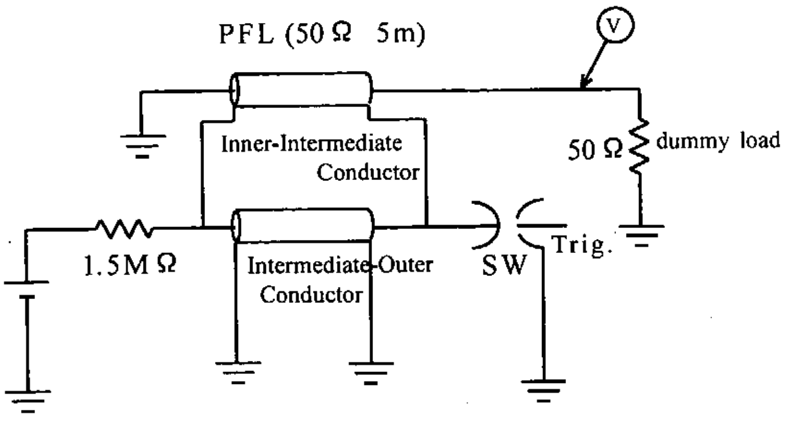

Fig. 6 Experimental circuit to simulate the double coaxial type PFL.

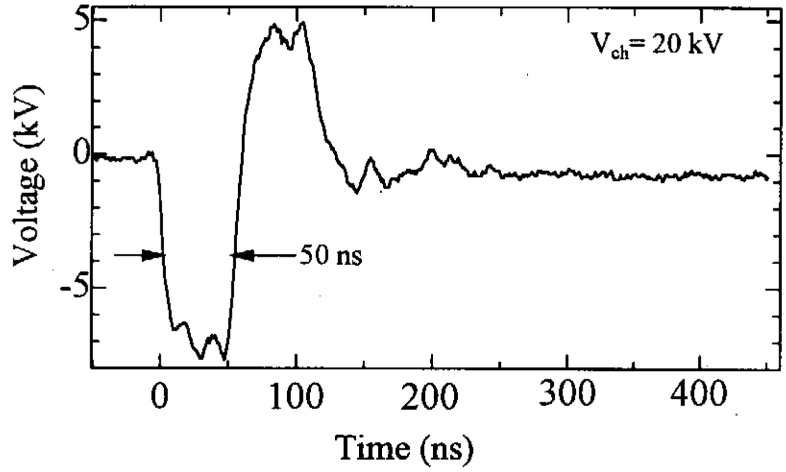

Fig. 7 shows typical waveform of the output voltage.

outer-intermediate conductor and intermediate-inner conductor of the double coaxial PFL), a discharge gap switch and a dummy load. The coaxial cables used are 5D2V type (Z = 50 Ω) and the length are 5 m each, which gives a single way transit time of 25 ns. Hence the circuit is expected to produce bi-directional pulses of τ_p = 50 ns and impedance 50 Ω. The coaxial lines are DC charged by a high voltage power supply.

Figure 7 shows typical waveform of the output voltage. As seen in the figure, bi-directional pulse is successfully obtained. In the first pulse (negative pulse) peak voltage of -7 kV is obtained with sharp rise of rise time around 15 ns. In contrast the voltage of second pulse is less than 5 kV and the waveform tend to become dull. The reduction of the voltage in the 2nd pulse seems to be due to the resistance of the discharge gap switch.

5. Conclusion

Two types of electrostatic linear accelerators (time of flight isolation type (type A) and bi-directional pulse type (type B)) are proposed as a substitute for an induction linac to accelerators a high current pulsed ion beam. Compare to the ion beam induction linacs, proposed accelerators are shown to be simple, low cost and a higher acceleration gradient is expected since magnetic cores or induction cells are not utilized. Electrical behaviors of both systems are numerically simulated and demonstrated the performances. In addition, two types of pulse forming lines are proposed to produce bi-directional pulses for the type B accelerator. The production of the bi-directional pulses was confirmed experimentally.

References

[1] D. Keefe, "Research on High Beam Current Accelerators", Particle Accelerators **11,** 187 (1981)

[2] A. Faltens, E. Hoyer, D. Keefe and L. J. Laslett, "Design /cost study of an induction linac for heavy ion for pellet-fusion", IEEE trans. on Nuclear Science, **NS-26** 3106 (1979).

[3] S. Humphries, Jr., and T. R. Lockner, "High power ion beam acceleration and transport", Applied Charged Particle Optics, Suppl. **13C**, ed. A. Septier (Academic, New York, 1980)

[4] T. Tanabe, A. Kanai, K. Takahashi, A. Tokuchi, K. Masugata, M. Ito, and K. Yatsui, "Inductive post acceleration of charge- and current-neutralized, intense pulsed ion beam", Phys. Rev. Lett., 56, 831 (1986).

[5] J. A. Nation, Particle Accelerators **10** 1, (1978).

[6] K. Masugata, "Proposal of an electrostatic multistage accelerator for high current pulsed ion beam" Nuclear Instruments and Methods in Physics Research, Section A 399(1) pp.1-4 (1997)

[7] K. Masugata, "High current pulsed ion beam accelerators using bi-directional pulses" Nuclear Instruments & Methods in Physics Research, Section A 411 pp.205-209 (1998)

[8] D. H. Sloan and E. O. Lawrence , Phys. Rev. **38** (1931) 2021.

[9] S. Houmphries, Jr., R.J.M. Anderson, J. R. Freeman, and L. Greenly, Rev. Sci. Instrum. **52,** (1981) 162.

[10] H. J. Bluhm, P. J. W.Hoppe, H. P. Laqua, and D. Rusch, Proc. IEEE **80**, (1992) 995.

[11] A. I. Pavlovskii, V. S. Bosamykin, G. D. Kuleshov, . I. Gerasimov, V. A. Tananakin and A. P. Klement'ev, Sov. Phys. Dokl., **20** (1975) 441.

[12] I. Smith, Rev. Sci. Instrum **50** (1979) 714.

[13] J. Ohmura, M. Ozawa, A. Okino, J-H. Park, K-C. Ko and E. Hotta, "Bidirectional Pulse Generator System for Linear Induction Accelerator", Proc. of 12th Int. Conf. on High-Power Particle Beams (BEAMS'98) (1998)

Investigation of Intense Electromagnetic Transient Phenomenon in Subnanosecond Regime

N. Shimomura,
Department of Electrical and Electronics Engineering, The University of Tokushima
Minami-josanjima, Tokushima

D. W. Scholfield,
Directed Energy Directorate, Air Force Research Laboratory
Albuquerque, New Mexico, USA

J. M. Gahl
Department of Electrical and Computer Engineering, The University of New Mexico
Albuquerque, New Mexico, USA

Abstract

One of the major drivers of pulsed power innovation is ultra-wide band technology. Subnanosecond risetimes with nanosecond or less pulse durations place this technology in a temporal regime that corresponds to microwave frequencies. These ultra-wide band devices have pushed pulsed power technology into a parameter space where there is little published data on breakdown. This paper describes the experimental determination of the Paschen curve for a variety of gases under the application of intense, transient, electric fields. The Paschen curves for hydrogen and helium are presented. For subnanosecond rise time pulses, there are typically very few free electrons in the discharge space generated by external radiation sources such as cosmic rays.

1. Introduction

Interest in gas breakdown phenomena for fast risetime pulses has recently increased. Subnanosecond risetimes with nanosecond or less pulse durations place this technology in a temporal regime that corresponds to microwave frequencies. The breakdown phenomena in High Power Microwave (HPM) machines and their supporting equipment, such as windows, is a critical matter for HPM development. Additionally, to obtain fast switching in pulsed power devices basic breakdown phenomena must be studied.

Paschen curves have been used to characterize breakdown phenomena in various gases in pulsed as well as DC conditions. Several theoretical studies have derived the Paschen curves for pulsed fields[1], especially in molecular nitrogen. In other studies relativistic effects have been taken into consideration[2]. Paschen curves have been obtained in experimental studies by using microwave sources[3]-[6] and pulsers[7],[8]. However, these experiments did not provide as much temporal information as the theoretical studies because of the absence of pulsers with extremely fast risetimes.

In this paper electromagnetic transient phenomena of gas in a subnanosecond time regime, as well as the Paschen curves of hydrogen and helium gas under these conditions, are presented. The work utilizes the Hindenberg series of hydrogen gas switched pulsers at the Air Force Research Laboratory located at Kirtland Air Force Base. In the presentation of the Paschen curve data, the importance of initial electron concentration within the discharge volume is discussed.

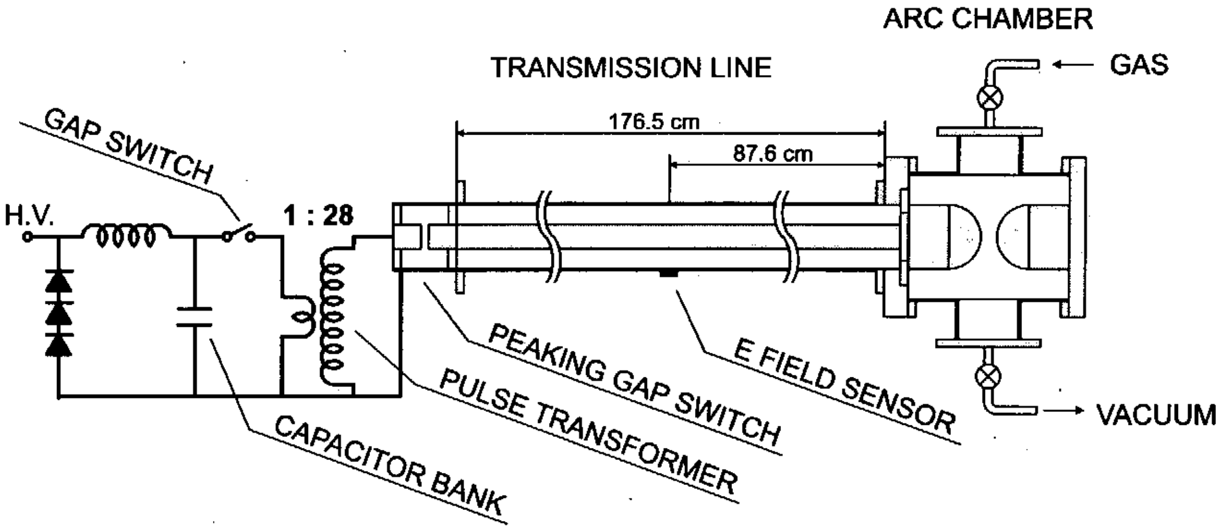

Fig. 1. Experimental schematic

2. Experimental Configuration and Diagnostics

Figure 1 shows the experimental configuration. The H2 pulser, which is one of the Hindenberg series of pulsers at the Air Force Research Laboratory, located at Kirtland Air Force Base, is utilized as the source. Pulses are generated by a pulse transformer of 1 : 28 windings ratio with an extremely short pulse forming line above a peaking gap switch. The capacitor bank of 16 nF, consisting of 8 capacitors (2 nF), is charged with a high voltage power supply. A gap switch conducts by self-breakdown and the capacitor bank drives the primary coil. The maximum charging voltage of the bank is 30kV. The pulse forming line

(PFL) is charged by the transformer. The peaking gap switch consists of two cylindrical electrodes plated with tungst-argent. When the peaking gap switch breaks, the pulse propagates through a transmission line to an arc chamber. For example with 30 kV charge, pulses having a magnitude of 400 kV and risetime of approximately 1 ns propagate down the transmission line.

The pulser and the arc chamber are connected by a 176.5 cm oil-filled coaxial transmission line, whose impedance is 40 Ω. Two hemisphere electrodes with diameters of 10.2 cm each are made from aluminum and are separation by an adjustable length of from 0 to 2.54 cm. Twice the pulse voltage developes on the gap due to the high (open) impedance before an arc discharge. Discharge phenomena occur in the gap at the center of the electrodes. The pressures of the gases, i.e., hydrogen and helium, were varied between 100 mTorr and 1000 Torr in these experiments.

Voltage waveforms are observed with a electric field sensor on the transmission line, whose sensitivity is 3.25 mV / (kV / m). The sensor was placed 87.6 cm away from the arc chamber to accommodate pulse width and transit time. Typical signals obtained with the sensor are shown in Fig. 2. Each of four waveforms are obtained by different helium pressures in the arc chamber. The voltage waves propagating from the generator are observed starting at 2 ns and ending at 8 ns, while the reflected waves at the arc chamber are observed starting at 11 ns.

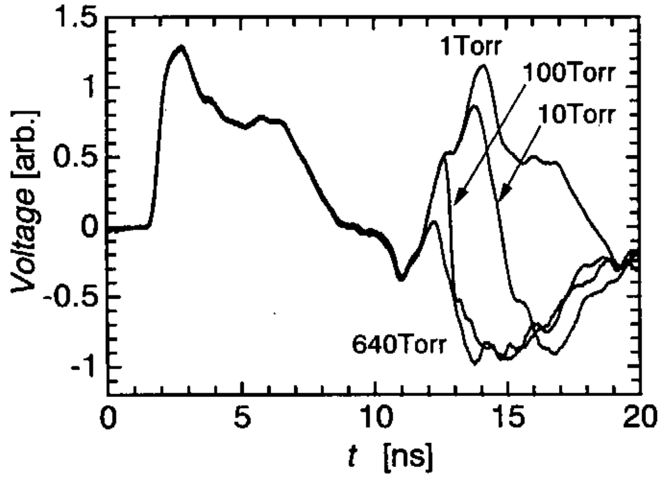

Fig. 2. Waveforms of E probe signal

In Fig. 2, various voltage waveforms have been plotted. All waveforms overlay up to 12 ns. They then separate from each other on the basis of pressure. The waveforms in Fig. 2 after 12 ns show the reflected pulses from the gap passing the E probe sensor. The presence of discharge between the electrodes generates different waveforms, therefore, the bifurcation of the traces indicate the beginning of discharge. The time to discharge is directly measured from waveforms. Because of capacitance the voltage between the electrodes is not exactly twice the incident voltage expected at a perfect open circuit.

The waveforms observed with the E field sensor are converted into voltage waveforms by taking the sensitivity of the sensor and the geometrical configuration of the transmission line into consideration. The voltage at the sensor on the transmission line is obtained by filtering using FFT (and inverse FFT), and a low pass filter. Figure 3 shows the equivalent circuit for determining, by numerical analysis, the voltage between the electrodes. The gap between the electrodes is assumed to be a capacitor. The circuit simulation was divided into about 2,000 combinations of L and C. The voltage across the gap and the ratio of voltage across the gap to the incident pulse voltage are shown in Fig. 4 for a gap length of 1.65 mm. Each voltage waveform obtained experimentally is multiplied by the ratio and the hold-off voltages are evaluated from the beginning time of the discharge.

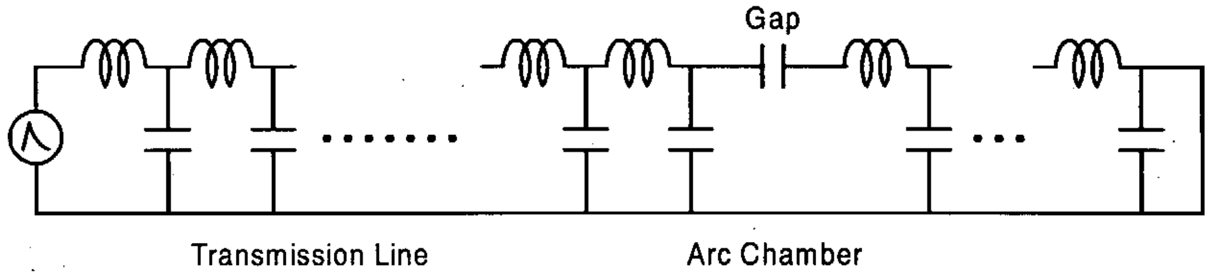

Fig. 3. Analysis Circuit

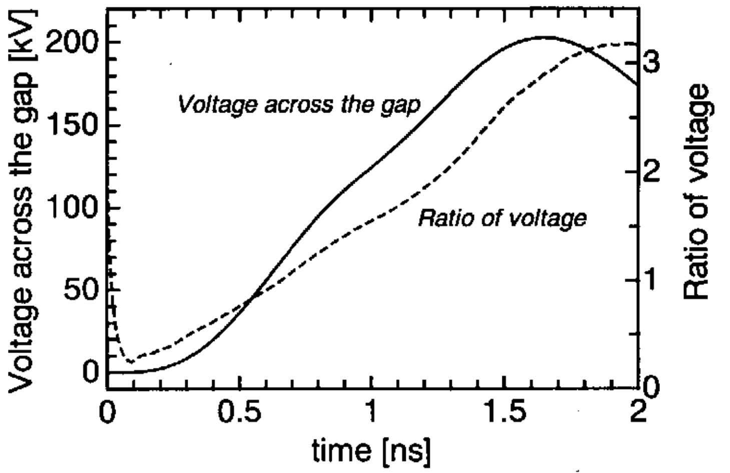

Fig. 4. Voltage across the gap and ratio of voltage across the gaps on incident voltage pulse.

3. Experimental Results and Discussion

The relationship between E_0/P and Pt for hydrogen gas is shown in Fig. 5. Here, E_0, P, t represent the hold off electric field, pressure of the hydrogen gas, and time to beginning of discharge (hold off time) respectively. The gap separation between the electrodes was 1.7 mm. The open symbols in Fig.5 indicate the data for 21kV of the charging voltage of the capacitor bank while the solid symbols indicate the data for 30kV. The various geometric figures within each grouping indicate data taken at a specific gas pressure. Note that the data obtained at specific pressures are distributed in a linear manner

The upper-right limit of the data forms a line of negative slope with the majority of the data distributed to the lower left of this line. Figure 6 shows the dependence of E_0/P on P (i.e., the data in figure 5 is re-plotted on another axis of abscissas). The upper limit of data suggests a line of slope -1, which implies that the hold-off electric fields, E_0, are approximately constant. This implies that, due to the extremely short discharge time, that most of the electrons present within the gap region are produced by electric field emission and/or the schottky effect. For DC breakdown hold-off electric fields are not constant with pressure and breakdown occurs after a formative time lag which is pressure dependent. This process, however, requires a sufficient number of electrons being present within the gap. E_0 in Fig. 5 signifies the electric field at breakdown, not the field of electric field emission, i.e. the electric field keeps increasing in the formative phase. Furthermore, the time (t) in the Paschen curve signifies the formative time lag only when there is sufficient initial electrons. In Fig. 5. if initial electrons are produced by the electric field emission as described above, applying voltage before electrons are produced does not result in breakdown.

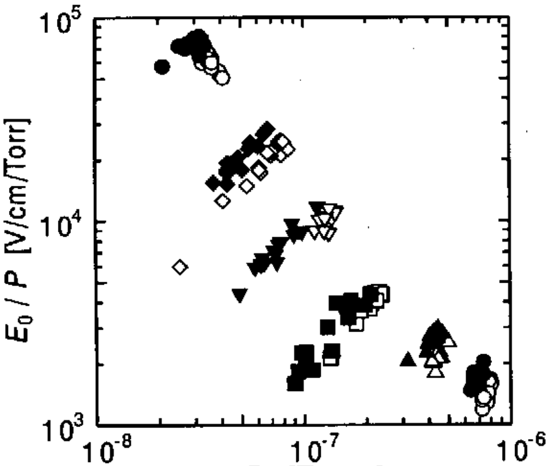

Fig. 5. The relation between E_0/P and Pt in using hydrogen. (The gap separation is 1.7 mm.)

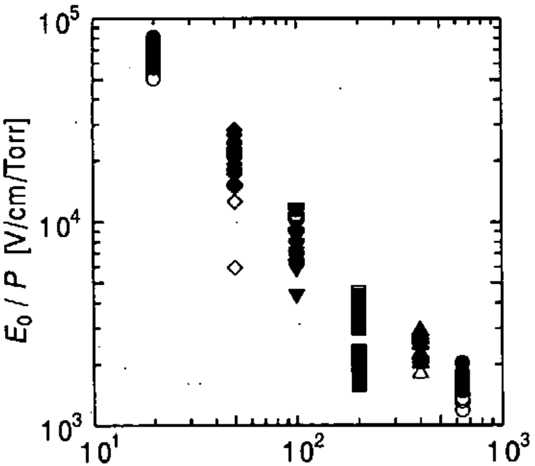

Fig. 6. The relation between E_0/P and P. (re-plotting of Fig. 5)

In general, Paschen curves present those conditions in which discharge can occur. Paschen curves show when an avalanche can be maintained, with the existence of sufficient initial electrons implicit. Although the discussion of initial electron concentration is not relevant in the case of DC breakdown, it can be the dominate phenomenon in the case of fast voltage pulses. Figure 7 shows a conceptual waveform for the electric field. E_E and t_E are the electric field that produces electrons by electric field emission and the application time, respectively. The final field indicated by the solid line is the field used to plot in Fig. 5, with the time t indicating the time to this final field.

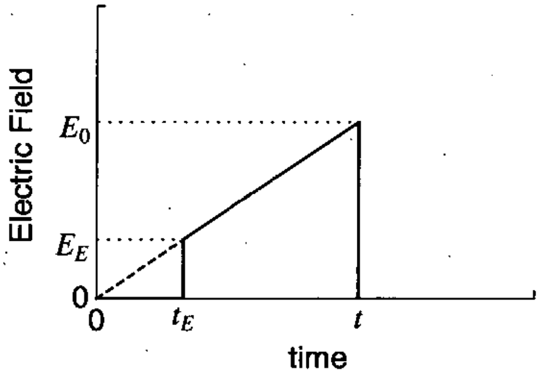

Fig. 7. Assumed waveforms of the electric field.

Over the years the concept of Paschen curve had been extended from for DC applied voltages to pulse voltages. For voltage pulses with relatively slow risetime this extension did not raise irreconcilable issues. However, as the pulse risetime shortens, certain issues arise. While sufficient initial electrons are assumed in theoretical calculations, the electrons are more often than not absent on experiments. Should the data of the electric field emission be referred to as Paschen curves? In this paper, the data which holds to the condition (or assumed conditions) of sufficient initial electrons are referred to as the Paschen curves.

Figure 8 is a plot of the data in Figure 5 with a Pashen curve superimposed. The Paschen curve is obtained by tracing the outlier data points about the lower threshold of the data. Two diamond symbols lay apart from the remaining body of the data. These two diamonds indicate that breakdown occurred at an unusually low hold off voltage and an unusually early time. Breakdowns exhibiting these characteristics were observed approximately once every 15 to 30 shots. It is unlikely that electric field emission is responsible for these results, it is more likely to be due to photo-ionization by cosmic rays. In this experiment the arc chamber does not utilize any mechanism to guarantee the existence of seed electrons. The existence of seed electrons in this experiment was dependent upon external sources. The probability of the production of cosmic ray induced electrons within a nanosecond is low, thus the dominant mechanism for these seed electrons which are present is the length of the electron lifetimes. Only the electrons which exist at the beginning of the applied pulse, such as the dashed line in Fig 7, contribute to the breakdown mechanism. The cosmic ray induced electron production method does not make a significant contribution, since the period required for breakdown is too short for field emission to occur. The period from the initial application of voltage to the appearance of electrons is generally called the statistical time lag. This period is typically long enough for the initial seed electrons to be produced by external factors.

Figure 9 plots the relationship between E_0/P and Pt for other gap separations. For all gap separations in fig. 9 the charge voltage was maintained at 30kV. Note that the hold off time for the data located in the lower left hand corner of the plot is less than approximately 100 picoseconds, leading to considerable measurement difficulty. In addition to any experimental error, there is also a physical factor at play. The data implies that the position of the initial electron within the gap affects the hold off time. The electron avalanche may progress from the initial position of the seed electrons to the anode in such a manner that a channel of electrical continuity is established, while the region between the cathode and the seed electrons initial position remains electrically isolated. Although the isolated region may finally obtain electrons from field emission enhanced by local breakdown - or by avalanched electrons - the result is that the hold off time is no longer constant.

The relationship between E_0/P and Pt for Helium is shown in Figure 10. The electrode gap separation was 1.7mm. The filled and blank symbols represent 21kV and 30 kV charge voltage respectively. An estimate of the Paschen curve based on the lower left hand outliers is plotted in Figure 10. The upper limit of the plotted data matches with that of Hydrogen. The correlation between Hydrogen and Helium supports the supposition that the production mechanism for the seed electrons is electric field emission. This appears to be independent of the species of the gas. While the plots of E_0/P versus Pt imply the influence of the formative phase as previously described, the gas species is the dominate factor in the formative phase. The delay which occurs while the electrons are produced by field emission is more dominant then the formative time lag.

In order to obtain more accurate Paschen curves, the experiment utilized a UV-source. The electrodes and their gap space were irradiated by UV light produced by a xenon lamp. A 150 W xenon bulb was located at 40 cm apart from the center of the electrodes out of the arc chamber and the light was guided to the discharge regime through lens and a quartz window. The relationships between E_0/P and Pt for Hydrogen and Helium are shown in Figure 11. The Solid and open symbols indicate the conditions with and without the UV source, respectively. The gap separation between the electrodes was 2.0 mm and the charging voltage of the capacitor bank was 30kV. Both the curves of Hydrogen and Helium have a shape which is approximately a Paschen curve, while the relative positions of them are shifted. Although the concentration of seed electrons may be lower than assumed for the theoretical calculations, it is reasonable to suppose that the concentration is sufficient for the magnitude of error in our diagnostic system. The electric field emission line of Hydrogen corresponds approximately to that of Helium. The data around Pt = 10^{-6} Torr s for Hydrogen are located about the electric field emission line. Under these conditions the formative time lag is considerable, and can not be neglected when the seed electrons are produced by the electric field emission.

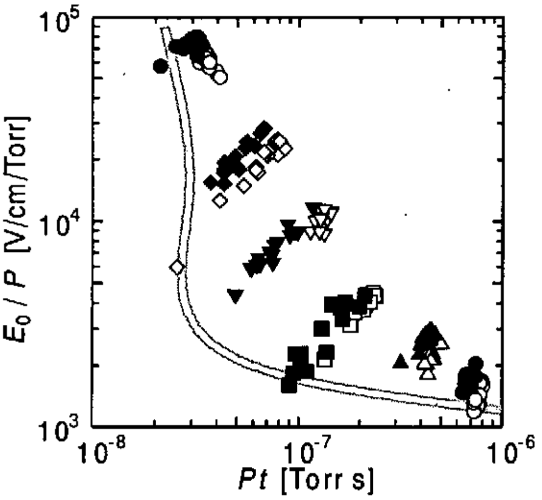

Fig. 8. Estimated Paschen curve of Hydrogen.

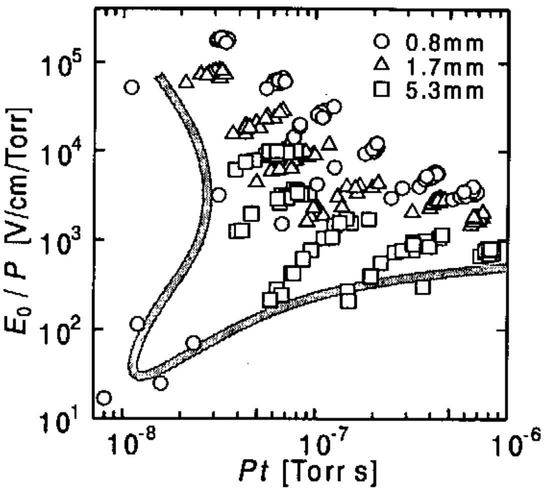

Fig. 9. Puschen curve of Hydrogen.

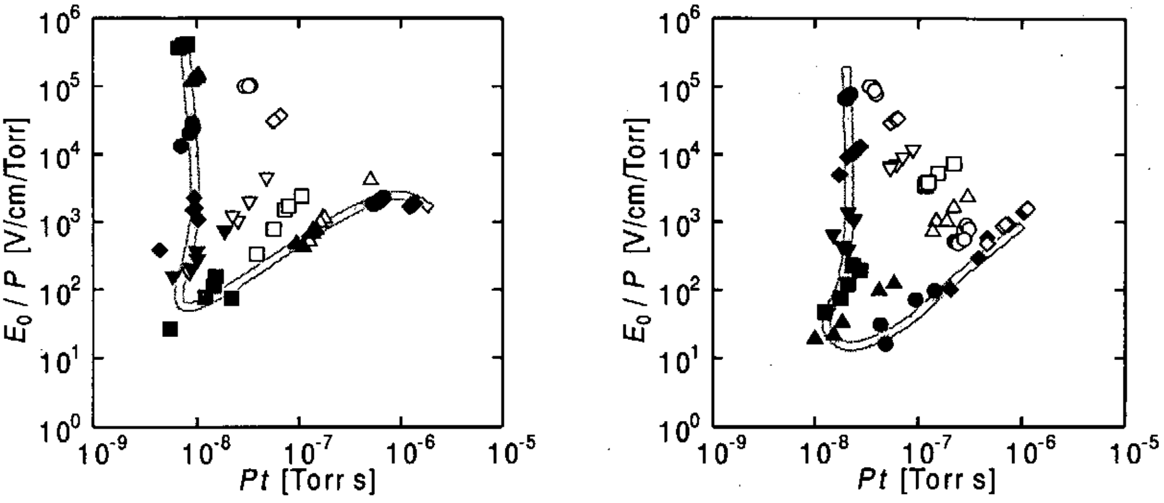

(a) Hydrogen

(b) Helium

Fig. 11 The relation between E_0/P and Pt. (The gap separation is 2.0 mm.)
(Black : with UV, White : w/o UV)

4. Conclusion

Breakdown phenomena in sub-nanosecond region were observed, with experimentally obtained Paschen curve presented. Although a sufficient value of initial electrons is assumed in theoretical Paschen curves, the probability of electrons existing during the beginning of applying electric fields is extremely low. Electric field emissions, consequently, supply virtually all initial electrons and the experimental results almost form a straight line. Nevertheless, several breakdown events induced by electrons produced by external radiation such as a cosmic ray might be observed, and tracing the outlier data points draw the Paschen curves. While the electric field emission induced breakdown is almost independent on the kind of gas (Hydrogen or Helium), the Paschen curve is affected by the gaseous species. All data are located in a region between the Paschen curve and the electric field emission curve. An intense continuous UV source was utilized for supplying seed electrons and the rational Paschen curves of Hydrogen and Helium were obtained.

Acknowledgement

This work was supported by the Air Force Research Laboratory.

Refferences

[1] Y. A. Lupan, Refined Theory for an RF Discharge in Air, Soviet Physics Technical Physics, Vol. 21, No. 11, Nov. 1976.

[2] G. Graham and R. A. Roussel-Dupr, Air Breakdown in the Relativistic Limit, Technical Documentary Report No. CONF-8905184—1, Los Alamos National Laboratory, Dec. 1989.

[3] A. D. MacDonald, Microwave Breakdown in Gases, Wiley, New York, 1966.

[4] S. J. Tetenbaun, A. D. MacDonald, and H. W. Bandel, Pulse Microwave Breakdown of Air from 1 Torr to 1000 Torr, Journal of Applied Physics, Vol. 42, p. 5871, 1971.

[5] A. W. Ali and T. Coffey, Naval Research Laboratory Memorandum No. 4320, 1980 (unpublished).

[6] C. A. Sullivan, W. W. Destler, J. Rodgers and Z. Segalov, Short-Pulse High-Power Microwave Propagation in the Atmosphere, Journal of Applied Physics, Vol. 63, No. 11, June 1988.

[7] P. Felsenthal and J. M. Pround, Nanosecond Pulse Breakdown in Gases, Physical Review, pp.1796-1804, Sept. 1965.

[8] D. W. Scholfield, J. M. Gahl, and B. W. Mullins, Investigation of the Paschen curve of nitrogen via the application of nanosecond pulsed electromagnetic radiation, Journal of Applied Physics, Vol. 76, No.3, p.1473, August 1994.

BEAM MODULATION
IN A STRONG BEAM-TURBULENT PLASMA
AND
ITS EFFECT ON BROADBAND MM RADIATION

Hiroshi Yoshida, Masaru Masuzaki, Shintarou Ooyama, Kenichi Natsume,
Ritoku Ando, and Keiichi Kamada

Department of Physics, Faculty of Science, Kanazawa University,
Kanazawa 920-1192, Japan

ABSTRACT

We ascertained, using two methods, the modulation of an intense relativistic electron beam (IREB) interacting with caviton fields in a plasma from which high-power broadband millimeter-wave radiation was emitted. One method was to measure the spectrum of radiation emitted by a part of the IREB passed across a newly devised waveguide pickup and the other was to measure synchrotron radiation emitted by the beam electrons passing through a bending magnet set outside of the interaction region. Both spectra obtained were compared with the spectra calculated using the frequency response of each method and the beam modulation spectrum obtained from the spectrum of the millimeter radiation from the plasma, respectively. The measured and calculated spectra agreed well.

I. INTRODUCTION

High-power broadband millimeter-wave radiation have been observed from IREB-plasma interaction systems [1-3]. Hereafter we call this radiation as, simply, the radiation, and its spectrum as the radiation spectrum. For the broadband radiation it is necessary for the plasma to be in a strong Langmuir turbulence state [4], in which creation, collapse, and burnout of cavitons are repeated [5]. Benford and Weatherall [6, 7, 8] proposed the collective Compton boosting model which says that the radiation is emitted by beam electrons accelerated by caviton fields and that beam density fluctuation is necessary for the high-power radiation. In this model the radiation spectrum should depend on the beam density fluctuation. Yoshida *et. al.* measured the radiation spectrum in a frequency range covering 18 to 140 GHz and found that the spectrum was nearly flat or increased slightly up to about 40 GHz, and decreased steeply above 40 GHz [9]. The observed spectrum , $P(\omega)$, could be expressed as

$$P(\omega) = I(\omega)V(\omega),$$

where $I(\omega)$ is the spectrum of the radiation from a single electron interacting with cavitons and $V(\omega)$ is the beam modulation spectrum. Assuming the beam modulation of Gaussian shape the beam modulation spectrum and the spatial beam distribution were estimated from the radiation spectrum.

To ascertain the relation between the radiation and the beam modulation further, we measured independently the spectrum of radiation emitted by beam electrons which passed across a newly devised waveguide pickup and the spectrum of synchrotron radiation emitted by beam electrons passing through a bending magnet. The equation mentioned above is also used. As $I(\omega)$, we took the frequency response of the pickup for TE_{10} mode in the former, and the spectrum of synchrotron radiation of a single electron in the latter. Each measured spectrum was compared with each calculated spectrum in which the modulation spectrum deduced from the radiation spectrum was taken into account.

II. EXPERIMENTAL SETUP

An IREB (1.4 MeV, 30 kA, and 30 ns) was injected into an unmagnetized plasma. Major components of the experimental system were a modified Pulserad 110A electron beam generator produced by Physics International, a stainless steel drift chamber, and a plasma gun system. The diode of the beam generator consisted of a carbon cathode of 36 mm diameter and a titanium foil anode of 20 mm thick. The injected beam current was around 10 kA when the anode-cathode distance was 30 mm. The drift chamber had two observation ports at 175 mm downstream from the anode. Electromagnetic-wave absorber, Eccosorb AN73, was put on the inner wall of the chamber. The chamber was evacuated to the pressure less than 5×10^{-5} torr. A pair of rail-type plasma guns was installed opposite to each other at 100 mm downstream from the anode. The plasma density, n_p, at 175 mm downstream from the anode was determined with a microwave interferometer and a triple probe as a function of the delay time after the gun firing, τ. The density became maximum at $\tau \approx 12$ μs and then decreased. In this experiment, τ was fixed at 30 μs at which the plasma density was about 3×10^{12} cm^{-3}.

For measurement of the beam modulation a waveguide pickup illustrated in Figure 1 was newly devised. The pickup consisted of a WR-42 waveguide with holes on the center of each broad side, an attachment with a hole of 1 mm in diameter and 12 mm in length to introduce the beam into the waveguide, a mini-Faraday cup, and an electromagnetic absorber to absorb the excited wave propagating to the end of the waveguide. When a modulated beam passes across the waveguide through holes, it excites electromagnetic waves which couple with waveguide modes. The frequency response of this pickup for TE_{10} mode was calculated applying Lorentz reciprocity theorem and the result is shown in Figure 2. The pickup was placed at 175 mm downstream from the anode and the centers of the holes were adjusted to lie on the chamber axis as shown in Figure 3.

Figure 4 shows the set up for the beam modulation measurement utilizing synchrotron radiation. An additional vacuum chamber was attached at the end of the drift chamber. A titanium foil of 20 μm thickness was put at 600 mm downstream from the anode to prevent intrusion of the plasma and the radiation into this additional chamber. A bending magnet (0.1 T) and a horn antenna were set at 600 mm and 680 mm downstream from the anode, respectively. Synchrotron radiation spectrum from a single electron was calculated (Figure 5) according to classical electromagnetic theory [10].

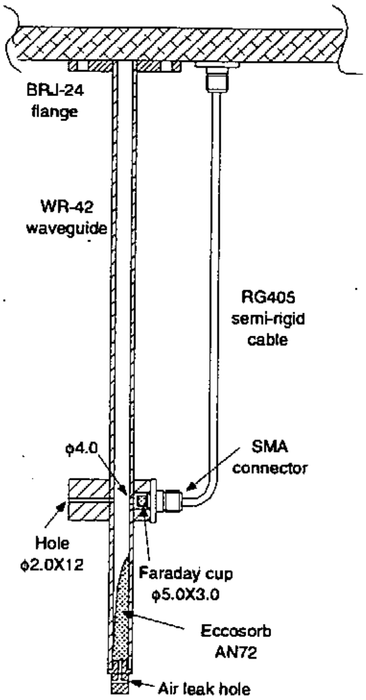

Figure 1. Waveguide pickup.

The radiation was received through horn antennas attached at the observation ports.

For determination of the spectra, a three-channel filter-bank spectrometer covering the frequency range of 18 to 60 GHz, a heterodyne spectrometer covering 60 to 90 GHz, and a three-channel filter-waveguide-combination spectrometer covering 73 to 140 GHz [9] were used. A list of the frequency ranges observed is shown in Table 1.

Table 1. Frequency ranges of the spectrometers.

Band	Freqency range [GHz]	Center frequency [GHz]
K	18-26.5	22.25
Ka	26.5 - 40	33.25
U	40 - 60	50
E-1	68 - 72.2	70.1
E-2	72.2 - 76.5	74.35
E-3	76.5 - 81	78.75
E-4	80.7 - 85.7	83.2
E-5	85.5 - 90	87.75
F-1	90 - 117 (140)	103.5
F-2	117 - 140	128.5

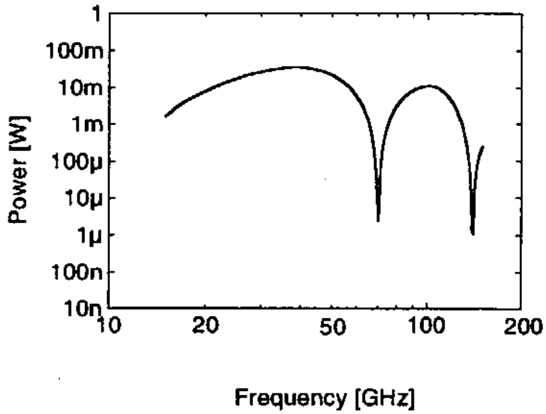

Figure 2. Frequency response of the waveguide pickup. Beam current: 100 mA, beam radius: 1 mm.

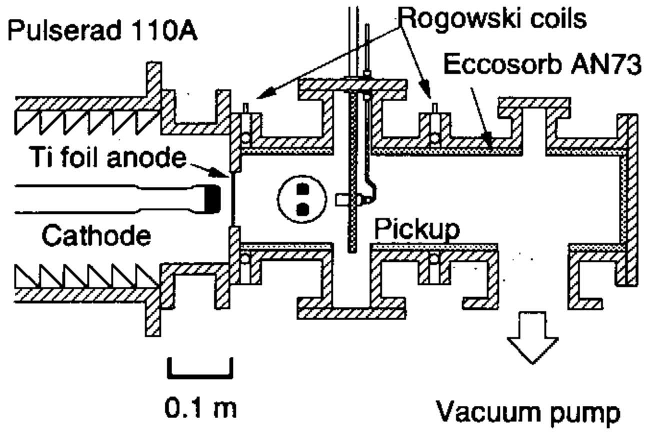

Figure 3. Experimental setup of the waveguide pickup.

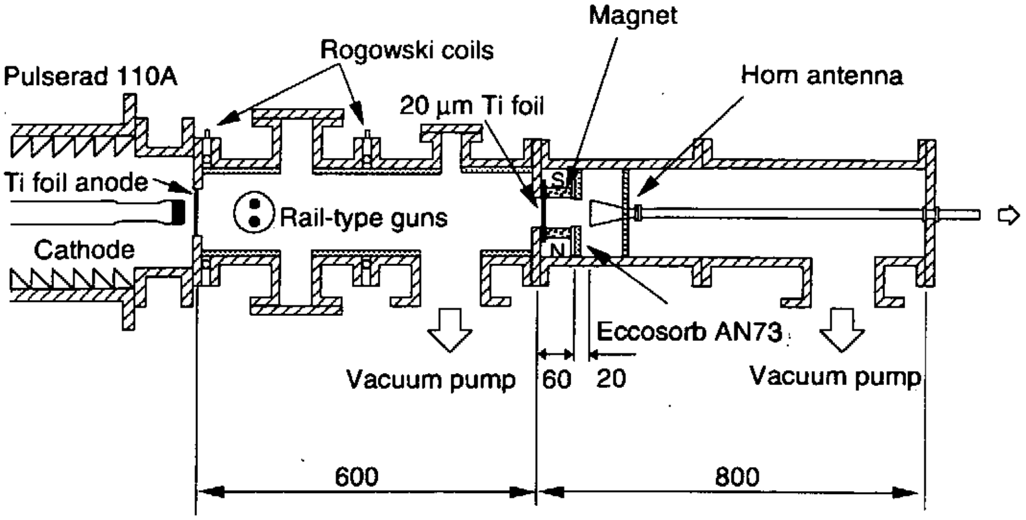

Figure 4. Experimental set up for the beam modulation measurement utilizing synchrotron radiation.

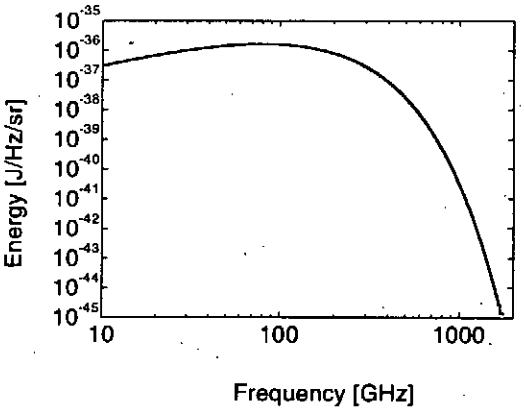

Figure 5. Synchrotron radiation spectrum.

III. RESULTS AND DISCUSSIONS

Figure 6 shows the experimental results. Dots in Figs. 6 (a) and (b) show spectra obtained in the waveguide pickup measurement and of the synchrotron radiation, respectively. The horizontal axes denote the center frequency of the passband in each channel. The vertical axis in Fig. 6 (a) indicates the power excited in the pickup by the beam. The unit, W/GHz/cm^2, on the vertical axis in Fig. 6 (b) denotes the power per unit area per unit frequency interval. Both spectra increased slightly up to 40 GHz and decreased steeply above this frequency. Figure 7 (a) shows the observed radiation spectrum. The vertical axis shows power normalized by the peak value. Figure 7 (b) shows the beam modulation spectrum, $V_{\mathrm{esti}}(\omega)$, estimated from the radiation spectrum as described in the Introduction [9].

Using the frequency response of the pickup, $I_{\mathrm{pick}}(\omega)$, and synchrotron radiation spectrum, $I_{\mathrm{syn}}(\omega)$, given in section II, we made fitting functions $P_{\mathrm{pick}}(\omega) = I_{\mathrm{pick}}(\omega) \times V_{\mathrm{esti}}(\omega)$ and $P_{\mathrm{syn}}(\omega) = I_{\mathrm{syn}}(\omega) \times V_{\mathrm{esti}}(\omega)$ and fitted them to the observed spectra. Solid lines in Figs. 6 (a) and (b) are $P_{\mathrm{pick}}(\omega)$ and $P_{\mathrm{syn}}(\omega)$, respectively.

In Figure 6 (a), we see a frequency dip in $P_{\mathrm{pick}}(\omega)$ caused by response of the waveguide pickup. This dip did not appear in the measured spectrum since passband of the spectrometers were about 5 to 20 GHz. The observed spectrum was similar to the fitted one except higher frequency side. This disagreement may be due to the poorness of the model used to calculate $I_{\mathrm{pick}}(\omega)$. In Figure 6 (b), the observed spectrum agrees well with the fitted one. These results ascertain that the IREB was modulated.

The origin of the beam modulation may be the beam-plasma instability. However, it is difficult to make clear the mechanism of the beam modulation from existing data. It remains as our future subject of study.

IV. CONCLUDING REMARKS

To ascertain whether the beam is modulated or not and to know the effect of the beam modulation on the radiation from the plasma in a strong Langmuir turbulence state caused by IREB-plasma interaction, the spectrum of radiation emitted by beam electrons which passed across a newly devised waveguide pickup and the spectrum of synchrotron radiation emitted by beam electrons passing through a bending magnet were measured in a frequency range covering 18 to 140 GHz. Each spectrum obtained by each method was compared with the corresponding calculated spectrum in which the beam modulation spectrum estimated from the radiation spectrum was taken into account. The observed spectra agreed well with the calculated ones. This result confirms the conclusion derived in [9] that the radiation from the plasma in a strong Langmuir turbulence state caused by IREB-plasma interaction is emitted by beam electrons interacting caviton fields and its spectrum depends on the beam modulation.

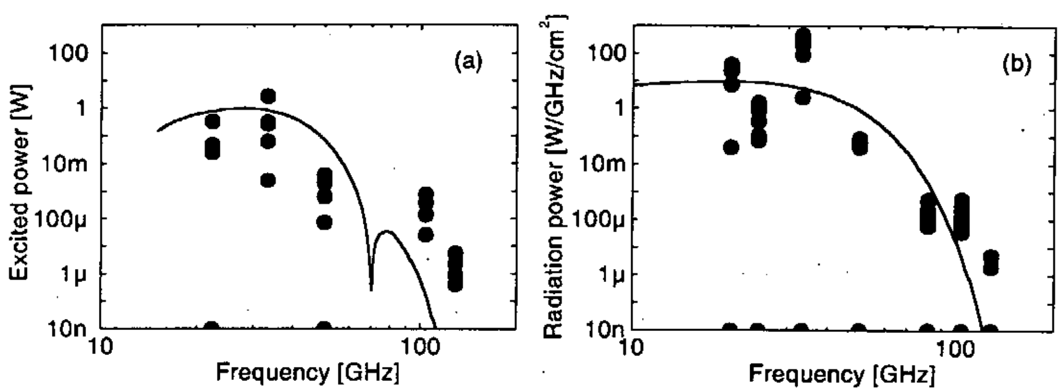

Figure 6. Beam modulation spectra. (a) waveguide pickup and (b) synchrotron radiation. Dots and solid lines show the experimental value and the fit functions, respectively.

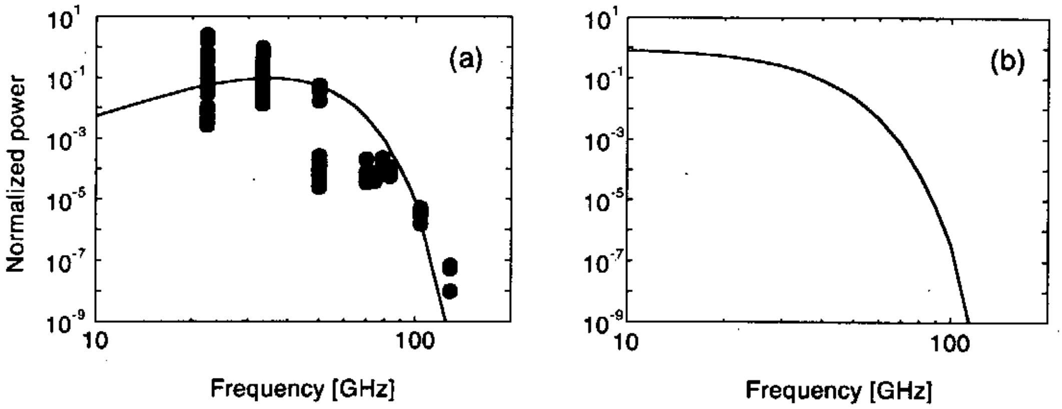

Figure 7. (a) An obtained radiation spectrum and the Gaussian fit curve taking the spectrum of the radiation from an electron accelerated by caviton field into account. (b) Beam modulation spectrum estimated from the radiation spectrum.

REFERENCES

[1] K. G. Kato, G. Benford, and D. Tzach, *Phys. Fluids*, **26**, pp. 3636-3649, 1983.

[2] M. S. DiCapua, J. F. Camacho, E. S. Fulkerson, and D. Meeker, *IEEE Trans. Plasma Sci.*, **16**, pp. 217-224, 1988.

[3] M. Masuzaki, H. Yoshida, R. Ando, K. Kamada, A. Ikeda, C. Y. Lee, and M. Kawada, in *Proc. of the 11th International Conference on High-Power Particle Beams*, Prague, Czech, 1996, **1**, pp. 339-342.

[4] M. Yoshikawa, M. Masuzaki, R. Ando, and K. Kamada, *J. Phys. Soc. Jpn.*, **65**, pp. 2081-2086, 1996.

[5] P. A. Robinson, and D. L. Newman, *Phys. Fluids B*, **2**, pp. 3120-3133, 1990.

[6] J. C. Weatherall, *Phys. Rev. Lett.*, **60**, pp. 1302-1305, 1988.

[7] G. Benford and J. C. Weatherall, *Phys. Fluids B*, **4**, pp. 4111-4120, 1992.

[8] J. C. Weatherall and G. Benford, *Astrophys. J.*, **378**, pp. 543-549, 1991.

[9] H. Yoshida, M. Masuzaki, S. Ooyama, R. Ando, and K. Kamada, "Measurements of broadband millimeter-wave radiation from an IREB-plasma interaction system," to be published in *IEEE Trans. Plasma Science*.

[10] J. D. Jackson, *Classical electrodynamics*, 2nd ed., John Wiley and Sons, 1975.

FOUR-STAGE AUTOACCELERATION OF AN INTENSE RELATIVISTIC ELECTRON BEAM

Daisuke Hasegawa, Kazuhiro Shimizu, Ritoku Ando, Keiichi Kamada and Masaru Masuzaki

Department of Physics, Faculty of Science, Kanazawa University, Kanazawa 920-1192, Japan

ABSTRACT

Experiments on four-stage autoacceleration were carried out to generate a sub-nanosecond intense relativistic electron beam. A series of four coaxial cavities with decreasing lengths were utilized as a four-stage cavity structure. An annular electron beam of 550 keV, 5 kA and 12 ns was injected into the structure. An autoaccelerated beam was obtained at the downstream side of the structure. The kinetic energy of the most accelerated portion of the beam was 1 MeV with duration of 0.8 ns. The decrease of the pulse duration showed good agreement with a model of the multi-stage autoacceleration.

I. INTRODUCTION

Generation of a short duration intense relativistic electron beam (IREB) is an interesting subject of study for, for example, application to high-power, short pulse millimeter-wave generation [1]. However, it is difficult for conventional pulse-forming-line systems to generate an IREB of short duration less than order of 1 ns. We proposed to compress pulse duration of an IREB after emission from a diode utilizing multi-stage autoacceleration process [2] which used a series of cavities with decreasing length. One-stage autoacceleration experiments with various energies of IREB were reported extensively [3-6]. The autoacceleration process depends on the properties of IREB, i.e. the strong self-electric field and the high β of the electrons. In the autoacceleration process, the kinetic energy of beam electrons is transferred from the first half of the beam duration to the second half through a simple coaxial cavity. Therefore, if the autoacceleration process is able to be applied repeatedly to the accelerated portion of the beam, the IREB with higher energy and shorter duration is available. An experiment of the two-stage autoacceleration [2] was carried out to demonstrate the multi-stage autoacceleration with decreasing length cavities.

Autoacceleration process [3-6] utilizes the mutual interaction between an IREB and a passive structure, and is reviewed briefly here [Fig. 1 (a) - 1 (e)] after Ref. 6. An IREB of particle energy eV_0 [Fig. 1 (b)], current $I_0(t)$ [Fig. 1 (c)], and beam duration t_0, propagates through a conductive drift tube immersed in a uniform axial magnetic field. A conductive coaxial cavity of impedance Z_c is connected to the drift tube via gap. The length of the cavity l is $t_0c/4$, where c is the velocity of light. As the IREB passes the gap, a current $I_1(z, t)$ is induced in the cavity and a voltage $V_1(t)$ appears across the gap. Transmission line theory is used to calculate $I_1(z, t)$ and $V_1(t)$. The current at the end of the cavity [Fig. 1 (d)] is expressed as

$$I_1(l, t - t_0/4) = 2I_1(0, t) - 2I_1(0, t - t_0/2) + \cdots \tag{1}$$

and the voltage across the gap $V_1(t)$ [Fig. 1 (e)] is

$$V_1(t) = Z_c\,[\,I_1(0, t) - 2I_1(0, t - t_0/2) + \cdots\,]. \tag{2}$$

As a result, beam electrons lose kinetic energy $eV_1(t)$ during the first half portion of the beam duration ($0 < t < t_0/2$) and gain the same amount of energy during the second half ($t_0/2 < t < t_0$) [Fig. 1 (f)]. The duration of the accelerated portion of the beam is equivalent to the round trip time of light in the cavity.

The principle of the multi-stage autoacceleration is to use the autoacceleration process repeatedly. A series of different length cavities utilized in multi-stage autoacceleration experiment is shown in Fig. 2. The length of the nth cavity is adjusted to the half of the (n-1)th cavity length, therefore, the duration of the most accelerated portion of the IREB after passing through the nth cavity is compressed to $1/2^n$ of its initial duration. Only the last one 2^nth portion of the initial

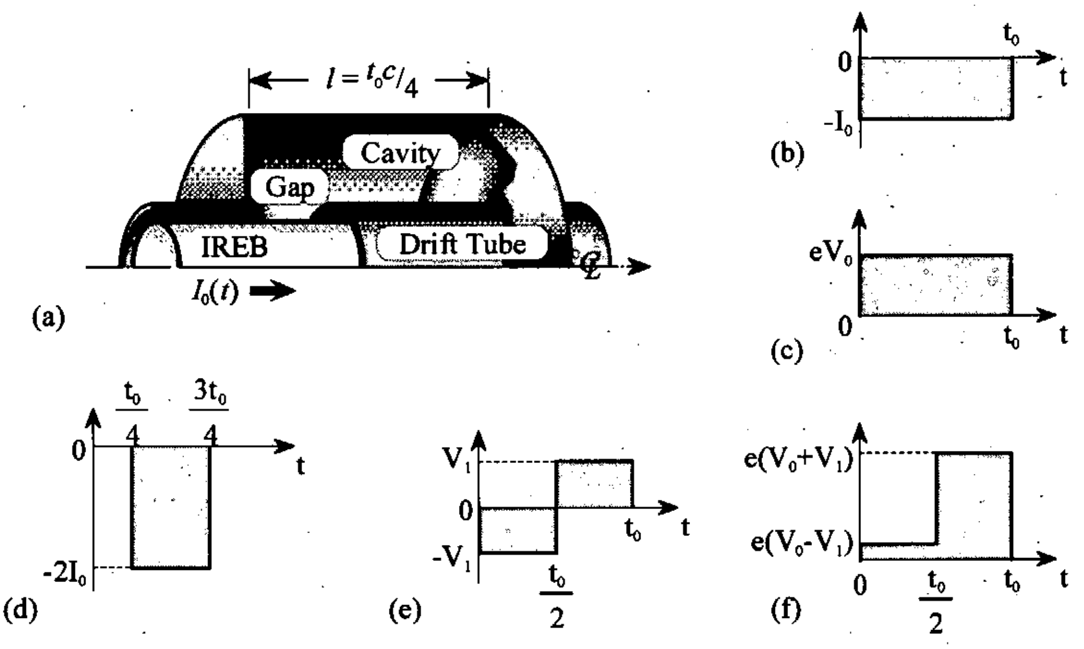

Fig. 1. (a) Simple model of the autoacceleration. (b) - (f) Ideal beam parameters for an autoacceleration experiment: (b) incident kinetic energy of beam electrons, (c) incident IREB current, (d) current at the end of the cavity, (e) voltage at the gap, and (f) kinetic energy of beam electrons after autoacceleration process.

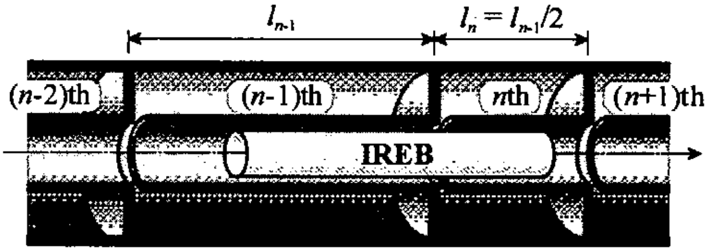

Fig. 2. Schematic of multi-stage autoacceleration.

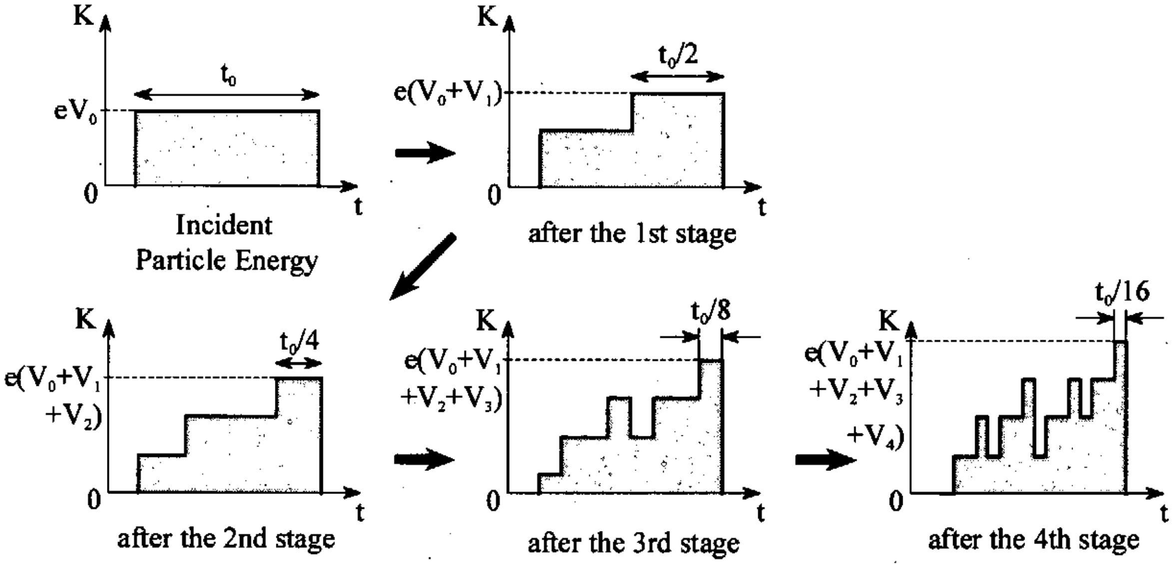

Fig. 3. Transition of kinetic energy of beam electrons in the four-stage autoacceleration.

beam duration is accelerated *n* times by the cavities. According to Eq. (2), the kinetic energy of the most accelerated beam electrons increases arithmetically when the same impedance cavities are used. Transfer process of the kinetic energy of beam electrons in the four-stage autoacceleration is shown in Fig.. 3. In the first-stage, the first and the second half portion of the beam duration is decelerated and accelerated, respectively. In the second-stage, the first and the third quarter portion of the beam are decelerated, while the second and the last quarter portion are accelerated. Therefore, the last quarter portion accelerated at both stages becomes the most accelerated portion after passing through the second cavity. In the fourth-stage, the process of deceleration and acceleration occurs alternately eight times. The most accelerated portion of the beam which is accelerated at all stages appears in the last one-sixteenth of the beam duration after passing through the fourth-stage cavity.

In this paper, we describe four-stage autoacceleration experiments. The applicability of Eq. (1) and (2) to the multi-stage autoacceleration process and the attainability of a sub-nanosecond IREB by the multi-stage autoacceleration are reported.

II. EXPERIMENTAL SETUP

A. Configuration

A Model 105A Pulserad of Physics International was used to generate an annular IREB. The Model 105A Pulserad utilizes a 5-stage, 1.25 kJ Marx bank for its primary energy store, and a 10 ns conventional Blumlein pulse forming line connected to the Marx bank.

A schematic of the four-stage autoacceleration apparatus is shown in Fig. 4 (a). An annular electron beam with diameter of 15 mm and thickness of 1 mm was injected from a foilless diode into a conducting drift tube with length of 2 m and inner diameter of 30 mm. Axial magnetic field of 1 T was applied by three solenoid coils of total length of 2.4 m. Each coil had compensating magnetic field coils at the both ends to hold the magnetic field strength constant at the joint of coil. The anode-cathode gap in the diode was 7 mm.

Typical waveforms of the diode voltage and the beam current are shown in Fig.'s 4 (b) and (c). The first cavity length l_{1st} was determined to be 90 cm and the gap length was 2 cm from a preliminary experiment. As the FWHM of the pulse duration of the measured beam current was 12 ns, which corresponds to the beam length of 3.6 m, as shown in Fig. 4 (c), the length of the first cavity was just a quarter of the beam length as expected by the model mentioned above. The first cavity with impedance Z_c = 76 ohm was connected to the drift tube via 2 cm gap at 20 cm

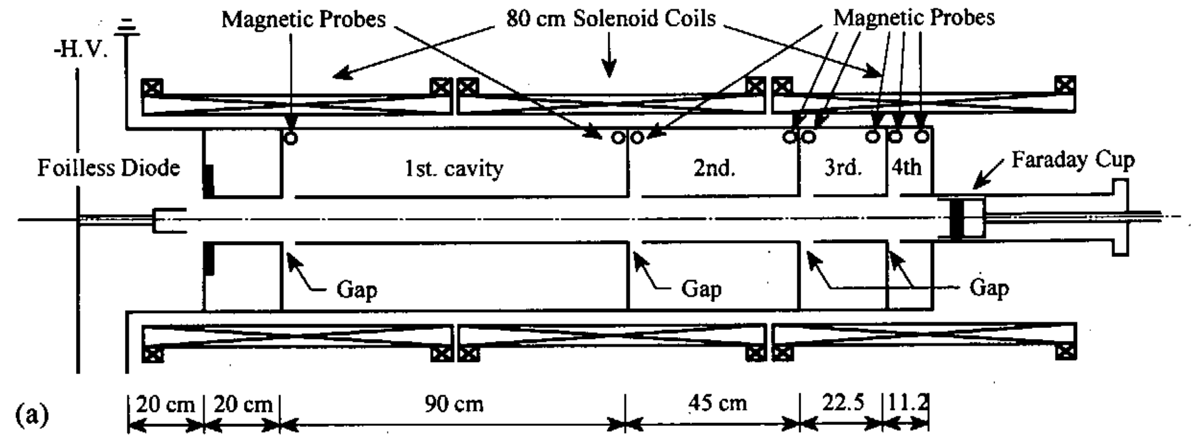

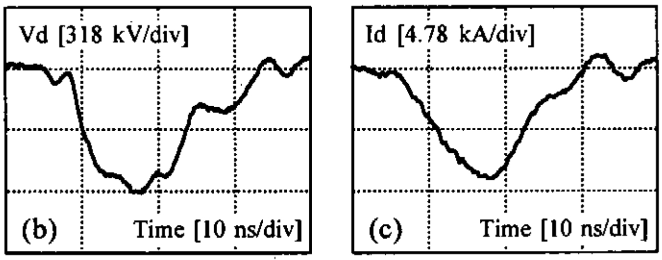

Fig. 4. (a) Experimental setup of the four-stage autoacceleration. Typical waveforms of diode voltage (b) and beam current (c).

downstream from the anode (z = 20 cm). The lengths of the second, third and fourth cavity with the same impedance Z_c = 76 ohm were 45 cm, 22.5 cm and 11.25 cm, respectively.

B. Diagnostics

A Faraday cup was used to measure the beam current at various locations along the axis in the drift tube and to estimate the kinetic energy of the beam electrons. The Faraday cup consisted of a carbon disk collector and a 0.012 ohm shunt resistor composed of chip resistors. Aluminum foils of different thicknesses were placed in front of the Faraday cup to measure the kinetic energy of the beam electrons by the range-energy relations.

Magnetic probes shown in Fig. 4 (a) were used to measure the beam current at each gap [$I_1(0, t)$] and the current at the end of each cavity [cavity current $I_1(l, t - t_0/2)$] in order to confirm Eq. (1) experimentally at each stage. The applicability of Eq. (2) to the multi-stage autoacceleration was investigated with the help of measured $I_1(0, t)$ and beam energy. The signals were monitored on Tektronix TDS 684A digitizing oscilloscope (1 GHz, 5 GS/s).

III. EXPERIMENTAL RESULTS

Typical waveforms of the beam current through different thicknesses of aluminum foils obtained by the Faraday cup are shown in Fig. 5. Beam current waveforms in the control experiment [Fig. 5 (a)] were measured by the Faraday cup at z = 50 cm, in which no cavities were mounted and the beam propagated through the straight drift tube. In the four-stage experiment [Fig. 5 (b)], the Faraday cup was located at z = 193 cm. Although the beam current disappeared in the control experiment with 0.9 mm aluminum foil, in the four-stage experiment electrons passed through a thicker aluminum foil. This indicates that the electrons were accelerated to higher energies in the four-stage experiment. These higher energy electrons were observed until the thickness of aluminum foil was increased to 1.5 mm. The duration of the most accelerated portion of the beam after passing through the four-stage cavity was about 0.8 ns which was equal to one-sixteenth ($1/2^4$) of the incident beam and it appeared in the last portion of the beam duration.

By placing aluminum foils of different thicknesses in front of the Faraday cup and measuring the penetrated current, the kinetic energy of the beam electrons was estimated. The ratio of the penetrated current through aluminum foils to the current detected without foil are plotted in Fig. 6. Using Fig. 6 and the range-energy relation for relativistic electrons [7], the electron kinetic energy in the most accelerated portion of the beam was estimated to be 1 MeV in the four-stage experiment. The electron kinetic energy in the control was estimated to be 550 KeV. Therefore, the energy gain of the most accelerated portion was estimated to be 450 keV.

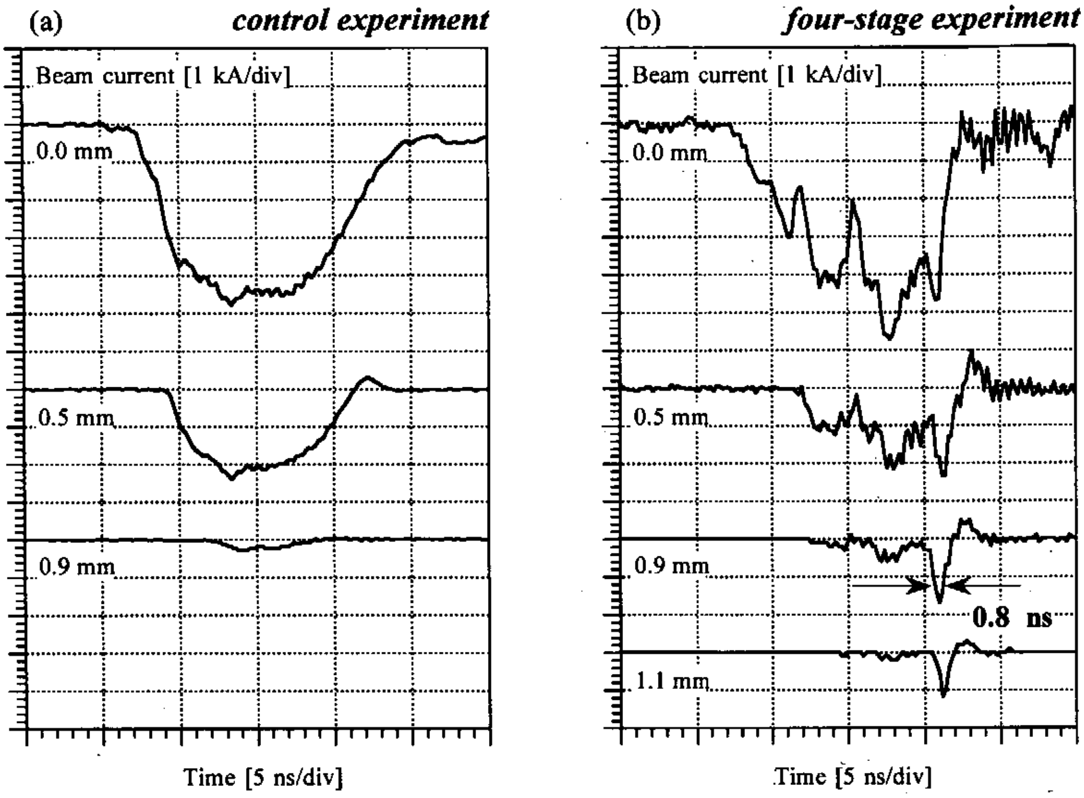

Fig. 5. Typical waveforms of Faraday cup signals with aluminum foil of different thickness, (a) current waveforms of the incident beam, and (b) current waveforms of the four-stage autoacceleration experiment.

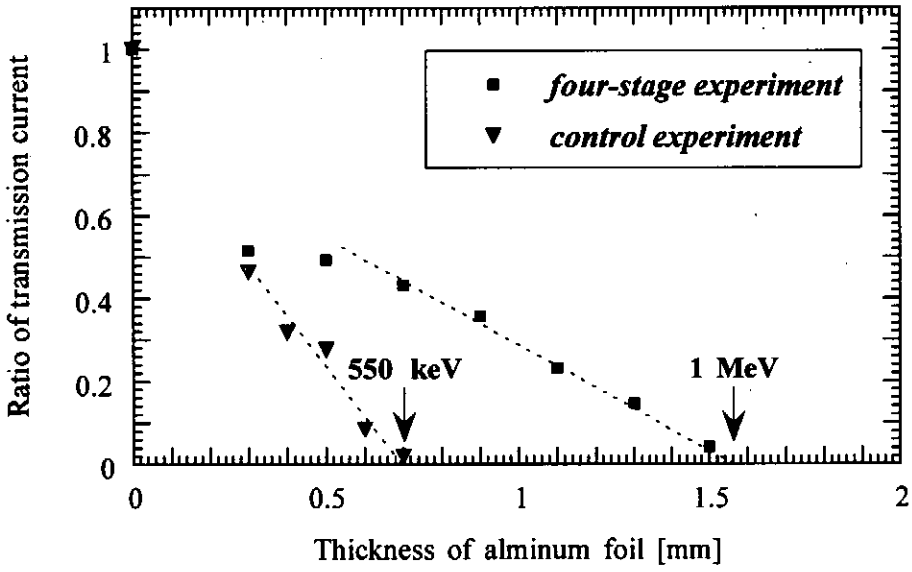

Fig. 6. Ratio of the penetrated current through different thicknesses of aluminum foil.

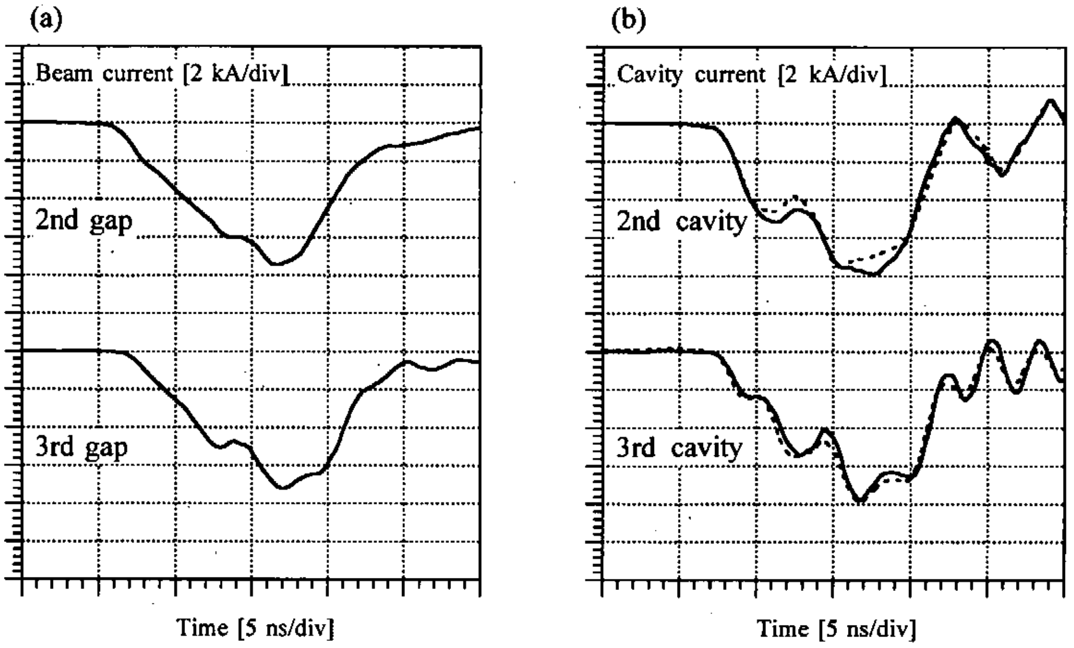

Fig. 7. (a) Beam current waveforms at second and third gap measured by magnetic probes, and (b) comparison between calculated cavity currents (solid lines) and measured cavity currents (dotted lines).

IV. DISCUSSIONS

Beam currents at each gap measured by magnetic probes are shown in Fig. 7 (a). In order to investigate the applicability of Eq. (1) and (2) to the multi-stage autoacceleration process, cavity currents calculated from measured beam currents at each gap are compared with measured cavity currents as shown in Fig. 7 (b). Since calculated and measured cavity currents at each stage agree well, equation (1) is judged to be applicable to the multi-stage autoacceleration. The voltage waveforms at each gap and the sum of the voltage waveforms are calculated from Eq. (2) using measured beam current at each gap as shown in Fig. 8. The sum of voltages which accelerated the last one-sixteenth portion of the initial beam duration is calculated to be 900 kV. So there is the difference between the calculated and the measured energy gain of the most accelerated portion, the latter being 450 keV. This difference between the calculated and the measured values may be caused by the shape of the waveform.

The 0.8 ns duration of the most accelerated portion of the beam is in good agreement with the round trip time (0.75 ns) of light in the fourth cavity. The decrease of the pulse duration of the most accelerated portion was realized by the multi-stage autoacceleration. However, the beam current waveform with aluminum foil shown in Fig. 5 (b) shows that decelerated electrons in 0-11 ns make the waveform shape far from the square. This unnecessary portion of the beam

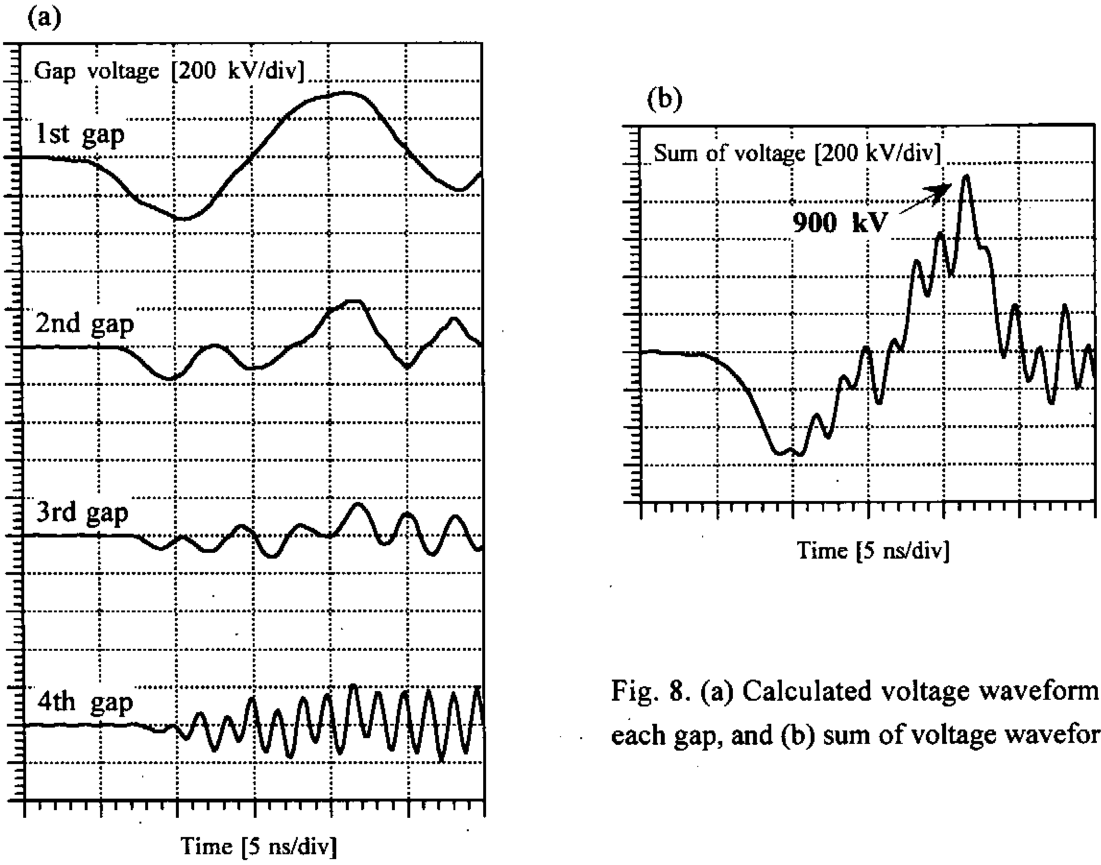

Fig. 8. (a) Calculated voltage waveforms at each gap, and (b) sum of voltage waveforms.

might make the energy transfer less than the expected. Moreover, when the 0.8 ns IREB obtained by the four-stage autoacceleration is used in some applications, these unnecessary decelerated electrons in 0-11 ns in the beam duration should be removed from the beam pulse.

An additional experiment using one-stage apparatus as shown in Fig. 9 was carried out to investigate the effect of the waveform shape to the autoacceleration process. To remove decelerated electrons, a titanium foil of 0.12 mm thickness was placed at the entrance of the drift tube as shown in Fig. 9. Typical waveforms of the beam current with and without the titanium foil are shown in Fig. 10 (a). The waveform shape of the beam current without foil was far from the square shape. The waveform shape with foil seemed to be a little bit better than that without foil. This is because most of decelerated electrons in the first half of the duration were removed from the beam by passing through 0.12 mm titanium foil. The acceleration voltages that should appear across the gap at the second stage are calculated from these beam current waveforms with the help of Eq. (2) as shown in Fig. 10 (b). Comparing the calculated waveforms, we notice that the decelerated electrons make the voltage shape at the second stage gap complicated. In the calculated acceleration voltage waveform without foil, the duration for the main acceleration part indicated by an arrow in Fig. 10 (b) is shorter than 3 ns which was the designed value for the

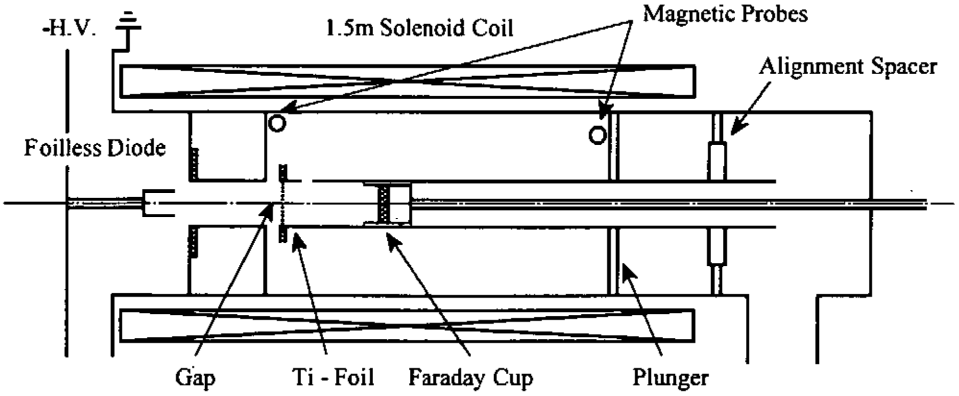

Fig. 9. Experimental setup of the one-stage autoacceleration.

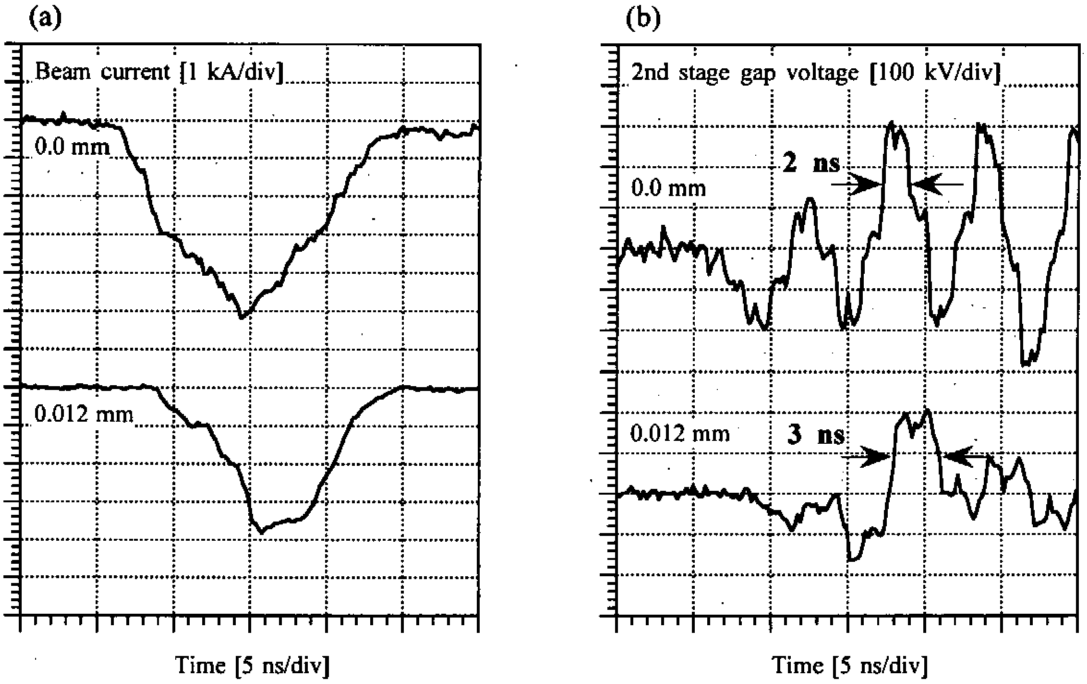

Fig. 10. (a) Typical waveforms of the beam current after one-stage autoacceleration, and (b) acceleration voltage which should appear across the gap at the second stage.

second stage. The calculated acceleration voltage waveform with foil shows that the shape of the main acceleration voltage is kept a square shape with designed duration. These results show that the decelerated electrons excite unnecessary voltage in the cavity for multi-stage autoacceleration.

V. CONCLUSIONS

The applicability of the autoacceleration process to the four-stage autoacceleration was demonstrated experimentally. The duration of the most accelerated portion of the IREB was $1/2^4$ of the initial duration after the four stage autoacceleration. Although the energy increase of the most accelerated portion was expected to increase arithmetically, the experimental results showed energy increase less than the expected. Decelerated electrons were suspected to be reason for the difference of energy increase between the model and the experiment. Therefore, the experimental apparatus should be improved to remove unnecessary decelerated electrons from the beam pulse.

The authors gratefully acknowledge Mr. Yoshida for his helpful discussions and Mr. H. Tsukuda and Mr. M. Kamada for their technical assistance.

REFERENCES

[1] N. S. Ginzburg et al., Phys. Rev. Lett. 78, 2365 (1997).

[2] K. Kamada, D. Hasegawa, H. Igarashi, T. Kusunoki, C. Y. Lee, H. Koguchi, R, Ando and M. Masuzaki, Proc. of the 11th Intern. Conf. on High-Power Particle Beams, vol. 1, p. 351 (1996).

[3] M. Friedman, Phys. Rev. Lett. 31, 1107 (1973).

[4] L. N. Kazanski, A. Klestov and A. N. Lebedev, At. Energ. 30, 27 (1971).

[5] I. A. Grishaev, A. N. Debik, V. V. Zakutin, I. I. Magda, Yu. V. Tkach and A. M. Shenderovich, sov. Phys. Tech. Phys. 19, 1087 (1975).

[6] M. Friedman, Appl. Phys. Lett. 41, 419 (1982).

[7] H. H. Seliger, Phys. Rev. 100, 1029 (1955).

Study of a Large Diameter Backward Wave Oscillator without Guiding Magnetic Field

Kazuo Ogura, Atsushi Ono, Osamu Watanabe

Niigata University, Niigata, 950-2181, Japan

1.Introduction

Extensive efforts have been devoted to developing high power Cherenkov devices, including the backward wave oscillator (BWO).[1, 2] BWO can be driven by an axially injected electron beam without initial perpendicular velocity and are particularly suited to operation with an intense electron beam. However, in order to confine an intense electron beam, a strong axial magnetic field has been used. Due to field coils, devices have become heavy and complicate. A high power BWO without guiding magnetic field (plasma-assisted slow wave oscillator) have been demonstrated as a compact, efficient and lightweight high-power microwave device.[3] Oscillation frequencies are in the range up to X-band. TE as well as TM mode radiations were observed. In the plasma-assisted slow wave oscillator, the electron beam propagation was achieved by utilizing the background plasma.

Plasma effects in vacuum microwave devices have been studied experimentally and theoretically. One common effect is neutralization of beam charge by the background plasma, allowing beam propagation in the slow wave device well above the space charge limited current. The plasma can also enhance the microwave output power of TM mode.[4-6] Although this plasma effect has been studied extensively, most analyses have considered only the one-dimensional (longitudinal) perturbed motion of the beam electron. Moreover, plasma effect on TE mode radiation from BWO's with and without magnetic field have not been clear.

In this report, the beam interaction with axisymmetric TM mode at zero-magnetic filed is examined. In the zero-magnetic filed case, the conventional Cherenkov and cyclotron interactions are degenerate and perturbed beam motions perpendicular as well as parallel to a finite magnetic field should be taken into account. The degenerate interaction in a periodically corrugated waveguide is presented. And then, we demonstrate a large diameter BWO without guiding magnetic field experimentally.

2.Beam interaction with axisymmetric TM mode at zero-magnetic field

For a magnetized electron beam, there exist three distinct beam modes, those are the slow ($\omega = k_z v_0 - \Omega/\gamma$) and fast ($\omega = k_z v_0 + \Omega/\gamma$) cyclotron modes and the Cherenkov mode ($\omega = k_z v_0$). Here, ω is the angular frequency of the perturbing electromagnetic field, $\Omega = eB_0/m_0$, m_0 and $-e$ are the non-relativistic cyclotron angular frequency, the rest mass and the charge of an electron, respectively, and γ is the relativistic factor. At zero-magnetic field, the cyclotron modes and the space charge modes become degenerate. In this case, the vertical beam motion is not restricted by the magnetic field. The change in the volume density ρ_1 caused by the longitudinal current is cancelled by the change caused by the vertical current. Therefore, there is no coupling due to ρ_1 between the beam and the axisymmetric TM mode and the surface charge σ_1 at the beam-vacuum boundary plays essential role in the degenerate interaction.[7]

The result of numerical analysis of degenerate interaction in a typical X-band slow wave structure (SWS) is shown in Fig.1, in which temporal growth rates are plotted by solid line (degenerate interaction) and dashed line (conventional Cherenkov interaction). The growth rate of the degenerate interaction becomes maximum around the beam energy 200-300 keV with beam current 100 A, Fig.1(a), and increases with increasing the beam current with beam energy 300 keV, Fig.1(b). It should be pointed out that the degenerate interaction is superior to the conventional Cherenkov interaction in the high current and the weakly relativistic energy regions.

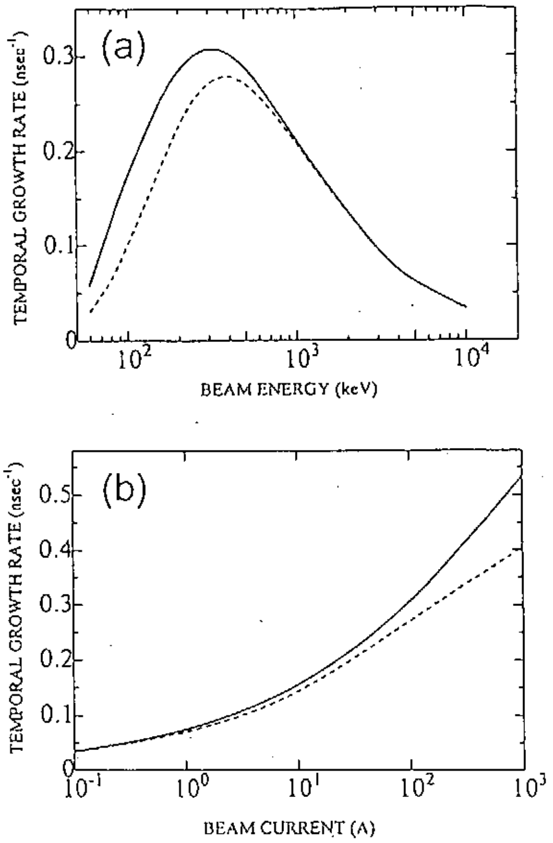

Fig.1 Comparison between degenerate and conventional Cherenkov interaction.

3.Experiment

Our BWO is schematically shown in Fig.2. The electron beam diode, the SWS and the beam collector are installed in a stainless steel vacuum vessel. The parameters of the SWS are as follows; average radius R_0=30 mm, corrugation amplitude h=1.7 mm and pitch length z_0=3.4 mm. These parameters are chosen so as to increase the oscillation frequency of fundamental TM_{01} mode up to 20 GHz. The total length $L=70z_0$=238 mm. This SWS is oversized with the mean diameter four times larger than the free space wavelength of the microwave output for TM_{01} mode.

Output voltage up to about 80 kV from a pulse-forming line is applied to a cold cathode. The axisymmetric emitting edge of the cathode is wrapped with velvet. An anode is copper mesh. The diode voltage is measured by a resistive voltage divider. For measurements of diode current, a Rogowski coil is placed between the cathode and the anode. Receiving antenna is a rectangular horn antenna. The coupling coefficient between output window and receiving antenna is determined by a vector

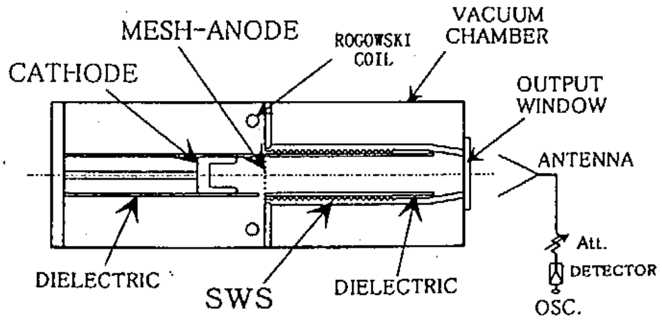

Fig.2 Schematic diagram of the large diameter BWO.

network analyzer for a circular TM_{01} mode. The absolute value of the output power of TM_{01} is estimated by using this coupling coefficient. Received signals are split into two branches by a multi-hole directional coupler. One consists of a short waveguide and forms a prompt signal. The other is a delay line waveguide typically 6 m long and forms a delayed signal. The signal frequency is able to estimate from the delayed time.

In this report, SWS is filled by helium gas. The electron beam propagation is monitored by a beam collector at various axial positions as shown in Fig.3. The beam collector is made of a stainless plate. Without helium gas (solid circle), beam current decreases with increasing axial distance from the anode. At the filling pressure p_{He}~80 mtorr (double circle), beam can propagate up to about 120 mm from the anode.

The output power from the large diameter BWO strongly depends on p_{He} as is shown in Fig. 3. The diode voltage and current at the peak of microwave signal are about 36 kV and 2000 A, respectively. At relatively low p_{He}, less than about 80 mtorr, no meaningful microwave power is observed. The microwave power increases sharply with p_{He}~120-130 mtorr. Maximum detected power is in the 1 W range. When the SWS is replaced by a straight cylindrical waveguide, the detected power remains in the noise level even in the pressure range p_{He}~120-130 mtorr. In Fig.3, the delay time of a delaied signal is about 40 nsec and the frequency is estimated to be about 20 GHz.

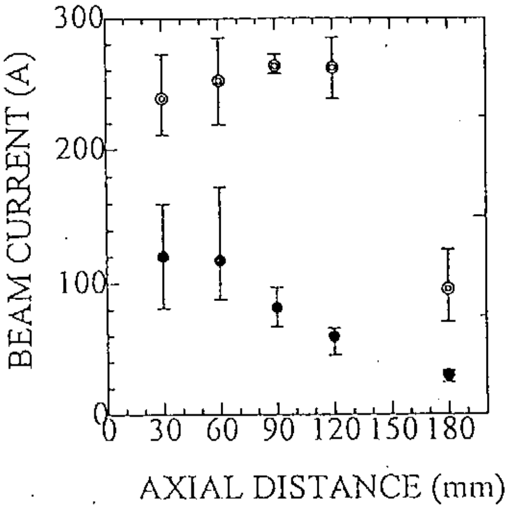

Fig.3 Beam propagation characters.

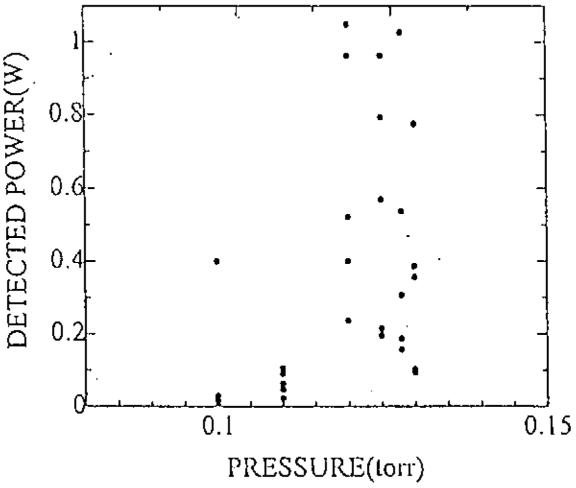

Fig.4 Detected microwave power versus filling pressure.

The preliminary radiation patterns are measured by moving the receiving antenna vertically with vertical and horizontal electric polarization. The pattern with the vertical polarization shows the axisymmetric TM mode radiation. The pattern with the horizontal polarization shows that TE mode comparable to the TM mode is radiated. The output power of the TM mode is less than 1kW and the corresponding electronic efficiency is less than 0.004 %.

4.Discussion and Conclusion

Without guiding magnetic field, the cyclotron modes and the space charge modes become degenerate and the surface charge σ_1 at the beam-vacuum boundary plays essential role. For our large diameter SWS with periodically corrugated wall, the degenerate interaction is superior to the conventional Cherenkov interaction in the high current region above 100 A and in the weakly relativistic energy region.

A large diameter BWO without guiding magnetic field is demonstrated experimentally. The beam propagation is achieved by filling SWS with helium gas. The oscillation mode of the BWO might be the axisymmetric TM mode as well as TE mode. The output power of the TM mode is less than 1kW, which corresponds to electronic efficiency less than 0.004 %.

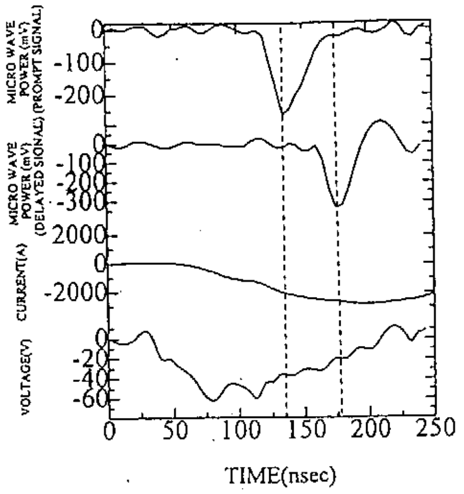

Fig.5 Wave forms of prompt and delayed signals of microwave power, beam current and beam voltage.

The TM mode radiation might be attributed to the degenerate interaction between the beam and the structure TM mode. TE mode radiation has also been observed in BWO,s with guiding magnetic field and has frequently be attributed to the cyclotron interactions. In our large diameter BWO, there is no magnetic field, which introduce the cyclotron interactions. There might be several possible TE mode radiation mechanisms, such as hydrodynamic beam-plasma interaction and vertical beam trajectories proposed in ref.3. Since the TE modes observed is seen like non-axisymmetric in our experiment and in ref.3, we point out that the hybrid mode interaction might be important. A self-consistent analysis of hybrid mode interactions is presently underway and will be presented in a future paper.

References

1. V.L.Granatstien and I.Alexeff: *High-Power Microwave Sources.* (Artech House, Norwood, MA, 1987)
2. J.Benford and J.Swegle: *High-Power Microwaves.* (Artech House, Norwood, MA, 1992)
3. D.M.Goebel, J.M.Butler, R.W.Schumacher, J.Santoru, and R.L.Eisenhart: IEEE Trans. Plasma Sci. **22** (1994) 547.
4. Y.Carmel, K.Minami, R.A.Kehs, W.W.Destler, V.L.Granatsein, D.Abe, and W.L.Lou: Phys. Rev. Lett. **15** (1989) 2389.
5. X.Zhai, E.Garate, R.Prohaska and G.Benford: Appl. Phys. Lett. **60** (1992) 2332.
6. K.Ogura, K.Minami, K.Kurashina, W.S.Kim, T.Watanabe, K.Ishi, and S.Sugito: Fusion Engneering Design **26** (1995) 365.
7. K.Ogura, T.Azegami, O.Watanabe and T.Watanabe; J. Phys. Soc. Jpn. 67 (1998) 3462.

SNOWPLOW MODELING OF HIGH-POWER PLASMA DEVICES

Igor V. Lisitsyn, Sunao Katsuki and Hidenori Akiyama

Department of Electrical and Computer Engineering, Kumamoto University,
2-39-1 Kurokami, Kumamoto 860, Japan.

ABSTRACT

The snowplow plasma behavior is suggested to be common for high-density plasma devices. A two-dimensional implosion of liners is studied employing a snowplow compression model. This is instead of the conventional one-dimensional cylindrical implosion of Z pinches where a wire array or a gas-puff liner, which has a cylindrical shape and an uniform mass distribution along the z-axis. Two-dimensional Z-pinch compression can be realized utilizing either a spherically shaped wire array or a double gas-puff liner with a special mass distribution along the z-axis. The results obtained from computer simulations show that both kinds of liners can be compressed in both the z and the r directions. This results in a uniform and a high-power heating of the spherical dynamic hohlraum placed inside the liner. The spherical, two-dimensional liner implosion increases the power density at the hohlraum surface, improves the symmetry of the capsule irradiation and helps partially in quenching of the Rayleigh-Taylor instability. Recent experiments and modeling of the plasma opening switches showed similar features to the Z-pinches. From this viewpoint, initial shaping of the plasma fill may significantly modify the following dynamics of a plasma device.

INTRODUCTION

Recently, Z pinches are used as the most powerful X-ray sources for numerous applications [1-3]. In a high-current Z pinch, the current flowing along the z-axis produces a strong azimuthal magnetic field resulting in an inward acceleration of the plasma shell. When the plasma stagnates at the geometrical centerline, the kinetic energy of the accelerated plasma particles is converted to a thermal energy in the collisions and a strong X-ray burst is generated.

Recent achievements in the X-ray generation during z-pinch implosion on the Z generator at 20 MA opened the door to important Inertial Confinement Fusion (ICF) applications [4]. The breakthrough in the liner fabrication—use of hundreds thin wires located at constant radius-allowed a significant increase in the x-ray intensity and in the efficiency of electrical to x-ray energy transformation. A record efficiency of approximately 15% was reached [5]. The rapid progress during the last five years resulted in 290 TW and 1.8 MJ in x-ray power and energy, respectively [6]. A Z pinch is also unique compared to other pulsed power loads allowing a power gain up to a factor of 10 when after a relatively slow liner compression (one hundred to several hundreds ns) the X-ray energy is released in a few ns.

It is noteworthy, that in the experiments on z-pinch implosion on the Z generator as well as on all lower power level generators are made with cylindrical wire arrays or cylindrical gas-puffs with uniform distribution of the liner mass along the *z*-axis. High current experiments with a relatively high liner mass showed good stability of the implosion and good radiation uniformity in the stagnation phase. In the final stage of the compression the liner is thin, relatively long (several cm's), hot and dense plasma column [6].

If the inner (dynamic) hohlraum is used the accelerated plasma shell reaches its cylindrical surface simultaneously and is heated from all sides to temperatures over 100 eV. In this application, the kinetic energy of an imploding shell heats the hohlraum without the pinch stagnation phase. Hot hohlraum emits X-rays to an ICF capsule resulting finally in the ignition. This approach is under consideration as one of the methods of capsule heating, which is competing with the vacuum hohlraum concept where the latter is placed outside of the Z pinch at larger radius. An estimate shows that a temperature of the dynamic hohlraum of the order of 300 eV is sufficient for the initiation of high yield fusion reaction [3].

The Plasma Opening Switches (POS) are frequently used to decrease the load risetime including Z pinch experiments [7]. POS conducts current from a capacitive storage for times ranging from tens of nanoseconds to over one microsecond. During the conduction phase, the POS plasma is assumed to displace axially and radially by J×B forces since the current in plasma has both radial and axial components. The current channel moves down the length of the switch and reaches its end where a magnetically insulated gap forms, mostly due to radial MHD plasma motion [8,9]. For the conduction phase a snowplow model has been shown to predict well the POS behavior [9]. The magnetohydrodynamic (MHD) model for the description of the microsecond POS operation was described firstly in Ref. 10. This model is basing on the assumption that the plasma undergoes a snowplow process during both conduction and opening phases.

The most important conclusion from the snowplow model is that the initial shape of the plasma fill can significantly affect the further behavior of the plasma. This allowed us to propose spherical liner-hohlraum arrangement in Z pinch modeling and modifications of the microsecond POS. Snowplow model lead to a deeper understanding of the POS physics.

SPHERICAL LINER ARRANGEMENT AND ITS IMPLOSION

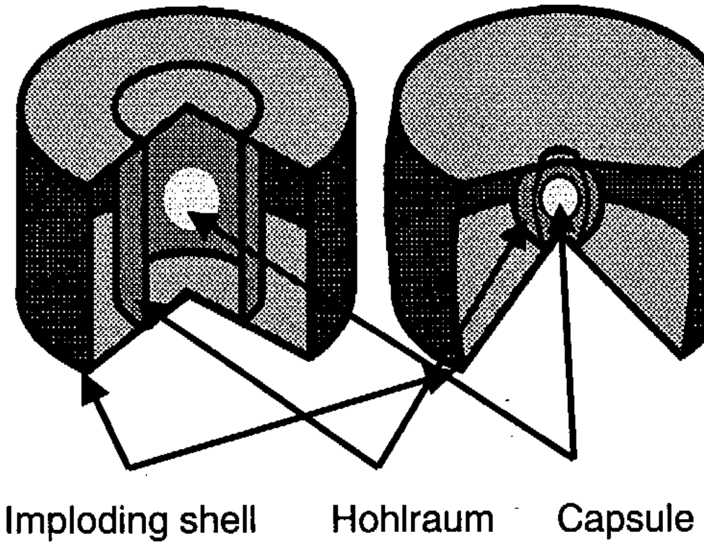

Fig. 1. Schematic diagrams of cylindrical (left) and spherical (right) liner-hohlraum-capsule arrangements.

In our approach, both the liner and dynamic hohlraum have a spherical shape. Fig. 1 shows schematic diagrams of both conventional cylindrical and spherical arrangements. In the simulations we used the parameters of a current source which is under consideration as the next step in the pulsed power ICF experiments, namely X-1 generator with 60 MA of the output current [5]. We used a simplified hydrodynamic snowplow 2-D implosion model [11,12] without a radiative part of the stagnation phase: the conversion of the kinetic energy into the thermal energy is omitted. This last part is responsible for the hohlraum heating and requires the inclusion of the equation of state that is beyond of our calculations. In our model the hohlraum is placed inside the pinch and the

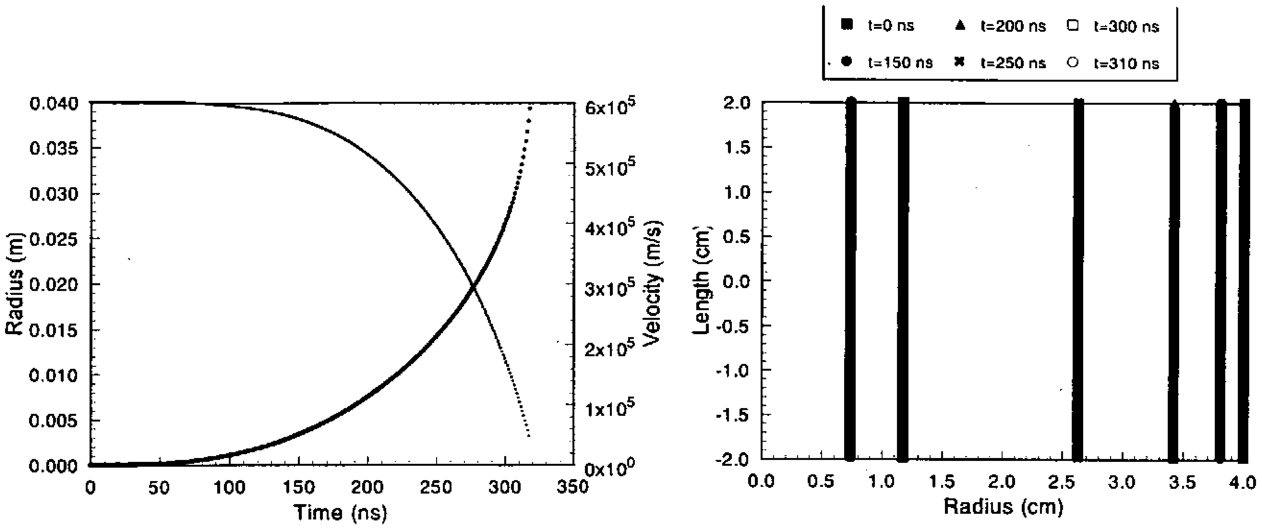

Fig. 2. Liner radius and velocity in time (b), dynamics of implosion of a cylindrical liner (b).

implosion ends at the finite radius. The elements of the conducting shell are accelerated by **j×B** force while equations of motion and continuity are solved in the cells of a moving grid. Since the current has both *r* and *z* components, the perfectly conducting fluid moves in both directions. A current risetime of 300 ns and a liner mass of 50 mg/cm are chosen. The initial liner radius at the center and the height are each 4 cm, which are reasonable for high-current Z pinch – hohlraum experiments.

The calculations of the implosion of a cylindrical liner showed the liner acceleration toward the centerline (*z*-axis) to the final kinetic energy of 50 MJ. Fig. 2 shows the dependence of the liner radius and velocity on time (a) and the location of the liner elements in time, liner implosion dynamics (b). The acceleration stops at 310 ns when the liner reaches the hohlraum placed at a radius of 7 mm.

The compression of a spherical shell is shown in Fig. 3 that corresponds to the right hand arrangement shown in Fig. 1. The initial shape of the liner is given by

$$r(t=0,n)=\sqrt{R^2-z^2(t=0,n)}-R+r_0$$

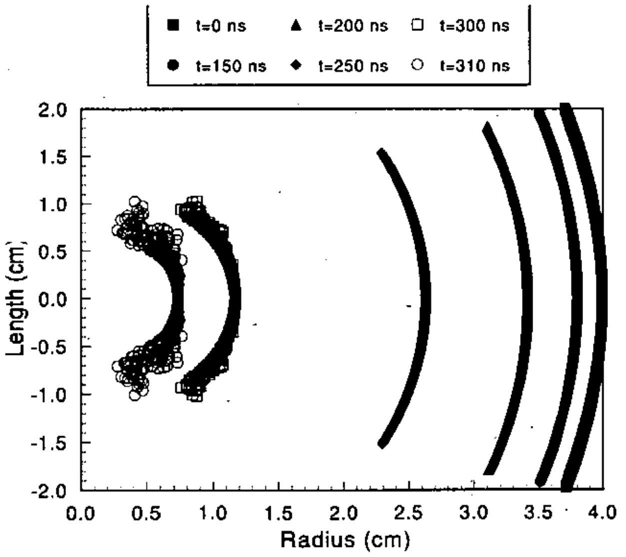

Fig. 3. Dynamics of the implosion of a spherical liner.

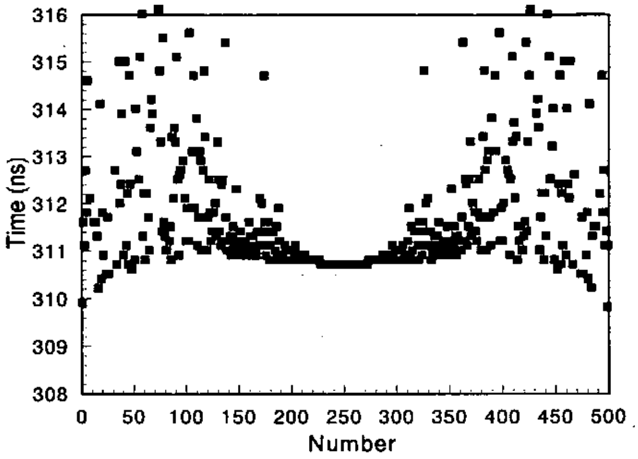

Fig. 4. Time, when liner elements reach the surface of the hohlraum.

where r and z are current coordinates, r_0 equals to 4 cm, and R is a variable radius of the liner curvature.

R is varied in the range from 5 to 10 cm. A curvature radius of $R = 7$ cm is found to be optimum for the simultaneous impact of the whole liner with a spherical hohlraum of 7 mm in radius. The elements of the liner reach the hohlraum surface within 3 ns as are shown in Fig. 4.

RAYLEIGH - TAYLOR INSTABILITY

The spherical shape of the liner has one more significant advantage. Under the magnetic field pressure it acts like an arc, which is more stable mechanically and thus decreasing the effect of the Rayleigh-Taylor (RT) instability [13]. The analysis [14] shows that in the compression of elastic-plastic solid shells, the spherical convergence is more stable compared to cylindrical convergence with azimuthal perturbation.

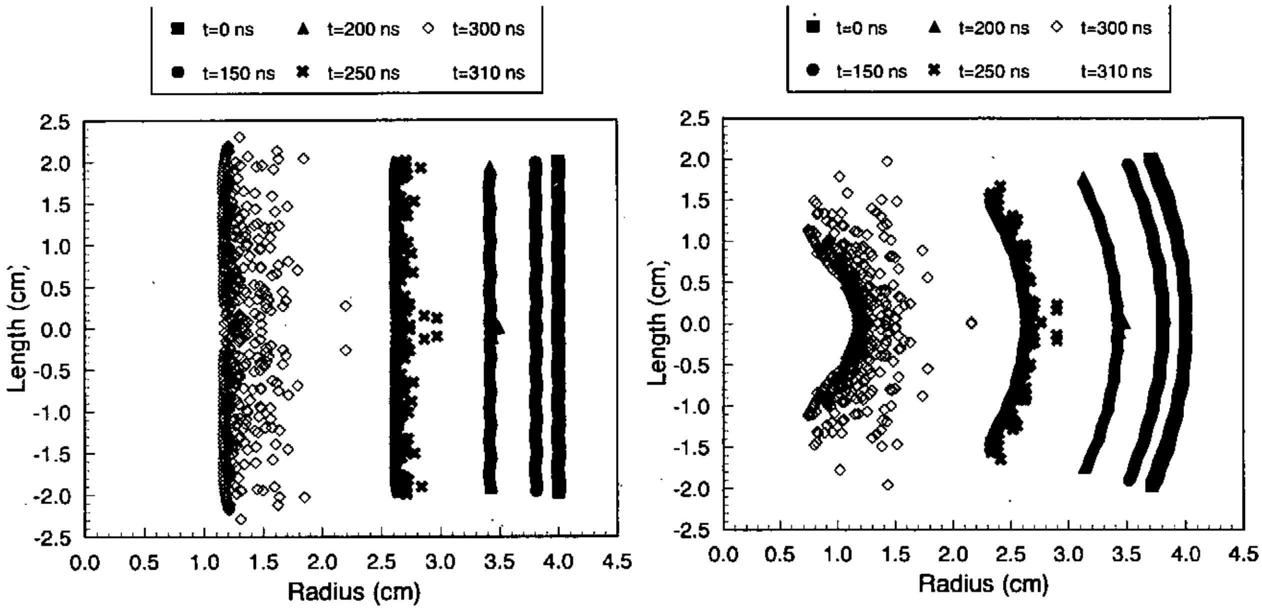

Fig. 5. Growth of RT instability in cylindrical (a) and spherical (b) liners.

Simulations are carried out to compare the growth of the instability in cylindrical and spherical liners. In order to excite the instability, the surface of the liner is initially perturbed. The perturbed component of the liner surface is taken as sinusoidal and is described in the code as

$$r_1(t = 0, n) = A \cdot \sin[k \cdot z(t = 0, n)]$$

where A is the amplitude of perturbation and k is the wave number. The implosion dynamics of cylindrical and spherical liners with initially perturbed surface is shown in Fig. 5. As is expected, the instability growth rate is less for the spherical shell.

DOUBLE-VALVE SINGLE-SHELL IMPLOSION

The approach described above is valid for wire arrays liners. The large mass of the liner and, correspondingly, the large wire diameter (approximately 60 μm if 100 gold or tungsten wires are employed) may not pose a serious technical difficulty in the fabrication of the array into a spherical shape. However, the spherical, 2-D implosion is possible even with a cylindrical liner having a variable mass along z-axis with a maximum at the midplane.

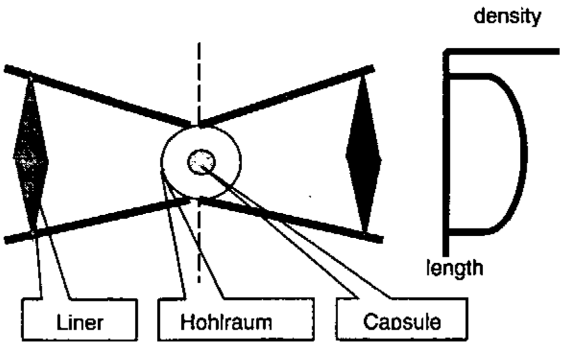

Fig. 6. Concept of double gas-puff liner.

This can be achieved using wires with variable thickness or with a double gas-puff liner where two separate annual valves are placed at opposite electrodes. A double gas-puff liner and an approximate mass distribution required for the 2-D implosion are schematically represented in Fig. 6.

The calculations of the implosion of this kind of liner are carried out using the same 2-D hydrodynamic code. The liner mass of average 50 mg/cm is too high for a conventional gas-puff, however, for a better comparison, the total liner mass is taken to be equal to the previous case. The initial mass distribution along the *z*-axis of a cylindrical liner and the dynamics of 2-D implosion are shown in Fig. 7 a and b, respectively. It is seen that the liner implodes along the *z*-axis, but the stability of the implosion is less compared to the case when the spherical liner is used. It is noteworthy, that the fabrication of a wire array liner with variable wire thickness is complicated and, maybe, difficult to achieve. However, some initial experiments at low currents, where comparatively low-density gas-puffs are used, can be conducted with a double gas-puff liner for the experimental verification of the implosion dynamics, stability, etc.

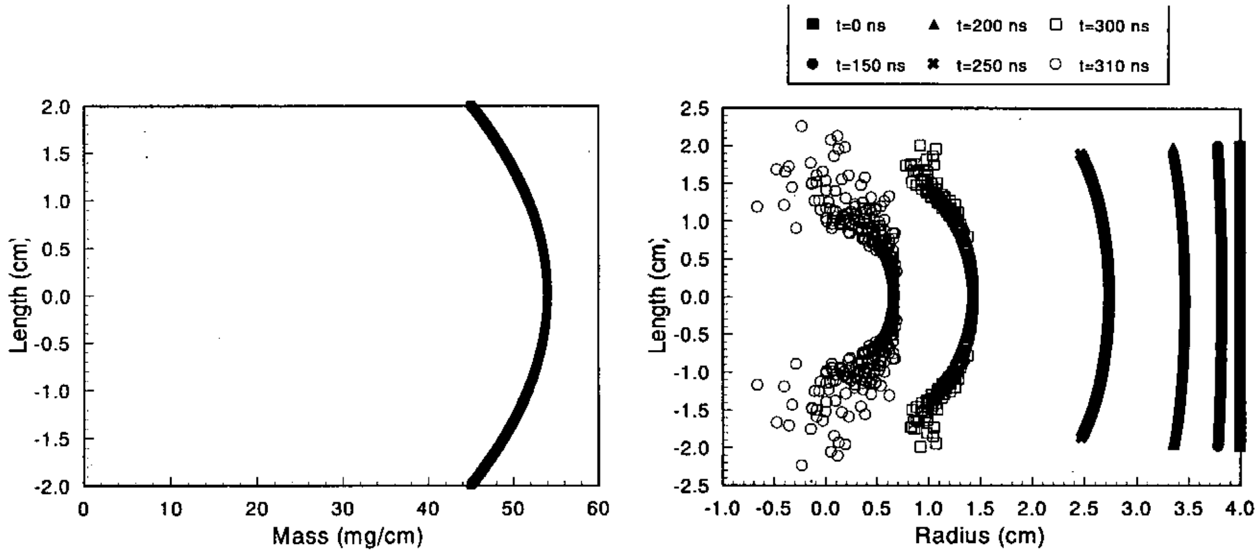

Fig. 7. Initial mass distribution along liner axis (a) and implosion dynamics of a liner with variable mass along z-axis.

In conclusion, it should be mentioned that the spherical liner implosions can have some advantages in the hohlraum experiments over those conducted with a conventional cylindrical liners. These advantages are: a higher power density due to 2-D liner implosion and a possibility to operate with spherical or quasi-spherical hohlraums instead of cylindrical by selecting the initial shape of the liner from a variety of geometries. It becomes possible to optimize the implosion with one more degree of freedom compared to recent studies.

SNOWPLOW MODEL IN MICROSECOND POS

The snowplow model in the description of the microsecond POS operation is developed in [8] and divided into to distinct phases.

For the conduction phase a snowplow criterion was obtained as a function of current, time, plasma density and length and electrode radii. The plasma develops a thin current carrying channel, which propagates along the switch in the direction of the load. Plasma pressure is taken negligible and the channel is radial and perpendicular to the power propagation direction. The important point obtained in this study is that the snowplow model is only one approach to obtaining hydrodynamic scaling for the conduction current.

During the opening phase a different model was employed. The gap near the cathode is taken pre-formed and its development is radial (current flows axially). The expansion of the vacuum gap is examined using both ion erosion and snowplow motion in radial direction only. It was shown that for the long-conduction-time experiments, the POS voltage scaling fits the snowplow dependency better than other dependencies.

However, in this model, the mechanism of the transition from the conduction phase to the opening phase is unclear. The major switch phases of operation are treated separately. The authors of [8] mentioned that the model might result in correct scaling even if snowplow represents incorrectly the detailed hydrodynamic processes in the switch plasma. At the time when the paper [8] was published, the plasma density measurements by laser interferometry were not available. Recently, this diagnostics have been used in numerous studies and provide new important information on the POS physics.

The snowplow model was used to predict and explain the scaling obtained in the study of the microsecond POS with the current 2-5 MA [9]. It was shown again that a snowplow scaling for the conduction phase predicts accurately the relationship among the magnetic field, conduction time, POS length and plasma density.

$$\frac{IT}{rl} \propto \sqrt{n}.$$

Here, I is the peak current, which is assumed to be proportional to T, the conduction time, r is the radius of the POS cathode, l is the length of the switch and n is the plasma density. The scaling has been verified using direct measurement of the plasma density.

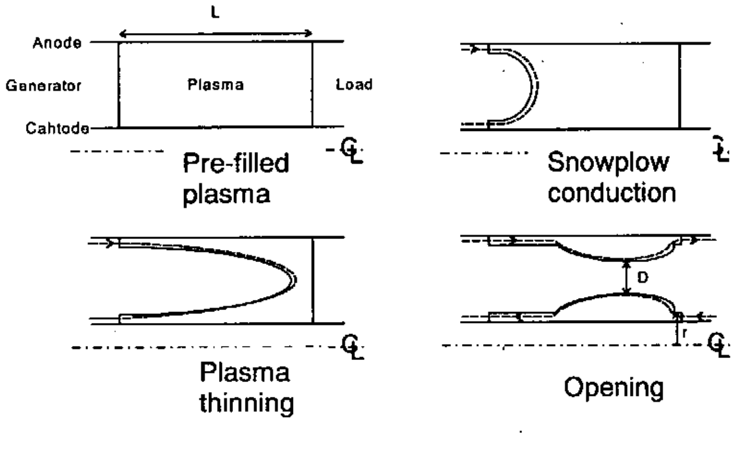

Fig. 8. Conventional sequence of snowplow POS operation [9].

The important transition between the snowplow conduction and magnetically insulated opening phases was suggested in 10. The low density needed to provide rapid opening at the end of the conduction phase results from a plasma thinning process. The current conducting channel during the conduction phase changes its shape from predominantly radial to radial – axial. Therefore, the plasma displacement during this phase has also radial component. A magnetically insulated gap forms through some combination of the plasma ion erosion and radial magnetohydrodynamic (MHD) motion. This results, finally, in the formation of the vacuum gap, where the electron flow is cut off by the azimuthal self magnetic field.

The interferometer measurements carried out in the number of experiments showed the decrease in the plasma density in the second half of the conduction phase explained as the plasma thinning and a very fast gap formation, corresponding in time to the opening phase. The measured vacuum gap spacing at the end of the opening phase is usually several mm – cm. In some experiments vacuum gap was not detected, in other experiments the gap with several cm of separation was instantly formed (several ns, during the time, which is comparable with the time response of the detection scheme). It the last case, the gap could significantly exceed the effective gap distance necessary for the magnetic insulation.

MOTION OF CURRENT-CONDUCTING CHANNEL IN POS PLASMA

The snowplow model of the plasma motion is developed on the basis of the following assumptions.

1. Current layer grabs all the plasma mass during its motion in POS plasma.
2. Plasma density is constant in POS.
3. Magnetic field is constant in POS.
4. Plasma pressure is negligible.
5. Current carrying channel is radial.

Assuming that the current through plasma I rises linearly, equation of motion for the current-carrying channel is

$$I = I_0 t;$$

$$M_i n \frac{d(lv)}{dt} = \frac{\mu I_0^2}{8\pi^2 r^2} t^2.$$

Here l is the variable length of switch changing in the process of the snowplow motion, M_i is the average ion mass, v is the snowplow velocity, n is the plasma density and r is the plasma radius. The right-hand side of the equation of motion represents Ampere's force.
Designating

$$c_1 = M_i n;\ c_2 = \frac{\mu I_0^2}{8\pi^2 r^2}. \quad c_1 \frac{d(lv)}{dt} = c_2 t^2.$$

the equation can be solved dividing the variables for the channel velocity as

$$c_1 l v = c_2 \frac{t^3}{3};\ c_1 \frac{l}{t} v = c_2 \frac{t^2}{3};\ \ v = \sqrt{\frac{c_2}{3c_1}} \cdot t.$$

Therefore, the current-conducting layer moves with constant acceleration:

$$a = \sqrt{\frac{\mu I_0^2}{24\pi^2 r^2 M_i n}};$$

and its velocity linearly rises with time.

After the current channel leaves the pre-formed plasma, it can move according to two different models. First model is realized if the current is still rising. Assuming it continues to rise linearly, the equation of motion of the current channel becomes

$$I = I_0 t;$$

$$M_i n l \frac{dv}{dt} = \frac{\mu I_0^2}{8\pi^2 r^2} t^2.$$

The acceleration of the current front is proportional to time squared:

$$a \propto t^2$$

And, if the current is close to its maximum, it can be assumed as constant during the end of the conduction phase and the opening phase:

$I = const;$

$$M_i nl \frac{dv}{dt} = \frac{\mu I^2}{8\pi^2 r^2}.$$

The channel is moving with a constant acceleration.

$$v = v_0 + at;$$

$$a = \frac{\mu I^2}{8\pi^2 r^2 M_i nl}.$$

Where v_0 is the velocity, which the channel obtained during the motion in the pre-formed plasma.

Therefore, there are two different phases within the phase of conductivity in a microsecond POS. The first phase lasts until the current-carrying channel reaches the load end of the pre-filled plasma. The second phase, the transition phase to the opening, is characterized by the motion of current-carrying channel downstream the initial plasma location.

According to the model developed for a microsecond POS and briefly described in previous section, a very important phase for a POS opening is the plasma thinning. The decrease in the plasma density, resulting finally in the opening, in the second half of the conduction phase was associated with the beginning of the radial motion of the plasma outward of the curved current channel. Corresponding decrease in the line-integrated plasma density was obtained in numerous interferometer measurements.

However, the degree of the plasma thinning is strongly dependent on the curvature of the current-conducting channel. If the current channel is mostly radial no plasma thinning is possible. Moreover, direct measurements of the magnetic field penetration into the microsecond POS made by set of B-dot probes [15] showed that the current channel is mostly radial. Therefore by our point of view the plasma thinning and corresponding transition between conduction and opening phases in a long-duration POS occurs mostly after the current-conducting layer leaves the pre-filled plasma. Since that time, the channel is not radial anymore, and plasma may leak. This is also in a good agreement with experiment [15].

There are two possibilities for the plasma thinning mechanism. A criterion can be the ratio *l*/*d* where *l* is the length of the switch and *d* is the radial distance between electrodes – interelectrode gap. If the ratio *l*/*d* is small the current conduction channel is mostly radial and the plasma thinning occurs after the current-carrying channel moves downstream of the initial plasma location. In the opposite case the shape of the current channel becomes important and the snowplow propagation inside the pre-formed plasma may result in the plasma thinning. Noteworthy, that low *l*/*d* ratio is realized in most plasma gun experiments, high *l*/*d* ratio is a good approximation to some flashboard experiments.

The quantity of plasma, which accelerates together with the current-conducting channel in the end of the conduction phase, depends on the initial plasma fill parameters. Therefore, the behavior of the POS and its electrical characteristics such as voltage and impedance will be also dependent on those parameters.

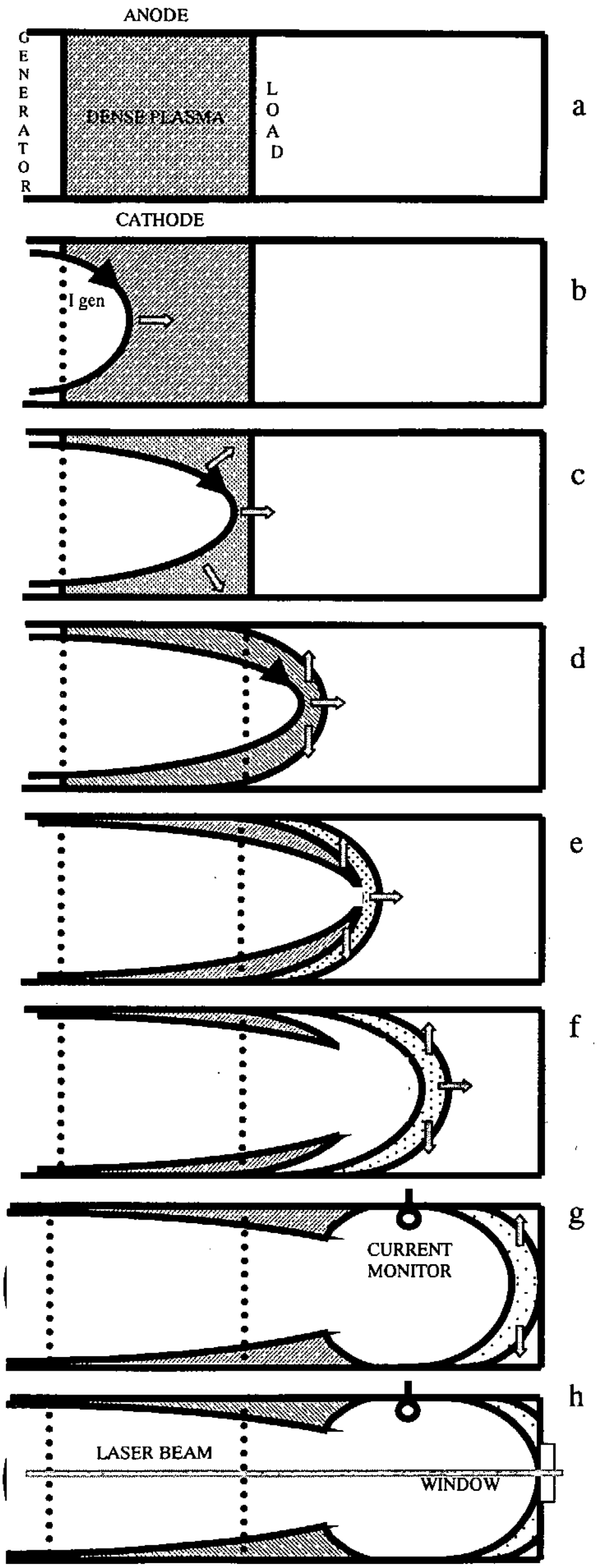

The sequence of the POS operation is shown in Fig. 9 and corresponds to the respective arrows on the Fig. 10 containing typical waveforms.

Fig. 9 (a) shows the pre-filled plasma in the POS region.

Fig. 9 (b) corresponds to a standard snowplow conduction phase with preliminary radial current-conducting channel.

Fig. 9 (c) shows the plasma thinning phase in Maxwell snowplow model. However, there can be no thinning in this phase as we mentioned above.

Fig. 9 (d) shows the current layer with the plasma ahead leaves the region of initial plasma fill.

Fig. 9 (e) shows the phase of the plasma thinning where the current has a significant radial component. The current layer accelerates toward the load loosing some plasma during its motion.

Fig. 9 (f) corresponds to a complete separation of the dense pre-filled plasma and comparatively low-density plasma at the current conducting channel. It is seen how large gap in dense plasma can develop without a formal opening, e.g. there is no current through the load.

Fig. 9 (g) corresponds to the opening when the load current monitor shows the increase in the load current. The interferometer can still detect some plasma density resulting in the incorrect conclusion that no vacuum gap is formed. Another indication of the POS opening is in the decrease of the generator current. This decrease can be due to fast increase in the generator circuit inductance due to the current channel motion while the magnetic flux $\Phi = LI$ is conserved.

Fig. 9 (h) correspond to the plasma recombination at the window and load endplate. The interferometer shows fast decrease in the plasma density at this moment. The measured gap can be very large because its expansion started long time ago at the time corresponding to Fig. 9 (g).

Fig. 9. Qualitative picture of POS operation. Description in the text.

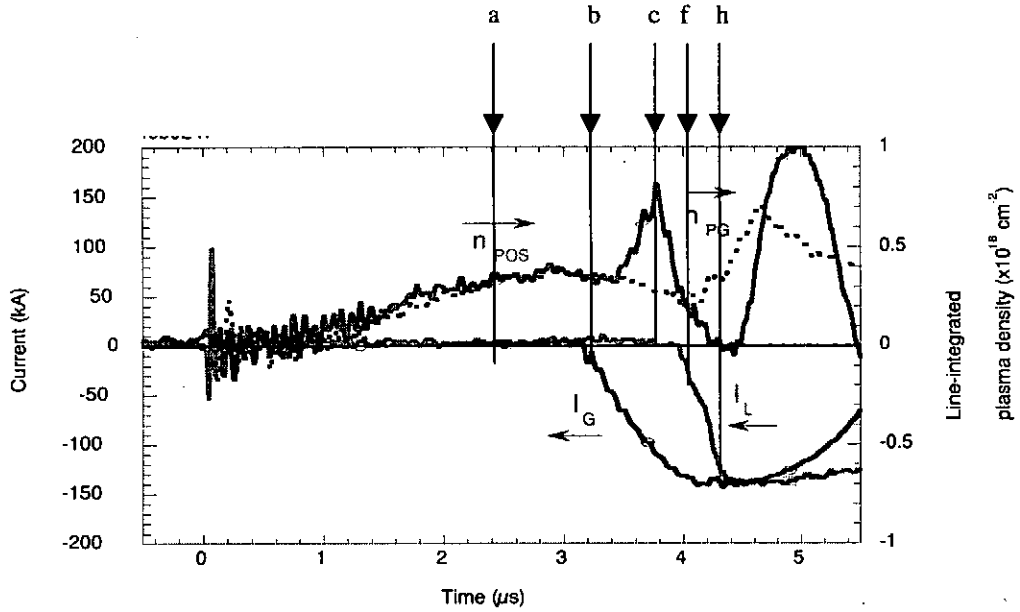

Fig. 10. Typical waveforms of the generator current I_G, load current I_L and line-integrated plasma densities with n_{POS} and without n_{PG} POS.

This explains different POS characteristics obtained with different plasma sources despite the plasma densities were similar.

The typical waveforms of the generator current, load current and line-integrated plasma densities are shown in Fig. 10. The arrows indicate the time moments during the switch operation, which correspond to the sketches in Fig. 9. The generator and load waveforms are standard for POS experiments. The plasma density waveform has several phases.

Initially, the POS plasma density follows the dashed line, which indicates the plasma density trace without current in the POS. Then, between points b and c the line-integrated plasma density rises over plasma gun value. A similar effect was observed in earlier measurements [16] of the plasma density in a cable gun POS. The ionization degree of the plasma and its average charge state are lower in the plasmas produced by the cable plasma guns and the density increases due to the ionization process.

The ionization of the plasma atoms/ions occurs probably at the current front. Assuming constant degree of ionization along POS plasma and taking into account that increase of the line integrated (along z-axis) electron density is proportional to the path of the current layer in plasma

$\Delta n \propto l$

Knowing that the current-carrying channel moves with constant acceleration with the preformed plasma, we obtain

$\Delta n \propto t^2$.

The line-integrated density increases with time squared. This corresponds well to the experimental data – increase of the plasma density in the first half of the conduction phase on Fig. 10.

After the plasma density reaches its maximum, it decreases monotonously down to zero. This is plasma thinning, which corresponds to sketches in Fig. 9 (d-g). Minimum density is observed in the end of the switching process.

Minimum plasma density often corresponds to the opening of the switch – moment when the load current monitor shows fast increase of the current. However, the time corresponding to the lowest plasma density can be delayed [17]. Sometimes plasma density does not become zero at any location in the POS plasma [16]. The way in which this is possible shown in Fig. 9 (g). If either the downstream part of the POS hardware is considerably long or only a small amount of the plasma is accelerated in the conduction-opening transition process, the opening and zero-density signal from an interferometer may coincide in time. The amount of plasma accelerated downstream the load is strongly dependent on the duration of the conduction phase. The increase of the conduction phase duration from 1 to 1.5 μs increases significantly this amount resulting in slow propagation of the current front in the downstream region [17].

Traditionally, the voltage generated during the POS opening is considered as an inductive voltage drop due to the fast current decrease in the upstream (generator, I_G) circuit of fast current increase in the downstream (load, I_L) circuit. The standard formulas for those voltages, which are equal, are

$$U_U = U_G - L_G \frac{dI_G}{dt} = U_D = L_L \frac{dI_L}{dt}$$

The changes in generator and load currents are usually considered as a result of the increase of the POS shunt impedance. The generator L_G and load L_L inductances are often taken constant. This is obviously correct from the viewpoint of the circuit analysis, however this model can incorrectly represent real physical processes in a POS.

If the current conducting channel is rapidly moving downstream, the voltage is generated due to the change of inductance, like in a Z pinch. Assuming a constant acceleration a of the current-carrying channel, the total inductance upstream the POS L can be written as

$$L = L_0 + L'(v_0 + \frac{at^2}{2})$$

Here L_0 is the generator inductance at the beginning of the conduction phase and L' is the characteristic inductance of the coaxial line (H/m), where the POS is placed. Taking into account that v_0 comparatively small and the magnetic flux is conserved (generator current close to its maximum) the time behavior of the generator current is:

$$I(t) = \frac{\Phi_0}{L(t)} = \frac{L_0 I_0}{L_0 + L'\frac{at^2}{2}};$$

The POS voltage (more exactly, the voltage between POS electrodes at the initial plasma location) can be calculated then as

$$V_{POS} = L_0 \frac{dI(t)}{dt} = L_0 \frac{d\left(\dfrac{L_0 I_0}{L_0 + L'\frac{at^2}{2}}\right)}{dt} = -\frac{L_0^2 I_0 L' at}{\left(L_0 + L'\frac{at^2}{2}\right)^2}$$

This dependence has a maximum, which occurs at the time calculated from the zero derivative of the formula for the POS voltage. Exact solution results in four order algebraic expression with very bulky, and, therefore, useless roots. However, taking into account that

$$L_0 >> L'\frac{at^2}{2}$$

at low t (t, here, is the duration of the conduction-opening transition phase, which is in proportion to the duration of the POS conduction phase) we obtain

$$V_{POS} \approx -L_0 I_0 L' at$$

Substituting

$$a = \frac{\mu I^2}{8\pi^2 r^2 M_i n l}; \quad \therefore n \propto IT$$

We find the final scaling for the POS voltage.

$$V_{POS} \propto I^2 / T$$

Here, I is the POS current T is the conduction time. This scaling is obtained from snowplow model without assumption [9] that the snowplow propagation changes its direction from axial to radial with the transition from the conduction to the opening phase.

Recent experiments substantiate the validity of the snowplow approach to the further improvement of the POS operation [18].

The characteristics of a microsecond plasma opening switch have been improved by the modification of the plasma source. The conventional cable plasma guns have been used in the experiments producing different directions of the plasma flow by changing guns' nozzles. The nozzles were arranged to provide the plasma flow, which is not exactly radial but has an angle to the gun axis. The experiments with the modified plasma guns were carried out with the upstream, downstream and azimuthally slanted plasma flow directions. The results are compared to a conventional radial flow plasma source. The plasma flow slanted in an angle of 30° downstream resulted in 50% improvement of the load current risetime and switch impedance.

The obtained dependencies can be explained in the frame of the snowplow POS model. The plasma ahead the current-conducting layer is displaced due to pressure gradient at the magnetic piston. The validity of the snowplow model is proven by adequate dependence of the POS conduction current versus plasma density in various long-duration POS experiments.

Assuming this model is valid for most POS experimental conditions, the distribution of the plasma density in the POS gap and initial shape of the plasma fill become very important. A significant modification of the plasma displacement parameters can be achieved by changing the initial parameters of the plasma fill.

REFERENCES

1. J.Shiloh, A.Fisher, and N.Rostoker, Phys. Rev. Lett. **40**, 515 (1978).
2. J.S.Pearman, and J.C.Riordan, J. Vac. Sci. & Technol. 19, 1190 (1981).
3. K.Murayama, T.Shinkai, S.Katsuki, and H.Akiyama, Jpn. J. Appl. Phys. **37**, 2676 (1998).
4. D.Cook, Proceedings of 11 th IEEE International Pulsed Power Conference, Baltimore, MD, (IEEE Publishing, Piscataway, 1997) pp. 25-36.
5. J.P.Quintenz, private communication. Will be published in Proc.12 th International Conference on High-Power Particle Beams, Haifa, Israel, 1998.
6. R.B.Baksht, I.M. Datsko, A.Yu.Labetsky, A.G.Russkikh, and A.V.Fedunin, Proc. 11 th International Conference on High-Power Particle Beams, Prague, Czech Republic, (Institute of Plasma Physics Publishing, Prague,1996) p. 522.
7. H.A.B.Bodin, A.A.Newton, and N.J.Peacock, Nucl. Fusion, **1**, 54 (1960).

8. W. Rix, D. Parks, J. Shannon, J. Thompson, and E. Waisman, IEEE Trans. Plasma Sci., **19** 400 (1991).
9. W. Rix, P. Coleman, J.R. Thompson, D. Husovsky, P. Melcher, and R.J. Commisso, IEEE Trans. Plasma Sci., **25**, 169 (1997).
10. R.J. Commisso, P.J. Goodrich, J.M. Grossmann, D.D. Hinshelwood, P.F. Ottinger, and B.V. Weber, Phys. Fluids B **4**, 2368 (1992).
11. T.Miyamoto, Nucl. Fusion, **24**, 54 (1984).
12. F.L.Curzon, A.Folkierski, R.Latham, and J.A.Nation, Proc. Roy. Soc., **257**, 348 (1960).
13. V.V. Vikhrev, V.V.Ivanov, G.A. Rozanova, Nucl. Fusion, **33**, 311 (1993).
14. E.L. Ruden, and D.E.Bell, J. Appl. Phys., **82**, 163 (1997).
15. V.M.Bystritskii, Ya.E.Krasik, I.V.Lisitsyn and A.A.Sinebryukhov, IEEE Trans. on Plasma Sci., **19**, 607 (1991).
16. B.V. Weber, D.D. Hinshelwood, and R.J. Commisso, IEEE Trans. on Plasma Sci., **25**, 189 (1997).
17. S. Kohno, Private communication (1998).
18. I. V. Lisitsyn, S. Kohno, Y. Teramoto, S. Katsuki and H. Akiyama, "Improved Operation of microsecond Plasma Opening Switch by Plasma Source Modification", Submitted to Phys. Plasmas, January 1999.

Improvement of the uniformity of the z-pinch plasma by a fast current provided by the ASO-X with POS

S. Katsuki, T. Nishi, Y. Teramoto, I. V. Lisitsyn, H. Akiyama

Department of Electrical Engineering and Computer Science, Kumamoto University, Kumamoto 860

K. Murayama

Yatsushiro National College of Technology, Yatsushiro 866

Abstract

This paper reports the first experiment of x-ray radiation from z-pinch plasma driven by an inductive voltage adder, ASO-X. Plasma opening switch was employed to shorten the rise time of the z-pinch current. Delay time from puffing gas to starting current was varied to investigate relation of implosion time to uniformity of plasma column, which was observed by a filtered pinhole camera. Experimental results show that the short implosion time contributes to improvement in the uniformity of the x-ray radiation along the z-axis.

1. Introduction

Pinched plasmas [1-5] have a potential as a radiation source of soft x-ray for industrial applications such as x-ray lithography, x-ray microscopy and so on because of their high x-ray output efficiency. x-ray laser using the z-pinch plasma is not far from achievable. In the pinched plasma, an intense x-rays are radiated from the dense and high temperature spots, so called "hot spots", which are caused by the plasma instability. In order to form the uniform high-density plasma filament, the plasma instability should be suppressed or get the plasma pinched faster than the time constant of plasma instability growing up.

ASO-X was constructed at Kumamoto University in 1997, as a new scheme of pulsed power generator a 3-staged inductive voltage adder, which provides 180 kV and 400 kA at 1.3 μs (1/4 T). ASO-X is equipped the plasma opening switch to shorten the rise time of the load current. ASO-X equips plasma opening switch (POS) to shorten the risetime of the load current. This paper reports the gas-puff z-pinch experiment using ASO-X. The behavior of the z-pinch plasmas and the spatial distributions of the hot spots are investigated.

2. Experimental Setup

A. Inductive voltage adder, ASO-X

Figure 1 shows the schematic configuration of ASO-X generator. ASO-X consists of 3 stages of capacitor banks witch are inductively coupled in series by magnetic cores (FINEMET, Hitachi

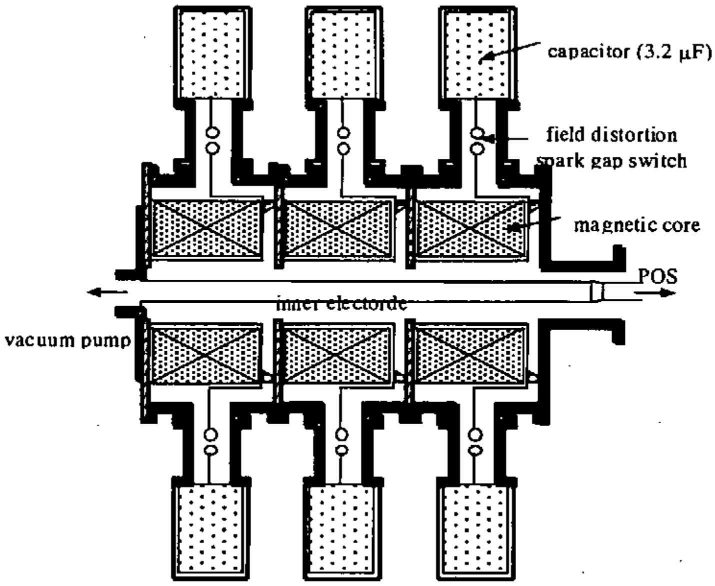

Figure 1. Schematic configuration of ASO-X generator

Metals), field distortion spark gap switches and POS. The length, width and height of ASO-X generator are about 3.0 m, 1.8 m and 1.6 m, respectively. The capacitance of each capacitor is 3.2 μF and the total inductance of the generator is approximately 330 nH. The maximum charging voltage at each capacitor is 60 kV and the total stored energy is 35 kJ. The maximum output voltage is 180 kV and the peak current is 400 kA with 1.4 μs of the quarter period. In this experiment the charging voltage was fixed at 30 kV. The field distortion spark gap switches are equipped and fired with the jitter within 30 ns. POS equips eight coaxial plasma guns to produce the plasma for switching operation.

B. Z-pinch electrodes

Figure 2 shows the schematic diagram of the POS and the gas-puff z-pinch section. The z-pinch consists of a fast magnetic valve, two electrodes placed in a vacuum vessel evacuated less than 10^{-4} torr. Ar gas is injected into the z-pinch region from an anode hole with a diameter of 5 mm by actuating the fast valve. The separation between the electrodes is 10 mm. A stainless mesh cathode with a diameter of 60 mm enables to reduce the gas stagnating near the cathode surface. [5-6] The transparency of the mesh is 81%.

C. Measurements

The behaviors of the plasma columns and the spatial distribution of hot spots in the case of ASO-X without operating POS and with operating POS were investigated. The behavior of the pinched plasmas were observed with an image converter camera (IMACON790, Hadland Photonics Ltd.) and

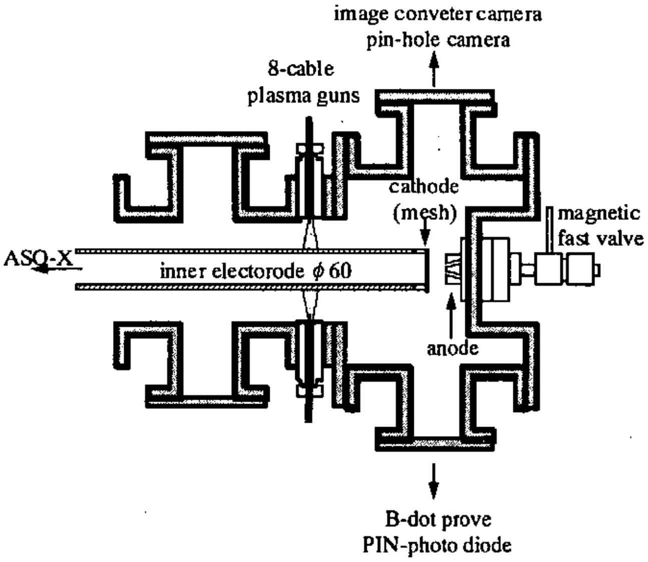

Figure 2. Configuration of z-pinch and POS sections

the spatial distribution of hot spots is observed with a pinhole camera (the diameter of pinhole is 400 μm and covered with a 3 μm-thick Al filter), respectively. Soft x-rays are detected by a PIN-photo diode covered with a 3 μm-thick Al filter and the source and load currents are measured with Rogowski coil and B-dot probe.

3. Experimental results

Figure 3 and 4 show the plasma current and x-ray waveforms for ASO-X. Fig. 3 is in the case of ASO-X without operating POS and fig. 4 is in the case with operating POS. In the fig. 4, the doted line I_G means the generator current and the solid line I_L means the load current flowing through the z-pinch plasmas. Without operating POS the current rise time is about $1\text{x}10^{11}$ A/s and the peak current value is about 170 kA. The soft x-ray is detected at 1.3 μs after the current begins to flow through the plasmas. On the other hands the current rise time becomes much faster (about $1\text{x}10^{12}$ A/s) for operating POS but the peak current value is same as that without operating POS. This means that POS does not consume the energy practically and the opening operation in POS is performed satisfactorily. The soft x-ray is detected 0.3 μs after the load current begins to flow.

Figure 5 and 6 show the framing photographs of the discharge luminosity and the waveforms of soft x-ray and image converter camera monitor signals for ASO-X without operating POS and with operating POS, respectively. The numbers of the soft x-ray waveforms correspond to the numbers on the photographs. The exposure time and inter-frame time for these photographs are 10 ns and 50 ns, respectively. In the case without operating POS, the plasma column is formed between the electrodes and no interference of the reflection of the injected gas is seen on the cathode surface in the photograph number 1. But the plasma column is pinched near the anode electrode strongly and the downward of the plasma column is spread radially. These are because the injected gas diffuses between the electrodes and the current flowing through the plasmas is not enough to pinch the column entirely until this time. In the next photograph number 2 the plasma column is bent obviously and kink (m=1) instability is seen. Furthermore the column disappeared partly. The soft x-ray is emitted around this time and t_s, the time from the beginning of the current flow thorough the plasma until emission of soft x-ray, is about 1.3 μs. In the soft x-ray waveform two peaks of the signal are detected. This means the radiation of soft x-ray is occurred twice continuously. Then the plasma column is torn off completely and diffuses between the electrodes. On the other hand the plasma column is stable along the z-axis at the number 2 on the photographs in the case of operating

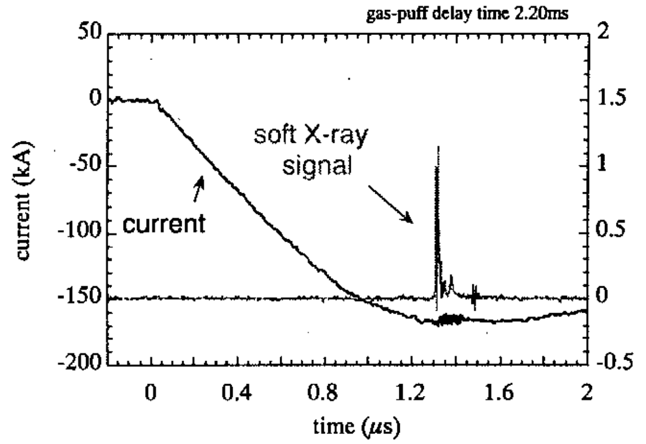

Figure 3. Current and x-ray waveforms for ASO-X without operating POS

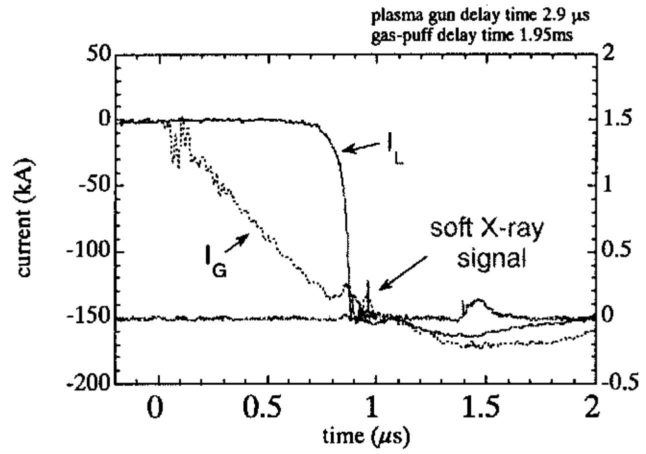

Figure 4. Current and x-ray waveforms for ASO-X with operating POS

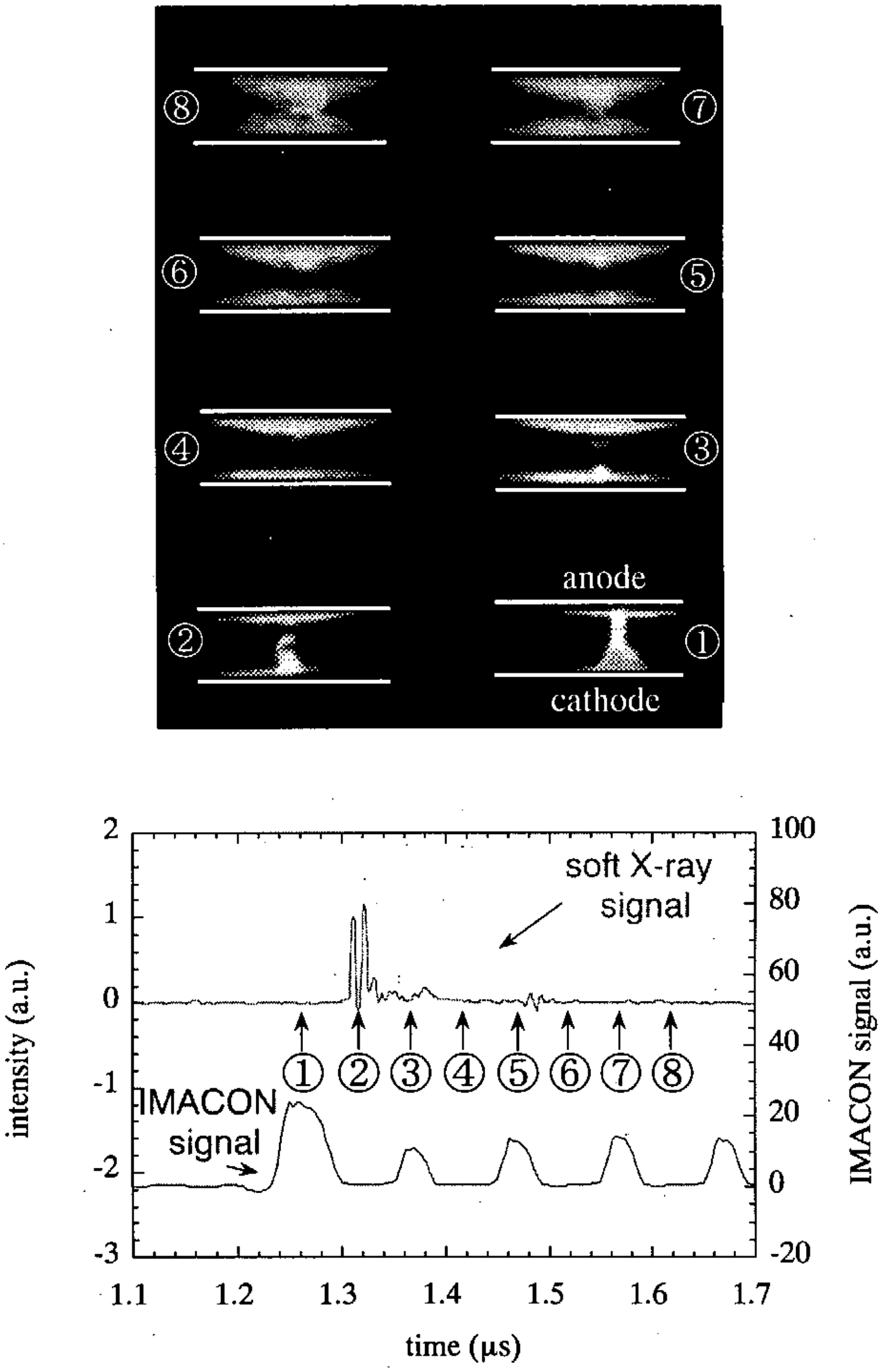

Figure 5. Framing photographs of the z-pinch plasmas and the waveforms of soft x-ray and image converter camera monitor signals for ASO-X without operating POS

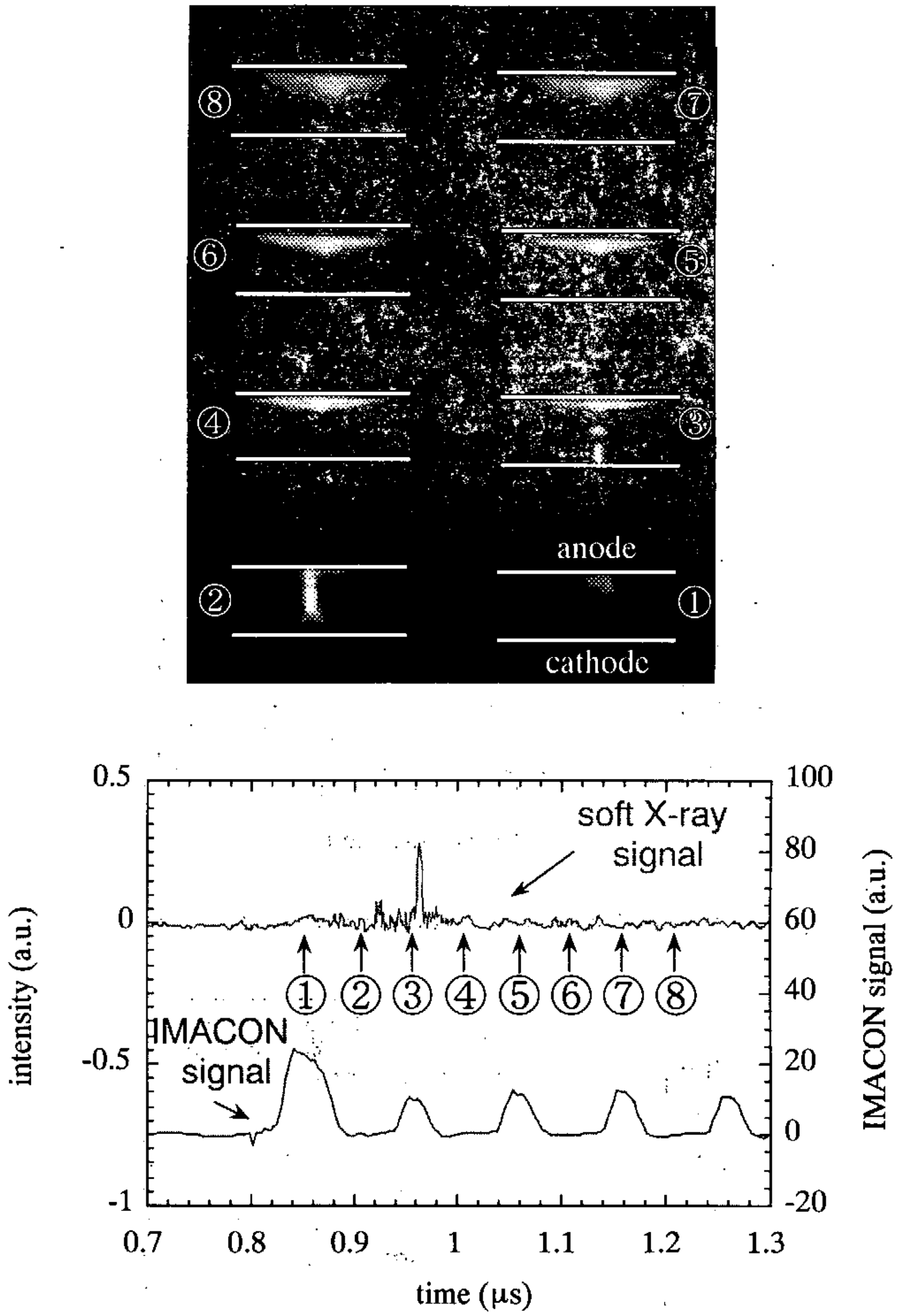

Figure 6. Framing photographs of the z-pinch plasmas and the waveforms of soft x-ray and image converter camera monitor signals for ASO-X without operating POS

POS although the parts of the sausage instability are seen near the anode electrode. Then the plasma column is torn off partly as same as that in the case of without operating POS but the bent of the plasma column is not seen in the photograph number 3. The soft x-ray signal is detected just after this photograph and the plasma column diffuses (photograph number 4 and after). The t_s is about 0.3 μs and it is very short compared with that in the case of without operating POS. This is because the current value necessary for the emission of the soft x-ray is attained in a shorter time for operating POS.

Figure 7 shows the dependence of the soft x-ray intensity on a delay time. The delay time defined

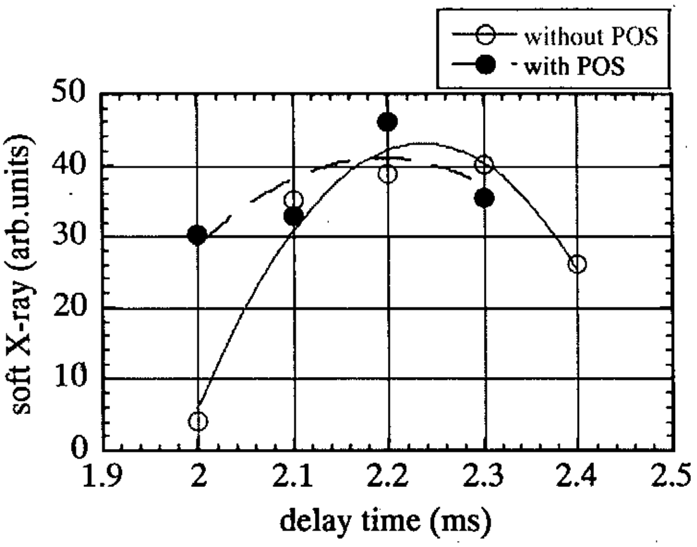

Figure 7. Relationship between soft x-ray intensity and the delay time.

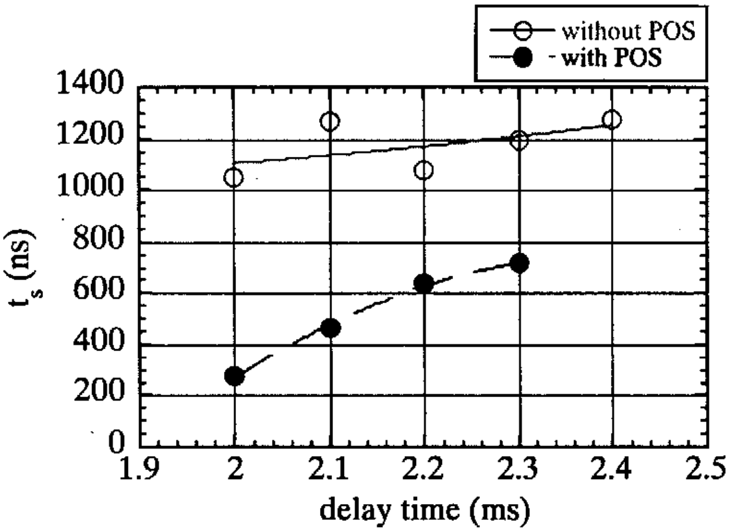

Figure 8. Relationship between t_s and the delay time

as the time difference between the beginning of the coil current for the fast opening valve and the beginning of the current flowing through the plasmas. The empty and solid circles correspond to the ASO-X without operating POS and with operating POS, respectively. These values are the average of several x-ray emissions for each delay time. Each intensity of soft x-ray in both cases is not so different considerably in this experiment.

The dependence of t_s on the delay time is shown in fig. 8. The t_s in the case with operating POS is less than that in the case without operating POS, for all delay times. This means the average velocity of pinched plasmas for operating POS is larger than that for without operating POS.

Figure 9 shows the spatial distribution of the hot spots taken by the pinhole camera with 3 μm-thick Al filter. The photographs (a) and (b) are for without operating POS and with operating POS and are taken at the same time on figure 5 and figure 6, respectively. In the photograph (a) the hot spots are clustered mainly near the anode electrode and the part of the hot spots strayed out the z-axis. The current rise time without operating POS is not enough to restrain the plasma instability and it is difficult to pinch the plasmas entirely between the electrodes then the hot spots are generated only near the anode. On the other hand a lot of the hot spots are distributed entirely along the z-axis in the case of operating POS and the deviation of the hot spots form the z-axis is smaller than that for without operating POS.

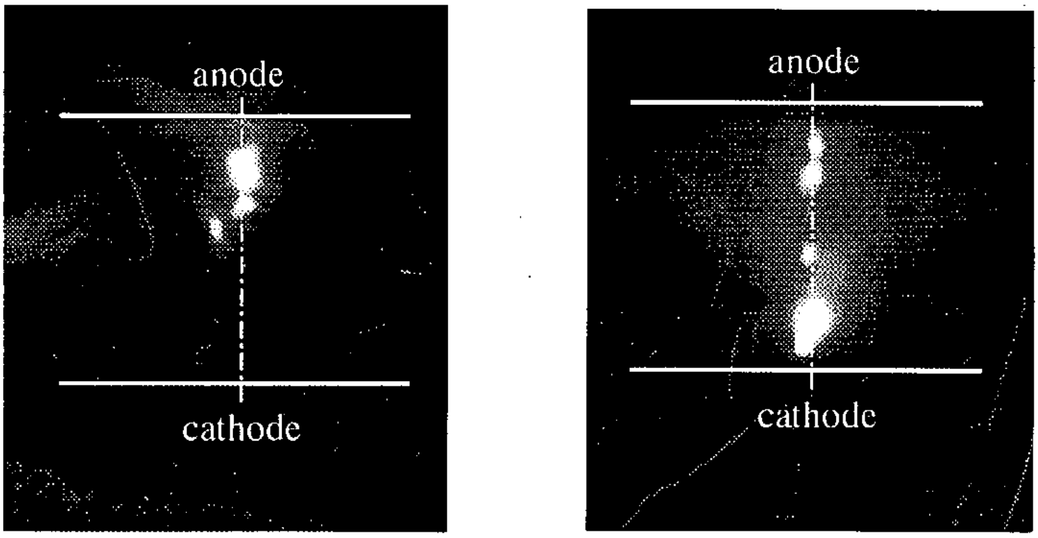

(a) (b)

Figure 9. Pinhole photographs of hot spots:
(a) for ASO-X without POS, (b) for ASO-X with POS

5. Conclusion

The behavior of the z-pinch plasma driven by ASO-X and the spatial distributions of the hot spots are investigated in different current waveform controlled by the plasma opening switch.

In the case of plasma driven by slow current, the kink instability was often observed. The hot spots are distributed near the anode and some hot spots are off the z-axis due to the kink instability. On the other hand in the case of plasma driven by fast current, the plasma column was formed more stably and the hot spots are distributed along the z-axis. Therefore, the fast current provided by the ASO-X with POS suppresses the kink instability and improves the uniformity of the z-pinch plasma.

References

1) J. Shiloh, A. Fisher, and N. Rostoker, Phys. Rev. Lett., 40 (1978) 515.

2) M. Badaye, R. Stempork, and R. P Gupta, Rev. Sci. Instrum. 61 (1990) 1457.

3) J. Bailey, Y. Ettinger, A. Fisher, and R. Feder, Appl. Phys. Lett. 40 (1982) 33.

4) J. Du, T. Ohata, K. Shimoda, and K. Hirano, Jpn. J. Appl. Phys. 64 (1995) 4185.

5) K. Takasugi, H. Suzuki, K. Moriyama, and T. Miyamoto, Jpn. J. Appl. Phys. 35 (1996) 4051.

6) K. Murayama, T. Shinkai, S. Katsuki, H. Akiyama, Jpn. J. Appl. Phys., 37 (1998) 2676.

7) K. Murayama, T. Nishi, S. Katsuki, I.V. Lisitsyn, H. Akiyama, Proc. of The Korea-Japan Joint Workshop on Plasma Technology and Application, EP-98-80 (1998).

Soft X-ray emission in the neon gas puff plasma focus

Takashi NAKASENDO, Haruhisa MARUYAMA, Yasushi ONO, Hiroyuki MAEDA, Katsuji SHIMODA, Takeshi YANAGIDAIRA and Katsumi HIRANO

Department of Electronic Engineering, Gunma University Kiryu, Gunma 376-8515, Japan

In a plasma focus with neon gas puff, correlation between the dynamic behavior of the plasma and the soft x-ray emission is discussed experimentally. Intense H-like and He-like lines of Ne ions were radiated in the period in which the pinched plasma sustained stably by visible streak mode observation. The emission ended with the extinction of the visible light. In the period, however, growth of macroscopic instabilities seemed to be $m = 0$ type were observed with the multi-framing soft x-ray camera. The soft x-ray emission began with the generation of the instabilities and ended with the disruption of the pinched column. The peak of the soft x-ray emission coincided with the micro-pinch generated in the plasma column. The electron temperature and density which were spectroscopically obtained were $\sim 2 \times 10^{21}$ and ~ 0.5 keV at the peak of the soft x-ray emission.

KEYWORDS: soft x-ray, z-pinch, plasma focus, gas puff pinch, soft x-ray spectroscopy, imaging spectroscopy, high-speed x-ray framing mode photography

§1. Introduction

Intense, impulsive and small size soft X-ray sources have been required not only for the ICF with homogeneous irradiation of the X-ray [1], but also for high density lithography,[2] X-ray microscope and laser excitation.[3,4] Recently, the pulse power generator has widely been employed as a power source of the soft X-ray generator. The plasma produced gas puff pinch with the pulse power generator is fairly stabler than the gas embedded pinch. [5] The plasma focus facility is also capable to produce a dense and stable plasma when a working gas is puffed immediately before the plasma focus discharge and compressed by a plasma sheet generated with an ordinary plasma focus discharge.[6]

In the plasma focus facility, the current sheet already carries a heavy current at the start of the radial pinch phase, and so the current and its rise time can be sometimes equivalent to those of the pulse power generators. Therefore, using the plasma focus facility with the gas puff, it is possible to perform almost the same experiments which are usually made with the pulse power generators for the soft X-ray generation.

In the conventional gas puff device, in which the working gas is cylindrically puffed between the electrodes, the pressure distribution concentrated on the side of the puffed gas cylinder is hardly obtained. In the plasma focus facility, a very thin current sheet is easily formed and the puffed gas can be compressed by the current sheet in the radial collapse phase.

When a gas is puffed through the inner electrode,[6)] the gas expels the embedded gas and fills the space in front of the inner electrode of the plasma focus facility. Then, the puffed gas is compressed and heated up to extremely high density and temperature by the current sheet. When a high Z-gas is employed as a puffed gas, the soft X-rays of K shell lines and L shell lines are easily generated. We have carried out experiments to characterize the soft X-rays with Ne and Ar so far. In the previous papers, we pointed out that the soft X-rays including K shell lines were generated before the disruption of the pinched plasma column when Ne was puffed.[7)] On the other hand, when Ar was puffed, the soft X-ray generation occurred at the disruption.[7)]

In this paper, we intend to make the mechanism of the soft X-ray generation clear by a simultaneous measurement with an imaging Bragg spectrometer,[8)] a high speed imaging system for visible and soft x-ray in streak mode,[9,10)] an image converter camera of visible light, a soft x-ray framing camera which is able to take successive four frames and a pinhole camera which enables to evaluate soft X-ray emission quantitatively.

§2. Apparatus

2.1 Plasma focus facility with gas puff

A Mather type plasma focus facility was used to generate a current sheet for compressing puffed high Z gases.[6)] The outer electrode of the facility is squirrel cage type. The diameters of the inner and the outer electrodes were 50 and 100 mm, respectively. Their lengths were 280 and 230 mm, respectively. The condenser bank consisted of $28 \times 1.56\,\mu$F, 80 kV capacitors. The facility was operated at the bank voltage of 45 kV and the bank current was estimated to be ~1 MA at its maximum. In the plasma focus device, an extremely rapid rising current can already be prepared at the beginning of the radial collapse phase because the plasma carries already a heavy current, that is nearly its peak at that time.

Neon was puffed with a fast acting valve through the inner electrode immediately before each discharge. The hydrogen base pressure of 5.0 Torr. and the neon plenum pressure of 3 atm were employed.

The schematic diagram of the plasma focus facility and the diagnostic tools which are viewed from the electrode axis are shown in Fig. 1.

2.2 Diagnostic tools

A variety of diagnostics are employed to clarify correlation betweeen macroscopic behavior of the pinched plasma and the soft X-ray emission. Diagnostic tools such as a high speed imaging system in streak mode which enables to record the X-rays and the visible light, an imaging Bragg spectrometer, an optical image converter camera in streak mode and the soft x-ray framing camera taking successive four frames are simultaneously used. The alignment of the tools also shown in Fig. 1.

2.2.1 Neutral gas probe

Density distribution of puffed Ne gas with time variation was measured with two movable pressure probes. A pressure transducer, XCQ-062-25A manufactured by Kulite semiconductor is installed in each probe. The frequency response of the probes including the transducer, the cable and the scope is better than 100 kHz.

2.2.2 Two channel imaging system in streak mode

The imaging system which has two channels an X-ray and a visible channel in streak mode is described in previous papers.[9,10] The system, which consisted of a combination of an microchannel plate (MCP) pinhole camera and a 10-channel arrayed PIN diode detector (International Radiation Detectors, AXUV-10EL), was operated to compose streak mode picture. In the X-ray channel, combination of the arrayed detector and the Be foil filter (25 μm in thickness) gives a spectral band for the soft X-ray imaging system between 1 $\sim$ 15 Å, which includes the spectral lines [NeX 12.19 Å (H-like Lyman α), NeIX 13.447 Å (He-like resonance line) and NeIX 13.549 Å (He-like intercombination line)] and continuous radiation ranging 8$\sim$9Å. In the visible channel, an IR cut resin filter (Kureha Chemical Industry, UCF-02) was mounted instead of the Be filter for x-rays.

Using the analog signals obtained from the arrayed detectors and the pinhole image taken by the pinhole camera, the time and spatially resolved X-ray image is restructured by the inversion technique. The system records the time variation of X-ray and the visible light intensity through the slit which is mounted in parallel to the electrode axis.

2.2.3 Image converter camera for visible light

An image converter camera (Hadland Photonics IMACON700) operating in streak mode was employed in order to observe the macroscopic behavior of the plasma. The camera viewed two regions of 4.0 and 9.0 mm from the inner electrode face through slits, 100 μm in width and mounted perpendicular to the electrode axis whereas the high speed imaging system mentioned in 2.2.2 observed through slits which were mounted in parallel to the axis.

2.2.4 Imaging Bragg spectrometer

An imaging Bragg spectrometer was constructed to analyze the soft x-ray emitted from the pinched plasma. An RAP (rubidium acid phthalate, $2d = 26.12$ Å) convex crystal with the diameter of 12.5 mm was installed, was employed in this spectrometer.[8] For the imaging, an entrance slit of 100 μm and 5 mm in width and length was used. The spectrometer was capable of collecting X-ray spectra in a 3 $\sim$ 20 Å region with the resolution power of > 600 and the dispersion of $< 1.1 \times 10^{-1}$ Å/mm. In this spectrometer, a pinhole image was simultaneously recorded with the spectral data on the same film. The pinhole image provided the base line to measure the wavelength. As the pinhole was installed on the slit plane, a precise identification of the wavelength was carried out, in spite of fluctuation of the X-ray source location from shot to shot. A Kodak TRI-X film is employed as a recording medium.

For a time resolved measurement of the spectral lines, X-ray sensitive PIN diode arrays (also International Radiation Detectors AXUV-10EL) for the soft X-ray detection were mounted at the locations at which the spectral line images were formed. When detection by the PIN diode was carried out, the photographic film was removed. In this experiment, the line emissions of NeX 12.19 Å (H-like Lyman α), NeIX 13.447 Å (He-like resonance line) + NeIX 13.549 Å (He-like intercombination line) and off line X-rays near the spectral lines were observed. Each PIN diode array was mounted so as to accept the spectrally analyzed images and the background X-rays at 4.0 and 9.0 mm from the inner electrode face.

2.2.5 Framing mode X-ray camera

An X-ray framing camera available for taking successive four frames is developed to observe macroscopic behavior during the soft X-ray emission from the pinched plasma.11) The camera consists of a pinhole array, Be foil filter, a microchannel plate and a CCD camera with which the soft X-ray images of plasma are recorded. The X-ray images are projected on four strip lines which are made from gold thin film on the MCP. These strip lines can be gated independently by four pulses. The interframe time and the exposure time are 2.5 ns and 0.22 ns, respectively. The spatial resolution of the camera system including the CCD camera is 90 μm. The combination of the Be and Ag foil filters (25 μm and 1 μm in thickness) and the MCP gives a pass band between 3 and 14 Åwhich accepts He-like and H-like spectral series of Ne. Characteristic of the framing camera is described in a previous paper precisely.11)

2.2.6 MCP pinhole camera

A soft X-ray pinhole camera with a quantitative image acquisition system has been developed for soft X-ray image observation with time resolution.12) A pinhole image of the X-ray source is made on the MCP through a pinhole and Be-Ag combination foil filter (25 μm and 1 μm in thickness, respectively) which prevents the visible light also emitted from the source. The combination of the filters and MCP gives a pass band between 3.7 and 7 Å, which accepts the wavelength of interest in the soft X-ray source. Using the MCP system we can evaluate in situ a number of photons which pass through the pinhole after taking absorption by the metal foil into account.

2.2.7 Auxiliary tool

The soft X-ray emission was monitored with an X-ray sensitive PIN diode which was coupled with a Be foil filter of 25 μm in thickness. The viewing field of the diode was limited by a collimator to observe only the plasma produced by the discharge.

§3. Results and Discussion

3.1 Density distribution of puffed N_2 gas

Spatial distribution of the puffed N_2 gas density at the beginning of the plasma focus discharge is shown in Fig. 2. We can calculate the line density of Ne atoms which is an initial condition of the discharge to be $\sim 1.0 \times 10^{18}$ /cm. The line density is comparable to fibers in fiber pinch experiments such as C, Al, W and cryogenic D_2 of several tens of μm in radius.

3.2 Evaluation of the plasma parameters

Figure 3 a) shows a typical example of the time integrated spectrogram. In order to identify wavelengths in the spectrogram, the spectrum on the photographic film was scanned with a scanner (EPSON FS-1200WINP). The results which integrated in axial direction are displayed in Fig. 3 b). With this results we can evaluate plasma parameters such as the electron temperature and density which are time integrated but radially resolved. The H-like Rydberg transitions in NeX 1s-np series were observed for $2 < n < 7$ in this shot, whereas He-like NeIX $1s^2$-1sn'p series were detected for $2 < n' < 6$. The soft X-ray intensity is displayed in a linear scale in this figure. The upper detectable limit in both series gives an electron density estimate of $n_e \sim 1.5 \times 10^{22}$ and $4.7 \times 10^{22}\mathrm{cm}^{-3}$ for $n = 7$ and $n' = 6$ according to the series merging technique based on Inglis-Teller theory,[13] that is $\log(N\,\mathrm{cm}^3) = 23.26 - 7.5\log n + 4.5\log z$, where N is the ion density and z is the effective nuclear charge.

A continuous spectra was observed in 8~9 Åwhich is caused by the radiative recombination and Bremsstrahlung.[14] The plasma temperature was estimated from the logarithmic intensity variation of the free-bound continuum of hydrogen like ions ($\propto exp(-h\nu/kT)$). The continuum had a linear slope yielding a electron temperature of 0.43 keV.

Employing the intensity ratio method which is theoretically derived by Mewe[15] we can obtain the electron temperature. The calculated results of the relationship between an intensity ratio $I(\mathrm{H}Ly\alpha)/(I(w) + I(y) + I(z))$ and the electron temperature T_e is also given in Ref.15, where $I(\mathrm{H}Ly\alpha)$, $I(w)$, $I(y)$ and $I(z)$ are the intensities of NeX 1s-2p, NeIX $1s^2\,{}^1S_0$-$1s2p\,{}^1P_1$, NeIX $1s^2\,{}^1S_0$-$1s2p\,{}^3P_1$ and NeIX $1s^2\,{}^1S_0$-$1s2s\,{}^3S_1$, respectively. However, $I(z)$ was not recognized in the spectrum shown in Fig. 3 a). From our experimental results shown in Fig. 3 b), 0.57 keV is obtained for T_e at the peak of each line intensity which corresponds to the values on the electrode axis.

3.3 Correlation between plasma evolution and soft X-ray generation

Figure 4 shows an example of correlation between the plasma evolution and soft X-ray emission. In this figure, a) is streak photographs taken with the image converter camera by visible light through two slits mounted at 4.0 and 9.0 mm from the inner electrode face and in perpendicular to the electrode axis which are at the same axial locations as that of the PIN diodes mounted in the imaging spectrometer. In each figure, the plasma is constricted toward the electrode axis with the radial velocity of $\sim 2.5 \times 10^7$ cm/s and then forms a pinched column at t_{p1} and t_{p2}. After t_{p}'s the diameter become less than 1 mm. The column lasts for $\sim$ 20 ns after formation of the plasma column at each axial position. The visible light in the streak images is emitted from a dense pinched plasma and surrounding halo. Therefore the radius observed by the streak image is always larger than that of the image which recorded with the imaging spectrometer as shown in Fig. 3 a). Disappearance of the plasma column is caused by the disruption of the discharge current at t_{d1} and t_{d2} owing to development of macroscopic instabilities such as $m = 0$ type. The differences between t_{p1} and t_{p2}, and t_{d1} and t_{d2} caused by the zippering effect, that is, the pinch of the plasma begins near the inner electrode surface and develops along its axis.

In this figure, b) and c) are the streak photograph which are taken with the 2-channel imaging system recording visible light and the soft X-rays in each channel. The lifetime of the plasma by x-ray observation is estimated to be 7 ns in this shot and is shorter than that observed with the visible light at the same axial position as shown in Figs. 4 a) and 4 c). It should be emphasized that the soft X-rays are emitted only a short period before the disruption of the pinched column.

Any remarkable changes was not recognized in the streak mode photograph, Fig. 4 c) in this period. However, it was revealed that drastic variation in the soft X-ray framing photograph occurred. Fig. 4 e) shows the framing pictures in this period which were taken for four shots. They are selected from shots more than 30, considering reproducibility which is monitored with analog signals from X-ray PIN diode. The pictures are displayed according to the time sequence.

Figure 4 e) corresponds to the rise of the analog signals from the monitor photodiode as shown in Fig. 4 d). Radial spikes recognized in (1) is considered as the beginning of the $m = 0$ type macroscopic instabilities. As shown in (2), growth of the instabilities are still going on. A further pinch in a small regions, that is a micropinch occurs near the inner electrode. In the phase from (3) to (4), it is seen that a part of the micropinch is disrupted. (5) and (4) are taken almost the same timing (but (5) is seen to be a little earlier than (4)), and the location to be disrupt is wiggled and radiates the soft Xrays with high luminosity. (6) shows that the plasma column is disrupted at several locations. It can be understood the reason that some author claimed the current in the plasma column is strongly deformed like a fractral.$^{16)}$ The luminosity at that location becomes weaker and another micropinch occurs at the location further from the electrode face as shown in (7). In (8) the second micropinch reached nearly at its maximum, and the part with low luminosity spread along the electrode axis. The luminosity of the second micropinch gets stronger rapidly as shown in (9) and attains its maximum at (10). A bright ellipse arround the micropinch seems to be the scattered X-rays from the surrounding thin plasma and the micropinch is nearly disrupted. This frame coincides with the maximum of the soft X-ray analog signal with the PIN diode. Even in (11) a luminous part which is seemed to be the remains of the disruption is recognized. In the frames after (12), the luminosity decreased gradually and the plasma ceases the X-ray emission. As seen in Fig. 4 a) and c), the plasma also ceases emission of visible light almost at the same time.

Therefore, it is concluded that the soft X-ray emission in this experiment begins with growth of macroscopic instability the pinched plasma column is stably sustained for 25 ns apparently as shown in Fig. 4 a), then instabilities seemed to be $m = 0$ type grow. This situation quite differs from the Ar puffing in which the soft X-ray are emitted after the disruption of the plasma column by the $m = 0$ type instabilities. This remarkable difference is ascribed to the difference of energy to obtain the highly stripped state to emit K shell lines between argon and neon. When the working gas is neon, measured T_e is ~ 0.5 keV whereas T_e was measured to be 1.5 keV for Ar puffing.

The signal from the spectral ranges including NeIX (13.447 Å) $1s^2$-$1s2p\,^1P_1$ + NeIX (13.549 Å) $1s^2$-$1s2p\,^3P_1$, NeX (12.19 Å) 1s-2p and off line signals (trace #1, #3, #4, and #6) are shown in Fig. 5 a). On-line signals (trace #2 and #5) rose at almost the same time in the compression phase. The full width at half-maximum (FWHM) of pulse coincided with the duration of the X-ray emitting phase which was measured by the imaging system in streak mode as shown in Fig. 4 b). Therefore, it can be considered that the X-rays observed with the imaging system mainly consisted of line emissions.

We obtained a time variation of the electron temperature as shown in Fig. 5 b). In this calculation, we are obliged to ignore absorption of NeX 1s-2p and NeIX $1s^2\,^1S_0$- $1s2p\,^1P_1$ lines. The resonance lines, especially NeX (12.19 Å) 1s-2p line were subjected to strong absorption by the surrounding plasma. However, even if we assume absorption of $20 \sim 80\,\%$, which $0.22 \sim 1.6$ of the optical depth in the surrounding plasma, the electron temperatures ranging $0.5 \sim 0.8$ keV is calculated according by Mewe.[15)]

When argon was puffed, as reported already, the imaging spectrometer revealed that the hot spots were densely aligned along the electrode axis in the plasma even if the spectrally integrated pinhole image showed a filament-like X-ray source.[17)] This is ascribed to i) the zippering effect of pinched plasma and ii) successive growth of macroscopic instabilities which always occured immediately after each micro-pinch. A rather higher electron temperature ($1 \sim 2$ keV) of the hot spots generated in argon plasma have been obtained, whereas almost the same electron density as neon puffing, $\sim 10^{22}/\mathrm{cm}^3$, are observed.[17)] Puffed neon easily attains highly ionized states such as He- and H- like ions when the electron temperature is less than 0.5 keV. It is considered that plasma heating by the beam-plasma interaction caused by instabilities in argon puffing is not required by soft X-ray generation in neon.

3.4 The soft X-ray output

The average output of the soft x-ray was ~ 200 J into 4π sr. We also evaluated the X-ray intensity to be 20 mJ/cm^2 at output window which was mounted on vacuum vessel in perpendicular to the electrode axis and at 20 cm from the electrode face.

§4. Conclusion

Using the convex Bragg spectrometer, we obtained the monochromatic images of the soft x-ray emitting spots formed by the spectral lines of $2 \leq n \leq 7$ for the NeX Lyman series and $2 \leq n' \leq 6$ for the NeIX $1s^2$-$1sn'p$ series.

The time variation of the electron temperature was evaluated using the line intensity ratio of NeIX $1s^2$-$1s2p\,^1P_1$ + Ne $1s^2$-$1s2p\,^3P_1$, NeX 1s-2p. These signals rose almost at the same time and showed a similar time variation. The FWHM of line emission measured with the PIN diode array mounted in the spectrometer was $5 \sim 8$ ns. The pulse width coincided with the lifetime of the soft X-ray source in the plasma which was observed by the soft X-ray imaging system in streak mode. Comparison between the two streak mode observations showed that the emission of the soft X-ray started in the latter half of the sustaining time observed by the visible light in streak mode and extinguished almost at the same time with the visible image which shows the disruption of the pinched column.

We observed correlation between the macroscopic instability of plasma and the process of the soft X-ray emission with a soft X-ray framing camera which is available to take four frames in a shot. This proves that the growth of the macroscopic instability causes the soft X-ray emission in the Ne puffing.

The electron temperature and density of the hot spots were estimated by several methods. The plasma temperature was obtained to be ~ 0.5 keV and ~ 0.43 keV from the line intensity ratio and the the logarithmic intensity variation, respectively. The electron density was estimated to be $\sim 1.5 \times 10^{22}/\mathrm{cm}^3$ by the series-merging technique based on Inglis-Teller theory. From the Benett relation, the electron density of $\sim 2 \times 10^{21}/\mathrm{cm}^3$ was estimated using the experimental results such as the electron temperature, the plasma radius and the pinch current. Line density of the puffed neutral neon was 1×10^{18} /cm and is consistent with that calculated for the plasma radius (0.01 cm) at the peak of the x-ray emission.

---

1) R. J. Leeper, T. E. Alberts, J. R. Asay, P. M. Baca, K. L. Baker, S. P. Breeze, G. A. Chandler, D. L. Cook, G. W. Cooper, C. Deeney, M. S. Derzon, M. R. Douglas, D. L. Fehl, T. Gilliland, D. E. Hebron, M. J. Hurst, D. O. Jobe, J. W. Kellogg, J. S. Lash, S. E. Lazier, M. K. Matzen, T. A. Mehlhorn, D. H. McDaniel, J. S. McGurn, A. R. Moats, R. C. Mock, D. J. Murton, T. J. Nash, R. E. Olson, J. L. Porter, J. P. Quintenz, P. V. Reyes, L. E. Ruggles, C. L. Ruiz, F. A. Schmidlapp, J. F. Seamen, R. B. Spielman, T. W. L. Sanford, M. A. Stark, K. W. Struve, W. A. Stygar, D. R. Tibbetts-Russel, J. A. Torres, M. Vargas, T. C. Wagoner and C. Wakefield: *Extended synopses 17th IAEA Fusion Energy Conference*, International Atomic Energy Agency, IAEA-CN-69 (1998) 15.

2) J. S. Pearlman and J. C. Riordan: J. Vac. Sci. Technol. **19** (1981) 1190.

3) G. Schmahl, B. Niemann, D. Rudolph, M. Diehl, J. Thieme, W. Neff, R. Holz, R. Lebert, F. Richter and G. Herziger, in *Springer Series in Optical Sciences X-ray Microscopy III*, edited by A. G. Miche, G. R. Morrison, and C. J. Buckley (Springer- Verlag, Berlin, 1992), Vol. 67, p. 66.

4) J. L. Porter, R. B. Spielman, M. K. Matzen, E. J. McGuire, L. E. Ruggles and M. F. Vargas: Phys. Rev. Lett. **68**, 796 (1992)
5) J. Du, T. Ohata, K. Shimoda and K. Hirano: J. Phys. Soc. Jpn. **64** (1995) 4187.
6) H. Kitaoka, A. Sakurai, T. Yamamoto, K. Shimoda and K. Hirano: J. Phys. Soc. Jpn. **64** (1995) 4191.
7) T. Yanagidaira, T. Yamamoto and K. Hirano: To be published in J. Phys. Soc. Jpn. **68** 3 (1999).
8) K. Hirano, N. Hisatome, T. Yamamoto and K. Shimoda: Rev. Sci. Instrum. **65** (1994) 3761.
9) T. Yanagidaira, M. Sato and K. Hirano: J. J. Appl. Phys. **35** (1996) 5862.
10) T. Yanagidaira and K. Hirano: Rev. Sci. Instrum. **68** (1997) 3074.
11) B. Shan, T. Yanagidaira, K. Shimoda and K. Hirano: To be published in Rev. Sci. Instrum. **70** 3 (1999).
12) Y. Takahama, J. Du, T. Yanagidaira and K. Hirano: Rev. Sci. Instrum. **65** 8 (1994) 2505.
13) J. Richter: *Plasma Diagnostics*: ed. W. Lochte-Holtgreven (North-Holland Publishing Company, Amsterdam, 1968) p. 38
14) N. J. Peacock, R. J. Speer and M. G. Hobby: J. Phys. **B 2** (1969) 798.
15) R. Mewe: Solar Phys. **22** (1972) 459.
16) A. B. Kukushkin and V. A. Rantsev-Kartinov: *Extended synopses 17th IAEA Fusion Energy Conference*, International Atomic Energy Agency, IAEA-CN-69 (1998) 235.
17) H. Kitaoka, T. Yamamoto and K. Hirano: J. Phys. Soc. Jpn. **67** (1998) 481.

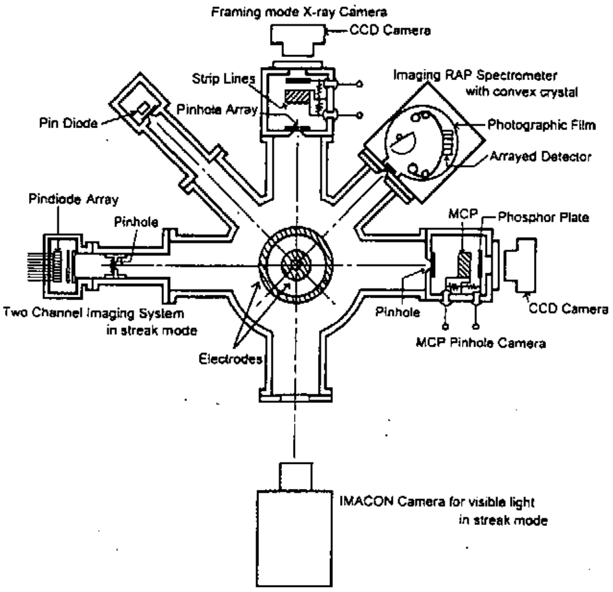

Fig. 1. Plasma focus facility and diagnostic tools.

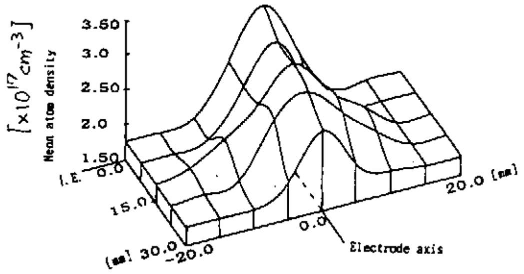

Fig. 2. Density distribution of puffed neon at the plasma focus discharge. I. E.: Inner electrode.

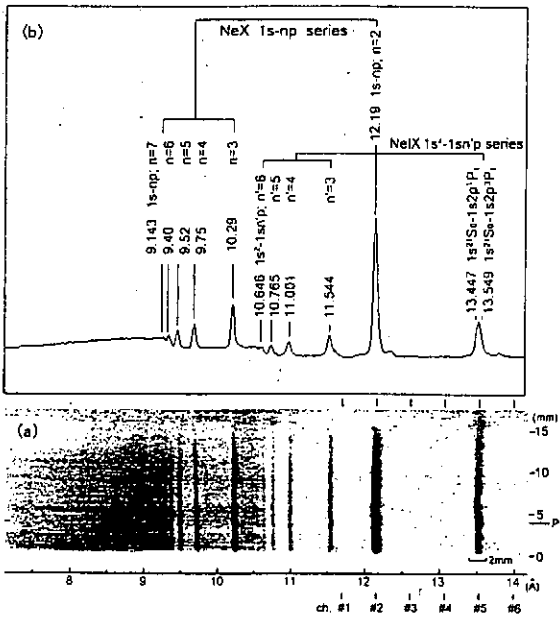

Fig. 3. Spectrum of neon plasma compressed by current sheet which is generated by the plasma focus discharge. a); Neon imaging spectrogram Ch. # 1-6 illustrate location of the active areas of the pin diode which employed to record the time variation of the spectral lines. b); spectrogram obtained by scanning a). Intensity is displayed in the linear scale.

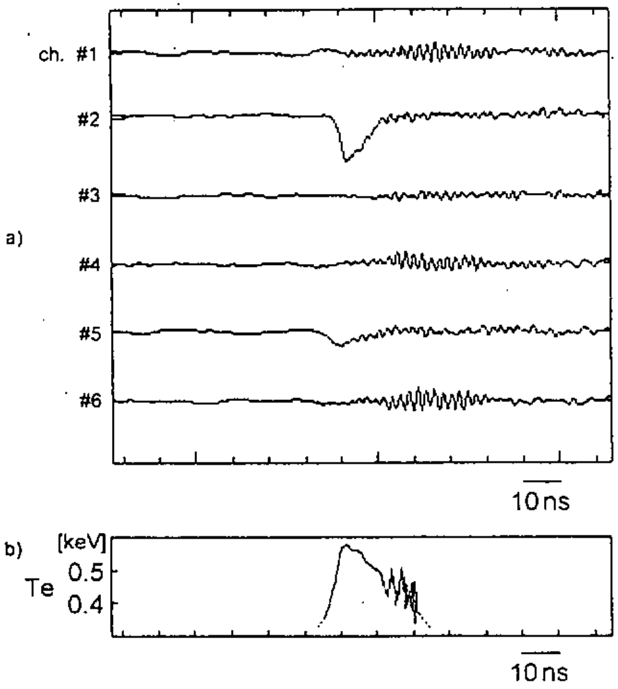

Fig. 5. a) Signals from the pin diode array which is mounted in the imaging spectrometer and channel # 2 and # 5 are located to accept the spectral lines of NeX 1s-2p 12.19 Å and NeIX $1s^2$-$1s2p\,^1P_1$(13.447Å) + Ne $1s^2$-$1s2p\,^3P_1$(13.549Å), as illustrated in Fig. 3a). b) Time variation of the electron temperature calculated from the signals of channels # 2 and # 5.

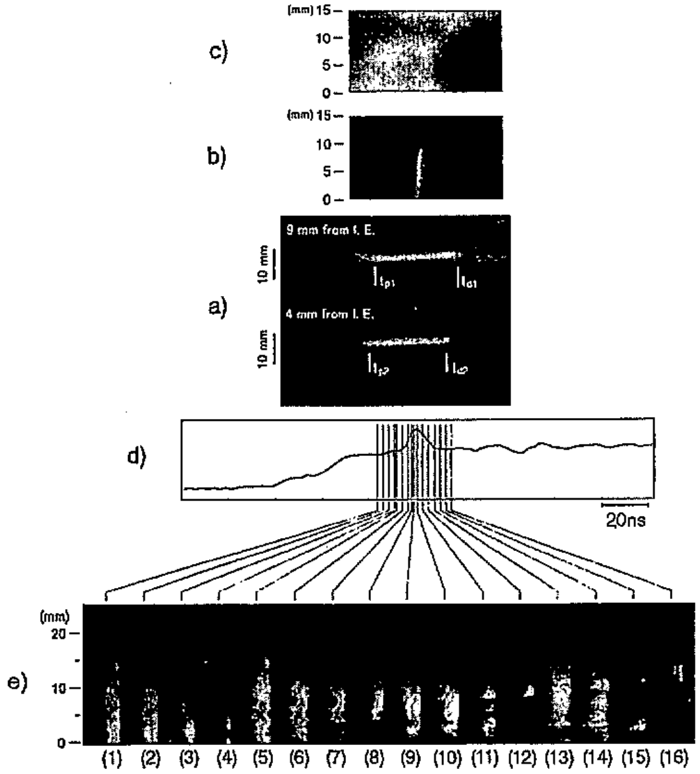

Fig. 4. Time correlation between the plasma behavior and soft x-ray emission of focused neon plasma. a) Streak photographs taken with the image converter camera in visible light through slits which are mounted perpendicular to the electrode axis and located at 4 mm, i) and 9mm, ii) from the inner electrode face. b) and c) are soft x-ray and visible streak photograph which are taken with the two channel imaging system through slits in parallel to the electrode axis. d) is an x-ray signal obtained with the x-ray sensitive pin diode. e) is the framing photographs taken with the farming mode x-ray camera.

Observation of x-ray emission and neutron yield from a compact plasma focus

A.Muravich, E.Baronova[*], Y.Mitamura, M.Lu[**], K.Sato, A.Baba, M.Horiuchi, K.Takasugi and T.Miyamoto

Nihon University, Atomic Energy Institute and College of Science and Technology
Kanda-Surugadai 1-8, Chiyoda-ku, Tokyo 101, Japan
[*] *Russian Research Center "Kurchatov Institute", Russia*
[**] *Hebei University, China*

§ 1. Introduction

Plasma focus geometry is interesting for generating not only conventional focus plasma but also several types of dense pinch plasmas. For example, dense sheet z-pinches can be produced, if plane electrodes are used instead of conventional cylindrical electrodes. The compact plasma focus device of Mather type was constructed for the producing of such a various dense plasma formation. Preceding the target experiments, we confirmed that the device could produce dense, hot plasma when the conventional cylindrical electrodes were used. In this paper, we describe the neutron and x-ray observations of this focus plasma that would be compared with the succeeding sheet z-pinch plasmas.

§ 2. Apparatus

The experiments were carried out on the plasma focus of Mather-type (Fig.1). The inner electrode (anode) length was 120 mm, diameter – 30 mm. The gas feeding system allows filling the chamber by mix of gases of two sorts with pressure higher than 0.4 Torr. The condenser bank consists of $6 \times 3.75\,\mu F$ capacitors with the maximum voltage 40 kV. Zero inductance of the arrangement is 27.8 nH. Typical maximum current was 3.0×10^5 A for the charging voltage 25 kV and the quarter period $\tau_{1/4} = 1.5\,\mu s$. In the present experiments the applied voltage was 25.0 ± 0.3 kV that corresponds to the total discharge energy 7.0 ± 0.2 kJ.

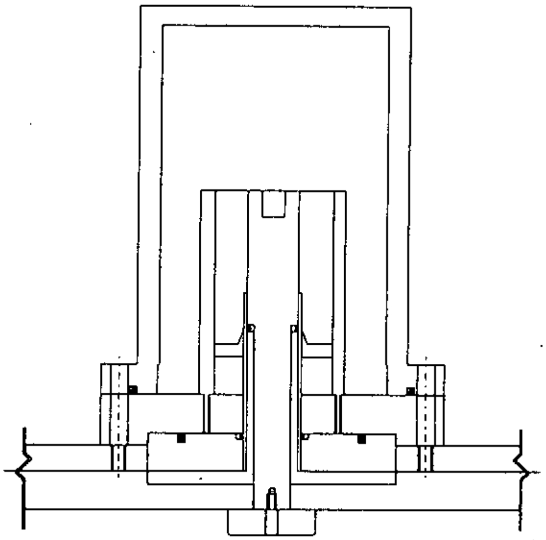

Fig.1. Scheme of the Mather-type plasma focus.

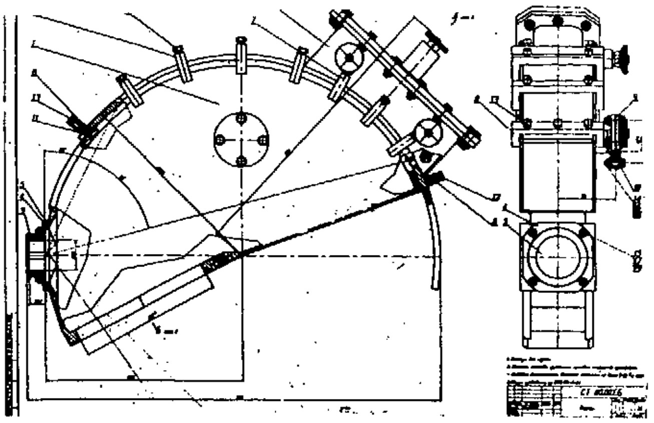

Fig.2a. Scheme of the x-ray spectrometer.

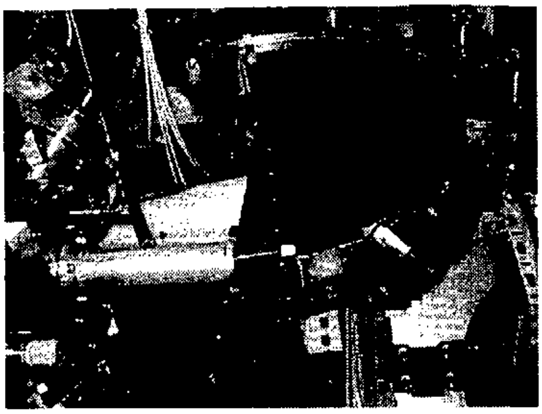

Fig.2b. Photograph of the x-ray spectrometer connected with discharge chamber.

X-ray spectrometer, soft x-ray pinhole camera (below SXR camera), neutron detector were used besides the current probes. X-ray spectrometer was created in the Kurchatov Institute (Moscow, Russia). Optical scheme of the device (Fig.2(a) and (b)) is similar to Iohann's one. The radius of Rouland circle is 250 mm and the range of reflecting angles is 20-80 degrees. Using of different x-ray crystals (with diameter up to 60mm) makes possible to analyze region of photon energies from 700 eV to several hundreds keV. Special technology was developed in the Institute of Crystallography (Moscow) to fabricate disperse element having both Iohannson's and Cauchois's properties. It is possible to use two crystals simultaneously, or to measure lines, reflected from two different reflecting planes of the same crystal. Using of a cassette film allows measuring spectra in 25-30 shots. It is also possible to use CCD, MCP, and framing camera to detect x-ray lines.

In the experiments spherical quartz crystal of Iohannson type was employed. Radius of the crystal curvature – 500 mm, lattice constant 2d=6,68 Å. Fuji x-ray film "AIF RX 50" was used for registration of the spectrum. Visible light was cut off by the $4\mu m$ Al + $12\mu m$ Mylar foil to decrease background spoiling of the film.

The SXR camera can take up to 24 images with magnification from 1:3 to 3:2. In the experiments we have used $200\mu m$ pinhole with the magnification 1:2 and 1:1.2, so the spatial resolution was about $600\mu m$ and $400\mu m$ respectively. X-ray passing through the pinhole was filtered by the $2\mu m$ Al foil therefore the SXR images are made by photons with the energies more than 1000 eV.

The silver-activated type neutron detector was used. The nuclei of Ag absorbing a neutron undergo β–decay with a half-life time depending on the isotope weight. Electrons produced in β–decay interact with plastic scintillator, and in turn produce photons that are registered by photo-multiplier. Signals of the photo-multiplier are amplified and then count by counter. The neutron detector was calibrated in the High-Energy Accelerator Research Organization (Tsukuba) using Am-Be neutron source.

§ 3. Results

§ 3.1. Current measurements

The typical signals of current *I* and its derivative *dI/dt* are shown in Fig.3. After the first *dI/dt* drop there is some pulsation of the signal during 600-700 ns and having the characteristic period 100-200 ns. The pulsation of *dI/dt* signal suggests that some secondary focus occur. As the time resolution of the Rogowskii coil estimated as less than 200 ns, the qualitative picture of the signal can be assured. However, quantitative values, for example, the amplitude of *dI/dt* will be not assured.

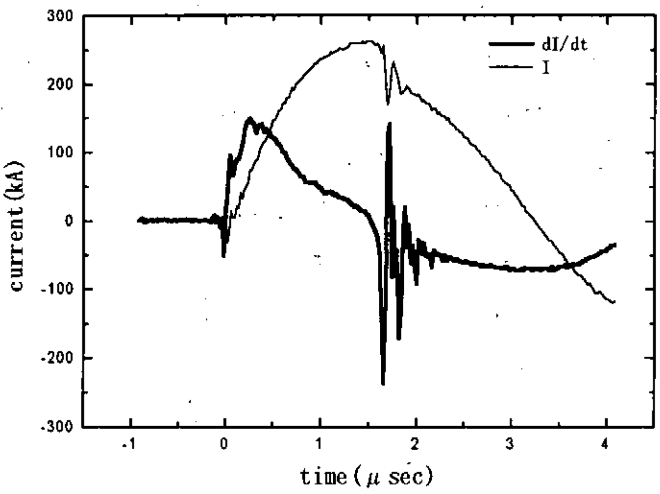

Fig.3. Signals of current *I* and its derivative *dI/dt*.

§ 3.2. Neutron measurements

The focusing time τ_f was determined as the period between the breakdown and the first current drop. The dependence of τ_f on the initial gas pressure is shown for deuterium in Fig.4. Characteristics of the focus strongly correlated with $\Delta_\tau = \tau_f - \tau_{1/4}$. If the absolute value of Δ_τ is relatively small (i.e., the focus occurs near moment of current maximum), the focus is considered to be strong. In the present experiments this condition was valid at the pressure range 4 – 7 Torr for the hydrogen and hydrogen and 5 – 8 Torr for the deuterium, respectively. Maximum

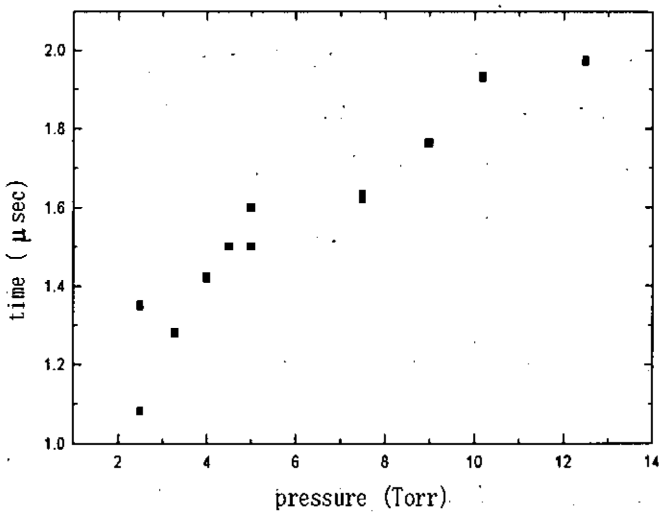

Fig.4. Time of occurrence of the focus versus deuterium pressure.

neutron yield from deuterium was observed at the pressure 6 – 8 Torr (see Fig.5). With increasing of $|\Delta_\tau|$ the current drop becomes smaller. In the best shots the number of neutron reaches 2×10^9. As angular anisotropy of the neutron flux does not taken into account, the yield is overestimated. The result was filled by the symbol ◇N in Fig.6, which was given by Michel et. al. The symbol ◇N₁ shows our result carried out alternatively using the 1 kJ plasma focus device. The neutron yield produced under an optimized condition of plasma focus was estimated by Vikhrev, assuming validity of the Bennett condition $\mu_0 I^2 = 16\pi NkT$ during the pinch phase which occur at the maximum current

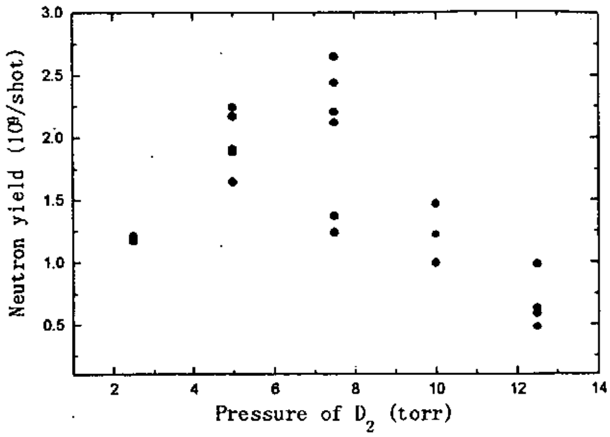

Fig.5. Dependence of the neutron yield on deuterium pressure.

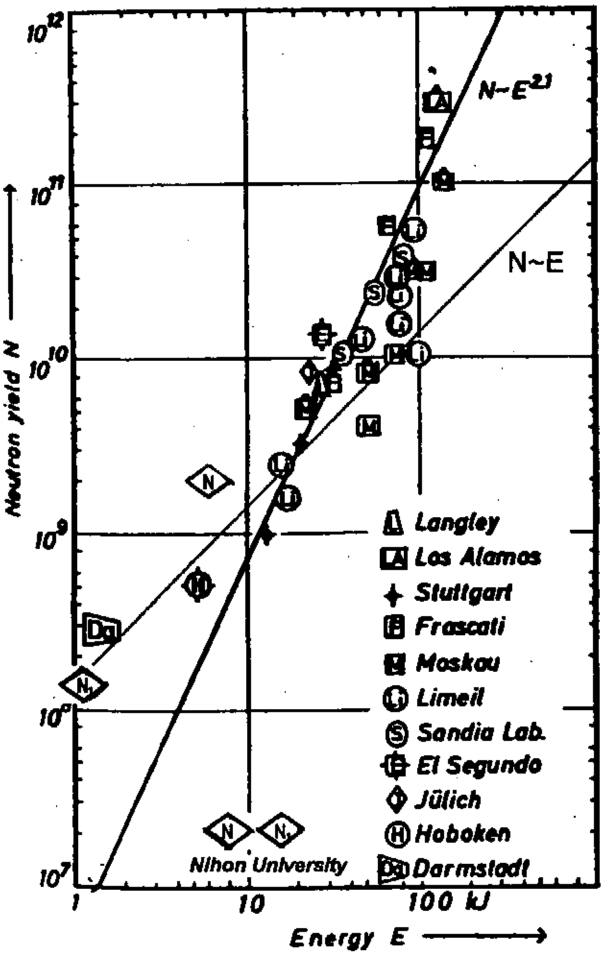

Fig.6. Neutron yield N against energy E.

$$I_{\max} \approx V\sqrt{C/L} = \sqrt{2E/L} = \sqrt{2E/(L_p+L_f)},$$

where E and L are the bank energy and inductance. The neutron yield due to thermal reaction is give as

$$Y_n^{(t)} = \int dt \int \frac{1}{2} n^2 <\sigma v> dV$$

$$= \frac{1}{3}\left(\frac{\mu_0 I_{\max}^2}{16\pi k}\right)^2 \int dt \int \frac{1}{S}\frac{<\sigma v>}{T^2} dz$$

$$\approx \frac{1}{3}\left(\frac{\mu_0}{8\pi kL}\right)^2 E^2 \int dt \int \frac{1}{S}\frac{<\sigma v>}{T^2} dz$$

On the other hand, the yield due to the beam-target model is given as

$$Y_n^{(b)} = \int dt \int n_b n <\sigma v>_b dV = \frac{\mu_0 I_{\max}^2}{16\pi k} \int dt \int \frac{n_b <\sigma v>_b}{T} dz = \frac{\mu_0 E}{16\pi k} \int dt \int \frac{n_b <\sigma v>_b}{T} dz$$

If the values of integral terms are approximately same at the optimized conditions of plasma focus devices optimized condition, the neutron yields based on both mechanisms are proportional to E^2 and E, respectively. Two lines drawn in Fig.6 are expressed these two relations.

§ 3.3. Measurements of the x-ray spectrum

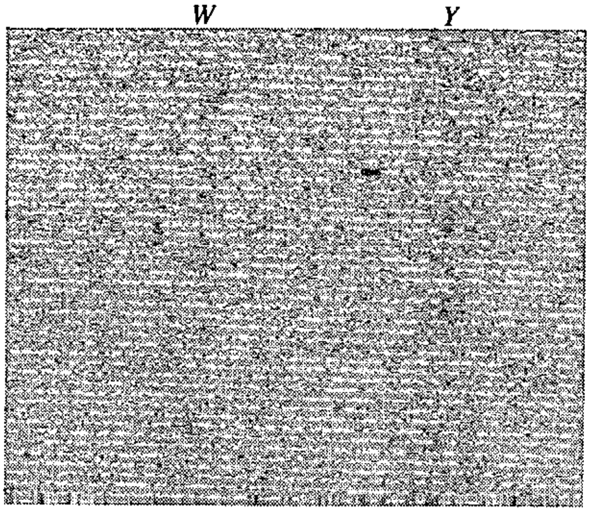

Fig.7. Images of *W* and *Y* lines obtained in a single shot.

Spectrum observation of the He-like Ar (Ar X Ⅶ) was provided. The wavelength of the most intensive (resonance) line λ_r is 3.94 Å. Basing on the Bragg's condition $m\lambda_r = 2d\sin\theta$, we set reflecting angle $\theta = 36.4$ degrees for getting the first order (m=1) spectrum. There were two factors that forced us to decrease intensity of registered x-ray radiation: plasma must not pollute the crystal and the x-ray film is strongly objected to spoiling by visible light. For this reasons two composite filters (each consists of 2μm Al + 2×3μm Mylar foils) were used for the protection of the crystal and diminishing of visible light, respectively. Mylar foils were necessary to prevent mechanical damage of Al foil. Despite the 3keV x-ray radiation was reduced approximately to one third by these two filters, it was strong enough to observe resonance line W (transition $1s^2$-$1s2p^1P_1$) and intercombination line Y ($1s^2$-$1s2p^3P_1$, etc) in the

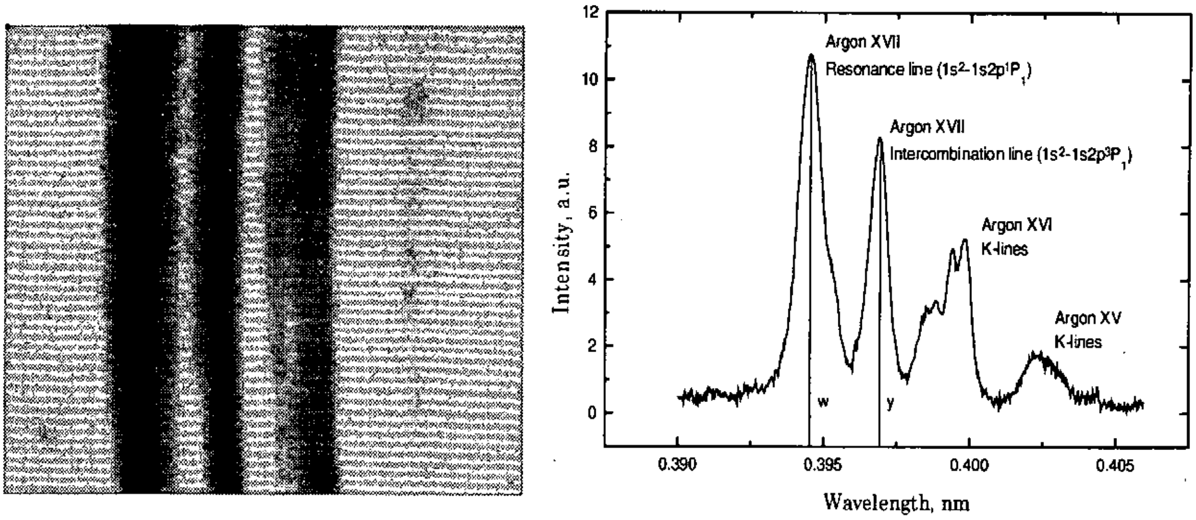

Fig. 8a and 8b. Photograph and profile of the spectrum obtained in 7 shots.

spectrum of single shots (Fig.7). In the total spectrum from 7 shots K-edges of ArXVI and ArXV are also could be clearly seen (Fig.8a). Profile of this spectrum (Fig.8b) shows good resolution of W and Y lines and gives an opportunity for the rough estimation of the hot plasma maximum density [3,4]. Interpolation of the W and Y lines by Gaussian profile gives the ratio of their intensities $R=I(Y)/I(W)\approx 0.53$. Basing on the assumptions of zero plasma opacity for the 3keV photons and local thermal equilibrium, the electron density in the emission points can be estimated as higher than10^{21} cm^{-3}. As could be seen from the pinhole photographs, only several hot spots having small-size (in the most cases one or two) radiate an x-ray harder 500eV. Proceeding from the presence of significant 3keV component in the radiation emitted by these hot spots we can estimate their temperature not less than 600-700eV.

§ 3.4. SXR pinhole photographs

At the plasma temperature of some hundreds eV the only mechanism of radiation for the both hydrogen and deuterium is bremsstrahlung, therefore the x-ray emission is weak and could not give an information about the plasma temperature. For this reason Ar was added as x-ray radiating matter in order to find hot plasma parts. Most of the Ar x-ray emission caused by the line radiation: L-shell lines (250-290 eV) and K-shell lines (3.1-3.3 keV). The L-shell radiation was cut by the filter (it was reduced by the factor more than 2×10^4), weakening of the K-shell radiation was about 1.5 times, so we suppose that all plasma images obtained by our pinhole camera are made by 3 keV photons of Ar K-lines. There were two series of the pinhole study of focus discharge. The first was performed with mix D_2 - Ar in order to find a correlation between structure and intensity of x-ray emission and neutron yield. In the second we tried to find maximum of the x-ray yield of mix H_2 - Ar depending on pressure and Ar mass concentration c_{Ar}. In the former there is some limitation on Ar concentration caused by decreasing of the average neutron yield with increasing c_{Ar}. In fact when c_{Ar} reaches only 10% the neutron yield decreases 3-4 times. For this reason in the case of D_2 - Ar mixture it was difficult to reach significant neutron yield and x-ray emission simultaneously. The obtained data don't demonstrate clear correlation between neutron yield and x-ray emission. In the latter it was found that strongest x-ray emission does not always occurs for small $|\Delta_\tau|$. From current measurements it was found that $|\Delta_\tau|$ is small for the hydrogen initial pressure region 4-7 Torr, but strongest x-ray emission was achieved at 8-11 Torr in spite of comparatively low current value in the time of focusing. We suppose it shows that increasing of the initial gas pressure causes growth of hot spot density but doesn't have so much influence on the hot spot temperature. Dependence of the x-ray intensity on the Ar mass concentration appears maximum at the c_{Ar}~25-30%.

§ 4. Summary

In the present experiments we obtained the following results:

1. Plasma focus device with I_{max}~3.0×10^5 A, dI/dt~2.2×10^{11} A/s and energy up to 7.0 kJ was constructed. Hot, dense plasma with $n_e \geqq 10^{21}$ cm^{-3} and temperature of several hundreds eV was produced.
2. Several types of diagnostics such as x-ray spectrometer, soft x-ray pinhole camera, neutron detector etc. were used to determine characteristics of produced plasma.
3. High-resolved spectrum of He-like Ar ions makes possible to estimate plasma temperature and density.
4. SXR pinhole observations of the x-ray yield from H_2 - Ar mix showed maximum of emission at Ar mass concentration 25-30% and pressure of mix 8-11 Torr. This pressure range differed from that for focusing at the current maximum (4-7 Torr).
5. Neutron yield from the pure deuterium has maximum pressure 6-8 Torr. In some shots it achieves value 2×10^9.

References

[1]. L.Michel, K.H.Schonbach and H.Fisher, "Neutron emission from a small 1-kJ plasma focus", Applied Phys. Lett., <u>24</u>(2), 57-59(1974).

[2]. V.V.Vikhrev, "Mechanism for neutron production in Z-pinches", Sov.J. Plasma Phys. 12, 262-270(1986).

[3]. A.V.Vinogradov, I.Yu.Skobelev, E.A.Yukov "About determination of the plasma density using He-like ions spectra", "Kvantovaya elektronika", Vol.**2**, №6 (1975), p.1165-1170 (in Russian).

[4]. F.B.Rosmej et.al "Soft x-ray spectra analysis in a high-current Z-pinch", AIP Conference Proceedings **299** (1994), p.552-559.

Electrostatic Control of Powder Injection for Z-Pinch Plasmas

Hidetoshi Ishihara, Yoshihiro Kawasaki, Mitsuhiro Sonoda, Shoichi Suzuki,
Yuan-Shing Liu, Koichi Yasuoka and Shozo Ishii
Department of Electrical and Electronic Engineering
Tokyo Institute of Technology
2-12-1 O-okayama, Meguro-ku, Tokyo 152-8552, Japan

Abstract

Electrostatic control methods of particle injection for the proposed new scheme of Z-pinch, powder Z-pinch, are discussed. The initial powder number density was shown to be controlled by varying the time constant of a voltage pulse for particle acceleration. A spatial distribution of injected powder flow is determined by the direction of particle velocity at injection hole. The direction can be controlled, when the electric field distribution between the acceleration electrodes is carefully designed. The tracks of powder particle motion were analyzed numerically in high electric fields to obtain appropriate electrode configurations.

1.Introduction

Z-pinch can easily generate high energy density and high temperature plasmas, and it concerned to use for efficient soft X-ray sources and nuclear fusion[1]. Z-pinch can be classified into two categories. Those are called dynamic and non-dynamic Z-pinch. The typical example of them are a gas-puff Z-pinch and a fiber Z-pinch, respectively. The advantage of the gas-puff Z-pinch is that dense plasmas can be created in a reproducible manner at the high repetition rate. Since puffing material must be gaseous state, solid elements are not applicable to the gas-puff Z-pinch. The fiber Z-pinch can also generate high density plasma from solid matter. However, it is difficult to set the fibers in the proper position between the main electrodes. We have proposed a new scheme of Z-pinch by solid powder injection that has both advantages of high repetition rate operation and having the high initial mass density. The principle of this scheme is that dense plasmas are created from powder accelerated and injected between the Z-pinch electrodes. The high voltage pulse is applied to the Z-pinch electrodes, immediately after the powder injection. The powder is evaporated and ionized in a high current discharge. High repetition rate operation is possible in the powder Z-pinch. Since almost every material becomes powder, spectra in the soft X-ray region emitted from the powder Z-pinch are expected to have wider range those from gaseous plasmas.

There are various methods for accelerating and injecting the powder. We choose electrostatic control of the powder having the advantage of easiness, compactness, good reproducibility, and to be operated in vacuum. In this paper, we examined some issues on the electrostatic control of powder injection for the Z-pinch. Varying the time constant of a voltage pulse for particle acceleration controls the injected powder number density. A spatial distribution of injected powder flow is determined by the direction of particle velocity at injection hole. The direction can be controlled, when the electric field distribution between the acceleration electrodes is carefully designed.

2. Experiments

(1)Experimental Setup

Spatial and temporal control of powder injection are required for the powder Z-pinch plasmas. The powder must be injected in a pulsed mode synchronizing with Z-pinch discharge. In addition, it is desirable that the powder injection system is small-sized and driven by a simple electrical circuit. The trial powder injection system was designed to be a parallel-plate type in order to examine controllability of the powder number density. Fig.1 shows the schematic diagram of the pulsed parallel-plate type powder injection system in which the circular shaped parallel-plate electrodes made of copper has a diameter of 100mm. An acrylic plastic cylinder with 5mm in height and the inner diameter of 80mm was used for an insulating spacer for the parallel-plate electrodes. The upper electrode has an injection hole with the diameter of 30mm. A stainless mesh electrode of 30 mesh to make a uniform potential gradient near the hole covers the hole. The powder used in this study consisted of copper particles with the diameter of 50μm.

When a pulsed voltage of -5kV was applied, the Coulomb force lifted the powder placed initially on the lower electrode upward. The pulsed voltages were generated by a CR discharge circuit composed of a capacitor *C* of 0.3μF, a resistor *R* and a gap switch. The discharge time constant τ was ranged from 3 to 60 ms by varying the resistance of *R*(=10, 50, 100, 200kΩ). The injection experiments were conducted in the air.

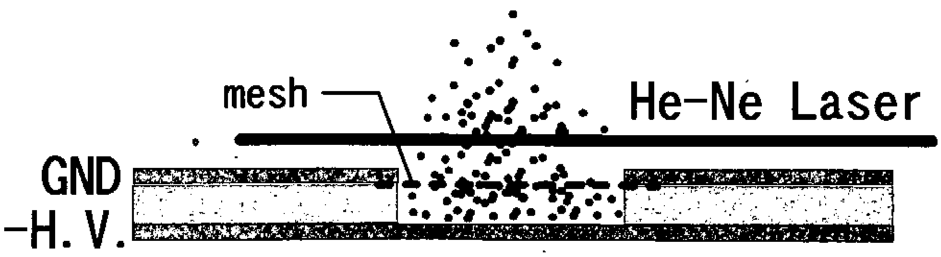

Fig.1: Experimental setup for the pulsed parallel-plate type powder injection system. The He-Ne laser beam is from right to left. The upper electrode has an injection hole with the diameter of 30mm because of apply the light attenuation measurement.

(2)Powder Number Density Measurement

The powder number density was obtained by measuring light attenuation of a He-Ne laser beam (λ=632.8nm) passing through the spouting powder[2]. The laser beam position was at 3mm apart from the upper electrode surface. When we measure the transmitted light intensity I_2 and I_1 through the region with and without powder, these intensities obey the Bouguer (Lambert-Beer) law,

$$I_2 = I_1 \exp\left(-nzA_p Q_{ext}\right) \tag{1}$$

where n, A_p, z and Q_{ext} are the powder number density, particle projected area ($A_p = \pi d^2/4$, d: particle diameter), beam path length in the powder, and the extinction coefficient, respectively. From the Mie theory we assumed $Q_{ext}=2$ for particles with the diameter of 50μm larger than the wavelength of the laser light of λ=632.8nm.

3.Trajectories of Injecting Particles

Behavior of injected powder particles can be predicted theoretically[2]-[6] by computing trajectories of moving particles. The trajectory can be obtained from the equation of motion with Coulomb force and viscous drag force.

$$m\frac{dv}{dt} = q\boldsymbol{E} - \left(m\boldsymbol{g} + 6\pi r\eta v\right) \tag{2}$$

where m $(= 4\pi r^3 \rho/3, \rho$: density), v, q, $\boldsymbol{E}$, $\boldsymbol{g}$, r and η are mass of a particle, velocity, charge, electric field, gravitational field, radius of powder particle and viscosity of air, respectively. When the powder particle is placed on the lower electrode, the inducted charge is given as follows[4],

$$q = \frac{2}{3}\pi^3 \varepsilon r^2 E_a = 4\pi\varepsilon r^2 E_a \times 1.65 \tag{3}$$

where E_a is the average electric field of V/L, where V is the applied voltage, and L is the electrode separation.

If the Coulomb force F_e is greater than the gravitational force F_g ($F_e > F_g$), the particle can detach from the lower electrode. After detachment, the Coulomb force drives the charged particle toward the upper electrode[5].

4.Results and Discussion

(1)Control of Powder Number Density

Fig.2 shows the temporal change of the applied voltages and the transmitted laser light intensities. The powder number densities are summarized in Table 1 for the discharge circuit time constants. Since the powder number density increased, as the time constant became longer, one can control the powder number density by changing the time constant.

The powder velocity at the mesh electrode and the transit time between the electrodes are both shown in Fig.3 for the powders with the diameter from 50μm to 300μm. In case of particles with the diameter of 50μm, they took 6ms to reach the mesh electrode. This shows that the time constant of 3ms is the shortest in our experiments.

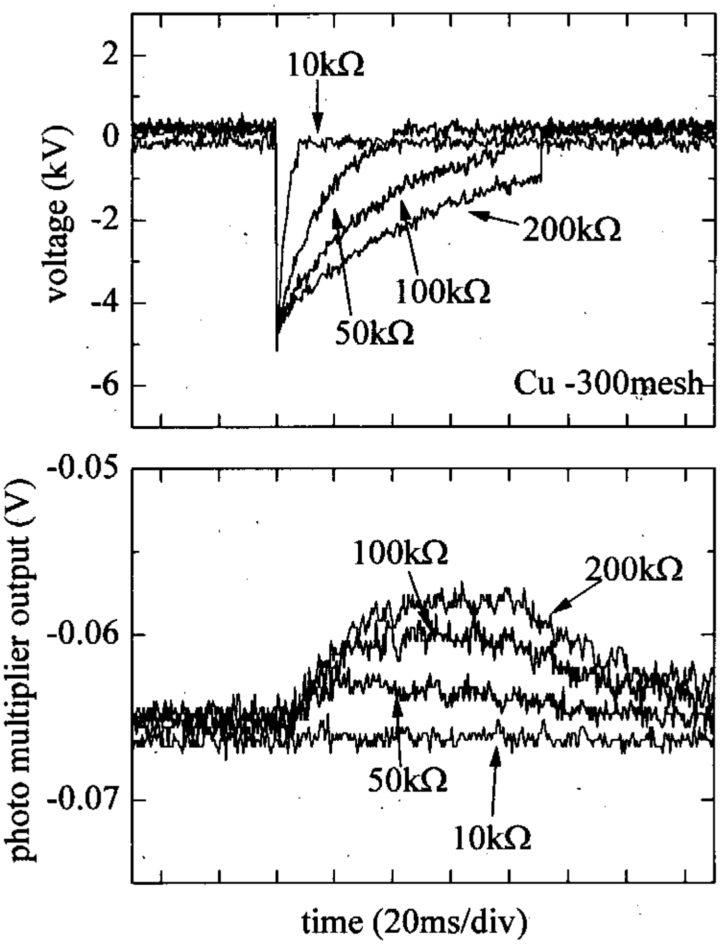

Fig.2: Temporal change of the applied voltages and the transmitted laser light intensities. Transmitted light intensity sets negative value. Large absolute value of PMT output shows intense intensity. Consequently, transmitted light intensity shows weakness because of attenuation by powder spouting.

Table 1: Powder number density by laser measurement.

Time constant (ms)	Transmittance (%)	Powder number density (cm^{-3})
3	--------------------------------	--------------------------------
15	95	4.4×10^2
30	92	7.1×10^2
60	89	9.9×10^2

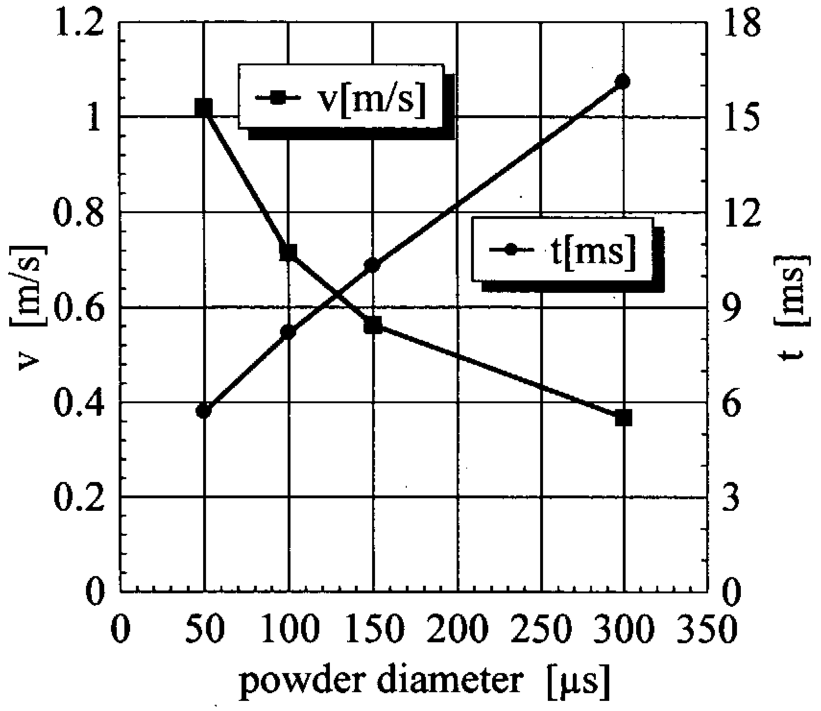

Fig.3: The change of powder velocity and transit time at the mesh electrode with the particle diameter.

(2)Analysis of the Parallel-plate Type Powder Injection System

Two-dimensional particle trajectories were obtained by solving equation (2) numerically. Since applied voltages and configuration of accelerating electrodes determine the trajectories, the numerical analysis of them is useful to design the powder injection system. Parallel-plate electrodes configuration is employed in the analysis. The injection hole at the center of the upper electrode has a diameter of 2mm. The electrode separation is 11mm. The applied voltage to the lower electrode is 8kV. We examined the influence of the viscous drag force on the particle trajectories by comparing the results in the air and vacuum. In both cases, the trajectories are similar for the particle with the diameter larger than 150μm as shown in Fig.4, in which the viscous drag force can be neglected. The electrode separation in dense Z-pinch is typically 10mm, so that we analyze the trajectories of the particle with the diameter of 150μm.

In the simple electrode configuration, a pair of plane electrodes, injected particles diverge to radial direction, that is not desirable for Z-pinch. Every trajectory of injected particles must be in parallel so that the diameter of powder flow is constant between the Z-pinch electrodes. The trajectory depends also on the initial particle position on the lower electrode. Fig.5 shows the trajectory of particles whose initial positions are different. The particles are bent owing to non-uniform electric fields near the injection hole as shown in Fig.6. The curvature for the particles placed initially far from the center is larger, because they pass near the edge of the hole where non-uniformity of the field is quite large. Fig.7 is a photograph of the divergent powder flow near the injection hole.

We can summarize the two issues to be solved for the powder injection system with parallel-plate electrodes for powder Z-pinch. Firstly, the divergent powder flow shown in Fig.8(a) must be improved. Secondly, since only the particles existing just under the hole of the upper electrode can pass through there, the ratio of the number of injected particles to that of initially present on the lower electrode is low as shown in Fig.8 (b).

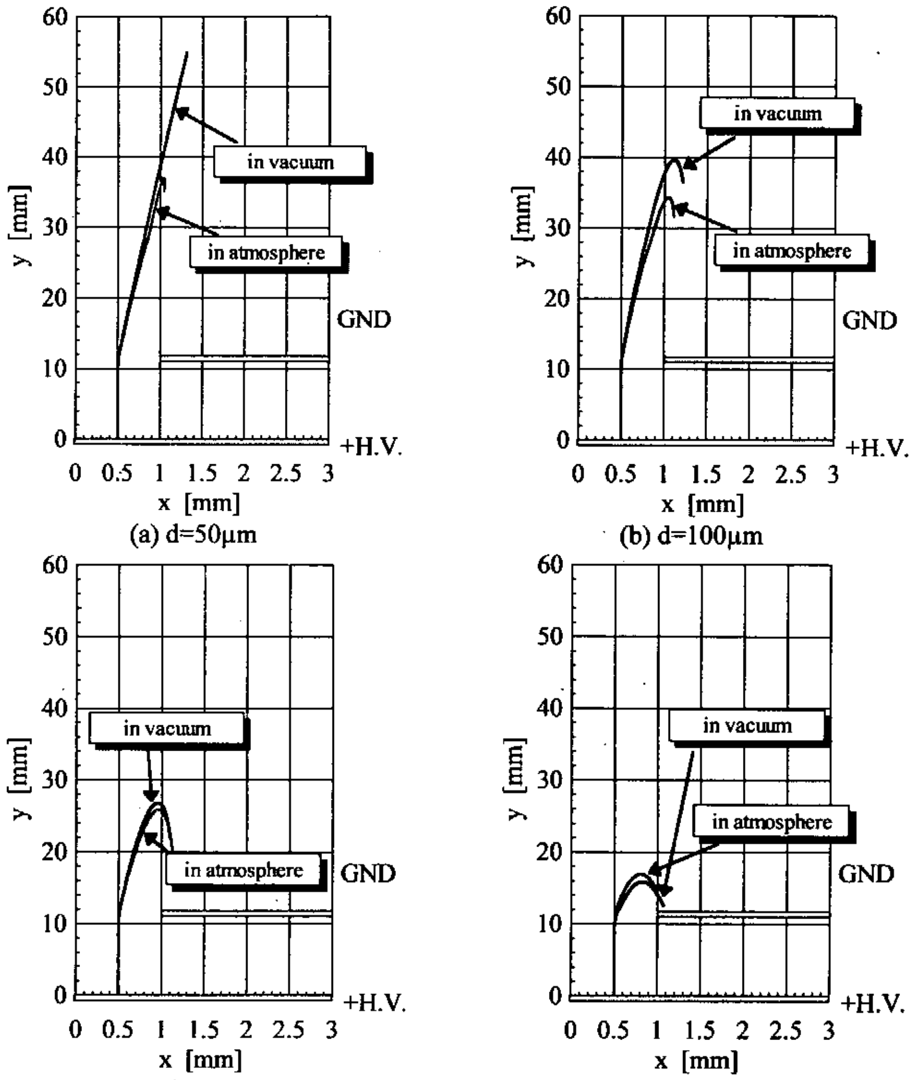

(a) d=50μm

(b) d=100μm

(c) d=150μm

(d) d=300μm

Fig.4: The influence of powder trajectories on the viscous drag varying the powder diameter. Both trajectories are similar for the particle with the diameter larger than 150μm.

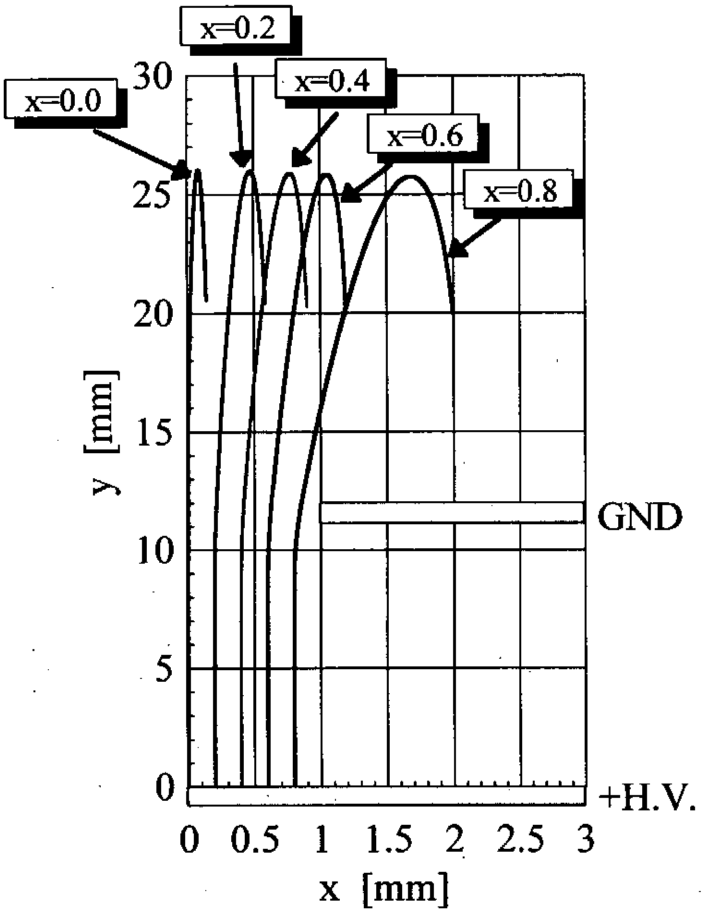

Fig.5: The influence of particle trajectories on the initial positions (copper powder, φ150μm). The injection hole at the center of the upper electrode has a diameter of 2mm. The electrode separation is 11mm.

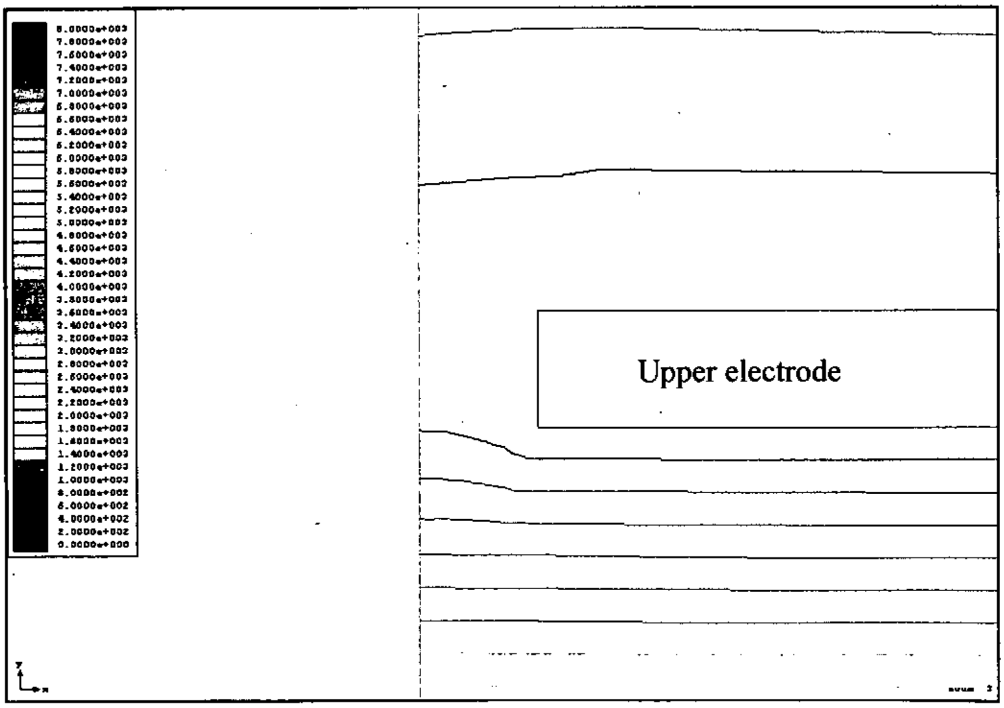

Fig.6: The electric potential near the injection hole.

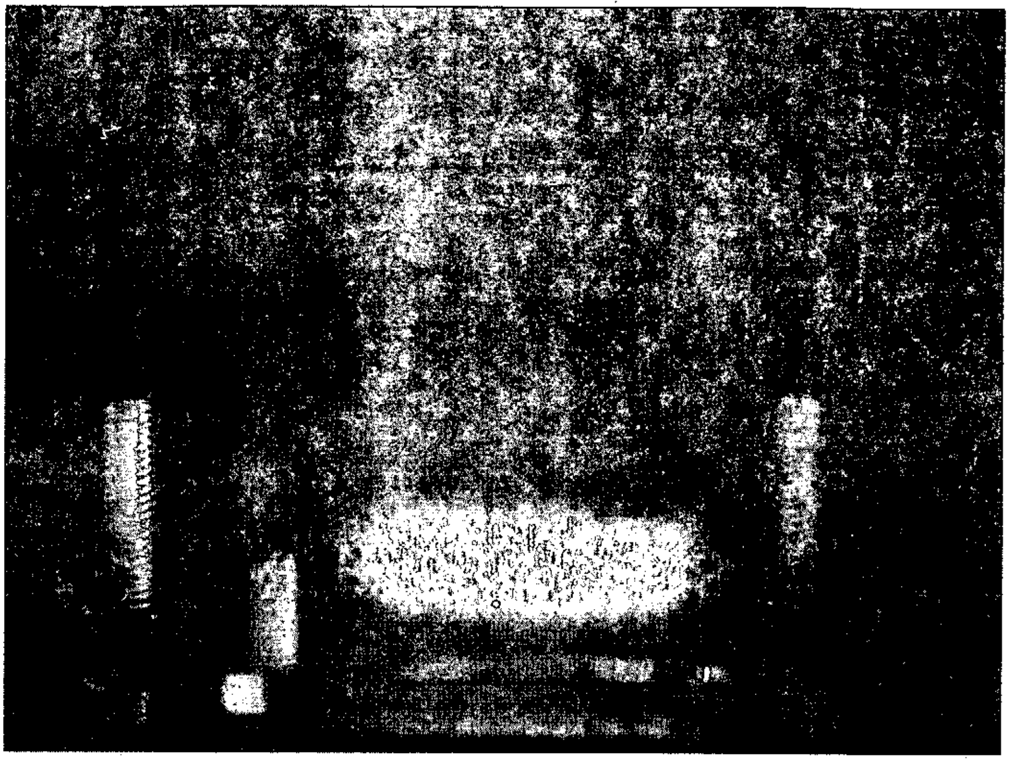

Fig.7: Photograph of the divergent powder flow near the injection hole because of non-uniformity electric field.

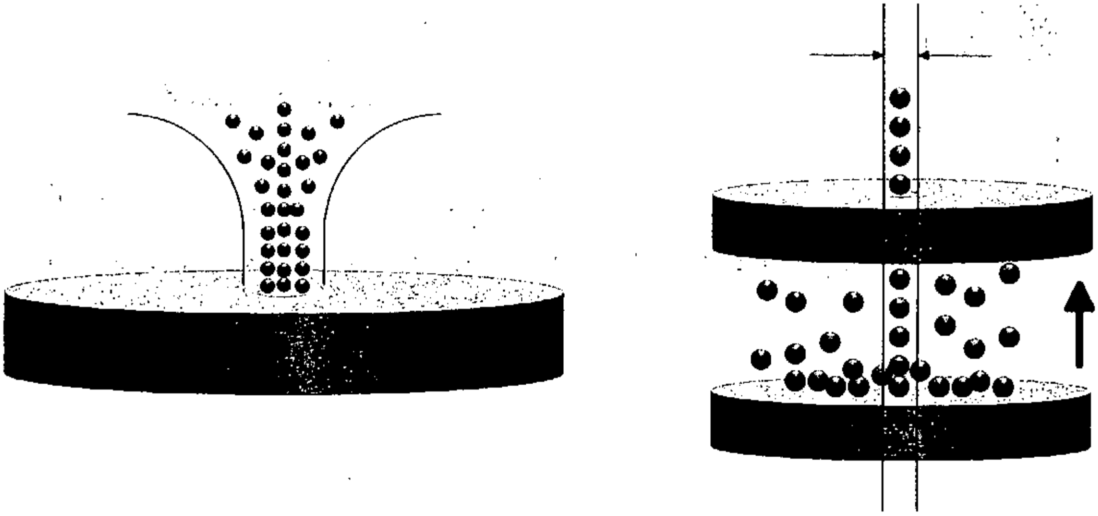

(a) Divergent powder flow

(b) Low powder spouting

Fig.8: The two issues in parallel-plate type powder injection system.

(3)Design of the Powder Injection System for Z-pinch

To overcome above mentioned problems, a focusing electrode is added between the parallel-plate electrodes. When the optimized voltages are applied to each electrode, the potential distribution between the electrodes becomes as shown in Fig.9.

The particle trajectories computed as before has a focused profile as shown in Fig.10. The particles are collected from wider radial position on the lower electrode. The focusing electrode controlled the trajectories and made the divergent profiles to be cylindrical. However, the maximum height of injected particles was reduced to about 30% of that without the focusing electrode.

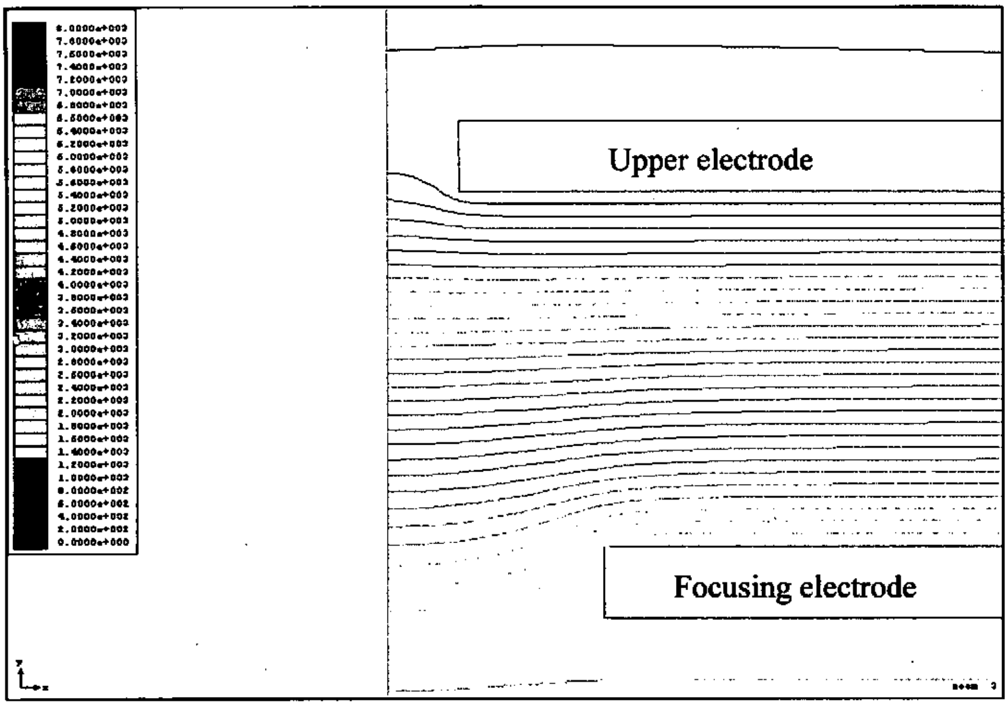

Fig.9: The electric potential near the injection hole adding the focusing electrode.

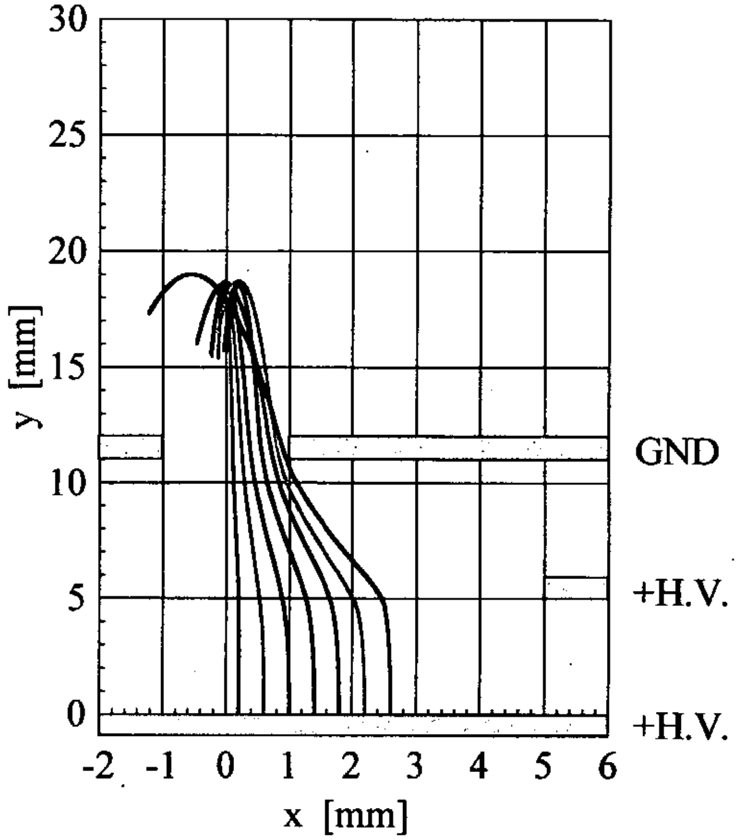

Fig.10: The influence of particle trajectories on the initial positions adding the focusing electrode (copper powder, $\phi 50\mu m$).

5. Conclusions

The control of powder number density for the Z-pinch has been established by using electrostatic control method. This method is useful for applied electrostatics in handling powder and or small particles. Results of the particle trajectories in high electric field by the numerical analysis have shown that focusing effect is enhanced by the additional electrode in parallel-plate type powder injection system. Moreover, it is quite possible to realize the appropriate powder injection system for the Z-pinch, when the electric field distribution between the acceleration electrodes is carefully designed.

References

[1] T. Miyamoto, J. Plasma Fusion Research, vol.74(8), pp. 855-76 (1998) [in Japanese].
[2] G. M. Colver and L. J. Ehlinger, IEEE Trans. Ind. Appl., vol.24(4), pp. 732-9 (1988).
[3] K. Asano, K. Yatsuzuka and Y. Higashiyama, J. Electrostat., vol.30, pp. 65-74 (1993).
[4] G. M. Colver, J. Appl. Phys., vol.47(11), pp. 4839-49 (1976).
[5] L. Dascalescu, M. Mihailescu and R. Tobazéon, IEEE Trans. Ind. Appl., vol.34(1), pp. 66-74 (1998).
[6] M. Glor, J. Electrostat., vol.15, pp. 223-35 (1984).

Breakdown Phenomena in Uniformly Distributed Powder

Mitsuhiro Sonoda, Yoshihiro Kawasaki, Hidetoshi Ishihara, Shoichi Suzuki,
Yuan-Shing Liu, Koichi Yasuoka and Shozo Ishii

Department of Electrical and Electronic Engineering
Tokyo Institute of Technology
2-12-1 Ookayama, Meguro-ku, Tokyo 152-8552, Japan

Abstract

We have proposed to use powder or fine particles instead of gases as an initial matter for plasma generation. Electrostatic handling techniques to make powder flow between discharge region were developed. The flow velocity and the powder number density were measured by employing laser light. Early phase of breakdown process in the air with powder was investigated.

1 Introduction

There are various advantages to use powder instead of gases as an initial matter for plasma generation. Applications of powder produced plasmas are space physics, high voltage insulation techniques, intense soft X-ray sources by Z-pinch, thin film formation in material science, decomposition of dust particles in semiconductor manufacturing process, and so on. However, few studies on plasma generation from powder are reported so far. Since powder is not easy to be put into discharge area as comparing with gases, one has to develop some experimental techniques for handling of powder to investigate physics of powder produced plasmas. We tried two schemes for handling of powder in discharge experiments, namely, ultrasonic vibration and pulsed electrostatic acceleration of powder. The ultrasonic vibration method enabled powder to flow smoothly through the nozzle connected to the discharge electrode. This was not suitable for pulsed discharge system in which precise fast synchronization between discharges and powder injection was required. In the pulsed electrostatic acceleration method, powder was lifted up by a pulsed electric field between electrodes that could not supply enough amount of powder for the experiments. Both methods were unpractical because of difficulty in controlling the powder number density and establishing a uniform powder distribution in the discharge region.

In this paper we report a new method to control powder and the experimental results on breakdown characteristics in the air with powder. The method is based on the principle that powder can be set in move by applying dc electric field uniformly between the electrodes. Electrostatic acceleration of powder by dc field is used in thin film deposition on the target [1]. Since the discharge volume is filled with powder in a steady state, spatial uniformity is better than by the ultrasonic vibration method. Pulsed powder injection can be accomplished by adding auxiliary electrodes to control powder motion electrically. The flow velocity and the powder number density were measured by employing a He-Ne gas laser and a high-speed video camera. The breakdown voltage dependence on the radius, materials, the polarity, and the powder number density was examined in the air with uniformly distributed powder.

2 Powder supplying system

A four electrodes powder supplying system was made to characterize parameters governing the powder motion. Plane-to-mesh acceleration electrodes were chosen for the system as shown in Fig.1. Fig.2 shows photographic view of the trial powder supplying system [2], [3].

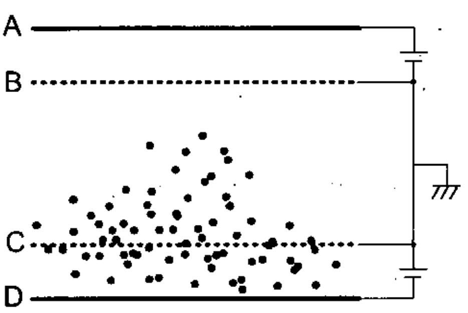

Fig. 1: Shematic diagram of powder supplying system

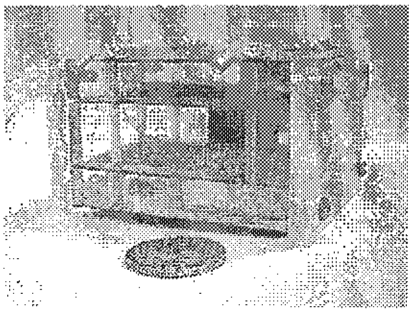

Fig. 2: Photograph of powder supplying system

The electrodes A and D are copper flat plates, B and C are copper meshes which are usually kept grounded or at the same potential. When a dc voltage is applied between electrodes C and D, the powder initially scattered on the plate D are charged by contact charging mechanism and are lifted up by Coulomb force. Some particles do oscillatory motion between C and D and some pass into the region B and C through the mesh electrode C. Since no electric field appears between B and C, electrodes for the breakdown voltage measurements will be placed in this region.

The average electric field at the surface of a spherical particle on the electrode is 1.65 times larger than that of ambient uniform electric field. The electric field at the surface gives the total charge Q of the particle which is written as [4],

$$Q = 1.65 \times 4\pi\epsilon_0 r^2 E_0 \tag{1}$$

where r is the radius of the particle, E_0 is the electric field between the charging electrodes, and ϵ_0 is the dielectric constant in vacuum. The minimum electric field to lift up a 50 μm copper particle is 2.23×10^5 V/m. It is 4.2×10^5 V/m for the 150 μm particle, which is smaller than the applied voltages employed in this study.

2.1 Powder number density measurement

The powder number density was obtained by measuring light attenuation of a laser beam passing through the volume filled with powder. The schematic diagram of laser light attenuation measurement is shown in Fig.3. The powder is assumed to have a uniform distribution in the volume.

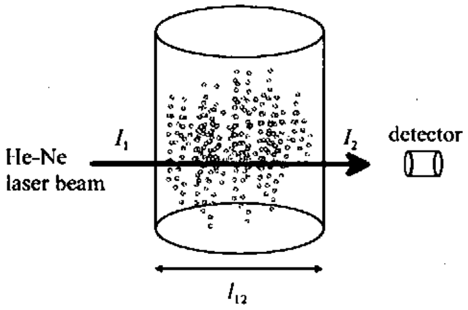

Fig. 3: Schematic diagram of light attenuation measurement

We assume that every particles have the diameter of D and laser light shadow of each particle does not cover the surface of other ones at the beam pass length of dl. The attenuation rate of incident laser intensity I can be expressed as

$$\frac{dI}{I} = -Q_{\text{ext}} \frac{\pi}{4} D^2 N dl \tag{2}$$

where N is the powder number density. The attenuation coefficient Q_{ext} is a constant depending on the particle diameter and material, and does not depend on the powder number density. We obtain the Bouguer-Lambert-Beer's law by integrating eq. (2).

$$-\ln \tau = -Q_{\text{ext}} \frac{\pi}{4} D^2 N l_{12} \tag{3}$$

where $\tau = I_2/I_1$ is the penetration rate, l_{12} is light pass length, and I_1 and I_2 are the incident and transmitted light intensity respectively. When the particle diameter is much larger than the wavelength of incident light, the attenuation coefficient Q_{ext} can be assumed to be 2 [5]. In this study, the particle diameter is typically about 100 μm that is larger than the He-Ne laser wavelength of 632.8 nm by the order of two. We can take $Q_{\text{ext}} \simeq 2$. By measuring the penetration rate, the powder number density can be obtained from the following relation,

$$N = -\frac{4 \ln \tau}{\pi - Q_{\text{ext}} D^2 l_{12}} \tag{4}$$

2.2 Control of powder number density

The spatial distribution of powder number density was measured by varying the position of incident laser beam which was described as the distance *h* from the electrode D in Fig.1. The diameter of laser beam was 0.7 mm. The powder is mainly accelerated by the electric field between the electrodes C and D. An additional electric field between the electrodes A and B can control the powder distribution. To confirm the effect of the field, the powder distribution was measured with and without the additional field. Both the electric fields were 6kV/cm. Fig.4 shows the results for the powder of copper particles whose diameter was about 150 μm. Fig.4 (upper) is the result without the additional field and (lower) is the one with the field. Since the additional field contributed to further acceleration, the powder distribution appears to be more uniform in Fig. 4(lower).

The acceleration voltage dependence on the powder number density was examined for the particles with various diameters. The powder particles employed had the diameters of 50 μm, 100 μm, and 150 μm. The results are shown in Fig.5. The powder number density was controlled by varying the acceleration voltages. For the breakdown voltage measurements on the particle diameter dependence, it is necessary to arrange the experimental condition in which the powder number densities are equal for the powders of particle with different diameters. The requirement is realized for the powders with the diameters of 100 μm and 150 μm powders when the acceleration voltages are critically adjusted. Since the powder number density of the 50 μm powder is much larger than that of others for the present voltage range, the above experimental condition cannot be satisfied.

The powder number density may depend on the total mass of powder initially placed on the electrode D. The dependence was measured by varying the initial mass of copper powder with the particle diameter of 150 μm. When the initial mass of powder was changed up to 0.5 g, the powder number density increased as shown in Fig.6. Further increase of the powder number density is not observed above 0.5 g. The physical explanation for the saturation in the powder number density change has not been obtained yet.

3 The velocity of accelerated powder

The powder flow velocity was obtained from the track length of the laser illuminated powder particles recorded in one flame of a high-speed video camera. The measurement system with the high-speed video camera (Redlake Imaging Corp. MotionScope HR) having the recording rates ranging from 60 to 8000 frame/sec and the shutter speed from 1/60 to 1/80,000 sec are shown in Fig.7.

The tracks of copper powders observed at the shutter speed of 1/125 second are summarized in Fig.8 at the acceleration voltage of ± 7 kV. The illuminating laser

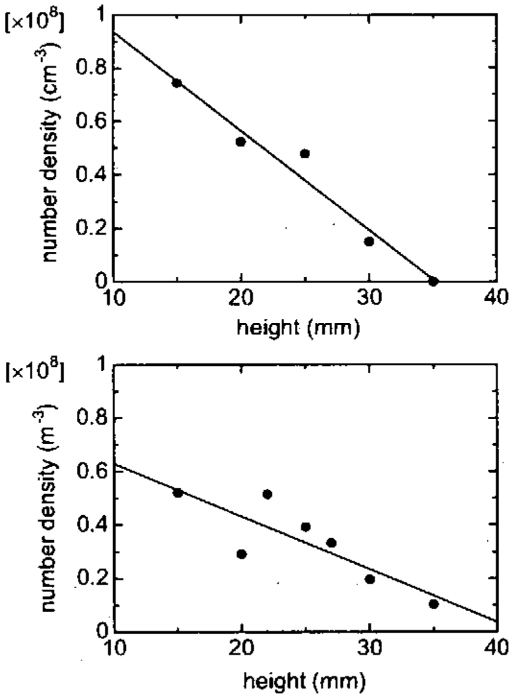

Fig. 4: Spatial distribution of powder number density

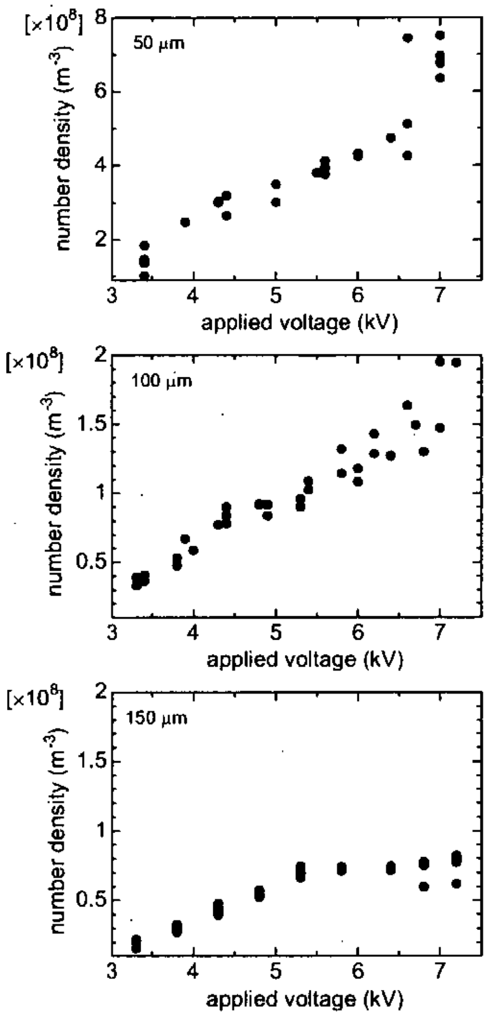

Fig. 5: Powder number density to the applied voltage between C and D

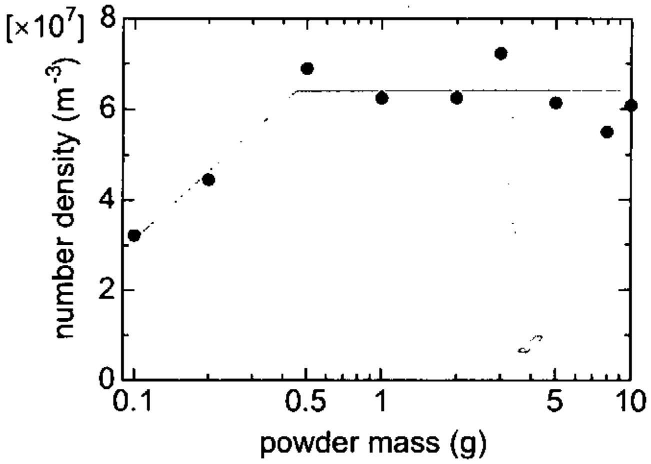

Fig. 6: Powder number density vs initial powder mass

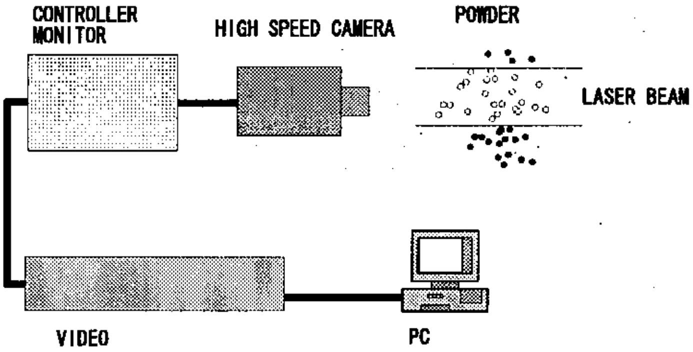

Fig. 7: Powder velocity measurement

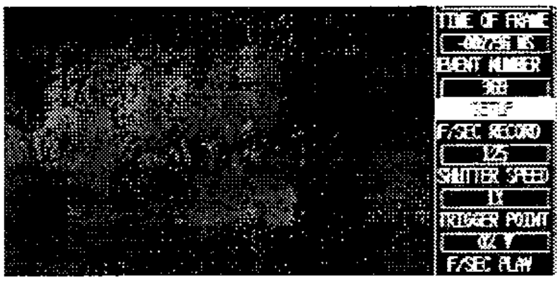

(a) -300 mesh
(50 μm)

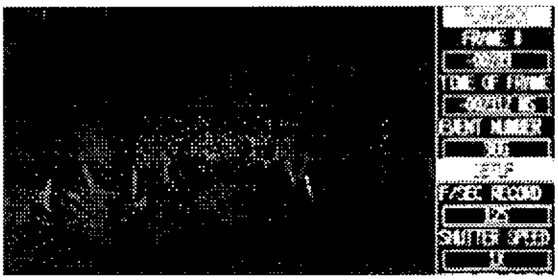

(b) -100 mesh
(150 μm)

(c) 0.3 mm

Fig. 8: Scattered image of copper particle

beam was expanded to have the diameter of 15 mm. The velocity was equal to the track length divided by the shutter speed. The average velocity of copper powder with the diameter of 150 μm are shown in Fig. 9. At the applied voltage of 7 kV, the velocity is 45 cm/s which agrees with the theoretical value based on Coulomb force. There existed particles to have extremely lower velocity than the average one described in Fig.9.

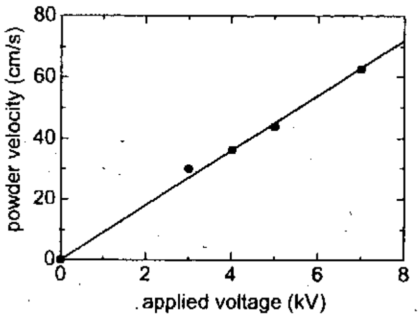

Fig. 9: Average velocity of copper powder with the diameter of 150 μm

4 The breakdown characteristics

One has to investigate discharge phenomena of the powder in vacuum to create powder produced plasmas. However, it is also important to investigate the discharge characteristics in the air with powder in order to obtain basic data for designing the plasma apparatus. Influences by powder in the air on the breakdown voltages were examined employing the chamber shown in Fig.1. A pair of rod electrodes with the diameter of 5 mm was inserted from both walls of the chamber. The particle diameter of powders examined was mainly 150 μm except for the measurement on particle diameter dependence. In the figures, the average breakdown voltages taken from five data are plotted.

4.1 Dependence on the powder number density

The powder number density is controlled by changing the electric fields between the acceleration electrodes AB and CD. When the discharge electrode gap length was changed, the breakdown voltages were measured with and without powder in the air. The results are summarized in Fig.10 when the powder number densities are varied. The breakdown voltages with the powder dropped down to 60 % of those without powder. In the present number density range, the breakdown voltage does not depend on the powder number density. This means that the breakdown voltage decreases as far as there exist a few powder particles.

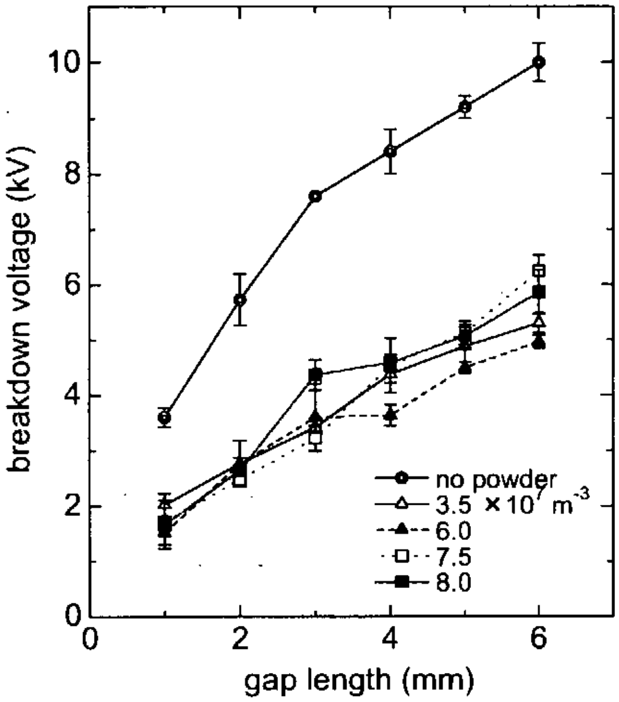

Fig. 10: Breakdown characteristics corresponding to the powder number density

4.2 Dependence on the particle diameter and material

The breakdown voltages are shown in Fig.11 for the copper particle diameters of 100 μm and 150 μm. The powder number density was kept constant as 6×10^7 m^{-3} for all measurements by controlling the acceleration voltage. The breakdown voltages do not depend on the particle size in the present diameter range.

Next, we measured breakdown characteristic changing particle material when powder number density was constant. Fig.12 shows the breakdown characteristics for copper and aluminum powder. The breakdown voltages do not depend on the powder materials.

4.3 Dependence on the polarity of particles and electrodes

Since the powder particles are charged in the acceleration region, the polarity of the powder will give some influence on breakdown voltage. The discharge electrodes were redesigned so that polarity effects could be clearly obtained. The experimental

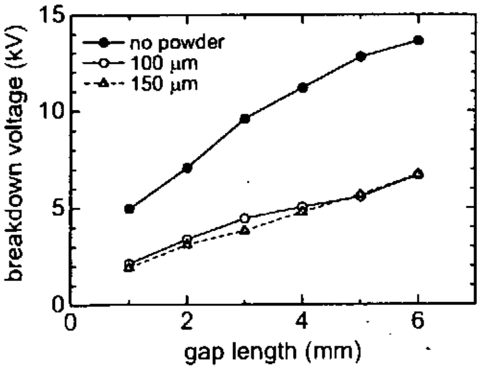

Fig. 11: Breakdown characteristics corresponding to the particle diameter

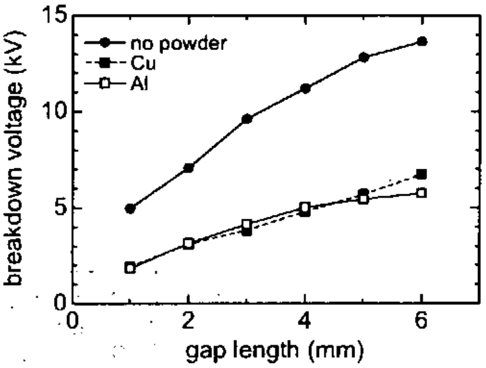

Fig. 12: Breakdown characteristics corresponding to the powder material

results are shown in Fig.13. The breakdown voltages do not depend on the polarity of charged powder and discharge electrodes neither.

5 Conclusions

In our powder supplying system, the powder number density is in proportion to the electric fields between the acceleration electrodes. We can make the discharge chamber filled with powder having desired powder number densities by changing the acceleration voltage.

There are no relationships between the breakdown voltage and powder parameters (number density, diameter, material, polarity of powder and electrodes).

Acknowledgments

The authors would like to thank Mr. Tomohiro Tanaka, Osawa-shokai Inc., for kind suggestions on the velocity measurements.

References

[1] Isao Sugai: Nucl. Instrum. & Methods A **397** (1997) 81.

[2] A. E. Pozwolski: Laser and Particle Beams **12** (1994) No.1, 65.

[3] C. R. James and F. Vermeulen: Can. J. Phys. **46** (1968) 855.

[4] A. Y. H. Cho: J. Appl. Phys. **35** (1964) No.9, 2561.

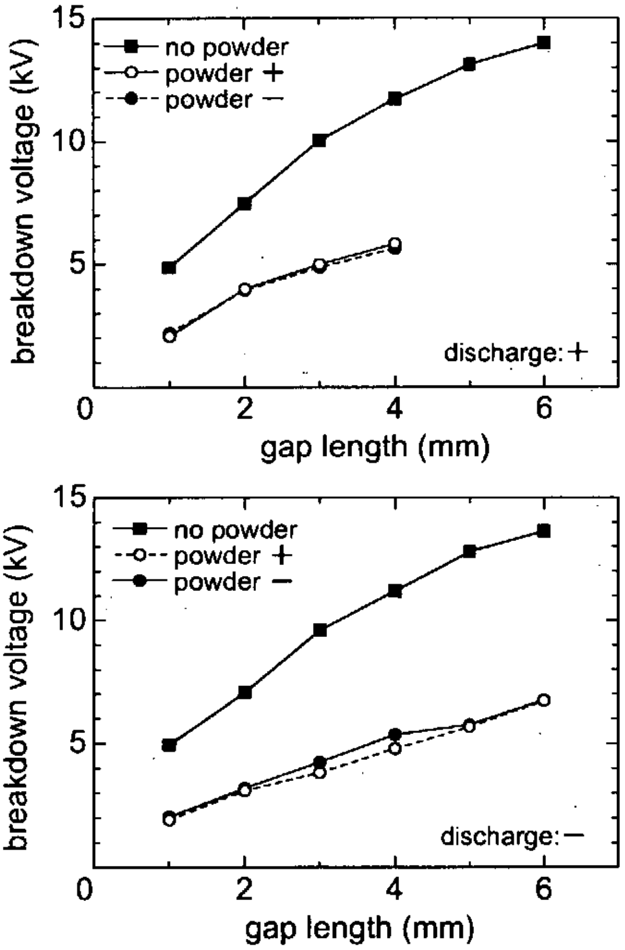

Fig. 13: Breakdown characteristics corresponding to the powder and discharge polarity

[5] H. C. Van De Hulst: *Light Scattering by Small Particles* (JOHN WILEY & SONS, Inc.) (1957).

High-Speed, Multi-Band Imaging of Pinched Plasma

Takeshi Yanagidaira, Yasushi Ono, Bun Han, Makoto Yamaguchi and Katsumi Hirano

Department of Electronic Engineering, Gunma University Kiryu, Gunma 376-8515

Emission from pinched plasma generated with plasma focus device with argon and neon puffing is observed. Using filtered photodiode array, temporally and spatially resolved intensities in visible (0.45-0.65 μm), infrared (0.75-1.0 μm) and x-ray (2-12 Å) range was simultaneously recorded in digital oscilloscopes and displayed in streak mode after processing the waveforms with software using inversion technique. When argon was puffed, the x-ray source was generated after the disruption of the pinched column. On the other hand, in the case of neon puffing, x-ray was observed during pinch. Measurement of intensities in the visible and infrared range showed $\sim \lambda^{-2}$ dependency expected in bremsstrahlung radiation. However, enhancement in visible range was detected after x-ray emission when neon was puffed.

§1. Introduction

Pinched plasmas, such as plasma focus, gas-puff z-pinch, and wire-array z-pinch, are intense sources of impulsive soft x-rays. In plasma focus with a gas puff, an intense soft x-ray radiation can be obtained from pinched plasma of puffed gas which is compressed and heated to a high temperature. The mechanism of plasma heating in plasma focus have been associated with beam-plasma interaction or turbulent which are results of instabilities grown on the plasma column. However, the mechanism have not yet clarified through simultaneous observations of plasma behavior and x-ray emission. In the previous papers,[1-3] we made time resolved observations of x-rays emitted from plasma focus with argon and neon puffing. There were differences in shape and duration of x-ray sources between experiments with argon and neon puffing. The species of puffed gas should be chosen in order to obtain suitable wavelength depending on applications of plasma focus x-ray source. The characteristics of x-ray source and heating mechanism for each gas is important in optimizing the condition of discharge to get maximum emission. It is helpful for clarifying the heating mechanism to observe radiations over wavelengths during pinch evolution with time- and spatial resolution. Observation in visible range have been employed to obtain macroscopic behavior.

When argon or neon is puffed from inner electrode just before the main discharge, plasma column with temperature around $0.5 \sim 2$ keV and electron densities of $10^{20} \sim 10^{22}$ cm^{-3} can be generated. On plasmas with such temperatures and densities, diagnostics by means of absolute intensity of visible to infrared range or the slope of x-ray spectra can be used to obtain plasma parameters.[4,5] Radiation in visible and infrared region mostly consists of continuous spectra due to *free-free* (bremsstrahlung) transitions. On the other hand, measurement of infrared radiation in plasma focus discharge had also been made to detect turbulence in pinched column.[6,7] When the electron drift velocity exceeded the electron thermal velocity or the phase velocity of ion sound wave, oscillations at frequencies around the plasma frequency, $\omega_p = \sqrt{n_e e^2/\epsilon m_e}$, and its harmonics might be excited and contribute to plasma heating by wave-plasma interactions. In plasma focus with gas puff,[2,3,8] $n_e = 10^{20} \sim 10^{22}$ cm^{-3} and radiation at plasma frequency would lie in visible or infrared range and so the observation of that range may detect turbulence in plasma.

In this paper, we intend to clarify the heating mechanism of plasma in argon and neon puff pinch through simultaneous observation of macroscopic behavior of pinch and x-ray radiation. Using filtered photodiode arrays, high-speed images of pinch evolution in streak mode was observed in visible, infrared and x-ray region.

§2. Apparatus

2.1 High-speed imaging system

The high-speed imaging system[1] is composed of an arrayed detector and software that processes data from the detection system by the inversion technique. The basic idea is to produce time-resolved images by processing the analog signals obtained by the arrayed detector.

In this experiment, we used 15-channel visible light, infrared and soft x-ray detector (Fig. 1) with one-dimensional spatial resolusion. It includes two linear photo diode array (International Radiation Detectors AXUV-10EL) for spatial resolution in the axial direction of plasma focus device. Combination filters were used for the detector; glass (thickness 4.3 mm) + visible light pass filter (Kureha Chemical Industry UCF-02) for visible light channels, glass (4.3 mm) + infrared pass filter (Fuji optical film IR88) for infrared and Al foil (1.5μm) for x-ray channels. The spectral response of the detection system is shown in Fig. 2. The viewing field of each element was 3 mm for axial and 15 mm for radial direction of the coaxial electrode of plasma focus device. The viewing filelds of the adjacent channels in the arrayed detector are designed to overlap each other. Therefore, the arrayed system enabled continuous detection over the whole area where the sources are generated. The rise time of the detection system was 1 ns. The analog signals from each channel was recorded at a sampling rate of 2 G samples/s in storage oscilloscopes (Hewlett-Packard 54542A and 54542C). The oscilloscopes can store analog signals from each cannel into DOS-compatible files.

At the inversion, the viewing field is divided into pixels numbered by J. The source intensity to be determined is expressed as $i(J,t)$, where t is the time. Let the quantities measured experimentally in the analog signals of the m-th channel be $V_m^{(m)}(t)$. Determination of $i(J,t)$'s is made possible by using the least-squares method. Corresponding to the presumed intensity $i(J,t)$, the analog signals is calculated as $V_m^c(t) = \sum_t S_m(J)i(J,t)$ where $S_m(J)$ is the sensitivity of the m-th channel at the pixel J. We compared the calculated $V_m^m(t)$ with their measured values by taking summation of the square of the residual R, where $R^2 = \sum_m \sum_t [V_m^c(t) - V_m^m]^2$. The maximum entropy criterion was introduced in order to select the best solution. The entropy measure in the image reconstruction is given by $S = -\sum_t \sum_J [(i(J,t)/\sum_J i(J,t)) \log (i(J,t)/\sum_J i(J,t))]$. The quantity to be minimized in finding the maximum entropy image is then $R^2 - \lambda S$. The maximum entropy image contains only such structures are required to fit the data. Fine structural details will appear in the reconstruction if and only if the data demand them. We used the genetic algorithm (GA) to find a solution of the intensity $i(J,t)$. GA model natural processes, such as selection, multiplication, crossover, and mutation of individuals. An initial population is created so that a set of presumed $i(J,t)$'s is coded into an individual. Then, the individuals are selected for the production of a new generation. All offspring are mutated with a certain probability. This cycle is performed until the optimization criteria are reached.

2.2 Plasma focus device as soft x-rays source

We used a Mather-type plasma focus device as a soft x-ray source. The inner and outer diameter of the coaxial electrodes were 50 and 100 mm. The length of the inner and outer electrodes were 280 and 230 mm, respectively. The anode (inner electrode) is hollow. The condenser bank consists of 28×1.56 μF capacitors. The device was operated at a bank voltage of 45 kV and an embedded H_2 gas pressure of 6 Torr. Additional gas was puffed with a fast acting valve through the anode hole immediately before each discharge.

§3. Results and discussion

The example of simultaneous observation in visible, infrared, and x-ray range for argon and neon puffing is shown in Figs. 3(a) and 3(b). These figures are in streak mode with viewing fields along the electrode axis. The intensities are displayed by contours which represent the locations with same intensity.

3.1 Argon puff

Figure 3(a) shows results for argon puffed discharge (shot # 6412). Emission in visible and infrared begin at locations near inner electrode (z = 0 mm) first. The emission started latter at further locations, demonstrating the zippering effect. Spotlike X-ray emission, shown as ‘A’, ‘B’ and ‘C’ in Fig. 3(a), were detected. When the source at ‘B’ is generated, the visible and infrared emission had almost disappeared, that may corresponds to disruption of pinched column. At ‘C’, the x-ray source was generated 8 ns after disappearance of visible and infrared emission from pinch.

Intense K-shell line emission (~ 3 keV) is usually observed in argon puffed discharges[2,8] and the electron temperature estimated from x-ray spectra was ~ 2 keV. Heating to high temperatures up to several keV may not achieved in the pinch phase. The x-ray emission may be ascribed to non-thermal electrons generated at the disruption phase in plasma focus[9] which can effectively excite inner-shell electrons of argon.

3.2 Neon puff

The result for neon puff pinch is shown in Fig. 3(b). Emission in visible range from locations around $z \sim 15\,\mathrm{mm}$ last longer until $t = 70\,\mathrm{ns}$. This may be ascribed to emission from plasma which flowed out axially from plasma column. X-ray source is generated at $t = t_1$, $z = 0 \sim 7$ mm, and after that the peak emission in visible range was observed. X-ray emission in this shot seems to have started in the process of heating during the pinch phase. In plasma focus discharges with neon puffing, spectra consists of line emission and continua from radiative recombination is observed in $8.5 \sim 14$Å range. In the previous paper, electron temperature of $\sim 0.4\,\mathrm{keV}$ is estimated from slope of continuous emission around 9Å.[3] The line emission would persist while the fractional abundance of hydrogen-like or helium-like ion is high enough compared to ions with other ionized states.

Immediately after the x-ray emission, the peak emission in the visible range was observed at $t = t_2$, $z = 0 \sim 7$. The peak emission in visible range cannot be ascribed to line radiation because at temperatures around 0.4 keV, neon will get highly stripped (average ionization state $Z \sim 9$) and there would be only a small fraction of ion which can emit line radiation in visible range. The detected enhancement in visible range may be related to radiation which corresponds to oscillation at the plasma frequency. Although the spectrum from such oscillation is expected to have spread and may contain harmonics, no enhancement in the infrared range was observed. This could be ascribed to absorption or cut-off in pinched column itself and surrounding thin plasma which we will consider in the next chapter.

3.3 Absolute intensity in visible and infrared region

Figure 4 shows the result for absolute intensity measurement in the two shots in visible and infrared range. The error bars represent the range of recorded intensities during each discharge. As shown in Fig. 4, the absolute intensities are in agreement with intensities expected for bremsstrahlung emission,[7]

$$I_\lambda = 3.3 \times 10^{-34} n_e^2 \lambda^{-2} Z L T_e^{-1/2}\ [\mathrm{W/cm^3/\mu m/sr}]$$

where n_e is the electron density in cm^{-3}, λ is the wavelength in μm, T_e is the electron temperature in eV, Z is the average ionization state of the ions and L is the length of plasma viewed in cm. However, intensity in infrared range was a little lower than expected from the λ^{-2} dependency of the curve. One of reasons for observed low intensity at the infrared range is the fact that the absorption coefficient[5] is proportional to λ^2 and absorption at surrounding plasma is increased at longer wavelengths.[5]

The other effect which may account for decreased propagation in plasma is the cut-off around the plasma frequency. When a plasma column have a radial density distribution like quadratic function with maximum on axis, radiations with frequency lower than ω_p defined at the point of departure for each emission cannot be observed from outside the plasma column. If we assume that ω_p was in visible range, the observed peak at t_2 in visible channels and no enhancement at t_2 in infrared, might also be explained.

In the contour plot of streak mode display in visible range, there were relatively fine structures compared to the result for infrared range. In the visible range, absorption by plasma column and the surrounding thin plasma is less important and observation in this range reflects the structures of emitting regions inside the pinched column. On the other hand, in infrared range radiation from dense regions will be masked and spatially averaged before it is observed.

---

1) T. Yanagidaira and K. Hirano: Rev. Sci. Instrum. 68 (1997) 3074.
2) T. Yanagidaira, T. Yamamoto, B. Shan and K. Hirano: To be published in J. Phys. Soc. Jpn. 68 (1999).
3) T. Yanagidaira, T. Yamamoto and K. Hirano: To be published in J. Phys. Soc. Jpn. 68 (1999)
4) *Plasma Diagnostic Techniques*: Ed. R. H. Huddlestone and S. L. Leonard, Academic Press, New York, Vol. 21, p. 244 (1965).
5) M. F. Kimmitt and G. B. F. Niblett: Proc. Phys. Soc. 82 (1963) 938.
6) R. S. Post and T. C. Marshall: Phys. Fluid 17 (1974) 452.
7) G. R. Neil and R. S. Post: Plasma Phys. 23 (1981) 515.
8) H. Kitaoka, T. Yamamoto and K. Hirano: J. Phys. Soc. Jpn. 67 (1998) 481.
9) T. Yamamoto, K. Shimoda and K. Hirano: Jpn. J. Appl. Phys. 24 (1985) 324.

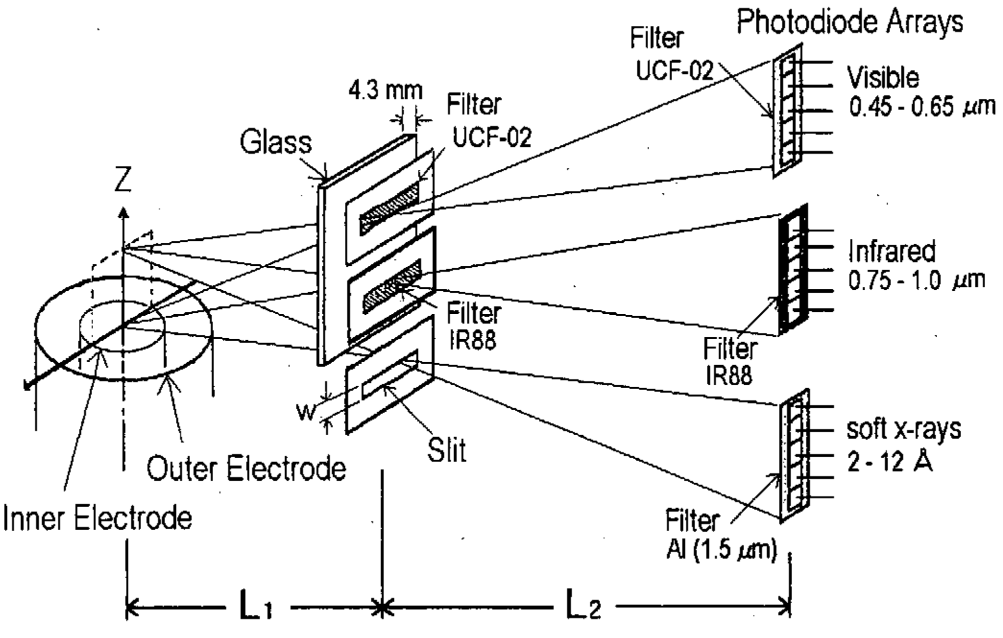

Fig. 1. Arrangement of diagnostic tools.

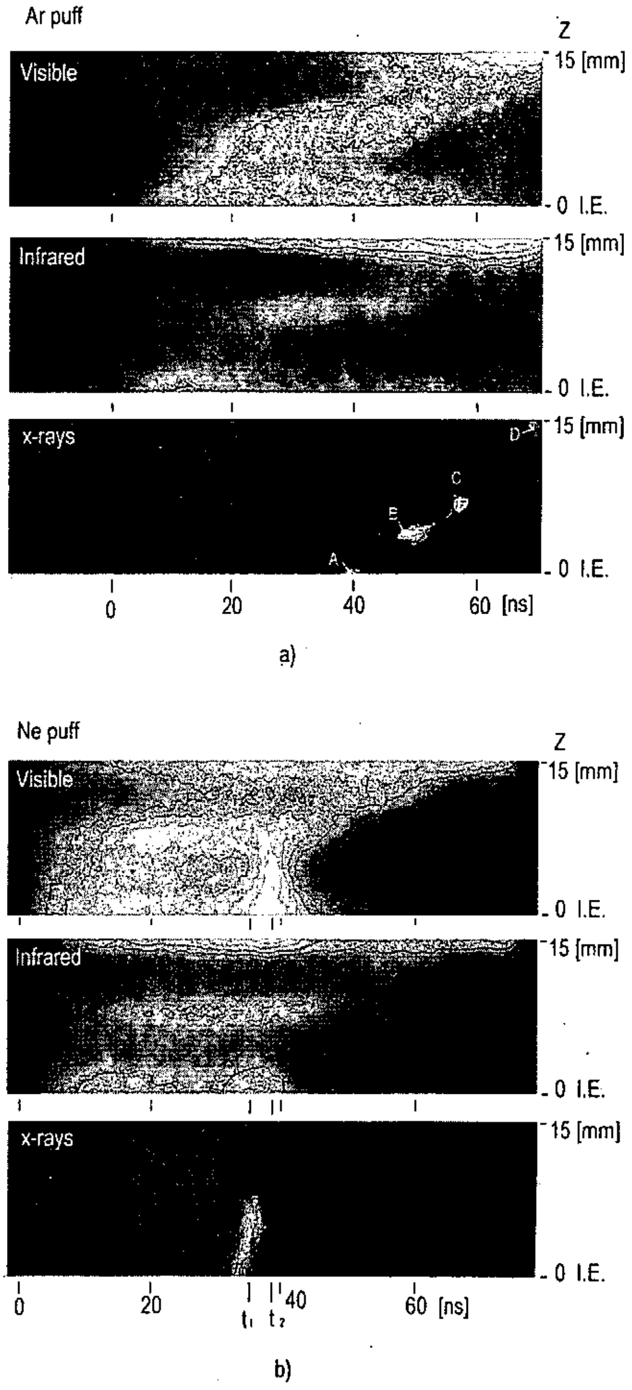

Fig. 3.- Experimental results for (a) argon puff and (b) neon puff.

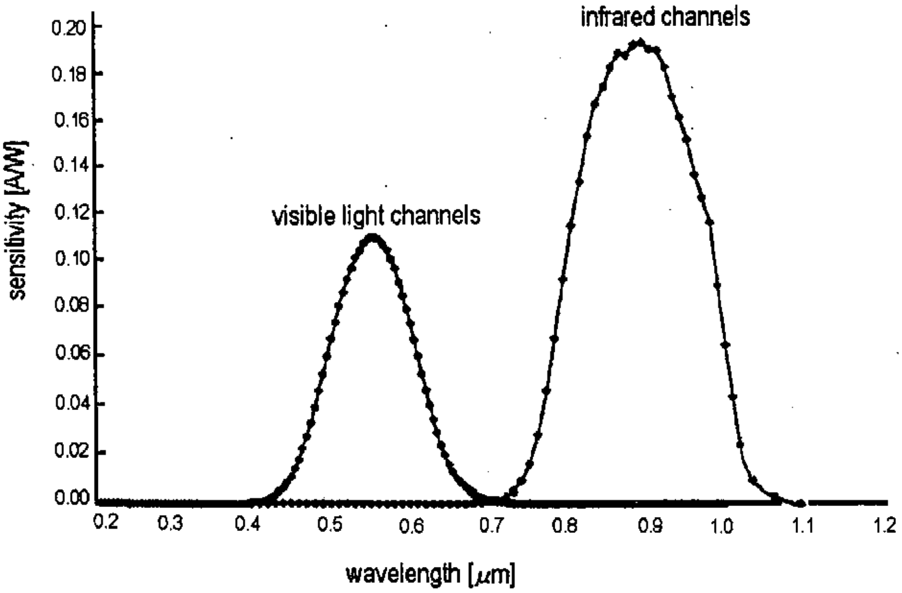

Fig. 2. Spectral response of visible, infrared and x-ray detection system.

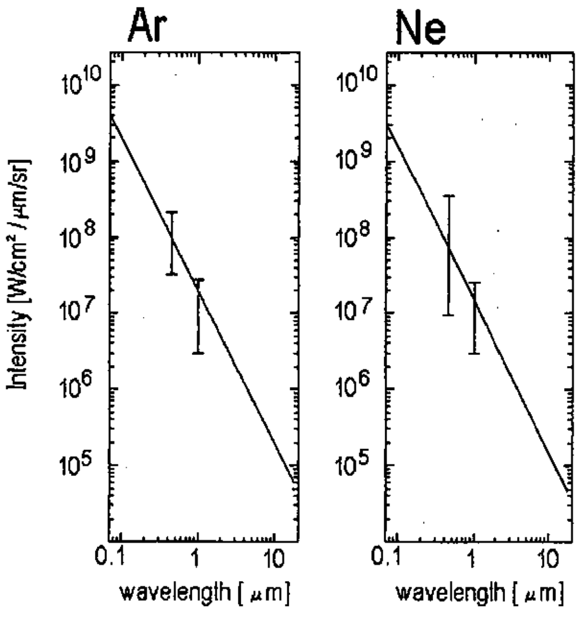

Fig. 4. Absolute intensities for (a) argon puff and (b) neon puff.

An imaging spectrometer with a convex crystal for a pulsed X-rays in plasma experiments

H. Maruyama, S. Kanuma, Y. Ono, T. Yanagidaira, K. Shimoda and K. Hirano

Department of Electronic Engineering, Gunma University,
Kiryu, Gunma 376-8515, Japan

An imaging spectrometer with a convex rubidium acid phtalate (RAP) crystal is designed and examined. Using the ray tracing technique based on the kinematical theory of diffraction, the resolution power, the dispersion, the linearity and the spatial resolution of the monochromatic image are discussed. The broadening by the rocking curve is also taken into account. Performance of the spectrometer is successfully examined using the so called hot spots as the soft x-ray source which are generated in the pinched plasma by the plasma focus facility with an additional gas puff.

KEYWORDS: soft x-ray, spectrometer, Bragg diffraction, convex RAP crystal, pinched plasma

§1. Introduction

Crystal spectrometers for soft X-rays have been developed for several decades.$^{1-4)}$ Recently development of crystals of longer 2d length and synthesized multilayer enabled to analyze the X-rays longer wavelength region. In plasma experiment, imaging spectrometers have demonstrated their usefulness. Employing an imaging spectrometer, we can carry out a spectrally resolved measurement including distributions of the electron temperature and electron density.

A convex crystal spectrometer is capable of measuring spectral distribution in wide spectral range of interest simultaneously. Therefore, it is an appropriate tool for the spectral analysis of pulsed X-rays.

However, the imaging spectrometer with convex curved crystal has mostly been used without considering the spatial resolution of spectrally analyzed image. Moreover, calibration for the wavelength in the case of the convex crystal is more complicated than that of a flat crystal.$^{5)}$ We intend to construct a spectrometer with a convex crystal and to examine it using a X-ray source generated in a Z-pinch plasma.

In general, the resolution power of the spectrometer is determined by broadening of the spectral line. There are two origins of broadening; one is caused by the spectrometer itself and the other is caused by X-ray sources. Typically, the formers are the finite source size broadening,[6)] the broadening by rocking curve[7)] and thermal diffuse scattering and so on. The latters are the Stark broadening, the Doppler broadening and the broadening by the plasma opacity, for example. Some of them have been used to evaluate plasma parameters. For example for the electron density measurement by Inglis-Teller method which expects the spectral line merging by the Stark broadening.

However, broadening by the X-ray source size is the principle itself to construct a monochromatic image on the recording medium. On the contrary, other broadenings mentioned above cause lowering of the spatial resolution.

In this article we designed an imaging spectrometer in which a convex curved crystal was employed and evaluated the spatial resolution of the image using a ray tracing technique based on the kinematical theory of diffraction. Then the performance of the spectrometer was examined using the soft X-ray source generated in the Z-pinch plasma.

§2. Design concept of the imaging spectrometer with the convex crystal

2.1 Ray tracing analysis

To carry out the ray tracing we adapt the coordinate system shown in Fig. 1 which is based on Kastner.[8)] In this system the origin is taken at the center of curvature of the convex curved crystal. An X-ray emitted from the point source at arbitrary location (a, b) reaches to the crystal at a point (u, v) and then diffracted in the direction which satisfies the Bragg condition. The diffracted X-rays intersects the circle of recording medium such as an X-ray sensitive film and MCP at the imaging point (x, y). The center of the circle is located at (p, q). These points can also be designated by the angles θ_1, θ_2 and θ_3 as shown in Fig. 1.

Using θ_2, we describe the point (u, v) as

$$\begin{aligned} u &= -r\sin\theta_2 \\ v &= r\cos\theta_2 \end{aligned} \tag{1}$$

where r is the radius of the convex crystal. Then the gradient of the straight line connecting between (a, b) and (u, v) is

$$\tan\theta_3 = \frac{r\cos\theta_2 - b}{-r\sin\theta_2 - a} \ . \tag{2}$$

Using the parameter $t\,(> 0)$ the equation of the line which connects between (u, v) and (x, y) and makes the incident angle θ_1, that equals to the reflected angle, is expressed as

$$\begin{aligned} x &= u + t\cos(2\theta_2 - \theta_3) \\ y &= v + t\sin(2\theta_2 - \theta_3) \ . \end{aligned} \tag{3}$$

The line intersects the circle of the recording medium at (x, y). Therefore,

$$(u + t\cos(2\theta_2 - \theta_3) - p)^2 + (v + t\sin(2\theta_2 - \theta_3) - q)^2 = R^2 \ , \tag{4}$$

where R is the radius of the recording medium circle.

For $t > 0$, the solution of Eq. 4 is

$$t = -(\beta\cos\alpha + \gamma\sin\alpha) + \sqrt{(\beta\cos\alpha + \gamma\sin\alpha)^2 + (R^2 - \beta^2 - \gamma^2)}\ , \tag{5}$$

where $\alpha = 2\theta_2 - \theta_3, \beta = u - p$ and $\gamma = v - q$, respectively. Substituting Eq. 5 into Eq. 3, we obtain the location of image on the recording medium, (x, y). In this situation the incident angle on the crystal is $\theta_1 = \theta_2 - \theta_3$.

2.2 Numerical calculation

In this paragraph, we carry out the calibration for wave length, calculation of the resolving power and the examination of linearity of the spectroanalyzed image on the recording medium.

2.2.1 Calibration for wavelength

For the calibration we calculate θ_2 so as to satisfy Eq. 2 and the Bragg condition

$$2d\sin\theta_1 = 2d\sin(\theta_2 - \theta_3) = m\lambda \tag{6}$$

by the Newtons iterative method, where m is an integer. When θ_2 is calculated, the location of the image is obtained by Eq. (3) with using Eqs. 1,2 and 5. Therefore the length of arc, l which is distance from the base point of wavelength to the point (x, y) on the recording medium is described as

$$l = R \cdot (\pi/2 + \theta_4)\ , \tag{7}$$

where

$$\theta_4 = \tan^{-1}\frac{-(x-p)}{y-q}\ .$$

It is clear from Eq. 7 that l is expressed as a function of only geometrical factors. Namely,

$$l = l(\theta_2, a, b, p, q, r, R)\ . \tag{8}$$

We carried out the numerical calculation of l using a subroutine described in FORTRAN. The subroutine consists of (1) To read $a, b, p, q, r, R, \lambda$ into a file, (2) to seek θ_2, which satisfy Eqs. 2 and 6, by the Newton's iterative method, (3) to obtain x and y by Eq. 3, (4) to obtain l using Eq. 7, and (5) to output $a, b, p, q, r, R, \lambda, \theta_2$ and l to the file. The calculated relationship between λ and l is shown in Fig. 2. To perform the calculation, parameters listed in Table. 1 are adapted.

Next, we obtain the spatial distribution of brightness of the finite size image which is formed by the finite size source. Contribution by infinitesimal line element of the finite size source, Δb to the brightness around (x, y) can be calculated as follows: Taking into account reflection around Bragg angle, we obtain reflection in the region of $\theta_2 + \Delta\theta_2$. Then the incident angle (=reflection angle) is given as

$$\theta' = \theta_2 + \Delta\theta_2 - \theta_3$$

$$= \theta_2 + \Delta\theta_2 - \tan^{-1} \frac{r \sin\theta_2 + \Delta\theta_2 - b}{-r \sin\theta_2 + \Delta\theta_2 - a} . \tag{9}$$

Therefore, the brightness caused by Δb to the image at $l = l(\theta_2 + \Delta\theta_2, a, b, p, q, r, R)$ is

$$\Delta i = i_0 \sigma(\theta' - \theta)\Delta b , \tag{10}$$

where θ is Bragg angle, σ is a function describing variation of the reflectivity according to variation of incident angle from θ. In Ref. 9, σ is described by the kinematical theory of radiation as

$$\sigma(\alpha) = \frac{\omega/2\pi}{\alpha^2 + (\omega/2)^2} , \tag{11}$$

where α is the angle measured from the refraction-shifted peak position , $\omega = \mu_l\lambda/(2\pi \sin\theta \cos\theta)$, θ is an angle to be satisfied by the Bragg condition and μ_l is the linear absorption coefficient. Here, we ignored peak-shift due to refraction in crystal that is the second term in the denominator. The numerical value of ω for RbAP crystal is also given in Ref. 9. We assume that the soft x-ray source in the plasma is cylindrical, namely the brightness is proportional to $\sqrt{(D/2)^2 - b^2}$, where D is the diameter of the source. Summation of Δi along l, in which b, θ_2 and $\Delta\theta_2$ are variables gives the brightness distribution on the recording medium. Procedure of the calculation was described by a shell script on a PC-UNIX (Linux) system and was followings; (1) to call the subroutine mentioned above with varying the parameters, (2) to determine the source intensity at b, (3) to record contribution for the brightness under the parameters according to Eq. 10, and (4) to make a file in which intensity distribution composed by sum of Δi. We can give the script the parameters p, q, r, R, d, D and the interested region of λ.

2.2.2 *Resolution power*

We calculate the FWHM, δl of the brightness distribution on the recording medium, using the results of previous section. The FWHM is determined by a subroutine which is developed to examine the calculated results of the brightness distribution. The procedure carried out in the subroutine is followings; (1) to detect the peak in the brightness distribution, (2) to find FWHM which belongs its peak and (3) to output the peak value, FWHM and the corresponding wavelength to the file. The resolution power, Δ is defined as

$$\Delta = \frac{\lambda}{\delta\lambda} . \tag{12}$$

We obtain $\delta\lambda$, if we convert the unit of δl into wavelength scale. Namely,

$$\delta\lambda = \frac{\partial\lambda}{\partial l} \delta l . \tag{13}$$

We ran the shell script using the parameters given in Table. 1 and $D = 0.5$ mm. The δl and $\partial\lambda/\partial l$ using the subroutine mentioned above, and so we obtain the resolution power by eq. 12. The results of calculation is given in Fig. 3.

2.2.3 Spatial resolution of the image

The spatial resolution on the recording medium is defined as δl, broadening of the image for $D = 0$. δl can be calculated by shell script. However, the spatial resolution on the source plane, Δb should be given as

$$\Delta b = (\partial l/\partial b)^{-1}\delta l\ . \tag{14}$$

The relationship between λ and Δb is shown in Fig. 4.

2.2.4 Linearity for source deviation

The relationship between l and b using λ as a parameter is shown in Fig. 5 which can be considered as a group of straight lines with the gradient of 0.346. This fact means that we can obtain the linear image of the source with the approximate magnification of 1/3 on the recording medium. And the magnification is constant for variation of λ.

§3. Comparison with experiment

3.1 Trially manufactured spectrometer and soft x-ray source

We designed and manufactured an imaging spectrometer based on the concept described in §2. The Ne K shell lines from 8 ~ 14 Å are used as an example of soft x-rays. A slit was mounted so as to lay its long side in the direction of wavelength dispersion. The slit, 100 μm × 7 mm and a pinhole (100 μm in diameter) were made on the same plane. The distance between the slit and pinhole was 1 mm. The pinhole image of the fluctuating source was simultaneously recorded on the recording medium for each shot. The image provides the base point for the wavelength measurement. Main geometrical parameters are tabulated in table I. In the perpendicular direction to the slit, the magnification of the spectrometer, that is the ratio the source to the image is determined by the ratio l_1 to l_2 where l_1 and l_2 is optical path length from the source to the slit and the slit to the recording medium, respectively. In the parallel direction to the slit, the magnification is restricted by $\partial l/\partial b$ of the spectrometer. The former was 0.699 and the latter was 0.346. However, both the magnification were adjusted in the same size by an image processing technique.

To block uninteresting emission and debris, the slit and the pinhole were covered by a Be foil 50 μm in thickness. We employed the photographic film Kodak TRI-X as the recording medium. The film has sufficient sensitivity for soft x-rays in this experiment.

A plasma focus facility with gas puff was employed as a soft x-ray source. The facility was energized by a capacitor bank of 45 μF. The experiment was carried out at a bank voltage of 45 kV. The puffed gases such as Ne, Ar, Kr are compressed by a current sheet which was generated by discharge through an embedded H_2 at a pressure of 5 Torr. The spectrometer was mounted in the radial direction to the electrode axis of the facility.

3.2 Performance of the spectrometer

An example of the spectrograph is shown in Fig. 6. It is seen that the thicker radius gives longer length of the image taken by a monochromatic x-rays. Complicated structures less than 0.8 mm in radius are recognized in the image depicted by the spectral line of NeX 12.19 Å 1s-2p. As the spatial resolution of the image is about 120 μm at this wavelength as shown in Fig. 4, it can be considered that the structure taken in the film is real one in the soft x-ray source. The electron temperature and density of the plasma have been evaluated to be $\sim$ 0.5 keV and $10^{21} \sim 10^{22}$ /cm^3, respectively.10) Estimated Doppler and Stark broadening brought from these plasma parameter are 3.3×10^{-3}Å and 1.6×10^{-2}Å.11,12) These correspond to the spatial resolution of 30 μm and 150 μm. This means that Doppler broadening can be ignored. However, Stark effect is serious cause lowering the spatial resolution in some region of the wavelength.

§4. Summary

We developed an imaging Bragg spectrometer with a convex RAP crystal using the ray tracing technique based on the kinematical theory of diffraction. Performance of the spectrometer was examined using hot spots generated in a Z pinch plasma. The hot spot is a small, intense and short-lived soft x-ray source including K shell line emissions. The spatial resolution, dispersion and spatial resolution of the monochromatic images are obtained on the recording medium for which we employed the photographic film, Kodak TRI-X.

---

1) N. J. Peacock, R. J. Speer and M. G. Hobby: J. Phys. B: Atom. Molec. Phys. **2** (1969) 789.

2) T. P. Donaldson, R. J. Hutcheon, M. H. Key and R. J. Urquhart: J. Phys. B: Atom. Molec. Phys., **9** (1976) 1645.

3) Y. Cauchois, R. Khérouf, C. Sénémaud, J. Thirion, C. Bruno and J. Chvallier: *SPIE X-Ray Instrumentation* **1140** (1989) 297.

4) D. B. Brown and M. Fatemi: J. Appl. Phys. **51** (1980) 2540.

5) K. Hirano, N. Hisatome, T. Yamamoto and K. Shimoda: Rev. Sci. Instrum. **65** (1994) 3761.

6) M. Gersten and J. E. Rauch: J. Appl. Phys. **53** (1982) 1297.

7) J. E. White: J. Appl. Phys. **21** (1950) 855.

8) S. O. Kastner: Appl. Optics **18** (1979) 374.

9) B. L. Henke, E. M. Gullikson and J. C. Davis: Atomic Data and Nuclear Data Tables, **54** (1993) 181.

10) T. Yanagidaira, T. Yamamoto and K. Hirano: To be published in J. Phys. Soc. Jpn. **68** (1999).

11) R. J. Tighe and C. F. Hooper, Jr: Phys. Rev. A **14** (1976) 1514.

12) C. D. Michelis, M. Mattioli: Nucl. Fusion **21** (1981) 677.

Convex crystal: RbAP			
2 d = 26.12	[Å]	r = 12.5×10^{-3}	[m]
a = -315.5×10^{-3}	[m]	b = 12.5×10^{-3}	[m]
p = 0	[m]	q = 12.5×10^{-3}	[m]
R = 100×10^{-3}	[m]		

Table I

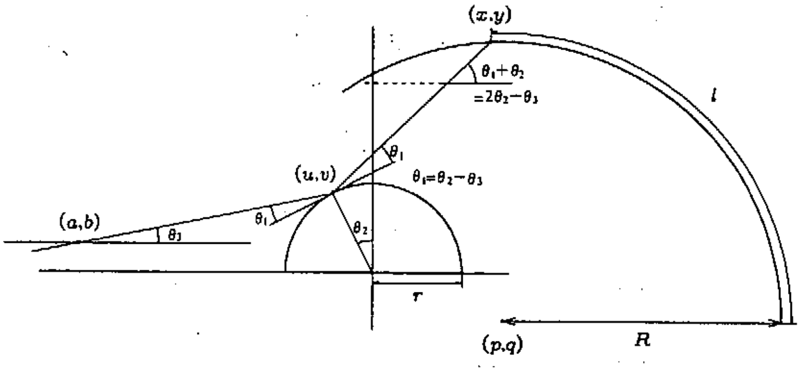

Fig. 1: Coordinate system used in ray tracing for the imaging spectrometer.

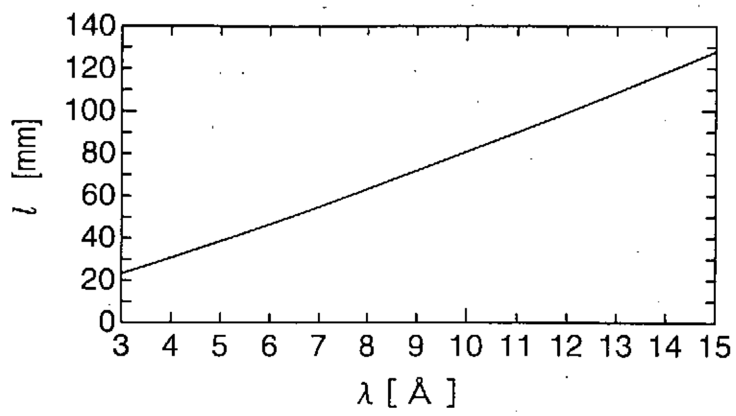

Fig. 2: Calculated relationship between λ and l using parameters listed in Table I.

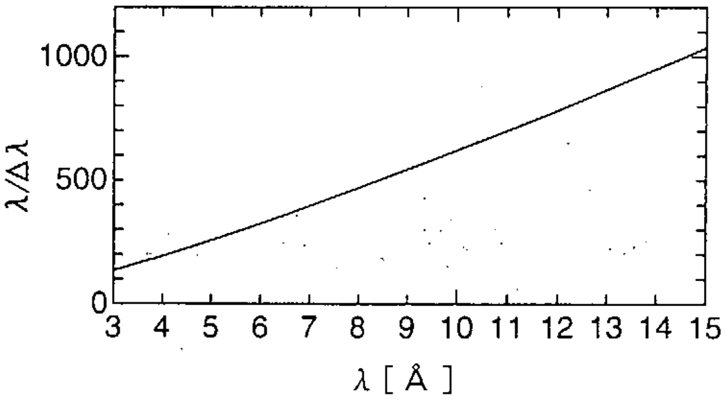

Fig. 3: Resolution power of the spectrometer using parameters listed in Table I and D = 0.5 mm (source diameter).

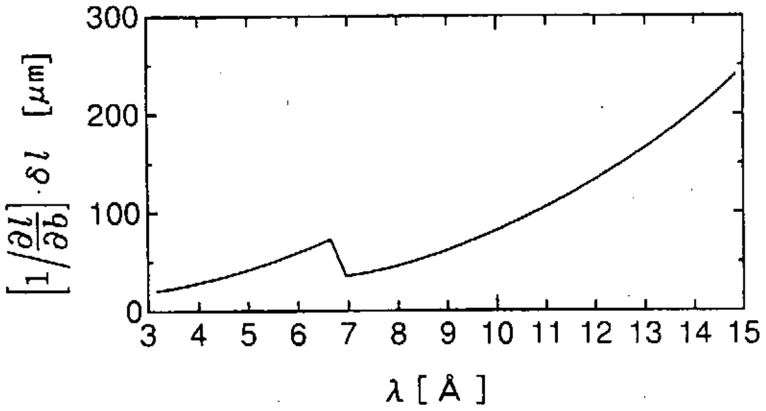

Fig. 4: Spatial resolution of image using parameters listed in Table I.

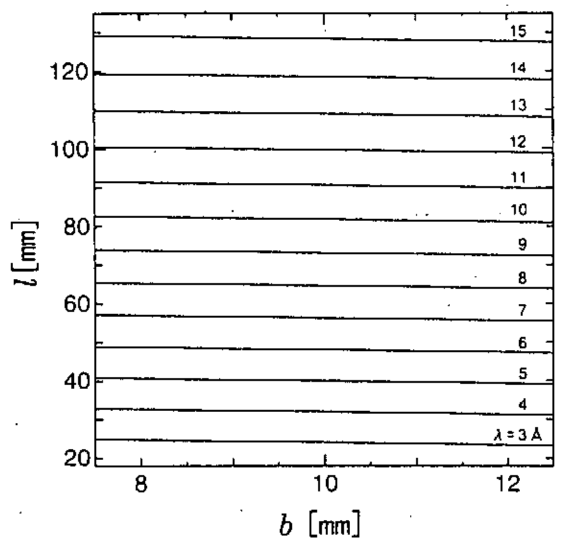

Fig. 5: Relationship between b and l for wavelengths between 3 and 15 Å.

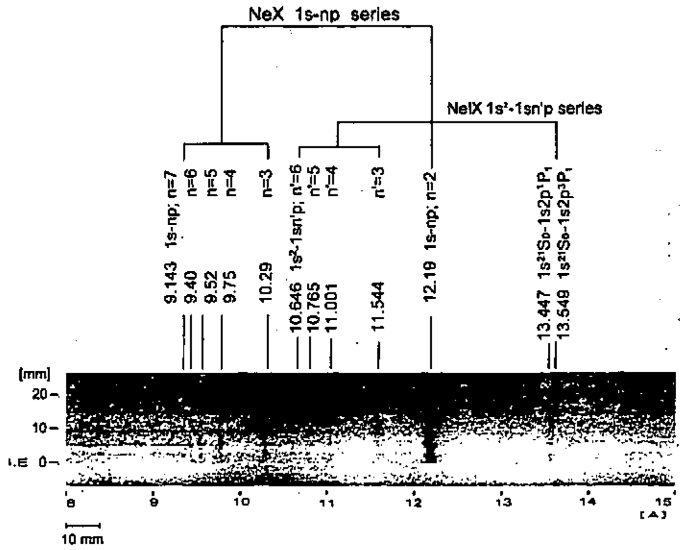

Fig. 6: An example of the spectrograph.

Publication List of NIFS-PROC Series

NIFS-PROC-1	"*U.S.-Japan on Comparison of Theoretical and Experimental Transport in Toroidal Systems Oct. 23-27, 1989*", Mar. 1990
NIFS-PROC-2	"*Structures in Confined Plasmas –Proceedings of Workshop of US-Japan Joint Institute for Fusion Theory Program–* "; Mar. 1990
NIFS-PROC-3	"*Proceedings of the First International Toki Conference on Plasma Physics and Controlled Nuclear Fusion –Next Generation Experiments in Helical Systems– Dec. 4-7, 1989*" Mar. 1990
NIFS-PROC-4	"*Plasma Spectroscopy and Atomic Processes –Proceedings of the Workshop at Data & Planning Center in NIFS–*"; Sep. 1990
NIFS-PROC-5	"*Symposium on Development of Intensed Pulsed Particle Beams and Its Applications February 20 1990*"; Oct. 1990
NIFS-PROC-6	"*Proceedings of the Second International TOKI Conference on Plasma Physics and Controlled Nuclear Fusion , Nonlinear Phenomena in Fusion Plasmas -Theory and Computer Simulation-*"; Apr. 1991
NIFS-PROC-7	"*Proceedings of Workshop on Emissions from Heavy Current Carrying High Density Plasma and Diagnostics*"; May 1991
NIFS-PROC-8	"*Symposium on Development and Applications of Intense Pulsed Particle Beams, December 6 - 7, 1990*"; June 1991
NIFS-PROC-9	"*X-ray Radiation from Hot Dense Plasmas and Atomic Processes*"; Oct. 1991
NIFS-PROC-10	"*U.S.-Japan Workshop on "RF Heating and Current Drive in Confinement Systems Tokamaks" Nov. 18-21, 1991,* Jan. 1992
NIFS-PROC-11	"*Plasma-Based and Novel Accelerators (Proceedings of Workshop on Plasma-Based and Novel Accelerators) Nagoya, Japan, Dec. 1991*"; May 1992
NIFS-PROC-12	"*Proceedings of Japan-U.S. Workshop P-196 on High Heat Flux Components and Plasma Surface Interactions for Next Devices*"; Mar. 1993
NIFS-PROC-13	「NIFS シンポジウム 「核燃焼プラズマの研究を考える－現状と今後の取り組み方」 1992年7月15日、核融合科学研究所」1993年7月 *NIFS Symposium "Toward the Research of Fusion Burning Plasmas -Present Status and Future strategy-", 1992 July 15, National Institute for Fusion Science*"; July 1993 (in Japanese)
NIFS-PROC-14	"*Physics and Application of High Density Z-pinches*", July 1993
NIFS-PROC-15	岡本正雄、講義「プラズマ物理の基礎」 平成5年度　総合大学院大学1994年2月 *M. Okamoto,* *"Lecture Note on the Bases of Plasma Pysics"Graduate University for Advanced Studies* Feb. 1994 (in Japanese)
NIFS-PROC-16	代表者　河合良信 平成5年度　核融合科学研究所共同研究 研究会報告書「プラズマ中のカオス現象」 *"Interdisciplinary Graduate School of Engineering Sciences" Report of the meeting on Chaotic Phenomena in Plasma*Apr. 1994 (in Japanese)
NIFS-PROC-17	平成5年度 NIFS シンオジウム報告書 「核融合炉開発研究のアセスメント」平成5年11月29日-30日　於　核融合科学研究所 *"Assessment of Fusion Reactor Development" Proceedings of NIFS Symposium held on November 29-30, 1993 at National Insitute for Fusion Science"* Apr. 1994(in Japanese)
NIFS-PROC-18	"*Physics of High Energy Density Plasmas Produced by Pulsed Power*" June 1994
NIFS-PROC-19	K. Morita, N. Noda (Ed.),

"*Proceedings of 2nd International Workshop on Tritium Effects in Plasma Facing Components at Nagoya University, Symposion Hall, May 19-20, 1994",* Aug. 1994

NIFS-PROC-20 研究代表者　阿部　勝憲　（東北大学・工学部）
所内世話人　野田信明
平成 6 年度　核融合科学研究所共同研究［研究会］「金属系高熱流束材料の開発と評価」成果報告書
K. Abe and N. Noda (Eds.),
"Research and Development of Metallic Materials for Plasma Facing and High Heat Flux Components"
Nov. 1994(in Japanese)

NIFS-PROC-21 世話人：森田　健治（名大工学部）、金子　敏明（岡山理科大学理学部）
「境界プラズマと炉壁との相互作用に関する基礎過程の研究」研究会報告
K. Morita (Nagoya Univ.), T. Kaneko (Okayama Univ. Science)(Eds.)
"*NIFS Joint Meeting "Plasma-Divertor Interactions" and "Fundamentals of Boundary Plasma-Wall Interactions" January 6-7, 1995 National Institute for Fusion Science"* Mar. 1995 (in Japanese)

NIFS-PROC-22 代表者　河合　良信
プラズマ中のカオス現象
Y. Kawai,
"Report of the Meeting on Chaotic Phenomena in Plasma, 1994" Apr. 1995 (in Japanese)

NIFS-PROC-23 K. Yatsui (Ed.),
"*New Applications of Pulsed, High-Energy Density Plasmas";* June 1995

NIFS-PROC-24 T. Kuroda and M. Sasao (Eds.),
"*Proceedings of the Symposium on Negative Ion Sources and Their Applications, NIFS, Dec. 26-27, 1994"*,
Aug. 1995

NIFS-PROC-25 岡本　正雄
新古典輸送概論（講義録）
M. Okamoto,
"*An Introduction to the Neoclassical Transport Theory" (Lecture note),* Nov. 1995 (in Japanese)

NIFS-PROC-26 Shozo Ishii (Ed.),
"Physics, Diagnostics, and Application of Pulsed High Energy Density Plasma as an Extreme State";
May 1996

NIFS-PROC-27 代表者　河合　良信
プラズマ中のカオスとその周辺非線形現象
Y. Kawai ,
"Report of the Meeting on Chaotic Phenomena in Plasmas and Beyond, 1995", Sep. 1996 (in Japanese)

NIFS-PROC-28 T. Mito (Ed.),
"*Proceedings of the Symposium on Cryogenic Systems for Large Scale Superconducting Applications",* Sep.
1996

NIFS-PROC-29 岡本　正雄
講義「核融合プラズマ物理の基礎 - I」
平成 8 年度　総合研究大学院大学　数物科学研究科　核融合科学専攻 1996年 10月
M. Okamoto
"Lecture Note on the Fundamentals of Fusion Plasma Physics - I" Graduate University for Advanced Studies; Oct. 1996 (in Japanese)

NIFS-PROC-30 研究代表者　栗下　裕明（東北大学金属材料研究所）
所内世話人　加藤　雄大
平成 8 年度核融合科学研究所共同研究「被損傷材料の微小体積強度評価法の高度化」研究会　1996年 10月　9日　於：核融合科学研究所
H. Kurishita and Y. Katoh (Eds.)
NIFS Workshop on Application of Micro-Indentation Technique to Evaluation of Mechanical Properties of Fusion Materials, Oct. 9, 1996, NIFS ; Nov. 1996 (in Japanese)

NIFS-PROC-31 岡本　正雄
講義「核融合プラズマ物理の基礎 - II」
平成 8 年度　総合研究大学院大学　数物科学研究科　核融合科学専攻　1997年 4月
M. Okamoto
"Lecture Note on the Fundamentals of Fusion Plasma Physics - II" Graduate University for Advanced

Studies; Apr. 1997 (in Japanese)

NIFS-PROC-32 代表者　河合　良信
平成8年度　核融合科学研究所共同研究　研究会報告「プラズマ中のカオスとその周辺非線形現象」
Y. Kawai (Ed)
Report of the Meeting on Chaotic Phenomena in Plasmas and Beyond, 1996; Apr. 1997 (mainly in Japanese)

NIFS-PROC-33 H. Sanuki,
Studies on Wave Analysis and Electric Field in Plasmas; July 1997

NIFS-PROC-34 プラズマ対向機器・PSI・熱・粒子制御合同研究会報告
平成 9 年 6 月 27 日（金）9:00 ～16:20　核融合科学研究所・管理棟 4 F 第 1 会議室
1997年　10月
T. Yamashina (Hokkaido University)
Plasma Facing Components, PSI and Heat/Particle Control June 27, 1997, National Institute for Fusion Science T. Yamashina (Hokkaido University) ; Oct. 1997 (in Japanese)

NIFS-PROC-35 T. Watari,
Plasma Heating and Current Drive; Oct. 1997

NIFS-PROC-36 T. Miyamoto and K. Takasugi (Eds.)
Production and Physics of High Energy Density Plasma; Production and Physics of High Energy Density Plasma; Oct. 1997

NIFS-PROC-37 (Eds.)T. Fujimoto, P. Beiersdorfer,
Proceedings of the Japan-US Workshop on Plasma Polarization Spectroscopy and The International Seminar on Plasma Polarization Spectroscopy January 26-28, 1998, Kyoto; June 1998

NIFS-PROC-38 (Eds.) Y. Tomita, Y. Nakamura and T. Hayashi,
Proceedings of the Second Asian Pacific Plasma Theory Conference APPTC '97, January 26-28, 1998, Kyoto; Aug. 1998

NIFS-PROC-39 (Ed.) K. Hirano,
Production, Diagnostics and Application of High Energy Density Plasmas; Dec. 1998

NIFS-PROC-40 研究代表者　加古　孝（電気通信大学）
所内世話人　渡辺　二太
平成 10 年度核融合科学研究所共同研究 研究会「プラズマ閉じ込めに関連する数値計算手法の研究」
Ed. by T. Kako and T. Watanabe
Proceeding of 1998-Workshop on MHD Computations "Study on Numerical Methods Related to Plasma Confinement Apr. 1999

NIFS-PROC-41 (Eds.) S. Goto and S. Yoshimura,
Proceedings of The US-Japan Workshop and The Satellite Meeting of ITC-9 on Physics of High Beta Plasma Confinement in Innovative Fusion System, Dec. 14-15, 1998, NIFS, Toki; Apr. 1999

NIFS-PROC-42 (Eds.) H. Akiyama and S. Katsuki,
Physics and Applications of High Temperature and Dense Plasmas Produced by Pulsed Power; Aug. 1999